Unraveling the interplay between composition, electronic band structure and electronic transport properties in n-type Mg_2X (X: Si, Sn) materials

A dissertation

submitted for the degree of

Doctor rerum naturalium

(Dr. rer. nat.)

By

Aryan Sankhla



Institut für Anorganische und Analytische Chemie

Justus-Liebig-Universität Gießen

Gießen, 2024

Unraveling the interplay between composition, electronic band structure and electronic transport properties in n-type Mg_2X (X: Si, Sn) materials

A dissertation

submitted for the degree of

Doctor rerum naturalium

(Dr. rer. nat.)

By

Aryan Sankhla

SUPERVISORS

Prof. Dr. W. Eckhard Müller

Prof. Dr. Peter J. Klar



Institut für Anorganische und Analytische Chemie

Justus-Liebig-Universität Gießen

Gießen, 2024

I dedicate this work to

my beloved

Mother (Mrs. Sudha Sankhla),

Father (Late Mr. Mahendra Sankhla)

&

Uncle ji (Late (Med.) Dr. Kushal Singh Gehlot).



Selbständigkeitserklärung

„Ich erkläre: Ich habe die vorgelegte Dissertation selbstständig und ohne unerlaubte fremde Hilfe und nur mit den Hilfen angefertigt, die ich in der Dissertation angegeben habe. Alle Textstellen, die wörtlich oder sinngemäß aus veröffentlichten Schriften entnommen sind, und alle Angaben, die auf mündlichen Auskünften beruhen, sind als solche kenntlich gemacht. Ich stimme einer evtl. Überprüfung meiner Dissertation durch eine Antiplagiat-Software zu. Bei den von mir durchgeführten und in der Dissertation erwähnten Untersuchungen habe ich die Grundsätze guter wissenschaftlicher Praxis, wie sie in der „Satzung der Justus-Liebig-Universität Gießen zur Sicherung guter wissenschaftlicher Praxis“ niedergelegt sind, eingehalten.“

Datum: 26/03/2024 Unterschrift

Acknowledgements

First and foremost, I want to sincerely thank my supervisors, Prof. Dr. Eckhard Müller and Jun.-Prof. Dr. Johannes de Boor for their continuous support through invaluable guidance, patience, constructive criticism, and encouragement throughout my Ph.D. tenure. I count myself fortunate enough to be mentored by the luminaries of the field of thermoelectric research.

I want to specially acknowledge my daily supervisor Jun.-Prof. Dr. Johannes de Boor who invested his time and energy to improve my understanding of science and the quality of this work. I have received his relentless support at different stages of my Ph.D. journey. The consistent mentorship and guidance from him were the cornerstone of my transformation from a naïve and motivated student to a self-reliant, perspicacious, and pragmatic researcher.

I am indebted to Prof. Dr. Peter J. Klar, who agreed upon being my second supervisor at the Justus-Liebig University of Giessen (JLU) and providing me pointers to further improve the quality of this thesis.

I was lucky enough to meet my office-mate *cum* friend Dr. Hasbuna Kamila (Mila). She is a gem of a person. She was the one who taught me band structure modelling and its interpretation. She was always there to discuss scientific problems and gave me valuable insights on my work. I am deeply thankful for her enduring presence and support during good and challenging times.

I am grateful to the other past and present members of my research group: Akash, Mohammad, Nader, Ngan, Antoine, Prasanna, Nhi, Julia, Sahar, Radhika, Sanyukta, Kalpna, Gustavo, Silvana, Nacho, Kunal, Laura, Venkatesh, Leo, Pawel, Gregor, Klaus, Severin, Matthias, Vidushi, Adina, Amandine, Roberto, Karsten, Lennart, Markus, Reinhard and Christian. All these guys made our department a happy, less stressful and a fun place. Besides, I would like to specially thank Mr. Przemyslaw Blaschkewitz for his continuous support with the measurement of thermoelectric properties. I am also thankful to Dr. Gagan Kumar Goyal and Mr. Prashant Sahu for valuable scientific discussions. I am deeply thankful for the late Dr. Dinesh K. Misra's guidance and encouragement during early days of my Ph.D. tenure. His kind and inspiring words were a source of strength and motivation for me, and he was the first person to give me the unofficial title of a 'Doctor'.

I would like to thank few members of my research group namely Mila, Radhika, Harshita and Amandine who spared their time to review some of the chapters of this thesis.

I want to mention a group of my friends, Dr. Diwakar Kashyap, Mr. Rajeshwar Sharma and Mr. Raghvendra Singh Yadav who were always there to support me during my Ph.D. journey. I would also like to thank my friends from my master's program (currently, in Germany): Dr. Tarachand Taak, Dr. Neeraj Upadhyay, Dr. Jai Prakash Kushwaha, Dr. Navid Hussain and Dr. Rakshit Dadarwal. They were the ones who always cheered me up, supported me and reduced my stress levels during this journey.

I would also like to thank my Master's thesis supervisor Dr. Pankaj Kumar Patro who introduced me to the field of thermoelectrics. The encouragement from Dr. Patro has been a consistent source of motivation for me during my Ph.D., which enabled me to stay focused on my goals.

I would like to express my heartfelt gratitude to my mother, Mrs. Sudha Sankhla, for her love, belief in me, and the sacrifices she made for me. Your hard work, sanskara and blessings have given me the strength to overcome any obstacle and made me the person I am today. You are the reason behind my success, Love you mama! I am grateful to my elder brother, Anupam, and my sister-in-law, Nidhi, for being such a positive influence in my life. Your love, constant support, and blessings have been the key to my success and happiness. I am deeply appreciative of my nephew, Hitarth, and niece, Toshini. A mere presence of these guys was a source of immense joy that made my yearly break even more memorable and relaxing. I would like to thank my lovely wife Vandana who understood my priorities and constantly motivated me during my thesis writing phase. Having such an amazing person as my partner has added value to my life.

In composing this work, I find it paramount to praise and thank almighty 'Shiva', whose boundless grace has transcended the pages of this work. While writing this, I am reminded of the palpable presence of god in the journey of this work and my life.

Above all, with profound humility and reverence, I offer Sashtanga Dandavat Pranama to my 'Guruji' (the divine architect of my life). I would like to dedicate this work to my guruji as well. I have been able to surmount challenges during this work due to his countless blessings, which made this academic achievement possible. He has been a guiding force behind my academic endeavors who also inspires me to delve deeper into knowledge. The presence of my guruji has transformed my life and his teachings have illuminated my life's journey with wisdom.

Lastly, I would like to acknowledge the DLR-DAAD fellowship (Fellowship no. 247) which was crucial for me to financially support my stay in Germany through most duration of my Ph.D. tenure.

List of abbreviations, symbols and notations

Abbreviations

TE	Thermoelectric
TEGs	Thermoelectric generators
RTGs	Radioisotope thermoelectric generators
NASA	National Aeronautics and Space Administration
TC	Thermocouple
PF	Thermoelectric power factor
DOS	Density-of-states
CB	Conduction band
B-field	Magnetic field flux
RTA	Relaxation time approximation
BTE	Boltzmann transport equation
SPB	Single parabolic band
AP	Acoustic phonon
AS	Alloy scattering
GB	Grain boundary
RT	Room temperature
VBM	Valence band maximum
CBM	Conduction band minimum
HEBM	High energy ball mill
SPS	Spark plasma sintering
MA	Mechanical alloying
PD	Point defects
CTE	Coefficient of thermal expansion
GCF	Geometric correction factor
DSP	Direct current sintering press
TEM	Transmission electron microscope
2PB	Two parabolic band
HT-$S\sigma$	High temperature setup for measuring the Seebeck coefficient and the electrical conductivity
HT Hall	High temperature Hall measurement facility
BPR	Ball to powder weight ratio
XRD	X-ray diffraction
SEM	Scanning electron microscope

EDS	Energy dispersive X-ray spectroscopy
SE	Secondary electrons
BSE	Back-scattered electrons
SAED	Selected area electron diffraction
CBED	Convergent-beam electron diffraction
HR-TEM	High-resolution TEM
HAADF	High-angle annular dark-field imaging (or Z-contrast imaging)
EELS	Electron energy-loss spectroscopy
FEG	Field emission gun
AC	Alternating current
vdP	Van der Pauw
FEM	Finite element modelling
CFC	Carbon-fiber reinforced carbon composite
LIA	Lock-in amplifier
RR	Reference resistor
DMM	Digital multimeter
S. D.	Standard deviation
DC	Direct current
R. D.	Relative deviation
GUI	Graphical user interface
RSS	Residual sum-of-squares
RMSD	Root mean square deviation
CMRR	Common-mode rejection ratio
FWHM	Full width at half-maximum

Symbols and notations

Fundamental constants

Quantity	Symbol	Values
Planck's constant	h	6.62×10^{-34} J s
Electron rest mass	m_0	9.1×10^{-31} kg
Boltzmann's constant	k_{B}	1.38×10^{-23} J K^{-1}
Reduced Planck's constant	$\hbar = h/2\pi$	1.05×10^{-34} J s
Fundamental electron charge	e	1.6×10^{-19} C

Physical quantities

Quantity	Symbol	Units
Time	t	s
Heat	Q	J
Energy	E	eV
Force	F	N
Length	x	m
Voltage	U	V
Resistance	R	Ω
Heat flow	$\dot{Q}$	W
Temperature	T	K
Electric field	$\vec{E}$	V m^{-1}
Electric current	I	A
Electrical power	P	W
Carrier acceleration	$\dot{v}$	m s^{-2}
Average temperature	$\bar{T}$	K
Hot side temperature	T_{H}	K
Cold side temperature	T_{C}	K
Temperature gradient	$\vec{\nabla}T$	K m^{-1}
Temperature difference	ΔT	K
Electric current density	j	A m^{-2}

Thermoelectric properties

Quantity	Symbol	Units
Density	ρ	g cm^{-3}
Hall voltage	U_{H}	V
Hall pre-factor	r_{H}	-
Hall coefficient	R_{H}	cm^3 C^{-1}
Lorentz number	L	V^2 K^{-2}
Peltier coefficient	Π	V
Thomson coefficient	τ	V K^{-1}
Magnetic field flux	B	T (or kg m^2 s^{-2}A^{-1})
Thermal diffusivity	α	m^2 s^{-1}
Thermal conductance	K	W K^{-1}
Conversion efficiency	η	-
Electrical conductivity	σ	S cm^{-1}
The Seebeck coefficient	S	μV K^{-1}
Total thermal conductivity	κ	W m^{-1}K^{-1}
Hole carrier concentration	p	cm^{-3}
Thermoelectric power factor	$S^2\sigma$	W m^{-1}K^{-2}
Lattice thermal conductivity	κ_{lat}	W m^{-1}K^{-1}
Bipolar thermal conductivity	κ_{bi}	W m^{-1}K^{-1}
Electron carrier concentration	n	cm^{-3}
Electronic thermal conductivity	κ_{el}	W m^{-1}K^{-1}
Hall carrier concentration of electrons	n_{H}	cm^{-3}
Thermoelectric figure of merit of devices	ZT	-
Specific heat capacity at constant pressure	c_{P}	J kg^{-1}K^{-1}
Dulong-Petit limit of specific heat capacity	c_{V}^{DP}	J kg^{-1}K^{-1}
Thermoelectric figure of merit of materials	zT	-
Voltage measurement for electrical conductivity	U_σ	V

Semiconductor physics related quantities

Quantity	Symbol	Units
Grain size	B	µm
Wave vector	k	m^{-1}
Fermi level	E_{F}	eV
Drift velocity	v_{d}	m s^{-1}
Barrier height	E_{B}	eV
Energy offset	ΔE	eV
Drift mobility	μ_{d}	cm^2 V^{-1}s^{-1}
Hall mobility	μ_{H}	cm^2 V^{-1}s^{-1}

Semiconductor physics related quantities (continued)

Quantity	Symbol	Units
Fermi function	f_0	-
Atomic density	N_0	cm^{-3}
Reduced energy	ϵ	J ($k_B T$)
Relaxation time	τ	s
Average energy	E_{avg}	eV
Specific heat	C_v	$J\ kg^{-1}K^{-1}$
Carrier mobility	μ	$cm^2\ V^{-1}s^{-1}$
Carrier scattering	s	-
Density of states	$g(E)$	$eV^{-1}\ m^{-3}$
The Fermi integral	$F_j(\eta)$	-
Valley degeneracy	N_V	-
Mobility parameter	$\mu_{0,s}$	$cm^2\ V^{-1}s^{-1}$
Scattering parameter	λ	-
Inertia effective mass	m_I^*	kg
Phonon group velocity	v	$m\ s^{-1}$
Phonon mean free path	l	nm
Relaxation time constant	$\tau_{0,s}$	-
Conduction band energy	E_C	eV
Atom fraction (Sn content)	x	-
Longitudinal elastic constant	C_l	Pa
Longitudinal speed of sound	v_l	$m\ s^{-1}$
Minimum energy of the band	E_0	eV
Deformation potential constant	E_{Def}	eV
Thermoelectric material parameter	β	-
Alloy scattering potential constant	E_{AS}	eV
Reduced electron chemical potential	η	J ($k_B T$)
DOS effective mass for a single valley	m_{SV}^*	kg
Net carrier concentration due to dopant (including intrinsic and extrinsic defects)	N_D	cm^{-3}
Total density of states (DOS) effective mass	m_D^*	kg

Quantities related to synthesis and measurement

Quantity	Symbol	Units
Thickness	d	mm
Diameter	D	mm
Sintering time	t_{sinter}	min
Annealing time	t_{anneal}	h

Quantities related to synthesis and measurement (continued)

Quantity	Symbol	Units
Tip spacing	s	mm
Order of reflection	n	-
Sintering temperature	T_{sinter}	K
Annealing temperature	T_{anneal}	K
Lattice spacing (d-spacing)	d'	Å
Wavelength of incident ray	λ	nm
Isothermal compressibility	β_{T}	Pa^{-1}
Geometrical correction factor	C	
Coefficient of thermal expansion	E_{t}	K^{-1}
Mg deficiency in $\text{Mg}_{2-\delta}(\text{Si, Sn})$	δ	-
Angle of incidence and reflection of incident ray	θ	°

Quantities related to the Hall measurement system

Quantity	Symbol	Units
Goodness-of-fit	R^2	-
Differential gain	A_d	-
Sample resistance	R_{S}	Ω
Internal resistance	$R_{\text{int.}}$	Ω
Differential voltage	U_d	V
Common-mode gain	A_{CM}	-
Open circuit voltage	U_{oc}	V
Outer circuit resistance	$R_{\text{C,I}}$	Ω
Correlation coefficient	$R_{\text{C.C.}}$	-
Amplified output voltage	U_a	V
Hall voltage at $B = 0$ T	$U_{\text{H},B=0}$	V
Common-mode input voltage	U_{CM}	V
Probe to edge (of sample) distance	a	mm
Voltage drop at positive terminal of the LIA	U_{P}	V
Voltage drop at negative terminal of the LIA	U_{N}	V
Number of points at each (magnitude of) B-field	$U_{\text{H,1B}}$	-
Number of sweeps (B-field) at each temperature point	S_{N}	-

Quantities related to the Arrhenius analysis

Quantity	Symbol	Units
Diffusion flux	J	atoms $cm^{-2}s^{-1}$
Activation energy	E_a	kJ mol^{-1} (or eV)
Molar gas constant	R	J $mol^{-1}K^{-1}$
Diffusion coefficient	D	cm^2 s^{-1}
Pre-exponential factor	A	h^{-1}
Concentration gradient	$\nabla\varphi$	atoms cm^{-4}
Chemical potential of Mg	μ_{Mg}	J mol^{-1}
Equilibrium (or rate) constant	K	h^{-1}
Pre-exponential factor (diffusion)	D_0	cm^2 s^{-1}
Activation enthalpy of diffusion process	$\Delta\mathrm{H}$	kJ mol^{-1} (or eV)
Chemical potential difference (with respect to Mg)	$\Delta\mu_{\mathrm{Mg}}$	J mol^{-1}

Other relevant quantities

h^+	Hole
e^-	Electron
$\dot{Q}_{\mathrm{in}}$	Absorbed heat
C_{L}	Light conduction band
C_{H}	Heavy conduction band
$\mathrm{Sn}_{\mathrm{Mg}}$	Mg on Sn site (anti-site)
$\sigma'(E)$	Differential conductivity
V_{Mg}	Mg vacancy (charged: V_{Mg}^{2-})
I_{Mg}	Mg interstitial (charged: I_{Mg}^{2+})
$\Xi(E)$	Transport distribution function
$n_{\mathrm{D,Sb}}^{+}$	Carrier concentration due to ionized donor Sb atoms
$n_{\mathrm{D,Mg}}^{+}$	Carrier concentration due to ionized donor Mg atoms
$n_{\mathrm{a,Mg}}^{-}$	Carrier concentration due to ionized acceptor Mg atoms
$R_{\mathrm{C,II}}$	Resistance of the outer circuit II (cables, feedthroughs, probes etc.)
$d\dot{Q}_{\tau}$	Thomson heat generated (or absorbed) at each infinitesimal length (dx)

TABLE OF CONTENTS

Zusammenfassung 1
Abstract 7
Chapter 1 Introduction 11
1.1 Thermoelectric effects 12
1.1.1 Seebeck effect 13
1.1.2 Peltier effect 14
1.1.3 Thomson effect 14
1.2 Thermoelectric devices and the thermoelectric figure of merit 15
1.3 Optimization of the thermoelectric efficiency 18
Chapter 2 Electronic transport theory, semiconductor transport models, transport coefficients and material basics on $Mg_2(Si,Sn)$ 23
2.1 Summary 23
2.2 Electronic transport theory 23
2.2.1 Carrier scattering 30
2.2.2 Carrier concentration and the Hall coefficient 30
2.2.3 Electrical conductivity and mobility 31
2.2.4 The Seebeck coefficient 34
2.2.5 Electronic contribution of thermal conductivity and total thermal conductivity 37
2.2.6 Optimization of thermoelectric figure-of-merit 39
2.2.7 Mixed conduction 40
2.3 Material basics of Mg_2X (X: Si, Sn) 42
2.3.1 Physical properties 42
2.3.2 An overview of TE properties of Mg_2X (X: Si, Sn) solid solutions 50
Chapter 3 Summary of Research 57
3.1 Summary 57
3.2 Scientific questions 57
3.3 Overview of the thesis 60
Chapter 4 Experimental methods 63
4.1 Summary 63
4.2 Synthesis 63
4.2.1 Mechanical alloying (MA) 63
4.2.2 High temperature sintering step 64
4.3 Characterization 69
4.3.1 Structural and chemical characterization 69
4.3.2 Characterization of thermoelectric transport properties 76
Chapter 5 Establishing and analysis of high temperature Hall measurements 85
5.1 Summary 85
5.2 Purpose and relevance 86
5.3 Theoretical background of van der Pauw method 86
5.3.1 The electrical conductivity 88
5.3.2 The Hall coefficient 89

5.4 Components of the measurement system 90
5.4.1 The magnet 91
5.4.2 Sample holder 91
5.4.3 Controlled recipient 92
5.4.4 Thermocouples 93
5.4.5 The heater 93
5.4.6 Measurement power supply and measurement of electrical signals 93
5.4.7 Switch system and multimeter 94
5.4.8 Electrical connections 94
5.5 Geometric correction factors 95
5.6 Measurement acquisition routine 95
5.7 Data analysis routine 96
5.8 An assessment of the quality and reliability of the Hall coefficient measurements 97
5.8.1 Hall voltage – ideal and real measurement 97
5.8.2 Error indicators 100
5.8.3 A Comparison of the measurements of the Hall coefficient and the electrical conductivity at room temperature 102
5.9 Results and discussion 104
5.9.1 Utilizing GCF equations and their validation 105
5.9.2 A comparison of the measurement of the Hall coefficient and the electrical conductivity on a reference specimen at high temperatures 108
5.10 Conclusion 111
Chapter 6 Understanding the synthesis mechanism of optimized n-type $Mg_2Si_{0.4}Sn_{0.6}$ and tuning the synthesis parameters 112
6.1 Summary 112
6.2 CRediT (Contributor Roles Taxonomy) author statement 112
Chapter 7 Attempt to modify the electronic band structure in Mg_2X (*X*: Si, Sn) for an optimization of thermoelectric properties 125
7.1 Summary 125
7.2 CRediT (Contributor Roles Taxonomy) author statement 125
Chapter 8 Influence of sintering duration on the transport properties and the critical role of Mg 132
8.1 Summary 132
8.2 CRediT (Contributor Roles Taxonomy) author statement 132
Chapter 9 Analyzing the effect of *in-situ* annealing on the thermoelectric properties of n-type $Mg_2Si_{0.4}Sn_{0.6}$ 144
9.1 Summary 144
9.2 CRediT (Contributor Roles Taxonomy) author statement 144
Chapter 10 Discussion 153
10.1 Summary 153
10.2 *In-situ* measurement of the electrical transport properties 154
10.2.1 Analysis of the transport properties measured at 773 K 155
10.2.2 *In-situ* measurement of transport properties while annealing at 848 K 160
10.3 Studying the kinetics of Mg loss in $Mg_2(Si,Sn)$ 161
10.4 Conclusion 177

Chapter 11 Conclusions and Outlook 179
11.1 Conclusions 179
11.2 Outlook 182
11.2.1 Optimization of synthesis methods 182
11.2.2 A detailed investigation of the microstructure using advanced techniques 183
Appendix A 186
A.1 Circuit of the Hall measurement system 186
A.2 Comparative measurement of the Hall carrier concentration – after implementation of correct GCF value and temperature dependence of the electrical conductivity 187
A.3 Temperature dependent Seebeck coefficient and electrical conductivity, and Hall coefficient and electrical conductivity data of p-type $FeSi_2$ 188
Appendix B 189
B.1 Predicting the electrical transport properties measured during *in-situ* annealing at 773 K 189
B.1.1 Two-band modelling using the non-annealed values of microscopic material parameters 194
B.1.2 Two-band modelling using the post-anneal values of the microscopic material parameters 195
B.1.3 Hall coefficient: Measured versus predicted (from different cases) 197
B.2 Temperature dependent thermoelectric properties of sample 4 (Measured before *in-situ* annealing at 773 K) 199
B.3 Temperature dependent thermoelectric properties of sample 3 and sample 4 (Measured after *in situ* annealing at 773 K) 200
References 201

List of figures

Figure 1.1 A schematic of the Seebeck effect in an open circuit condition where a) an n-type and b) a p-type semiconductor is under temperature difference $\Delta T = T_{\mathrm{H}} - T_{\mathrm{C}}$. Here, T_{H} is the hot-side temperature and T_{C} is the cold-side temperature, and ΔT is shown to increase from T_{C} to T_{H}. The charge carriers namely, electrons e^-(n-type) and holes h^+ (p-type) diffuse preferentially from the hot side to the cold side, respectively, until the induced voltage U is generated that opposes a further diffusion of carriers from hot side to the cold side. The induced voltage (a difference in electric potential) for an n-type and a p-type semiconductor is labelled as U_{e} and U_{h}, respectively. 13

Figure 1.2 Schematic of a TE uni-couple comprising of a p- and n-type semiconductor that represents a) power generation and b) cooling mode respectively. Note that the semiconductor legs are connected *via* metal interconnects (represented in grey). The red and blue color represents hot side and cold side, respectively. 15

Figure 1.3 Theoretical efficiency (η) of a TE generator as a function of ΔT (with $T_{\mathrm{C}} = 300$ K) for a range of $z\bar{T}$. The plot has been reprinted (adapted) with the permission from [18]. 17

Figure 1.4 Temperature dependence of zT values for some typical classes of (a) n-type and (b) p-type bulk TE materials. In the legend of these plots TAGS stands for $(GeTe)_{1-x}(AgSbTe_2)_x$ while SKD and LAST stand for Skutterudites and lead antimony silver telluride, respectively. The plot has been reprinted (adapted) with the permission from [20]. 18

Figure 1.5 zT as a function of n in the range $10^{18} - 10^{21}\mathrm{cm}^{-3}$. $zT_{\max}$ is obtained in the range of $10^{19} - 10^{20}$ cm^{-3}. $PF_{\max}$ is obtained at higher n than zT. The plot has been reproduced (adapted) with the permission from [1]. 19

Figure 1.6 a) T-dependent zT of $Mg_{2-\delta}(Si_{0.3}Sn_{0.7})_{0.98}Sb_{0.02}$ reported by Yin *et al.* [42] ($\delta = -0.16$), Zhang *et al.* [43] ($\delta = 0$ to -0.14), Yin *et al.* [44], Zhang *et al.* [41] ($\delta = -0.16$), Liu *et al.* [45] ($\delta = -0.1$) and Zhang *et al.* [46] (no information on δ). n at room temperature (RT) (b), and c) T-dependent κ is shown for the samples in respective reported studies. 21

Figure 2.1 a) $f_0(\mathrm{E})$ at different temperatures and b) its derivative as a function of energy E. The plot has been reproduced (adapted) with the permission from [66]. 26

Figure 2.2 Schematic of a CB along with the position of E_{F} and E_{avg} for (a) low and (b) high carrier concentration n. 35

Figure 2.3 (a) The Seebeck coefficient S as a function of η at 300 K and $\lambda = 0$. (b) Experimentally measured $S(n_{\mathrm{H}})$ for Bi- and Sb-doped $Mg_2Si_{0.3}Sn_{0.7}$ at 300 K. The plot in (b) has been reproduced (adapted) from Ref. [83] with permission from the Royal Society of Chemistry. 36

Figure 2.4 Schematic of a CB along with the change in position of η with temperature in the $E(k)$ plot. η decreases towards the CB edge and beyond as temperature increases. 37

Figure 2.5 Different strategies employed for phonon engineering that are categorized into methods affecting each component of κ_{lat}, such as specific heat (C_{v}), phonon group velocity (v), and mean free path (l). The figure has been reproduced (adapted) from Ref. [84] with permission from the Royal Society of Chemistry. 38

Figure 2.6 Crystal structure of Mg_2X (X = Si, Ge, and Sn) compounds. The octahedral interstitial sites (4b) can be occupied by Mg. The plot has been reprinted with permission from [93]. 42

Figure 2.7 Band structure schematic showing the energy dependence of the electronic bands, both valence and conduction bands, on Sn content in $Mg_2Si_{1-x}Sn_x$ based on DFT calculations. Particularly, the energetic position of the heavy conduction band (C_{H}) which contain electrons with a higher m^*_{SV}, and the light conduction band (C_{L}) which contain electrons with a lower m^*_{SV}, vary with the Sn content. The composition of $x = 0.65 \sim 0.7$ shows a convergence of these two conduction bands. This figure has been reprinted with permission from [99]. 43

Figure 2.8 a) Classification of point defects and b) Illustration – Intrinsic (top) and Extrinsic (bottom) point defects. The figure is (b) has been re-printed under the terms of the Creative Commons Attribution-Non Commercial-No Derivatives License and requires no permission for non-commercial use [121]. 45

Figure 2.9 a) zT of $Mg_2Si_{1-x}Sn_x$ (with $x = 0 - 1$) as a function of doping density at 700 K. The plot has been reproduced from the results reported by Bahk *et al.* [23]. The measured n_H and the experimental zT reported by Liu *et al.* [83] ($x = 0.7$) (Bi-doped) and Søndergaard *et al.* [157] ($x = 0.6$) (Sb-doped) is shown. E vs k schematic for these compositions is shown in (b) that represents the convergence of the conduction bands responsible for an enhancement of the Seebeck coefficient, and thus, zT shown in (a). A schematic of the corresponding Brillouin zone is also shown in (c) [83]. The presented figure has been reprinted with permission from [23, 83, 157] respectively. 51

Figure 2.10 Plots showing variation in a) n, b) m_D^* and c) μ before and after annealing $Mg_2Si_{0.3}Sn_{0.7}$ [42] (study number 1), $Mg_2Si_{0.4}Sn_{0.6}$ [165] (study number 2) and $Mg_2Si_{0.5}Sn_{0.5}$ [146] (study number 3), all doped with ~0.067 at.% Sb. Note that for Kato's study the annealing was conducted in different Mg partial pressure environment (Mg-rich (10 Pa) and Mg-poor (0.1 Pa)). Some microscopic material parameters such as m_D^* for Kato's data and m_D^* and μ corresponding to Zhang's study shown here were *not* published but numerically obtained by analyzing RT thermoelectric properties from corresponding reports using a SPB model developed for the work presented in this thesis. 53

Figure 2.11 T-dependent S and σ of $Mg_2Si_{1-x}Sn_x$ with $x = 0, 0.6, 0.7$ and 1. The data is taken from the reports published by Bux *et al.* [115], Goyal *et al.* [166], Yin *et al.* [42, 44], Liu *et al.* [45, 83, 99], Zhang *et al.* [41, 43, 46] and Zhu *et al.* [167]. Each of these studies used $3 - 7$ at.% excess Mg to compensate for the Mg loss. Note that the transport properties of Sb doped compositions of both binaries are shown for comparison. 54

Figure 2.12 Calculated [171] (dashed green) and experimental κ_{lat} (symbols) of undoped [83, 166, 172] (with $x = 0 - 1$), n-type [83, 99, 166, 170] and p-type [114, 120] $Mg_2Si_{1-x}Sn_x$ at 300 K. 55

Figure 4.1 Schematic of changes occurring in a powder compact at microscale, which is subjected to high temperature sintering. (a) Loose powder particles after cold pressing. (b) Initial, (c) intermediate and (d) final stage of sintering. The figure has been reprinted (adapted) with the permission from [183, 184]. 65

Figure 4.2 Geometrical models for (a) intermediate stage and (b) final stage sintering proposed by Coble *et al.* [182]. The plot has been reprinted (adapted) with the permission from [185]..... 66

Figure 4.3 Work flow of the synthesis route, characterization and the analysis of the n-type Mg_2X (X: Si, Sn) and their solid solution prepared using HEBM. There are two synthesis steps: MA (by HEBM) and DSP. The sintered materials are characterized for structural, chemical and TE properties.... 68

Figure 4.4 (a) A scheme highlighting two atomic planes separated by a spacing, d', with incident and diffracted waves (Bragg's law) and (b) a schematic of the D5000 diffractometer setup [192]. The figure has been reprinted (adapted) with the permission from [191]. 70

Figure 4.5 A schematic illustration of the interaction volume (teardrop shaped) between a focused electron beam and a solid sample showing a variety of generated signals. The figure has been reprinted (adapted) with the permission from [195]. 72

Figure 4.6 A schematic illustration of electron beam-specimen interaction in a TEM column showing a variety of signals generated. The image has been taken from [196]. 75

Figure 4.7 (a) Mounted sample in the sample holder and (b) system of the mechanical and electrical connections for the HT-$S\sigma$ facility. Note that the sheath of thermocouples acts as current feed for electrical conductivity measurement. This image has been reprinted with the permission from [197]..... 76

Figure 4.8 Temperature dependence of (a) the Seebeck coefficient S and (b) the electrical conductivity σ of $Mg_{2.06}Si_{0.385}Sn_{0.6}Sb_{0.015}$ while heating up and cooling down the sample. 78

Figure 4.9 Schematic sketch of the sample holder for the Hall measurement in a van der Pauw geometry. 80

Figure 4.10 Schematic illustration of the laser flash method for thermal diffusivity measurement. The right sub-figure shows a zoom-in of the furnace where the sample is placed. These images are reprinted from [205]. 82

Figure 4.11 Plot showing signal measured from the rear side (facing the detector) of the sample that corresponds to a temperature rise at the sample surface, as a function of time. The plot has been reconstructed from [206].....83

Figure 5.1 Different specimen and contact geometries for the measurement of both the Hall voltage U_{H} and measured voltage (U_{σ}) corresponding to the electrical conductivity of a specimen using the traditional and the van der Pauw method, respectively. Probe positions for electrical conductivity σ measurement with the traditional and the van der Pauw method is shown in (a), (c) and (d) respectively. The Hall coefficient R_{H} measurement using the traditional and the van der Pauw technique is shown in (b) and (e). The direction of the magnetic field ($\vec{B}$) is represented by $\otimes$ meaning that the field is perpendicular and inwards the plane (away from the reader) with respect to the specimen in (b) and (e).....87

Figure 5.2 a) Schematic of the Hall measurement system, and the corresponding b) electrical circuit of the measurement system. 90

Figure 5.3 a) The sample holder integrated on the measuring head of the Hall facility. The sample holder is zoomed-in showing thermocouple probes in b), while c) shows the schematic of the van der Pauw configuration for the Hall measurement (for comparison). The probe-to-edge distance, a, indicates that the probes do not exactly lie on the sample edges. The specimen is d) mounted on the sample holder and e) pressed on the thermocouple tips with help of a ceramic stub. The specimen is supported by a piston on the other face of specimen. 92

Figure 5.4 Schematic change of the Hall voltage U_{H} with a change in the magnitude of B-field with respect to time t, with the direction of voltage drop in a) one direction, and b) in other direction. Note that the direction of voltage drop depends on the phase difference between the measured and the reference signal, explained in detail in relevant section below. c) & d) show U_{H} as a function of the magnitude of B-field from the black rectangular box in a) and b), respectively. Note that the U_{H} data shown here is synthetic data which is referred to as ideal. 98

Figure 5.5 2Y-plots showing a change of U_{H} and the magnitude of B-field with respect to time t. The plots show a) real (close to ideal), b) real (scattered) conditions while c) and d) show poor signal output with respect to change in the magnitude of B-field. 99

Figure 5.6 a) $U_{\mathrm{H},B=0}$, b) $R_{\mathrm{C.C.}}$ of U_{H} and B, and the c) $s\left(\frac{\partial U_{\mathrm{H}}}{\partial B}\right)$ ($\approx 10^{-10}$) across AC and BD configurations. The standard deviation is calculated after each filtering step (elaborated in the technical report [208]) of the data analysis program. The red and the blue data points in (c) and (d) correspond to heating and cooling temperatures respectively.....101

Figure 5.7 RT a) Hall carrier concentration & c) electrical conductivity of five different samples (both p-type and n-type) measured on the Hall facilities at DLR, IIT Bombay and JLU Gießen with van der Pauw configuration of the sample holder, and the corresponding relative deviation in b) n_{H} & d) σ measurement. Note that the n_{H} and σ measurements were carried out at relatively low temperature ($T \approx 277$ K) in the Hall facility at JLU Gießen.....103

Figure 5.8 a) Construction of the model in ANSYS, Inc. for a FEM of the sample holder with the color indicating the potential field forming U_{H}, (b) a schematic to show the position of the probes and the direction of B-field.....106

Figure 5.9 P and Q with respect to (a/D) for a) symmetric and b) asymmetric case. The relative deviation between P and Q for the respective cases is shown in blue. 107

Figure 5.10 T-dependence of a) R_{H} and b) relative deviation in the measurement. The red and blue curve in sub-figure (b) shows a relative deviation $(1 - (R_{\mathrm{H,DLR}}/R_{\mathrm{H,Aarhus}}))$ between the R_{H} measured at the HT Hall setup at DLR (with GCF according to van der Pauw's original work and the improved FEM derived values) and Aarhus University. 109

Figure 5.11 Temperature dependent a) electrical conductivity measured on HT-$S\sigma$ setup, Hall setup at DLR and Aarhus University, respectively, and b) relative deviation $(1 - (\sigma_{\mathrm{others}}/\sigma_{\mathrm{DLR,HT\ Hall}})$ between the measurement data conducted at different (HT-$S\sigma$ and Aarhus) facilities. 110

Figure 10.1 T-dependent measurement of a) S and b) σ of sample 3 ($Mg_{2.06}Si_{0.385}Sn_{0.6}Sb_{0.015}$) during a first thermal cycle. Figure c) and d) show S and σ measurements: cooling data during first thermal cycle (shown in (a) and (b)), measurement during heat-up ramp to reach $T_{\mathrm{anneal}} \approx 773$ K and a prediction (using SPB model) of T-dependent properties. SPB parameters used to predict the transport properties in (c) and (d) are $m_{\mathrm{D}}^{*} = 2.4m_0$, $n = 2.09 \times 10^{20}$ cm^{-3} and $E_{\mathrm{Def}} = 10.35$ eV, respectively. 155

Figure 10.2 The measurement of – a), b) S and c), d) σ of sample 3 ($Mg_{2.06}Si_{0.385}Sn_{0.6}Sb_{0.015}$) at $T_{\mathrm{anneal}} = 773$ K. 156

Figure 10.3 *In-situ* measured electrical conductivity σ of sample 3 (in HT-$S\sigma$) and sample 4 (HT Hall) at $T_{\mathrm{anneal}} = 773$ K, respectively; note the different x-axes. 157

Figure 10.4 a) S and b) σ of sample 5 (non-annealed $Mg_{2.06}Si_{0.385}Sn_{0.6}Sb_{0.015}$) measured at 848 K for a duration of nearly 2.5 hours. Note that the measurement temperature was not stable in the beginning of *in-situ* measurement. The actual measurement temperature (in K) is indicated close to the blue data points, while points in red indicate that the desired T_{anneal} is reached. 160

Figure 10.5 Schematic model of Mg loss in $Mg_2(Si,Sn)$. Note that the Mg chemical potential (μ_{Mg}) is different in the sample ($\mu_{\mathrm{Mg(s)}}$) and in the annealing surrounding ($\mu_{\mathrm{Mg(g)}}$). 165

Figure 10.6 Calculated charged defect formation energies of $Mg_2Si_{1-x}Sn_x$ ($x = 0.6$) in a) Mg-rich and b) Mg-poor environment. X in the figure legend refers to Si or Sn. The figure has been re-printed under the terms of the Creative Commons Attribution-Non Commercial-No Derivatives License and requires no permission for non-commercial use [147]. 168

Figure 10.7 $N_{\mathrm{D}}(t)$ and $\sigma(t)$ of (a) sample 1, (b) sample 3, (c) sample 4 and (d) sample 6 measured at T_{anneal} (710 K, 773 K and 848 K) in HT-$S\sigma$ and HT Hall facilities, respectively. $N_{\mathrm{D}}(t)$ for both non-annealed parameters and post-annealed parameters in b) are obtained by 2PB modelling of the *in-situ* measured thermoelectric properties. 170

Figure 10.8 $\ln(K)$ (in units of h) vs $1/T_{\mathrm{anneal}}$ (Arrhenius plot) from the rates determined by the exponential fitting of the $N_{\mathrm{D}}(t)$ and $\sigma(t)$ plots. The green curve is plotted using K estimated from $\sigma(t)$ measured in HT Hall while the orange (■) and blue (●) data points correspond to K estimated by fitting $\sigma(t)$ and $N_{\mathrm{D}}(t)$ measured in HT-$S\sigma$, and predicted from 2PB modelling, respectively. K at 848 K is estimated from extrapolation of the plots of both measured $\sigma(t)$ (in HT-$S\sigma$ facility) (□) and $N_{\mathrm{D}}(t)$ (○). 171

Figure 10.9 Carrier concentration n ($\approx N_{\mathrm{D}}$ at RT) of the samples sintered at 973 K for different durations. 173

Figure 10.10 Sample holder design of a) HT-$S\sigma$ and c), d) HT Hall facilities. In b) a picture of the sample after *in-situ* measurement in the HT-$S\sigma$ is shown which gives an idea about the sample area directly exposed to the annealing atmosphere while e) shows a schematic of a HT Hall sample indicating the surface area that is directly exposed to the annealing environment. Dotted lines show the boundaries of sample area exposed due to the design of the ceramic piston (covering back side of the sample) on which the sample is mounted while the solid black lines highlight the boundaries of sample area exposed due to the design of ceramic stub (on the front side of the sample) used to fix the sample on the holder. The image in (a) has been reprinted with the permission from [197]. 175

Figure A.1 A pictorial representation of the high temperature Hall measurement facility at DLR highlighting different electrical connections. 186

Figure A.2 a) RT Hall carrier concentration n_{H} of five different samples (both p-type and n-type tabulated in Table 5.1 in the main text) measured on the Hall facility at DLR (both with van der Pauw GCF and FEM corrected GCF values), IIT Bombay and JLU Gießen with a van der Pauw configuration of the sample holder, and b) the corresponding relative deviation in the measurement. The discrepancy between the n_{H} measured at DLR and other labs are a bit different after using the FEM corrected GCF, but the agreement is roughly as before. 187

Figure A.3 Temperature dependent electrical conductivity measured at JLU Gießen and HT-$S\sigma$ facility (at DLR). Note that the last data point measured at 277 K is highlighted which is shown in Figure 5.7 in the main text. 187

Figure A.4 Temperature dependent a) S and b) σ of p-type $FeSi_2$ specimen measured on HT-$S\sigma$ with both the heating and cooling curves of the measurement. 188

Figure A.5 Temperature dependent a) Hall coefficient and b) electrical conductivity of p-type $FeSi_2$ specimen which shows both the heating and cooling curves of the measurement. 188

Figure B.1 Temperature dependent a) Seebeck coefficient and b) electrical conductivity of sample 3 measured during cool-down from $T_{\mathrm{anneal}} \approx 773$ K. 189

Figure B.2 Flowchart of the approach to determine N_{D} from the measured Seebeck coefficient S and a two-band model. Microscopic material parameters of valence band are taken from [256] (kept constant) while different values of conduction band parameters ($m^*_{\mathrm{D,CB}}$ and $E_{\mathrm{Def,CB}}$) were chosen for different limiting cases. Here, S_{max} is the maximum absolute value of the Seebeck coefficient. The values of Seebeck coefficient, experimental $S_{\mathrm{max,exp}}$, and predicted $S_{\mathrm{max,2PB}}$ are compared to determine E_{g} and thus, N_{D}. 190

Figure B.3 Comparison of the absolute values of both measured and predicted Seebeck coefficient as a function of annealing duration and doping concentration N_{D} respectively. 193

Figure B.4 a) $S(N_{\mathrm{D}})$ predicted using a 2PB model, b) N_{D} vs t_{anneal} fitted using an exponential decay function, and the measured (at 773 K) and the predicted c) S, and d) σ, respectively. Note that the transport properties were predicted by employing non-annealed microscopic material parameters (NAP) in the 2PB model. 194

Figure B.5 a) $S(N_{\mathrm{D}})$ predicted using a 2PB model, b) N_{D} vs t_{anneal} fitted using an exponential decay function, and the measured (at 773 K) and the predicted c) S, and d) σ, respectively. Note that the transport properties were predicted by employing post-anneal microscopic material parameters (PAP) in the 2PB model. 196

Figure B.6 Comparative plot showing the R_{H} (corresponding to sample 3) predicted from 2PB model by plugging the different values of microscopic material parameters (NAP and PAP), as discussed, and the measured R_{H} (sample 4). 197

Figure B.7 T dependent a) S and b) σ of sample 4 measured at the HT-$S\sigma$ facility before *in-situ* measurements. c) n_{H} and d) σ of sample 4 during heat-up ramp for the *in-situ* measurement at the HT Hall facility. 199

Figure B.8 T dependent a) S and b) σ of sample 3, and c) R_{H} and d) σ of sample 4. These properties are measured during cooling after high-temperature *in-situ* annealing at $T_{\mathrm{anneal}} = 773$ K. 200

List of tables

Table 2.1 Expressions of the different scattering mechanisms (with $\lambda = 0$) and their dependence on T, m^*_{SV} and other microscopic material parameters [57, 67, 73, 74]. 32

Table 5.1 Sample code and composition for the specimens measured at different facilities. 102

Table 10.1 Sample number, measurement facility, T_{anneal} and t_{anneal} employed for the *in-situ* annealing measurement. S, σ and n_{H} measured at room temperature and density-of-states effective mass m^*_{D} predicted from the SPB model both before (B) and after (A) *in-situ* annealing are tabulated as well. The values with asterisk are predicted from an assumed m^*_{D}. 154

Table 10.2 The Arrhenius parameters (E_{a} and A) obtained by fitting ln (K) vs $(1/T_{\mathrm{anneal}})$. Note that the N_{D} was predicted from the two-band model while σ was measured in HT-$S\sigma$ and HT Hall facilities, respectively. 172

Table B.1 The values of the microscopic material parameters (N_{D}, $m^*_{\mathrm{D,CB}}$, $E_{\mathrm{Def,CB}}$) used for the 2PB modelling of *in-situ* measured thermoelectric properties. 191

Table B.2 List of microscopic material parameters other than the ones highlighted in Table B.1 employed for single- and multi-band modelling of electrical transport properties. 192

Zusammenfassung

Auf Mg_2X (X: Si, Sn) basierende Mischkristalle sind moderne thermoelektrische (TE) Materialien im mittleren Temperaturbereich (300 K – 900 K). Insbesondere n-leitendes $Mg_2Si_{1-x}Sn_x$ im Bereich $x = 0{,}6 - 0{,}7$ zeigt hervorragende TE Eigenschaften. Diese Materialien besitzen eine niedrige Massendichte, gute Umweltverträglichkeit und basieren auf gut verfügbaren und kostengünstigen Ausgangsstoffen. All diese Eigenschaften machen diese Materialien zu einer hervorragenden Wahl für die Herstellung von thermoelektrischen Modulen zur Stromerzeugung. Trotz der nachgewiesenen exzellenten TE Eigenschaften besteht ein offensichtlicher Bedarf an weiterer Forschung, um die Beziehungen zwischen Zusammensetzung, Synthese, Mikrostruktur und Eigenschaften dieser Materialien zu verstehen.

Die Motivation dafür ergibt sich aus der Tatsache, dass die bisher angewendeten Laborsyntheserouten in der Regel Tage bis Wochen für die Herstellung einer Materialcharge benötigen sowie aus der mangelhaften Reproduzierbarkeit der TE Eigenschaften von Proben mit nominell gleicher Zusammensetzung. Letzteres könnte auch auf ungenügende Genauigkeit bei der der Durchführung der Synthese zurückzuführen sein. Für die Entwicklung effizienter $Mg_2Si_{1-x}Sn_x$ TE Module sollte daher eine Syntheseroute zur Herstellung von $Mg_2Si_{1-x}Sn_x$-Materialien mit hoher Reproduzierbarkeit und kurzer Prozessdauer entwickelt werden. Außerdem sollten Syntheseparameter, die die TE-Eigenschaften beeinflussen, sowie die mikroskopischen Materialparameter, die durch eine Variation der Syntheseparameter beeinflusst werden, identifiziert werden.

Weiterhin ist die Hochtemperaturstabilität von $Mg_2Si_{1-x}Sn_x$-Materialien eine große technologische Herausforderung, die es zu bewältigen gilt, damit die Module langfristig funktionieren und ihre maximale Effizienz beibehalten. Frühere Studien haben gezeigt, dass die Temperaturstabilität von n-leitendem $Mg_2Si_{1-x}Sn_x$ bei etwa 800 K – 875 K durch Mg-Verluste beeinträchtigt wird. Diesen Studien mangelt es jedoch an einer angemessenen Methodik, da die Hochtemperaturtemperung zu einer Materialzersetzung und der Bildung von Sekundärphasen führt. Infolgedessen ist ein Vergleich der vor und nach dem Tempern gemessenen TE-Eigenschaften nicht aussagekräftig, da die nach dem Tempern gemessenen Eigenschaften für Mischphasenmaterial repräsentativ sind. In diesen Studien wurde auch der Degradationsmechanismus nicht genau beschrieben, und aus der berichteten Mikrostruktur können keine Rückschlüsse auf den Mechanismus gezogen werden. Diese Untersuchungen

unterstreichen die Tatsache, dass das praktisch relevante Thema der thermischen Stabilität von $Mg_2Si_{1-x}Sn_x$ tiefer untersucht werden muss.

Daher liegt der Schwerpunkt dieser Arbeit auf der Untersuchung der Beziehungen zwischen Zusammensetzung, Synthese, Mikrostruktur und Eigenschaften von n-Typ Mg_2X (X: Si, Sn) Mischkristallen und den Auswirkungen einer langfristigen Wärmebehandlung auf die elektrischen Transporteigenschaften dieser Materialien unter Verwendung von halbleiterphysikalischen Modellen.

Die Ladungsträgerkonzentration (n) ist ein grundlegender Parameter, der optimiert werden muss, um die besten TE-Eigenschaften eines jeden Materials zu erreichen. Daher wurde eine bereits vorhandene Hall-Anlage im Haus erfolgreich für Hochtemperaturmessungen ($T = 300$ K – 723 K) von $Mg_2Si_{1-x}Sn_x$ weiterentwickelt. Die Hall-Anlage ist in der Lage, gleichzeitig den Hall-Koeffizienten (R_H) und die elektrische Leitfähigkeit (σ) in einer van der Pauw-Konfiguration zu messen. Die Unsicherheit in den Signalen, die dem σ der Messung entsprechen, wurde untersucht, teilweise aufgelöst und quantifiziert. Der Einfluss einer nicht idealen Kontaktgeometrie auf die Messung wurde mit Hilfe von Finite-Elemente-Simulationen untersucht. Für bestimmte relevante Fälle wiesen die aus der Simulation und dem analytischen Ausdruck abgeleiteten Werte eine relative Abweichung $(\mathrm{R.D.}) > 5\,\%$ auf, so dass die Ergebnisse des analytischen Ausdrucks mit Hilfe der Simulationsergebnisse weiter korrigiert werden konnten. Raumtemperatur- und T-abhängige Messungen von R_H und σ an Mg_2(Si,Sn) und p-Typ $FeSi_2$ in der Hall-Anlage des DLR und anderen internationalen Forschungslabors zeigten eine gute Übereinstimmung der absoluten Messwerte mit einer relativen Abweichung von $\mathrm{R.D.} \leq 8\,\%$.

Zum besseren Verständnis der Beziehung zwischen Zusammensetzung, Synthese, Mikrostruktur und Eigenschaften wurde Sb-dotiertes $Mg_2Si_{0.4}Sn_{0.6}$ durch mechanisches Legieren synthetisiert. Anhand einer eingehenden Mikrostrukturanalyse wurde der Bildungsmechanismus dieses Materials durch mechanisches Legieren im Detail untersucht. Die Mg-Sn-Phase bildet sich leicht, gefolgt von einer langsamen Si-Diffusion in der duktilen Matrix. Die Untersuchungen zeigten jedoch, dass die Pulverprobe selbst nach umfangreicher Vermahlung nicht phasenrein war, weshalb ein Hochtemperaturverdichtungsschritt hinzugefügt wurde, der eine erfolgreiche Synthese der gewünschten Zusammensetzung ermöglichte. Die Wirkung der Syntheseparameter (Mahldauer, Sinterdauer und Temperatur) wurde systematisch untersucht. Die TE-Eigenschaften wurden durch die Mahldauer kaum beeinflusst. Allerdings nahm die Ladungsträgerkonzentration mit zunehmender Sinterzeit und Temperatur ab, was zu einer beobachtbaren Auswirkung auf die TE-Eigenschaften führte. Die

maximale TE-Leistung, gekennzeichnet durch eine TE-Kennzahl $zT \sim 1{,}4$, wurde für Proben erreicht, die 20 Minuten lang bei 973 K gesintert wurden.

Eine mikrostrukturelle Analyse auf TEM-Basis wurde an den Proben durchgeführt, die für verschiedene Dauern (10 min, 20 min und 40 min) bei 973 K gesintert wurden. Diese Analyse wurde mit dem Ziel durchgeführt, die Empfindlichkeit der TE-Eigenschaften gegenüber der Sinterdauer zu beobachten. Eine Verlängerung der Sinterdauer führte zu Mg-verarmten Korngrenzen und lokalen Inhomogenitäten in der Zusammensetzung. Die Transporteigenschaften dieser Proben wurden unter Verwendung eines Einzelparabelbandmodells (SPB) unter der Annahme von akustischen Phononen (AP) und Legierungsstreuungsmechanismen (AS) analysiert. Die Analyse ergab einen Ladungsträgerverlust, eine Abnahme der Ladungsträgerbeweglichkeit (μ) und eine Verringerung der Wärmeleitfähigkeit des Gitters (κ_{lat}) mit zunehmender Sinterdauer. Die geringere Beweglichkeit der Probe (mit längerer Sinterdauer 40 min) war auf eine kombinierte Wirkung von zunehmender Elektron-Phonon-Wechselwirkung (höhere Verformungspotenzialkonstante E_{Def}) und lokalen Inhomogenitäten in der Zusammensetzung zurückzuführen, die beide mit Mg-Verlusten einhergehen. Die veränderte Temperaturabhängigkeit der elektrischen Leitfähigkeit konnte durch die Berücksichtigung der Korngrenzenstreuung (GB) zusammen mit AP und AS reproduziert werden, wodurch die beobachteten Veränderungen der Mikrostruktur mit dem TE-Transport in Verbindung gebracht werden konnten. Die Kompensation zwischen einer niedrigeren Wärmeleitfähigkeit und der Mobilität der 40-minütig gesinterten Probe führte zu einer ähnlichen TE-Leistung wie bei kurzzeitig gesinterten Proben, mit $zT = 1{,}3 \pm 0{,}18$ für alle Proben. Das Fehlen eines starken Einflusses der Sinterdauer deutet darauf hin, dass $Mg_2Si_{1-x}Sn_x$ Materialien und damit auch die daraus hergestellten TE-Module einen gewissen Mg-Verlust verkraften können, ohne dass sich ihre Leistung verschlechtert.

Theoretische Untersuchungen haben Scandium (Sc) als Dotierselement für Mg_2X Materialien vorgeschlagen, da es zur Bildung von resonanten Zuständen in der elektronischen Bandstruktur führen könnte, die den Seebeck-Koeffizienten (S) und die gesamte TE-Leistung erheblich verbessern könnten. Dementsprechend wurde die Wirkung der Substitution von Mg durch Sc in Mg_2X *binären* und ihren Mischkristallen experimentell untersucht. Die TE-Eigenschaften wurden durch den Zusatz von Sc zu Mg_2X material nicht verbessert, was die Ergebnisse der theoretischen Studie widerlegt.

Die Auswirkung des Langzeittemperns auf die Transporteigenschaften von $Mg_2Si_{1-x}Sn_x$ wurde bei verschiedenen Temperaturen weiter untersucht. Die gewählten Temperaturen lagen in der Nähe des Betriebstemperaturbereichs von $Mg_2Si_{1-x}Sn_x$ basierten TE-Modulen. Aus den eigenen Untersuchung geht hervor, dass der Mg-Verlust unvermeidlich ist. Was fehlt, ist das Ausmaß und die Geschwindigkeit des Mg-Verlustes bei höheren Temperaturen. Darüber hinaus ist unklar, ob der mikroskopische Mechanismus der Degradation temperaturabhängig ist oder nicht. Vor diesem Hintergrund wurden die elektrischen Transporteigenschaften von sechs thermoelektrisch identischen Proben *in-situ* in zwei verschiedenen Versuchsanordnungen gemessen: S und σ (drei Proben), und R_{H} und σ (die anderen drei Proben) während des Temperns bei 710 K, 773 K and 848 K. Alle Proben waren weitgehend einphasig, ohne Anzeichen einer Entmischung nach dem Glühen über mehrere hundert Stunden. Die *in-situ* gemessenen Eigenschaften wurden mit Hilfe eines SPB- und eines Zwei-Parabelband-Modells (2PB, ein Leitungs- und ein Valenzband) analysiert. Die Analyse ergab einen Verlust von Majoritätsträgern aufgrund des fortschreitenden Mg-Verlustes bei fortschreitender Temperung. Außerdem wurde eine Verringerung der Mobilität aufgrund eines Anstiegs von E_{Def}, und eine Verringerung der effektiven Masse der Zustandsdichte (m_{D}^{*}) beobachtet. Diese Veränderung der genannten mikroskopischen Materialparameter könnte direkt mit einem fortschreitenden Mg-Verlust oder einer aufgehobenen Entartung der Leitungsbänder in $Mg_2Si_{0.4}Sn_{0.6}$ zusammenhängen.

Es wurde ein mikroskopisches, mehrstufiges Modell des Mg-Verlustes entwickelt, das den Mg-Transport von der Probe zur Umgebung qualitativ erklärt. Zeitkonstanten (und Raten) wurden aus der Veränderung der Ladungsträgerkonzentration und der *in situ* bei verschiedenen Temperaturen gemessenen elektrischen Leitfähigkeit geschätzt. Die Raten wurden in den Arrhenius-Ausdruck eingesetzt, um die Aktivierungsenergie für den gesamten Prozess zu bestimmen. Die Aktivierungsenergie wurde mit der Höhe der mit dem Mg-Transport verbundenen Energiebarrieren verglichen, um den begrenzenden Schritt in der Transportkette des Mehrstufenmodells zu bestimmen. Es wurde festgestellt, dass der Mg-Transport durch Mg-Leerstellen dominiert wird, da diese eine geringe Bildungs- und Migrationsenergie aufweisen. Mit dem etablierten Mechanismus wurde festgestellt, dass die beobachteten Veränderungen der Transporteigenschaften und die Unterschiede in der Rate und dem Frequenzfaktor von der Gestaltung der Messaufbauten abhängig sind. Die Ergebnisse dieser Arbeit beschreiben einen bisher *unbekannten* Synthesemechanismus für hochleistungsfähige n-Typ Mg_2(Si,Sn)-Mischkristalle durch mechanisches Legieren. Die Auswirkung der Syntheseparameter auf die Materialeigenschaften wird analysiert, was die Diskrepanzen in den Materialeigenschaften erklärt, die in verschiedenen Literaturen berichtet werden. Eine Auswirkung der

Hochtemperaturdegradation von n-Typ $Mg_2(Si,Sn)$ wird durch die Analyse von *in situ* gemessenen Transporteigenschaften verstanden, die die betroffenen mikroskopischen Materialparameter und das Ausmaß ihrer Verschlechterung aufzeigen. Schließlich wird die Kinetik des Mg-Verlusts in $Mg_2(Si,Sn)$-Mischkristallen des n-Typs anhand der Änderung der Konzentration der Hauptladungsträger beschrieben und ein Modell des Mg-Verlusts in $Mg_2(Si,Sn)$-Mischkristallen des n-Typs entwickelt.

Abstract

Mg_2X (X: Si, Sn) based solid solutions are state-of-the-art thermoelectric (TE) materials in the intermediate temperature range (300 K – 900 K). Particularly, the n-type $Mg_2Si_{1-x}Sn_x$ (with $x = 0.6 - 0.7$) shows excellent TE properties. These materials possess features such as a low mass density, abundant and economic precursors, and less interference to human and environmental health. All these characteristics makes these materials a prominent choice for the fabrication of modules for power generation. Even though these materials show a high TE performance, there is an obvious need for further research to understand the composition-synthesis-microstructure-property relationships for these materials. The motivation comes from the fact that the employed synthesis routes usually take days-to-weeks to prepare one batch of these materials, poor reproducibility of TE properties, and a large difference (beyond measurement uncertainty) in the TE properties of samples with nominally the same composition, as per the literature reports. The discrepancy could arise from the employed method, where the systematics are poorly understood i.e. more than one synthesis conditions (duration, number of repetitions of high temperature heating or milling etc.) could be responsible for the cited deviation in the TE properties. These aspects need to be systematically addressed. Therefore, for the development of efficient $Mg_2Si_{1-x}Sn_x$ modules, a synthesis route with optimized parameters should be established which can be achieved by utilizing a technique to prepare $Mg_2Si_{1-x}Sn_x$ materials with excellent reproducibility in relatively less time, identifying the synthesis parameters which influence the TE properties, and analyzing the TE properties to identify the microscopic material parameters affected due to a variation in synthesis parameters. Besides, for a long-term functioning and sustenance of maximum efficiency of $Mg_2Si_{1-x}Sn_x$ based modules, the high temperature stability of $Mg_2Si_{1-x}Sn_x$ materials is a significant challenge to overcome. Previous studies reveal that the high temperature (800 K – 875 K) stability of n-type $Mg_2Si_{1-x}Sn_x$ materials is compromised by Mg loss. However, these studies lack proper methodology as the high-temperature annealing causes material degradation beyond the actual composition, which results in the formation of secondary phases. As a result, a comparison of TE properties measured before and after annealing hold no significance as the properties measured after annealing are representative of mixed-phase material. These studies also lack a proper detailing of the degradation mechanism and no conclusions about the mechanism can be drawn from the reported microstructure. These investigations highlight the fact that the practically relevant topic of thermal stability of $Mg_2Si_{1-x}Sn_x$ materials needs to be addressed well. In this regard, the measurement of TE properties should be conducted by simulating the operation conditions of TEGs made from these

materials. A measurement of TE properties of these materials at high temperatures of annealing would show a direct effect of heat-treatment on the TE properties. Moreover, a modelling-based analysis of measured properties will provide the extent of changes in the microscopic material parameters. Such an investigation would enable a systematic understanding of the different stages of the degradation mechanism of $Mg_2Si_{1-x}Sn_x$ materials.

Therefore, the focus of this work is to investigate the composition-synthesis-microstructure-property relationships in n-type Mg_2X (X: Si, Sn) solid solutions, and the effects of long-term heat treatment on the thermoelectric transport properties of these materials, using semiconductor physics-based models.

Carrier concentration (n) is one fundamental parameter that needs to be optimized for achieving best TE properties of any material. Therefore, a pre-existing in-house Hall facility is successfully advanced for high temperature measurements ($T = 300\ \mathrm{K} - 723\ \mathrm{K}$) of $Mg_2Si_{1-x}Sn_x$ materials. The Hall facility is capable to simultaneously measure the Hall coefficient (R_H) and the electrical conductivity (σ) in a van der Pauw configuration. The uncertainty in the signals corresponding to the σ measurement was addressed, partially resolved and quantified. The effect of non-ideal contact geometry on the R_H measurement was investigated using finite element simulations. For certain relevant cases, R_H values deduced from simulation and analytical expression showed a relative deviation (R. D.) $> 5\ \%$, and so, the results of the analytical expression could be furthermore corrected using simulation results. Room temperature and T-dependent measurement of R_H and σ on $Mg_2(Si,Sn)$ and p-type $FeSi_2$, respectively, in the Hall facility at DLR and other international research labs showed good agreement in their absolute measured values with $\mathrm{R.D.} \leq 8\ \%$.

For a better understanding of composition-synthesis-microstructure-property relationship, Sb-doped $Mg_2Si_{0.4}Sn_{0.6}$ was synthesized using mechanical alloying. Employing an in-depth microstructure analysis, the formation mechanism of this material was studied in detail using mechanical alloying. The Mg-Sn phase forms readily followed by slow Si diffusion in the ductile matrix. However, the investigations showed that the powder sample was not phase pure even after extensive milling and therefore a high-temperature compaction step was added, enabling a successful synthesis of the desired composition. The effect of synthesis parameters (milling time, sintering time and temperature) was studied systematically. TE properties were hardly influenced by milling duration. However, carrier concentration reduced with an increase of sintering time and temperature which led to an observable effect on TE properties. Maximum TE performance, characterized by a TE figure-of-merit $zT \sim 1.4$, was achieved for samples sintered at 973 K for 20 min.

A TEM based microstructural analysis was performed on the samples sintered for different durations (10 min, 20 min and 40 min) at 973 K. This analysis was done with an objective to identify the reason of the sensitivity of TE properties to the sintering duration. An increase in the sintering duration resulted in Mg-depleted grain boundaries and local compositional inhomogeneities in the material. The transport properties of these samples were analyzed upto 700 K by using a single parabolic band (SPB) model under the assumptions of acoustic phonon (AP) and alloy scattering (AS) mechanisms. Analysis revealed carrier loss, a lowering in carrier mobility (μ) and a reduction in lattice thermal conductivity (κ_{lat}) with increasing sintering duration. A lower mobility for the sample (sintered for prolonged duration 40 min) was due to a combined effect of increasing electron-phonon interaction (higher deformation potential constant E_{Def}) and local compositional inhomogeneities, which are both associated with Mg loss. The altered temperature dependence of electrical conductivity could be reproduced by considering grain boundary (GB) scattering together with AP and AS, thus, linking the observed changes of the microstructure with the TE transport. The compensation between both a lower κ_{lat} and μ of the sample sintered for 40 min led to a similar TE performance as short-term sintered samples, with $zT_{\mathrm{max}} = 1.3 \pm 0.18$ for all samples. The absence of any strong influence of sintering duration on zT_{max} indicates that $Mg_2Si_{1-x}Sn_x$ materials, and hence the TE modules made from them, can accommodate some Mg loss without their performance being degraded.

Theoretical investigations have suggested scandium (Sc) as an impurity element for Mg_2X materials that introduces resonant levels in the band structure, which could greatly enhance the Seebeck coefficient (S) and the overall TE performance. Correspondingly, the effect of the substitution of Mg by Sc in Mg_2X binaries and their solid solutions was experimentally investigated. The TE properties showed no enhancement due to an addition of Sc to Mg_2X material, thus, disproving the results of the theoretical study.

The effect of long-term annealing on the transport properties of $Mg_2Si_{1-x}Sn_x$ was further investigated at different temperatures. Chosen temperatures were near and beyond the operation temperature range of $Mg_2Si_{1-x}Sn_x$ based TE modules. It is clear from the last investigation that the Mg loss is inevitable. The missing part is the extent and the speed of Mg loss at higher temperatures. It is furthermore unclear whether the microscopic mechanism of degradation is temperature dependent or not. Considering this, the electrical transport properties of six thermoelectrically identical samples were measured *in-situ* in two different setups: S and σ (three samples), and R_{H} and σ (other three as-prepared samples) during annealing at 710 K, 773 K and 848 K. All samples were largely single phase with no hints of de-mixing after

annealing for several hundred hours. *In-situ* measured properties were analyzed using a SPB and a two parabolic band (2PB, one conduction and one valence band) model. The analysis revealed a loss of majority carriers due to ongoing Mg loss as annealing progressed. Besides, a lowering of μ, due to an increase in E_{Def}, and a reduction in the density-of-states effective mass (m_{D}^{*}) is also observed. This change in said microscopic material parameters could be directly related to an ongoing Mg loss or a lifted degeneracy of conduction bands in $Mg_2Si_{0.4}Sn_{0.6}$, respectively.

A microscopic, multi-step model of Mg loss was developed which qualitatively explains the Mg-transport from sample to the annealing atmosphere. Time constants (and rates) were estimated from the change of majority charge carriers and the electrical conductivity measured *in situ* at different temperatures. Rates were plugged in the Arrhenius expression to determine the activation energy of the complete degradation process. The activation energy was compared with the height of energy barriers associated with Mg-transport to judge the limiting step in the transport chain of multi-step model. Mg-transport was found to be dominated by Mg-vacancies owing to their low energy of formation and migration energy. With the established mechanism, the observed changes in the transport properties and the differences in rate and the frequency factor were found to be dependent on the design of measuring setups. This governs the degradation process by allowing one or more steps to act as a dominant mechanism of multi-step transport chain.

The findings in this thesis provide a description of previously *unknown* synthesis mechanism of high performance n-type $Mg_2(Si,Sn)$ solid solutions using mechanical alloying. The effect of synthesis parameters on material properties is analyzed which explains discrepancies in the material properties reported in different literature reports. An effect of high-temperature degradation of n-type $Mg_2(Si,Sn)$ is understood by analyzing *in situ* measured transport properties which revealed the affected microscopic material parameters and the extent of their deterioration. Finally, the kinetics of Mg-loss in n-type $Mg_2(Si,Sn)$ solid solutions is known by utilizing the change in the majority charge carrier concentration and a model of Mg-loss in n-type $Mg_2(Si,Sn)$ is developed.

Chapter 1 Introduction

On Earth, the different forms of life are driven by energy. In the past, the human species, in particular, has discovered and exploited many resources of energy (fossil fuels (oil), natural gas, coal, nuclear energy etc.) to accumulate large amounts of usable energy. Amongst these resources, the utilization of fossil fuels has caused detrimental effect on the environment (e.g. through greenhouse gas emissions) that include global climate changes and the Ozone layer depletion. In the last century, a variety of alternative sources of energy (e.g. solar, wind, bioenergy etc.) were devised to tackle the ever-increasing energy demand that lighten the load on conventional energy resources and limit the effects of utilizing non-renewable energy sources on the climate. However, these energy sources cannot be solely utilized for two reasons, first, the limited capacity of energy production and second, the limited capacity of required means of the storage of energy produced. This has intensified the exploration of more effective sources of power generation than the available state-of-the-art technologies. Alongside this, there is an ongoing search for other renewable energy sources that could complement the existing alternative sources of energy as well. Among all such sources, the technology based on the thermoelectric (TE) effects has proved to be a promising as a supportive energy source. The thermoelectric technology can be utilized to scavenge and harness waste heat to produce electrical energy [1, 2]. This technology has a great potential since nearly two third of the produced energy is rejected in the form of heat, which is independent of the energy resources (non-renewable or renewable) [3]. The conversion of heat to electricity is possible by the utilization of thermoelectric generators (TEGs). TEGs have numerous advantages over other energy conversion devices: they provide direct energy conversion unlike many heat engines that convert thermal energy to mechanical energy which is eventually converted to electrical energy [4], possess no moving parts and no working fluids. TEGs are maintenance free, and have proven to have a long lifespan, and have other advantages such as noiseless operations and loss-less scalability.

Until now, TEGs have been used only in niche applications like radioisotope thermoelectric generator (RTG) [5, 6] that are employed on the spacecrafts, and the protection of gas pipelines against corrosion [7]. The automotive industries [8-10], the sensors and microelectronics sector [11] have also tested TEGs, where these generators have shown promising results as well. TEGs have shown great technological potential and maturity as a core element in RTGs. As a result, RTGs have found their application in spacecrafts (e.g. Voyager, Cassini etc. and in the Curiosity rover) for different exploratory extra-terrestrial missions executed by the NASA and the

Russian Space Agency over the last four decades [5, 6]. In automobile industries, manufacturers have tested TEG prototypes by installing them in different components of cars and trucks. While BMW has tested Bi_2Te_3 and PbTe based modules in various models of their cars, the General Motors have demonstrated the potential of skutterudites based TEGs in their light-duty trucks [11]. In microelectronics, the TEGs are used as micro-generators for powering (by a few mW or µW) self-sufficient sensor nodes in manifold systems. In this direction, *Laird™ thermal systems* have developed thin-film TEGs to power wireless sensors while *Perpetua® by Grace* have developed miniaturized TEGs for their application in wireless communication sector [11]. The other field of applications where thermoelectric technology holds its potential include nuclear power plants [12, 13], jet turbines of commercial flights [14], solar thermoelectric generators [11] etc. In summary, the utilization of TEGs in the aforementioned sectors underscores the potential to lighten the burden on the conventional energy sources.

Our team at the Department of Thermoelectric Materials and Systems at the German Aerospace Center (DLR) is working to develop efficient inorganic TE materials and TEGs for automotive and space applications. These inorganic materials are core components of a TEG that are fabricated using a variety of synthesis methods and techniques. The electronic transport properties of these materials are understood, predicted and optimized by utilizing semi-classical semiconductor physics-based models. These optimized materials are then used to construct TEG prototypes, which are optimized experimentally and numerically to improve their final output efficiency.

In conclusion, the advantages and promising results of thermoelectric technology, and the active research and development focused on optimizing several parts of the thermoelectric devices makes it feasible to employ these devices as a mandatory component for future technological applications.

A knowledge of basic principles is needed to advance further in the field of thermoelectrics and therefore the different thermoelectric effects are discussed in the upcoming section.

1.1 Thermoelectric effects

The field of thermoelectricity encompasses three separately identified effects, namely the Seebeck effect, the Peltier effect and the Thomson effect. In this section, each of these phenomena is briefly discussed. The interrelation between each of these effects is also briefly discussed.

1.1.1 Seebeck effect

This effect is named after the German-Baltic physicist T. J. Seebeck but there are some hints in the previously published literature which report that Aepinus or Volta discovered this effect [15, 16]. In a circuit made of two dissimilar conductors that was held at different temperatures, Seebeck observed a deviation in the magnetic needle positioned near this arrangement [2, 16]. Later, Oersted coined the term 'Thermoelectricity' and explained the said phenomena, stating that an electric current in the circuit is generated due to the temperature difference between the junctions of two conductors.

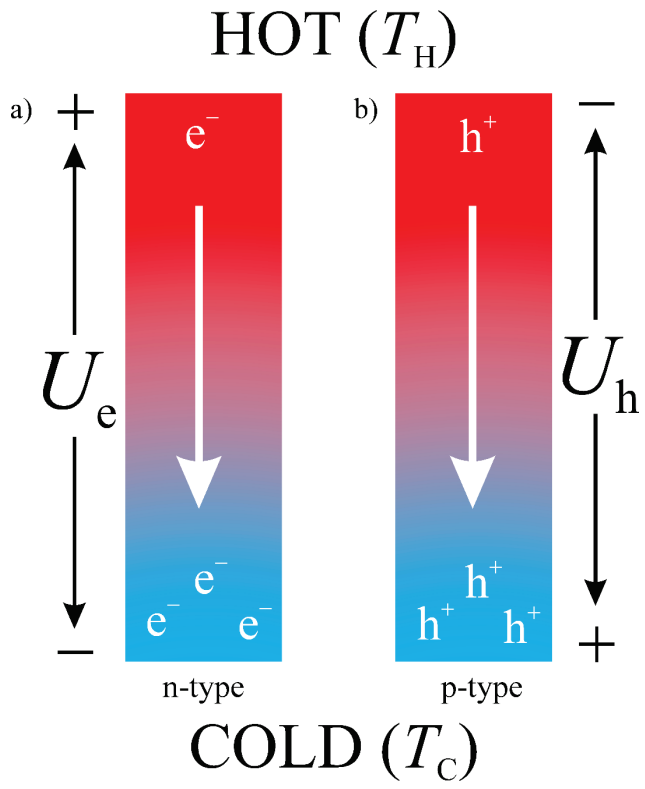

Figure 1.1 A schematic of the Seebeck effect in an open circuit condition where a) an n-type and b) a p-type semiconductor is under temperature difference $\Delta T = T_H - T_C$. Here, T_H is the hot-side temperature and T_C is the cold-side temperature, and ΔT is shown to increase from T_C to T_H. The charge carriers namely, electrons e^-(n-type) and holes h^+ (p-type) diffuse preferentially from the hot side to the cold side, respectively, until the induced voltage U is generated that opposes a further diffusion of carriers from hot side to the cold side. The induced voltage (a difference in electric potential) for an n-type and a p-type semiconductor is labelled as U_e and U_h, respectively.

Assuming an exemplary case of an n-type material (shown in Figure 1.1(a)), when a T-difference is created across this material, the electrons on the hot side gain a higher kinetic energy and instantaneously migrate (on average) to the cold side. Note that electrons (e^-) are

the majority charge carriers in an n-type material. This leads to the formation of an electric potential difference across the material that opposes further carrier diffusion when an equilibrium is reached (Figure 1.1(a)). The induced electric field is opposite to the applied temperature gradient ($\vec{\nabla}T$) that is expressed as ($\vec{E} = S_n\vec{\nabla}T$), and vice versa for p-type materials (Figure 1.1(b)), where holes (h^+) are the majority carriers [16].

The thermocouples (TCs) that are commonly used for probing temperatures in various applications are based on the Seebeck effect. The physics related to the Seebeck coefficient will be discussed in the subsection 2.2.4 of Chapter 2.

1.1.2 Peltier effect

This effect is named after J. C. A. Peltier who discovered this phenomenon in 1834 [2, 15]. He conducted an experiment by passing current (I) through a junction in a circuit which is composed of two different materials M_1 and M_2. Depending on the direction of the current flow, he found that heat is either generated or absorbed at this junction. The heat generated or absorbed per unit time is known as Peltier heat ($\dot{Q}$), and the effect is known as Peltier effect. The Peltier heat relates to the current I by the expression: $\dot{Q} = \Pi I$, where Π is the Peltier coefficient. Thomson applied the laws of thermodynamics to a TE circuit, assuming it to be a reversible system, and showed that the Peltier coefficient Π is related to the Seebeck coefficient S by following relation, called first Kelvin relation:

$$\Pi_{\mathrm{M1}} - \Pi_{\mathrm{M2}} = (S_{\mathrm{M1}} - S_{\mathrm{M2}})T \qquad \text{Equation (1.1)}$$

1.1.3 Thomson effect

The Seebeck coefficient S is temperature dependent for almost all materials. When a temperature gradient is maintained in such (homogeneous) materials, their Seebeck coefficient varies with the variation of temperature across the material. When a current I is passed through a material subject to a temperature gradient, a local heat (related to the Peltier effect) is generated due to the difference in the Seebeck coefficient S of two adjacent regions in the material. This generated heat is proportional to the temperature gradient and current I in a form of an expression given as [2, 15]:

$$d\dot{Q}_\tau = -I\tau\frac{\partial T}{\partial x}\,dx \qquad \text{Equation (1.2)}$$

where $d\dot{Q}_\tau$ is the Thomson heat generated (or absorbed) at each infinitesimal length (dx) along the length of the current carrying conductor. This heat is generated (or absorbed) due to the applied temperature gradient and supplied current. This effect was found by Thomson (later known as Lord Kelvin) and correspondingly, τ is called the Thomson coefficient, and expressed as: $\tau = T\ (dS/dT)$.

All the aforementioned thermoelectric effects provide a base for the design and optimization of highly efficient TE devices for power generation or cooling applications. In the coming section, the TE devices are briefly discussed from an application point-of-view.

1.2 Thermoelectric devices and the thermoelectric figure of merit

TE devices are heat engines and like all other heat engines, these devices follow the laws of thermodynamics. A TE device comprises of many p-type and n-type semiconductor TE materials, usually in pairs, connected electrically in series and thermally in parallel.

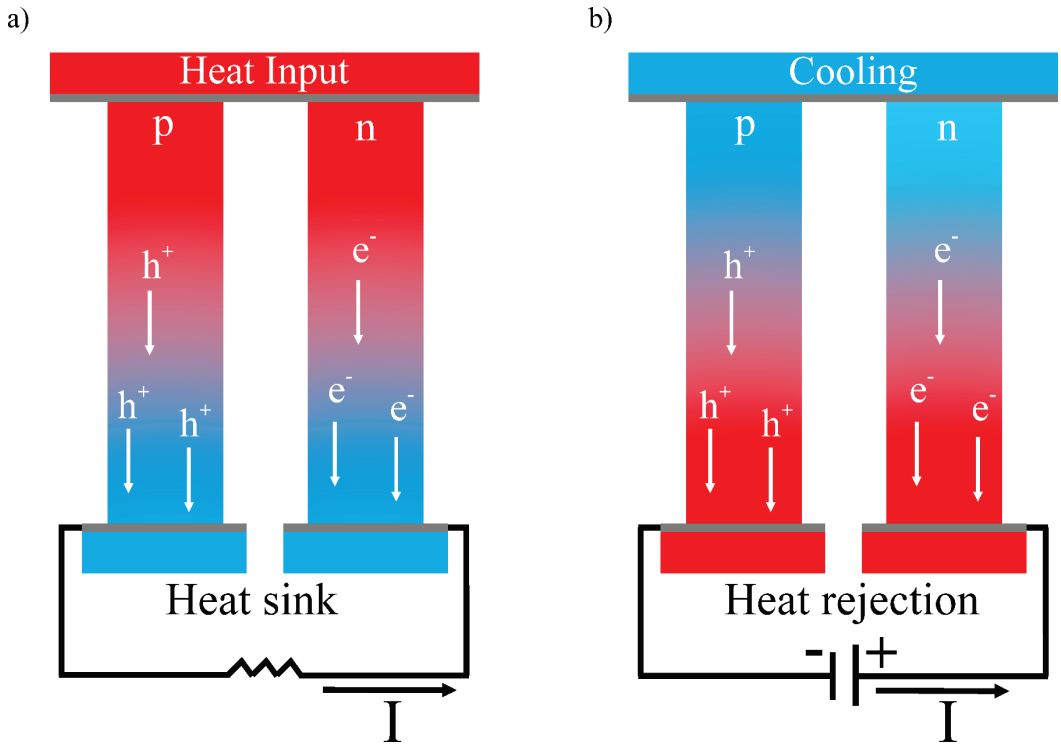

Figure 1.2 Schematic of a thermoelectric uni-couple comprising of a p-type and an n-type semiconductor that represents a) power generation and b) cooling mode respectively. Note that the semiconductor legs are connected *via* metal interconnects (represented in grey). The red and blue color represents hot side and cold side, respectively.

The construction of these devices is identical for their operation in either refrigeration or power generation mode. A π–shaped uni-couple (or pair) of p-type and n-type semiconductors is shown in Figure 1.2 that represents their arrangement in a TE device. The power generation mode is based on the Seebeck effect (see Figure 1.2(a)), whereas the refrigeration mode, as shown in Figure 1.2(b) is based on the Peltier effect.

The performance of a TEG can be characterized by its conversion efficiency (η) which is the ratio of output electrical power ($P = \dot{Q}_{\text{in}} - \dot{Q}_{\text{out}}$) to the absorbed heat ($\dot{Q}_{\text{in}}$) at the hot junction:

$$\eta = P/\dot{Q}_{\text{in}} \qquad \text{Equation (1.3)}$$

Here, $\dot{Q}_{\text{out}}$ is the output heat flow. In the power generation mode, the maximum efficiency (η_{max}) of a TE device, assuming temperature independent materials properties, is given by [17, 18]:

$$\eta_{\text{max}} = \frac{T_{\text{H}} - T_{\text{C}}}{T_{\text{H}}} \frac{\sqrt{1 + Z\bar{T}} - 1}{\sqrt{1 + Z\bar{T}} + \frac{T_{\text{C}}}{T_{\text{H}}}} \qquad \text{Equation (1.4)}$$

Here, the TE figure-of-merit of a device (Z) is defined as [17]:

$$Z = \frac{S_{\text{pn}}^2}{RK} \qquad \text{Equation (1.5)}$$

Z is determined by the individual thermoelectric properties of p-legs and n-legs and other components used in constructing a TE device. Here, S_{pn} is the Seebeck coefficient of the device which is a summation of the Seebeck coefficients (S_{p} and S_{n}) of the p-type and n-type legs expressed as $S_{\text{pn}} = N\ (|S_{\text{p}}| + |S_{\text{n}}|)$, where N is the number of p-n leg pairs. The resistance (R) of a device is the sum of series resistance of p-legs and n-legs, contact resistances, bridge resistances etc., and K is the total thermal conductance of the device, respectively. Note that utilizing the properties of p-type and n-type legs is an ideal assumption, in reality, the ΔT at the legs would be relatively lower compared to the ΔT at the device as temperature drops are ought to occur due to parasitic thermal resistance of the ceramic insulation plates, electrical bridges etc. The ratio $(T_{\text{H}} - T_{\text{C}})/T_{\text{H}}$ is the Carnot efficiency, and $\bar{T}$ is the average of T_{H} and T_{C}. η_{max} is limited by the Carnot efficiency and therefore to achieve a large η_{max}, the difference between T_{H} and T_{C} should be large and Z should be maximum. However, the values of η close to the Carnot efficiency are generally not achieved since $Z\bar{T}$ is limited due to the material properties.

Consequently, efforts are made to maximize Z and to increase η_{max}, by optimizing the TE properties of the p-type and n-type legs. Z equals the figure-of-merit for a material (z), if the TE properties of each leg of a uni-couple are similar (except the sign of the Seebeck coefficient) with ideal contacts i.e. no contributions of thermal and electrical contact (and other) resistances, and no thermal bypass. z can then be expressed by material properties:

$$z = S^2\sigma/\kappa \qquad \text{Equation (1.6)}$$

Here, σ is the electrical conductivity and κ is the total thermal conductivity. $S^2\sigma$ in the expression is known as the thermoelectric power factor (PF). Multiplying temperature (T) on either side of Equation (1.5) and Equation (1.6) makes the figure-of-merit (z) a dimensionless quantity (zT) [17], which is the commonly used notation across various reports. Z is distinguished from z for a clear differentiation whether the properties of a device or a material, respectively, are discussed.

The device efficiency η as a function of ΔT is shown in Figure 1.3. Note that the efficiency can increase if the ΔT is large or the figure-of-merit of materials employed for the construction of TE devices is large.

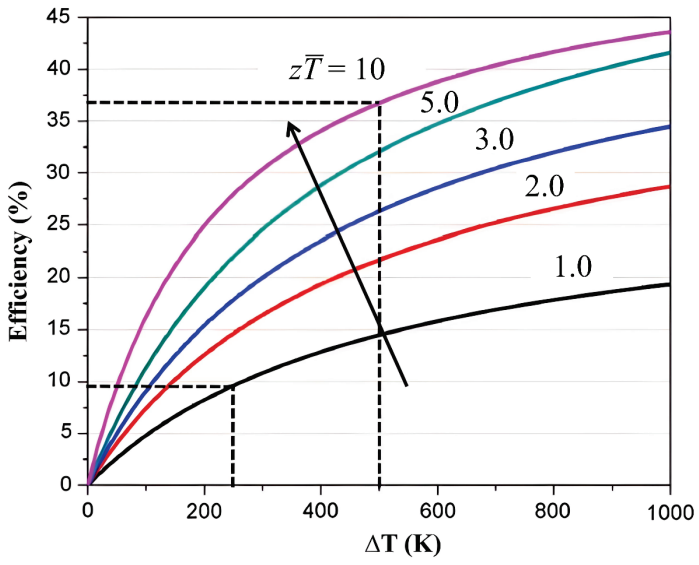

Figure 1.3 Theoretical efficiency (η) of a TE generator as a function of ΔT (with $T_C = 300$ K) for a range of $z\bar{T}$. The plot has been reprinted (adapted) with the permission from [18].

Although the value of zT is not limited theoretically [19], materials with a peak $zT \geq 2$ are rarely reported. This can be observed from Figure 1.4 where only p-type PbTe and p-type SnSe have peak $zT \geq 2$. Figure 1.4 also shows that only a single conduction type of these materials shows good zT e.g. a p-type, but their counterparts do not and vice versa. A few exceptions to the stated fact are Skutterudites, PbTe, half-Heuslers and Bi_2Te_3 class of materials which show $zT > 1$ in the low temperature range for both p-type and n-type materials.

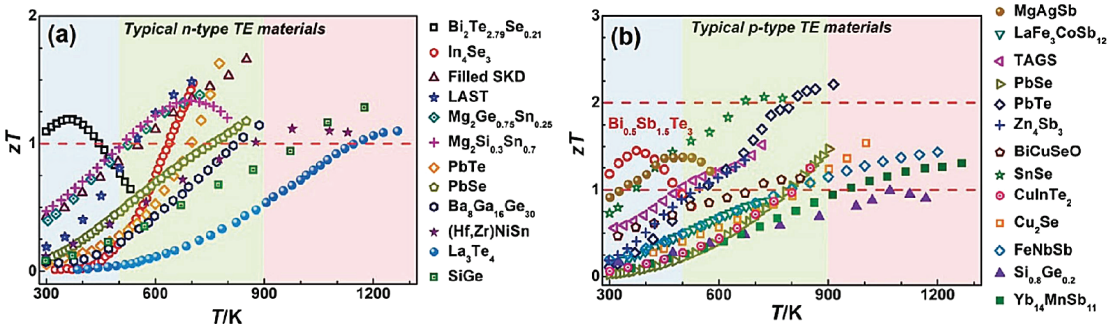

Figure 1.4 Temperature dependence of zT values for some typical classes of (a) n-type and (b) p-type bulk TE materials. In the legend of these plots TAGS stands for $(GeTe)_{1-x}(AgSbTe_2)_x$ while SKD and LAST stand for Skutterudites and lead antimony silver telluride, respectively. The plot has been reprinted (adapted) with the permission from [20].

Besides, most of the heat generated in a variety of industrial processes lies in the intermediate temperature range (500 K – 900 K) and correspondingly different material classes are discovered and explored in this range. The best of those have a peak $zT \approx 1.3 - 1.8$, but amongst these materials, the n-type Mg_2X (*X:* Si, Sn) solid solutions stands out owing to their precursor abundance, environmental compatibility and low mass density. These characteristics makes Mg_2X (*X:* Si, Sn) materials one of the preferred material classes for application purposes.

1.3 Optimization of the thermoelectric efficiency

Maximizing thermoelectric performance of any material necessitates a fine balance between the electrical and thermal transport properties. The thermoelectric properties (the Seebeck coefficient S, the electrical conductivity σ and the thermal conductivity κ) are interlinked through the carrier concentration (n), which is one of the necessary parameters for the optimization of any prospective thermoelectric material. The dependence of the thermoelectric properties on the carrier concentration can be observed in Figure 1.5.

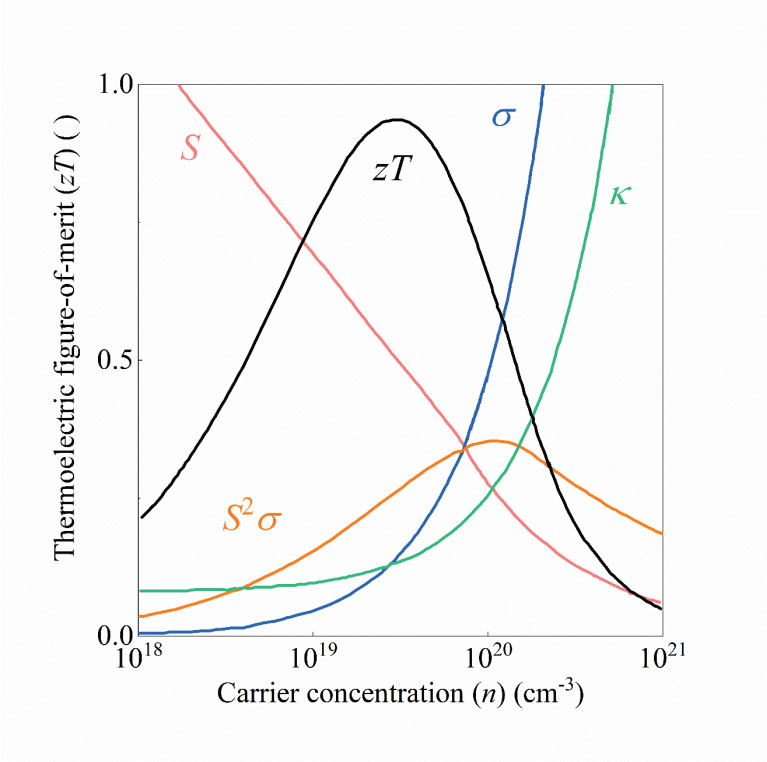

Figure 1.5 zT as a function of n in the range $10^{18} - 10^{21}\text{cm}^{-3}$. zT_{max} is obtained in the range of $10^{19} - 10^{20}$ cm^{-3}. PF_{max} is obtained at higher n than zT. The plot has been reproduced (adapted) with the permission from [1].

Figure 1.5 shows that there is an evident compromise between the Seebeck coefficient S and the electrical conductivity σ which should be finely tuned to achieve maximum thermoelectric performance. It can be furthermore observed that zT_{max} can be achieved with the carrier concentration n ranging between $10^{19} - 10^{20}$ cm^{-3} (depending on the material system).

For a further enhancement of TE performance, both electrical conductivity and the Seebeck coefficient have been enhanced, both individually or simultaneously, by employing different strategies such as engineering the band structure of the materials to enhance the band degeneracy (including orbital and valley degeneracy) [21, 22], energy filtering [23-25], introducing resonant states [26, 27], modulation doping [28, 29] etc. Band degeneracy means that different bands possess the same or comparable energy within a belt of $\leq 1\ k_{\text{B}}T$. When these bands have nearly identical energy of the band edge, it is called orbital degeneracy. Besides, if the edge of a single band is found at other points in the Brillouin zones than its center where these are symmetric due to the symmetry of the crystal, it is called valley degeneracy [21]. Energy filtering means suppressing (or filtering out) the population of low-energy charge carriers for an enhancement of the Seebeck coefficient with only a minor reduction of electrical conductivity [25]. The density of states (DOS) is distorted by introducing a resonant impurity in the parent compound which increases the Seebeck coefficient in a nearly T-independent way

(e.g. substituting Tl in place of Pb in PbTe) [27]. The resonant impurity creates an additional energy level that *resonates* with the dominant band of the parent compound, particularly, in a narrow energy range near the Fermi level. The concept of the DOS is explained in the later part of the introductory section (section 2.2) of Chapter 2. An approach to enhance the electrical conductivity of a material is *via* modulation doping. In this, the carriers are spatially separated from their parent impurity atom, which reduces an influence of ionized impurity scattering [29].

The expression of zT (Equation (1.6)) can be re-formulated to highlight electronic (κ_{el}) and lattice (κ_{lat}) contributions to the total thermal conductivity (κ) as:

$$zT = \frac{S^2\sigma}{\kappa_{\mathrm{lat}} + \kappa_{\mathrm{el}}}T \qquad \text{Equation (1.7)}$$

κ_{el} scales with σ as shown in Figure 1.5, and it is discussed in detail in sub-section 2.2.5 of Chapter 2. Therefore, a majority of studies have employed different strategies to reduce the lattice thermal conductivity κ_{lat} [30-35] to maximize zT. However, minimizing κ_{lat} while maintaining large conductivity σ is difficult as the centres that scatter the phonons also scatter the charge carriers. Therefore, different strategies have been employed to scatter the phonons without affecting the carrier transport. Some of the most relevant strategies are solid solution formation [32, 36], nanostructuring [37] (as discussed in 2.3.1.5), nanoscale precipitation [38], and lamellar structures by the exploitation of phase diagram of corresponding materials [39] etc.

Conventionally, an optimum carrier concentration n can be achieved by the selection of a suitable extrinsic defect(s), adjusting its concentration and a synthesis method that guarantees a sufficiently high dopant incorporation. A suitable dopant species can be deduced by its valency, with the help of defect energetics calculations, or by using the Hume-Rothery rule [40]. The concentration of these dopants can be optimized using well established semiconductor transport models as explained in detail in section 2.2 of Chapter 2.

The importance of synthesis method is at the core of achieving optimized material properties. Different literature reports show that different synthesis methods for the same composition often lead to different TE properties. This is exemplified by a figure-of-merit zT plot (in Figure 1.6) for n-type Mg_2Si-Mg_2Sn based solid solutions. Generally, these materials show a high figure-of-merit $zT \approx 1.3 - 1.4$. Note that the zT values correspond to the same starting composition $Mg_{2-\delta}(Si_{0.3}Sn_{0.7})_{0.98}Sb_{0.02}$ which are reported in different cited literature reports. The value of δ can be positive or negative whether the material is deficient or

overconcentrated in Mg, respectively. Generally, for the synthesis of these compositions, excess Mg is used to compensate for Mg loss at higher temperatures of compaction or annealing. A variation in the sample properties could be due to differences in the employed synthesis routes in the production of samples in each study. For example, Zhang *et al.* [41] have used melt spinning as well as solid state reaction, followed by plasma activated sintering, to produce two different samples, one from each stated process labelled as 1 & 2, respectively, see Figure 1.6.

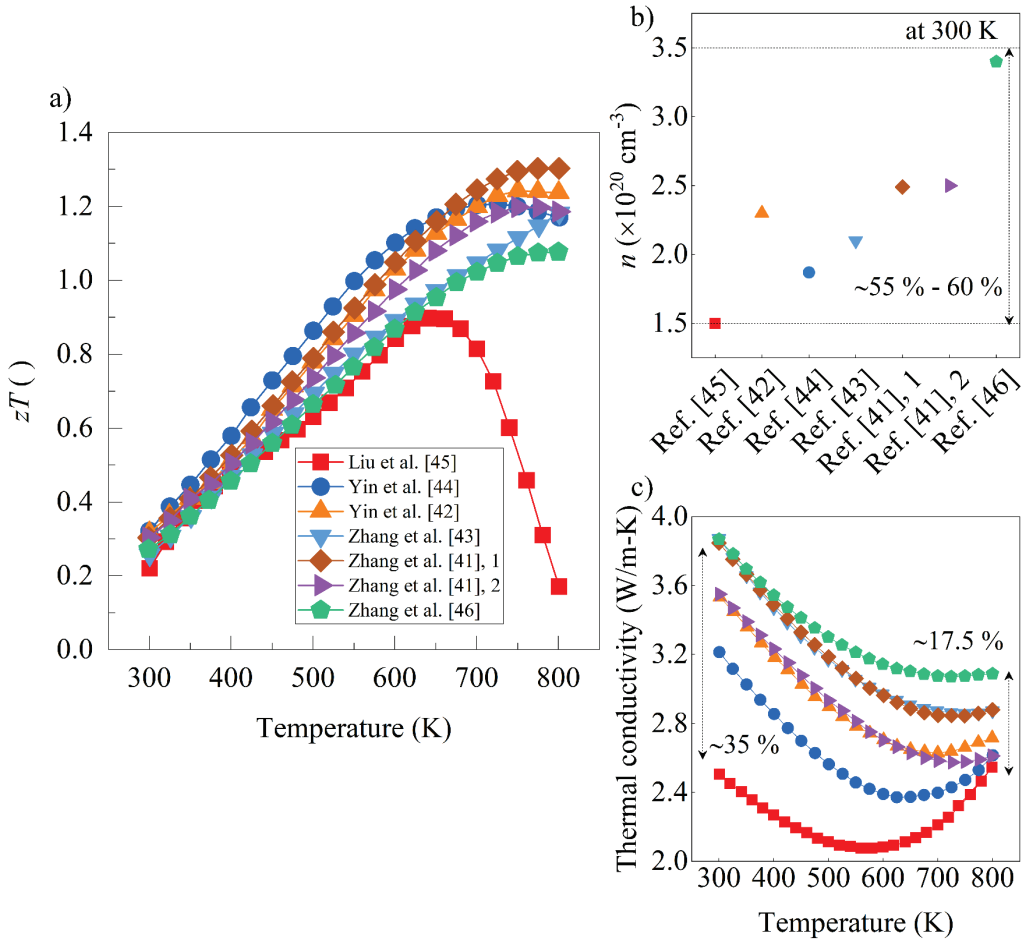

Figure 1.6 a) T-dependent zT of $Mg_{2-\delta}(Si_{0.3}Sn_{0.7})_{0.98}Sb_{0.02}$ reported by Yin *et al.* [42] ($\delta = -0.16$), Zhang *et al.* [43] ($\delta = 0$ to -0.14), Yin *et al.* [44], Zhang *et al.* [41] ($\delta = -0.16$), Liu *et al.* [45] ($\delta = -0.1$) and Zhang *et al.* [46] (no information on δ). n at room temperature (RT) (b), and c) T-dependent κ is shown for the samples in respective reported studies.

There is an evident variation in the zT reported in different studies as shown in Figure 1.6 (a), which could arise from a variation in (thermo-)electrical or thermal properties or both. Both n at RT and T-dependent κ for samples with respective composition are shown in Figure 1.6 (b)

and Figure 1.6 (c), respectively. The results show a large discrepancy at RT as well as at highest measurement temperature, respectively. The major reasons can be an off-stoichiometry of the synthesized material, a low dopant incorporation, formation of secondary phases in the material etc. that are all related to the synthesis route. A likewise large variation in n and κ are observed for other materials systems such as PbTe–PbSe [47, 48] and PbTe–PbS solid solutions [49, 50]. Note that the differences in each property are larger than the typical measurement uncertainties, and therefore, the error bars are not shown here for better visibility [51, 52].

A further common problem in the optimization of the (long-term) performance of TE materials is their thermochemical stability. This could be affected by preferential stability of the binary phases compared to the solid solutions, i.e. a miscibility gap as reported e.g. for Mg_2Si-Mg_2Sn, PbS-PbTe, PbTe-GeTe etc. [49, 53], or a high vapor pressure of one or more chemical constituents [54, 55]. This leads to difficulties during the material synthesis and its optimization, and the experimental optimization of the TE device for their operation at elevated temperatures for prolonged duration. Moreover, a high temperature exposure of material can cause a variation in the concentration of one or more elements in these materials. This variation can lead to observable variations in their transport properties and efficiency of TE devices made from these materials.

Chapter 2 Electronic transport theory, semiconductor transport models, transport coefficients and material basics on $Mg_2(Si,Sn)$

2.1 Summary

This chapter discusses the theory of electrical transport in a semiconductor. The band structure models that are used to analyze and predict the high temperature thermoelectric transport properties are discussed. These models consist relevant expressions of the transport coefficients (solutions of the Boltzmann transport equation (BTE)), which are used to describe carrier transport phenomena in thermoelectric semiconductors are also discussed in detail. Besides this, the thermal conductivity is discussed briefly highlighting different approaches to reduce it. In the later section of this chapter, the physical and thermoelectric properties of Mg_2Si-Mg_2Sn are discussed in detail.

2.2 Electronic transport theory

As briefly discussed in the last chapter, zT of a material needs to be maximized to increase the efficiency of a TEG at its operation temperatures. Achieving $zT_{\max}$ depends on optimizing the TE properties i.e. S, σ, and κ that are interdependent *via* the carrier concentration n and other material properties. An efficient optimization of n and the corresponding TE properties therefore necessitates an in-depth understanding of the electronic band structure and the transport of charge carriers in the material under an influence of external forces (e.g. applied temperature gradient, $\vec{E}$). There are a lot of textbooks available where one can refresh concepts related to the electronic band structure [56-60]. Herein, the electrical transport in semiconductors is briefly discussed with a focus mainly on the heavily doped semiconductors.

Semiconducting materials are well suited for TE applications as discussed in Chapter 1 and therefore the current discussion will focus on these materials. Semiconductors are characterized by the presence of an energy gap in the band structure that ranges between 0 eV $-$ 3 eV in width (at 0 K). At 0 K, there are no free carriers in a pure semiconductor material (i.e. with no impurities or defects). But for the TE applications, these semiconductors are heavily doped (by an impurity element) to achieve a high density of free charge carriers. Specifically, these impurities introduce localized states that either provide electrons or trap them which makes the

material an n-type or a p-type semiconductor, respectively [56]. For example, a phosphorus atom is substituted in a silicon crystal to make it an n-type semiconductor. The phosphorous atom has an extra electron in its outer shell compared to the silicon atoms. These extra electrons are bound to the phosphorus atoms at low temperatures (≤ 100 K) while at higher temperatures, these electrons gain energy from the thermal energy, that elevates these donor electrons into the conduction band (CB). The energy required to elevate these electrons (called the excitation energy of the donor state) is less than the energy required to elevate the electrons that form a covalent bond. These donor electrons move in the semiconductor while the phosphorous ion is fixed in the crystal. This type of substituted atom that donate an electron to the CB in a semiconductor are called donor impurity atom. The following discussion of the fundamentals of carrier transport is made by considering electrons as majority charge carriers and therefore assuming an n-type semiconductor.

An external perturbation (e.g. $\vec{E}$), exerts a force (F) on the electrons given by $F = m\dot{v} = -e\vec{E}$. Here, $\dot{v}$ is the acceleration and m is the scalar mass of electrons. When the electron is in a three-dimensional crystal lattice, m is replaced by an effective mass tensor m_{ij}^*. m_{ij}^* accounts for the interaction between the periodic potential of the crystal lattice and the drifting electrons. The inverse of m_{ij}^* is proportional to the curvature of the energy of a band (E) with respect to the wave vector (k) i.e. $E(k)$ [56, 61]:

$$\left(\frac{1}{m^*}\right)_{ij} = \frac{1}{\hbar^2}\frac{\partial^2 E(k)}{\partial k_i \partial k_j} \qquad \text{Equation (2.1)}$$

Here, i, j are the direction of electron drift and the direction of force, respectively. Generally, the acceleration $\dot{v}$ of electrons and the force F are not collinear. For simple cubic systems with a parabolic relationship between the energy and wavevector near the band edge, all the off-diagonal terms ($i \neq j$) in the m_{ij}^* vanish. Therefore, three (inertial) effective mass components (m_{xx}^*, m_{yy}^* and m_{zz}^*) would then describe the acceleration of carriers near the band edge. This is expressed as:

$$m_{ii}^* = \hbar^2 \left(\frac{\partial^2 E(k)}{\partial k_{ii}^2}\right)^{-1} \qquad \text{Equation (2.2)}$$

Therefore, the $E(k)$ relationship, assuming that the conduction band minimum is located at zero wavevector, can be rewritten as:

$$E(k) = E_C + \frac{\hbar^2 k_x^2}{2m_{xx}^*} + \frac{\hbar^2 k_y^2}{2m_{yy}^*} + \frac{\hbar^2 k_z^2}{2m_{zz}^*} \qquad \text{Equation (2.3)}$$

Here, $\hbar$ is the reduced Planck's constant ($\hbar = h/2\pi$) and h is the Planck's constant, E_C is the energy at the conduction band edge, k_i are the wave vectors in the Brillouin zone, aligned in different principal axes with $i = x, y$ and z. Note that the system of principal axes is centered at a band minimum (or band extremum) such that the system of principal axes and the k-space co-ordinate system are parallel to each other [62]. For the materials with a spherical Fermi surface, ($E(k_x) = E(k_y) = E(k_z)$) near the CB minima, e.g. for n-type $Mg_2(Si,Sn)$ [63] or GaAs, there can be one effective mass to account for effective masses across all each principal axes such that $m^*_{xx} = m^*_{yy} = m^*_{zz}$. The inertia mass, also called as the conductivity mass, m^*_I, for a single valley (for an anisotropic parabolic dispersion) is defined as a harmonic mean of effective mass along each principal axes: $m^*_I = 3/(1/m^*_{xx} + 1/m^*_{yy} + 1/m^*_{zz})$ [64], which, for a spherical Fermi surface is: $m^*_I \equiv m^*_{ii}$. Besides, the effective mass for the calculation of the density of states and the Seebeck coefficient, called a density-of-states effective mass (m^*_D), is separately defined. If $E(k)$ is different (e.g. anisotropic dispersion, i.e. ellipsoidal or more complicated Fermi surface) for different principal axes [64], then m^*_D is a geometric mean of m^*_{ii} (the effective mass corresponding to each valley aligned at each principal axis). This is given as $m^*_D = \sqrt[3]{N_V^2 m^*_{xx} m^*_{yy} m^*_{zz}}$, where N_v is the valley multiplicity. The DOS effective mass for a parabolic isotropic dispersion (spherical Fermi surface) is defined as $m^*_D = \sqrt[3]{N_V^2 (m^3_{ii})} = N_V^{2/3} m^*_{SV}$. For a single valley system (in a spherical Fermi surface), $m^*_{SV} = (m^*_{xx} m^*_{yy} m^*_{zz})^{1/3}$ are called as the single valley (density-of-states) effective mass (also called the band edge mass). Note that m^*_{SV} is *equivalent* to the conductivity mass ($m^*_I \equiv m^*_{SV}$) for a spherical Fermi surface which is the case here (for Mg_2Si-Mg_2Sn based materials). They would however, have different values if the Fermi surfaces are non-spherical [57, 59, 64]. Different effective masses described here are useful for the prediction and an understanding of the electrical conductivity and the Seebeck coefficient which will be discussed in sub-section 2.2.1, 2.2.3 and 2.2.4.

The transport properties result from the motion of electrons which makes the determination of the number of carriers available for conduction quite crucial. According to the Pauli's exclusion principle [65, 66], any given quantum state can be occupied by only one carrier, and therefore, the number of carriers contributing to the conduction are a function of these quantum states. The number of available energy states in a band are known as the density of states (DOS), denoted by $g(E)$. For a bulk (3D) semiconductor, it is expressed in an infinitesimal manner defining the number of states existing between an interval E and $E + \delta E$. For an extrinsic n-

type semiconductor, the corresponding density of electronic states per unit volume near the CB edge is given as:

$$g(E) = \frac{1}{2\pi^2}\left(\frac{2m_D^*}{\hbar^2}\right)^{1.5}(E - E_C)^{0.5}, E \geq E_C \qquad \text{Equation (2.4)}$$

Note that Equation (2.4) includes the contribution of the two spin states allowed for each quantum state; E is the energy of the CB. The density of carriers, n, contributing to the electrical transport is obtained by integrating over all the occupied states in the band. This is expressed as [56]:

$$n = \int_0^\infty g(E) f_0(E) dE \qquad \text{Equation (2.5)}$$

$f_0(E)$ is the Fermi-Dirac (FD) distribution function describing the probability of an electron occupying a quantized state (with an energy E) in a band at temperature T. It is given by [57, 67]:

$$f_0(E) = \left\{1 + \exp\left[\frac{E - E_F}{k_B T}\right]\right\}^{-1} \qquad \text{Equation (2.6)}$$

Here, E_F is the Fermi level (also called the Fermi energy at $T = 0$ K). $f_0(E)$ gets disturbed from its equilibrium under the effect of an external perturbation ($\vec{E}$, $\vec{B}$, applied temperature gradient etc.).

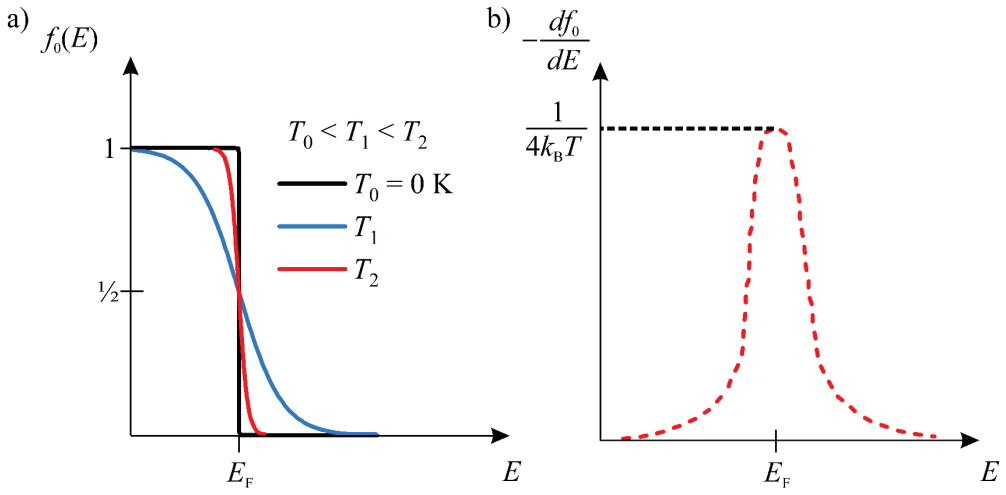

Figure 2.1 a) $f_0(E)$ at different temperatures and b) its derivative as a function of energy E. The plot has been reproduced (adapted) with the permission from [66].

Figure 2.1(a) shows that at $T_0 = 0$ K, $f_0(E) = 0$ for $E > E_F$ while $f_0(E) = 1$ for $E < E_F$. This means that all states below E_F are filled and all states above E_F are empty, therefore, the plot looks like a step function. As temperature increases with $T_0 < T_1 < T_2$, the probability of finding electrons at higher available energy states become higher. This can be observed from the figure where for $T > T_0$, the quantum states below E_F are partially empty and the states above E_F are partially filled. Independent of temperature T, when $E = E_F$, $f_0(E) = 0.5$, it means that there is equal probability of finding and not finding an electron in a state at this energy, respectively. Both E and the E_F are commonly normalized with respect to thermal activation energy to $\epsilon = (E - E_C)/k_B T$ and $\eta = (E_F - E_C)/k_B T$, which are called the reduced energy (ϵ) and the reduced chemical potential (η) respectively. Besides, different statistical distribution functions are defined to explain the interactions between large number of particles in a system. A semiconductor is regarded as degenerate if it follows FD statistics and non-degenerate semiconductor if it obeys Maxwell-Boltzmann (MB) statistics (not discussed here). In a condition where the ratio $(E - E_F)/k_B T < -2$, these distribution functions start to deviate from each other, and therefore employing a suitable function is critical for description of the system [57, 68]. The probability distribution function ($f_0(E)$) can be re-written as:

$$f_0(E) = \{1 + \exp(\epsilon - \eta)\}^{-1} \qquad \text{Equation (2.7)}$$

Also, replacing $E_C = 0$, the DOS expression can be re-written as:

$$g(\epsilon) = \frac{1}{2\pi^2}\left(\frac{2m_D^*}{\hbar^2}\right)^{1.5} (\epsilon\, k_B T)^{0.5} \qquad \text{Equation (2.8)}$$

The electrical conductivity is one of the basic thermoelectric properties which is classically introduced in the framework of the Drude model. The Drude model explains that the origin of electrical conductivity σ is due to the flow of electrons in the direction of electric field $\vec{E}$, here simplified to scalar E, with an average velocity known as drift velocity (v_d). Then, the resulting current density (j) is given by [61, 69]:

$$j = env_d \qquad \text{Equation (2.9)}$$

On the other hand, Ohm's law defines j in terms of conductivity σ of a material as $j = \sigma E$ which gives [61, 69]:

$$\sigma = en\, v_d/E \qquad \text{Equation (2.10)}$$

The Drude model treats electrons as classical non-interacting particles which experience a force $F = e\vec{E}$. The acceleration $\dot{v}$ is assumed to occur for some average (scattering) time (τ), followed by the scattering of these particles by an obstacle (a scattering center). Therefore, an average velocity due to scattering can be given as: $\int_0^\tau \dot{v}dt = \int_0^\tau \frac{eE}{m} dt = \frac{eE\tau}{m} = v_\mathrm{d}$; in accordance with the Newton's second law. On substituting v_d in Equation (2.10), a familiar expression is obtained: $\sigma = ne^2\tau/m$. From this expression, the drift mobility (μ_d) of electrons is defined as: $\mu_\mathrm{d} = e\tau/m = v_\mathrm{d}/E$. This makes Equation (2.10) to be re-written as:

$$\sigma = en\mu_\mathrm{d} \qquad \text{Equation (2.11)}$$

This classical theory of free electrons in metals was consistent with Ohm's law and accounted for a wide range of electrical properties. This theory however had some limitations out of which, the relevant ones are mentioned here. The dependence of conductivities for metals, declines with an increasing temperature while for semiconductors, it varies exponentially with $1/T$. The deceasing conductivity in metals come from the temperature dependence of the relaxation time τ; the relaxation time decreases with increasing temperature. On the other hand, the relaxation time of semiconductors also decreases with increasing temperature but this effect is quite overwhelmed due to the increasing carrier density with temperature. This results in an exponential increase in electrical conductivity with temperature. Furthermore, this older theory resulted into the difference in the measured and calculated Seebeck coefficient of metals by a factor of 100. For the prediction of the Seebeck coefficient of metals, the use of classical statistical mechanics instead of quantum statistical mechanics results in this deviation. The classical statistics underestimates the density of carriers in a system with large number of carriers, and therefore leads to a large (calculated) Seebeck coefficient. Due to the same reason, the differences in the Seebeck coefficient of metals and semiconductors (roughly, a factor of 100) remained unexplained by this theory. The discrepancies in the 'sign' of the Seebeck coefficient and the Hall coefficient were also unexplainable, often predicted incorrectly using the classical theory [59].

The drawbacks of the classical free electron theory were partially resolved by the quantum mechanical free electron theory proposed by Sommerfeld, however, the discrepancy with the sign of transport coefficients (mentioned above) persisted. Later, band theory was proposed by Bloch, Kronig and Penny, and others which provided a more realistic description of electrons in a semiconducting solid. The band theory was proposed since the Sommerfeld's theory failed to explain why few materials are conductors while others are semiconductors. Sommerfeld's

model assumed that the conduction electrons in metals experience a constant (zero) potential while moving in the crystal and are only restricted by the crystal surface.

The band theory rather came up with a better description of an electron in the crystal. According to the band theory, the crystalline potential is periodic owing to a periodic arrangement of positively charged ions in the crystal. Therefore, the motion of electrons in a crystal is explained by the Schrödinger's equation that includes the periodic potential experienced by these electrons. The band theory of solids provides a better explanation of the electron transport in solids including semiconductors (with the fact that the discretized energy levels are separated by forbidden energy zones, called band gaps).

Besides, on application of an external field, the electrons are no longer in the equilibrium condition but move in an orderly fashion. Out of different methods of describing the carrier transport phenomena in semiconductors, the Boltzmann transport equation (BTE) (within relaxation time approximation (RTA)) is used to describe motion of carriers in the presence of externally applied fields. The Boltzmann transport equation (BTE) describes carrier transport under the applied external field in multi-dimensional phase space (of position and momentum, total six dimensional) at finite temperatures [70]. The BTE allows the description of the carrier transport in real materials in which the macroscopic changes in the material are governed by microscopic effects (e.g. collision that impede the transport of carriers). The BTE takes large computational effort and extended duration to solve it. Therefore, the solutions of the BTE, which are the equations of different transport coefficients, are utilized to understand and predict carrier transport in semiconductors. It is assumed that the deviation of $f_0(E)$ from the equilibrium, due to external perturbations, is not large and the relaxation of this distribution function back to equilibrium is described by the concept of RTA. The use of the RTA is justified under two cases: the collisions between carriers are elastic in nature, and second the probability of scattering of carriers is equal along any direction i.e. it is isotropic. Nevertheless, the second approximation is only satisfied for spherical energy surfaces, discussed in the beginning of this section, and needs an inclusion of the scattering anisotropy for understanding transport phenomena in e.g. materials with ellipsoidal surfaces such as Si or Ge [57].

The different transport coefficients and the carrier scattering will be shortly discussed in the upcoming section. The discussion of different transport coefficients/properties is based on the single parabolic band (SPB) model.

2.2.1 Carrier scattering

As shown in the last section, μ is directly related to the relaxation time (τ). Relaxation time is the inverse sum of the individual scattering times (τ_s) of different processes existing simultaneously in a material, in accordance with the Matthiessen's rule [57]:

$$\frac{1}{\tau} = \sum_s \frac{1}{\tau_s} \qquad \text{Equation (2.12)}$$

Here, the subscript s refers to the different types of scattering mechanisms. These various types of scattering mechanisms are commonly described by a power law as a function of ϵ, given by $\tau_s = \tau_{0,s}\epsilon^{\lambda-1/2}$. In this expression, $\tau_{0,s}$ is the relaxation time constant of the scattering process, which can be a function of microscopic material parameters and temperature, and λ denotes the scattering exponent [57]. A carrier drifting under an influence of external perturbation can be scattered by a number of mechanisms such as acoustic phonon (AP) scattering, alloy scattering (AS), grain boundary (GB) scattering, dislocation scattering, point defect scattering, ionized impurity scattering and optical phonon scattering etc. [57]. The scattering mechanism relevant to Mg_2X (X: Si, Sn) materials are correlated with the mobility μ and discussed in sub-section 2.2.3.

2.2.2 Carrier concentration and the Hall coefficient

The carrier concentration n is a central parameter to understand and optimize the thermoelectric performance of any material as shown in Figure 1.5. By the substitution of Equation (2.7) and Equation (2.8) in Equation (2.5), the following expression is obtained:

$$n = 4\pi\left(\frac{2m_D^* k_B T}{h^2}\right)^{1.5} F_{0.5}(\eta) \qquad \text{Equation (2.13)}$$

Here $F_{0.5}(\eta) = \int_0^\infty \{1 + \exp(\epsilon - \eta)\}^{-1}\epsilon^{0.5}d\epsilon$, is called the Fermi integral of order 0.5.

The carrier concentration n is determined experimentally from the Hall coefficient (R_H) (Equation (2.14)) measurement, see Chapter 5. Within the SPB approximation, R_H and n are related by [57, 67]:

$$R_H = \frac{1}{n_H e} = \frac{r_H}{ne} \qquad \text{Equation (2.14)}$$

Where, n_H is the Hall carrier concentration. The Hall pre-factor r_H incorporates scattering effects that cause deviation between n and n_H. The r_H is given as [57, 67]:

$$r_H = \frac{3}{2} F_{0.5}(\eta) \frac{(1/2 + 2\lambda) F_{2\lambda - 1/2}(\eta)}{(1+\lambda)^2 F_\lambda^2} \qquad \text{Equation (2.15)}$$

In cases where a minority band contributes to the transport properties, the R_H measurement and corresponding model equations are utilized for analyzing transport properties, as discussed in sub-section 2.2.7.

2.2.3 Electrical conductivity and mobility

The solution to the BTE gives the electrical conductivity σ for a material. The electrical conductivity of a material assuming an SPB transport with scattering exponent $\lambda = 0$ [57] is given as:

$$\sigma = \int_{-\infty}^{+\infty} \sigma'(E)\, dE$$
$$= \frac{8\pi e^2 {m^*_{SV}}^{0.5} (2k_B T)^{1.5}}{3h^3} \tau_0 F_0(\eta) \qquad \text{Equation (2.16)}$$

The $\sigma'(E)$ is the differential conductivity at a given energy E due to the motion of each electron under the influence of external perturbation. $\sigma'(E)$ is integrated over the energy levels in the CB, and $1/\tau_0 = \sum 1/\tau_{0,s}$. $\sigma'(E)$ is further elaborated as $\sigma'(E) = e^2 \Xi(E) \left(-\frac{\partial f_0(E)}{\partial E}\right)$, where $\Xi(E)$ is called the transport distribution function. This function is related to the group velocity of the carriers in the direction of the applied external perturbation, relaxation time τ and the dispersion relation of carrier energy in the (first) Brillouin zone [71]. Besides, $\sigma'(E)$ also consists of a derivative of the distribution function $\left(-\frac{\partial f_0(E)}{\partial E}\right)$ [71, 72], shown in Figure 2.1(b), that is centered at E_F. This is called as the 'Fermi window' and it shows the energy interval where the carriers flow. This means that only those quantum states that are a few $k_B T$ above and below the Fermi level E_F contribute to the electrical conduction, and not all the states below E_F. Moreover, the position of this window depends on the position of the Fermi level E_F.

As cited before in section 2.2.1, relaxation time constant $\tau_{0,s}$ is related to the relaxation time (τ), and this $\tau_{0,s}$ is a macroscopic average of electron relaxation times which results from the interaction of carriers with different scattering centers e.g. lattice defects, carriers, irregularities caused by phonons [67]. The different types of scattering mechanisms relevant for Mg_2X materials have been tabulated (Table 2.1) along with their dependence on other parameters such

as temperature, m^*_{SV} and the elastic constant for longitudinal vibrations C_l etc. [57, 73, 74]. The elastic constant is given by the expression: $C_l = v_l\rho$, here, v_l is the longitudinal speed of sound and ρ is the mass density of the specimen.

Table 2.1 Expressions of the different scattering mechanisms (with $\lambda = 0$) and their dependence on T, m^*_{SV} and other microscopic material parameters [57, 67, 73, 74].

Scattering mechanism (s)	λ	m^*_{SV} dependence of $\tau_{0,s}$	T dependence of $\tau_{0,s}$	$\tau_{0,s}$
Acoustic phonons	0	$(m^*_{SV})^{-1.5}$	$T^{-1.5}$	$\frac{\pi\hbar^4 C_l}{\sqrt{2}\, E_{Def}^2 (m^*_{SV} k_B T)^{1.5}}$
Alloy scattering	0	$(m^*_{SV})^{-1.5}$	$T^{-0.5}$	$\frac{8N_0\hbar^4}{3\sqrt{2}\,\pi\, x(1-x)E_{AS}^2 {m^*_{SV}}^{1.5}(k_B T)^{0.5}}$
Grain boundary		$(m^*_{SV})^{-0.5}$	$T^{-0.5}e^{(-T^{-1})}$	$Be\ (\frac{1}{2\pi m^*_{SV} k_B T})^{0.5} \exp(-\frac{E_B}{k_B T})$

The corresponding drift mobility μ_d is obtained by the substitution of σ (from Equation (2.16)) and n (from Equation (2.13)) in Equation (2.11), and the expression of μ_d is written as [57]:

$$\mu_d = \frac{2e}{3m^*_{SV}}\tau_0 \frac{F_0(\eta)}{F_{0.5}(\eta)} \text{ (since } m_I^* \equiv m^*_{SV}) \qquad \text{Equation (2.17)}$$

The Hall mobility $\left(\mu_H = \frac{\sigma}{en_H}\right)$ can be experimentally measured and it is related to μ_d as [57]:

$$\mu_d = \frac{4}{3}\frac{F_0^2(\eta)}{F_{0.5}(\eta)\, F_{-0.5}(\eta)}\mu_H \qquad \text{Equation (2.18)}$$

And, the Hall mobility is related to the mobility parameter by the relation [57]:

$$\mu_H = \mu_0 \frac{F_{-0.5}(\eta)}{2F_0(\eta)} \qquad \text{Equation (2.19)}$$

μ_H and μ_d are a function of the Fermi level E_F *via* the Fermi integrals. The dependence of these quantities on the Fermi integrals makes the utilization of both these quantities inappropriate to understand the effect of each scattering mechanism on mobility μ and for a prediction of optimum carrier concentration. Therefore, the mobility parameter μ_0 is utilized instead of μ_H and μ_d. The mobility parameter can be expressed by Equation (2.20) after an algebraic re-arrangement of Equation (2.18) and Equation (2.19):

$$\mu_0 = \frac{3}{4}\frac{F_{0.5}(\eta)\,F_{-0.5}(\eta)}{F_0^2(\eta)}\frac{2F_0(\eta)}{F_{-0.5}(\eta)}\frac{2e}{3m^*_{\mathrm{SV}}}\tau_0\frac{F_0(\eta)}{F_{0.5}(\eta)} = \frac{e\tau_0}{m^*_{\mathrm{SV}}} \qquad \text{Equation (2.20)}$$

The μ_0 is extracted from the measured values of n utilizing the Fermi integrals. Later, the mobility parameter is predicted by incorporating different scattering mechanisms (listed in Table 2.1) in the Matthiessen's rule. The carrier scattering mechanism for most thermoelectric materials can be obtained by fitting the experimental data assuming a SPB model. Some materials might not obey single parabolic transport, then, other physical models (considering non-parabolicity, multi-band transport etc.) should be implemented for analyzing the transport properties. At high temperatures, AP scattering is the most dominant amongst all scattering mechanisms. Besides this, alloy scattering (AS) needs to be considered as an additional scattering mechanism for understanding transport in the Mg_2X solid solutions. According to the power law, the energy dependence of the relaxation time τ, which is limited by AP and AS, is given by $\tau_{\mathrm{AP/AS}} \sim \epsilon^{-0.5}$ with $\lambda = 0$. Each scattering mechanism that is relevant to the work (listed in Table 2.1) presented in this thesis is briefly elaborated in the following part.

The AP scattering [75] is a consequence of carrier-phonon interaction as described by Bardeen and Shockley. Generally, the atoms in a semiconductor possess thermal energy at temperatures $T > 0$ K which leads to a random vibration of atoms around their lattice position. A random vibration of atoms causes a perturbation of the periodic potential that scatter the carriers by interacting with them [56, 76]. In case of AP, the neighboring atoms in the lattice move in the same direction [77]. μ_{d} is computed using the Equation (2.17) by replacing τ_0 for AP scattering from the Table 2.1. The equation shows dependence of τ_0 ($\propto \mu_0$) on E_{Def} which is the deformation potential constant. E_{Def} characterizes the interaction potential between electrons and phonons, which is why it is also called as electron-phonon interaction potential. E_{Def} of common inorganic TE materials has been reported in the range between $5 - 35$ eV [76]. A low E_{Def} translates to a weak interaction between carriers and phonons. A weak interaction could lead to a low scattering of carriers and thus a high mobility μ. Consequently, this could lead to good TE properties given that the other parameters are optimized.

The carrier scattering in alloys due to a random distribution of component atoms on the respective lattice sites is referred as alloy scattering [78]. The relaxation time due to AS is given by the expression [57] in Table 2.1. In the expression of the mobility parameter for the alloy scattering, N_0 is the total number of atoms per unit volume (in the material) while E_{AS} is the

alloy scattering potential which accounts for the carrier scattering effects by the fluctuations (caused by the atomic disorders, e.g. solid solutions).

The GB scattering mechanism has been found to effectively scatter charge carriers near or below RT [79]. GB scattering stems from atomic defects that could be present at the grain boundaries in a material. These defects are incompletely bonded atoms which form trapping states for carriers and immobilize them [73]. GB scattering was found relevant for n-type Mg_2Si materials [74], leading to a lower conductivity near $300\ \mathrm{K} - 400\ \mathrm{K}$, and could be probably active for $Mg_2(Si,Sn)$ based solid solutions as well. This is because MgO can also be formed as an impurity in these materials like n-type Mg_2Si. The magnitude of electrical conductivity is affected by the grain size (B) and the barrier height (E_{B}) as can be seen from Table 2.1. The scattering of carriers due to dislocations, neutral impurities, and ionized impurities are not discussed because they are not highly relevant for Mg_2X material system but they can be referred from [80].

Using computational tools, the SPB model can be easily scripted and the parameters such as E_{Def}, E_{AS}, and μ_0 can be extracted from the experimental data. The temperature dependent conductivity can be predicted using the SPB model by plugging these extracted parameters. Note that the transport properties are predicted till the temperature point, where a negligible influence of minority carrier band is found.

2.2.4 The Seebeck coefficient

The Seebeck coefficient quantifies the re-distribution of carriers in a material whose ends are at a temperature difference. While any difference in temperature between the sample ends can induce a thermovoltage, a temperature difference of a few K is needed for the measurement of thermovoltage. A difference in the Fermi function due to the applied temperature difference is the physical reason for the generated Seebeck voltage. The Seebeck coefficient S in the conduction band is derived from the relationship of Cutler and Mott [69, 81, 82]:

$$S\sigma = -\frac{k_B}{e}\int_0^{\infty}(\epsilon-\eta)\,\sigma'(\epsilon)d\epsilon \qquad \text{Equation (2.21)}$$

Equation (2.21) consists of a difference between the reduced energy and the reduced Fermi level weighted with the differential conductivity ($\sigma'(\epsilon)d\epsilon$) due to electrons at a reduced energy ϵ. The integration of weighing factor to the total conductivity due to carriers in a band i.e. $(\int_0^{\infty}\sigma'(\epsilon)\,d\epsilon)/\sigma)$, gives an understanding that the Seebeck coefficient S is related to the energy difference $(\epsilon-\eta)$ i.e. the average energy ϵ at which the carriers flow with respect to

the Fermi level η [69, 72]. The Seebeck coefficient (Equation (2.21) can be re-written by implementing ($\epsilon = E_{avg}/k_B T$ and $\eta = E_F/k_B T$) as:

$$S = -\frac{1}{eT}(E_{avg} - E_F) \qquad \text{Equation (2.22)}$$

Therefore, $(E_{avg} - E_F)$ is called the electronic energy transported per electron. Besides, doping leads to a change in the E_F as well as E_{avg} which influences the Seebeck coefficient [56, 72]. The Seebeck coefficient S of low doped semiconductors is quite large because E_F is far below E_{avg}, which is near the band edge where the carriers flow. For a heavily doped semiconductor, a lower Seebeck coefficient is observed because the difference between E_F and E_{avg} decreases. Each of these mentioned cases can be intuitively understood by the illustration in Figure 2.2.

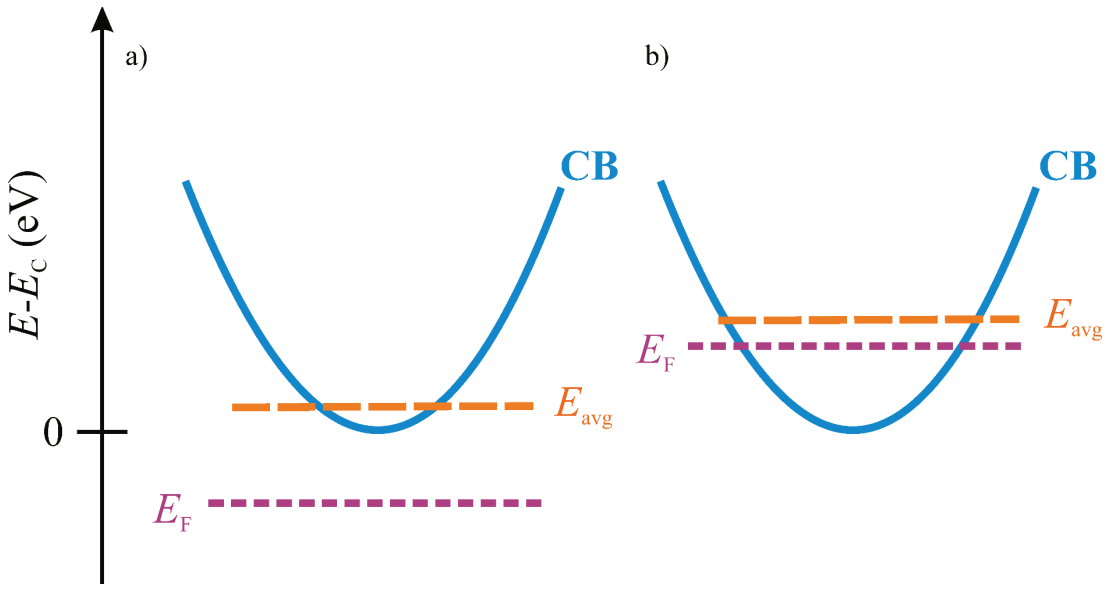

Figure 2.2 Schematic of a CB along with the position of E_F and E_{avg} for (a) low and (b) high carrier concentration n.

For a low doped semiconductor, the tail of the Fermi window (Figure 2.1(b)), briefly discussed in 2.2.3, coincides with the bottom of the CB and consequently, the electrical conductivity is limited by the carrier states near the band edge. Unlike this case, the Fermi window lies deep within the band for a heavily doped semiconductor that has more states contributing to the transport [56, 72]. A simplified expression of the Seebeck coefficient S for a SPB transport can be devised from the Equation (2.21) and rewritten as Equation (2.23). The reduced Fermi level η can be directly calculated from the measured Seebeck coefficient by [67]:

$$S = \frac{k_B}{e}\left(\frac{(2+\lambda)F_{\lambda+1}(\eta)}{(1+\lambda)F_\lambda(\eta)} - \eta\right) \qquad \text{Equation (2.23)}$$

A complete derivation of this expression from the BTE can be looked up in [68]. The reduced Fermi level (η) dependence of the Seebeck coefficient can be observed from Figure 2.3(a), which shows that the Seebeck coefficient S decreases as η increases and vice-versa. The value of η is calculated from Equation (2.23) and the chosen model assumptions, and it is related to n and m_D^* as given in Equation (2.13) for a particular temperature (here, S vs η at $T = 300$ K is shown in Figure 2.3(a)).

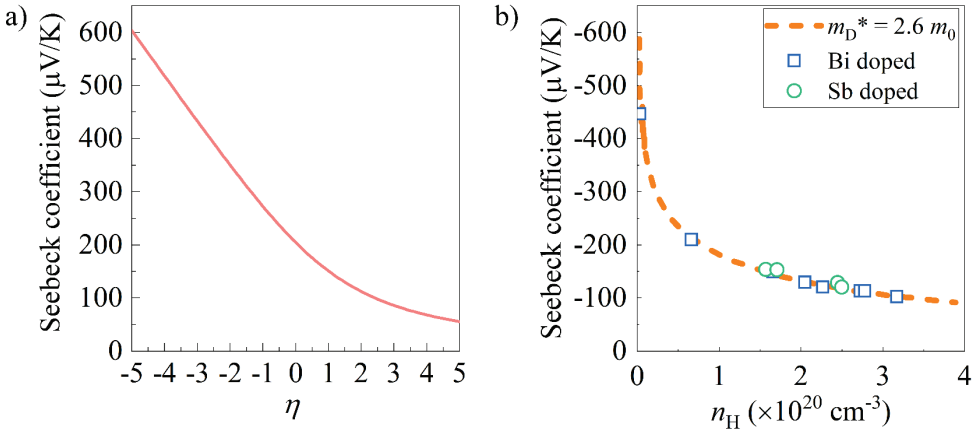

Figure 2.3 (a) The Seebeck coefficient S as a function of η at 300 K and $\lambda = 0$. (b) Experimentally measured $S(n_H)$ for Bi- and Sb-doped $Mg_2Si_{0.3}Sn_{0.7}$ at 300 K. The plot in (b) has been reproduced (adapted) from Ref. [83] with permission from the Royal Society of Chemistry.

For high degeneracy (e.g. metals or heavily doped semiconductors) i.e. $\eta \gg 0$, and so the Equation (2.23) can be re-expressed by a second order approximation of the Fermi integral ($F_j(\eta) = (\eta^{j+1}/j+1) + (j\pi^2/6)\,\eta^{j-1}$), which limits the S as [1, 81]:

$$S = \frac{8\pi^2 {k_B}^2}{3eh^2} m_D^* T \left(\frac{\pi}{3n}\right)^{\frac{2}{3}} \qquad \text{Equation (2.24)}$$

This expression shows that the Seebeck coefficient depends on m_D^* as well as n which must be high and low, respectively, for a high Seebeck coefficient. This expression can be utilized to gain a qualitative understanding of electrical transport in thermoelectric materials since good thermoelectric materials are heavily doped semiconductors. Besides, Figure 2.4 shows the temperature dependence of η assuming that n and m_D^* are T-independent.

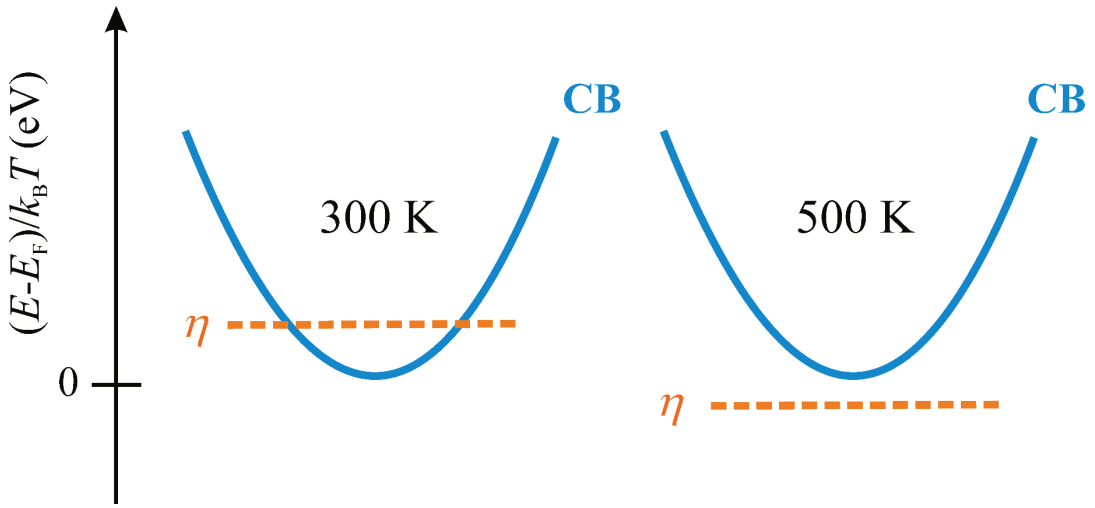

Figure 2.4 Schematic of a CB along with the change in position of η with temperature in the $E(k)$ plot. η decreases towards the CB edge and beyond as temperature increases.

For a fixed n, η decreases (moves towards the CB minima) with increasing temperature since the higher energy states get more heavily populated. Intuitively, the Seebeck coefficient increase with increasing measurement temperature thus, reflecting that the reduced Fermi level (η) decreases.

2.2.5 Electronic contribution of thermal conductivity and total thermal conductivity

An improvement of TE performance can be accomplished by optimizing the material such that the contribution of the electrical transport properties is as large as possible with a low thermal conductivity κ. Achieving a low κ without having an adverse effect on the power factor has been the central theme of thermoelectric research for the past few decades and it is one of the key challenges to overcome. The thermal transport in a material is a broad topic of research in itself and here it is only discussed briefly, since the focus of this work is largely based on understanding the electrical transport in $Mg_2(Si,Sn)$.

In any solid, heat can be transported in a number of different ways (phonons, free electrons or holes, excitons, photons etc.). The thermoelectricians mainly focus on thermal conductivity which is written as $\kappa = \kappa_{el} + \kappa_{lat} + \kappa_{bi}$. The total thermal conductivity has contributions from the electronic κ_{el}, lattice κ_{lat} and bipolar thermal conductivity (κ_{bi}) (due to the formation of $e^- - h^+$ pairs).

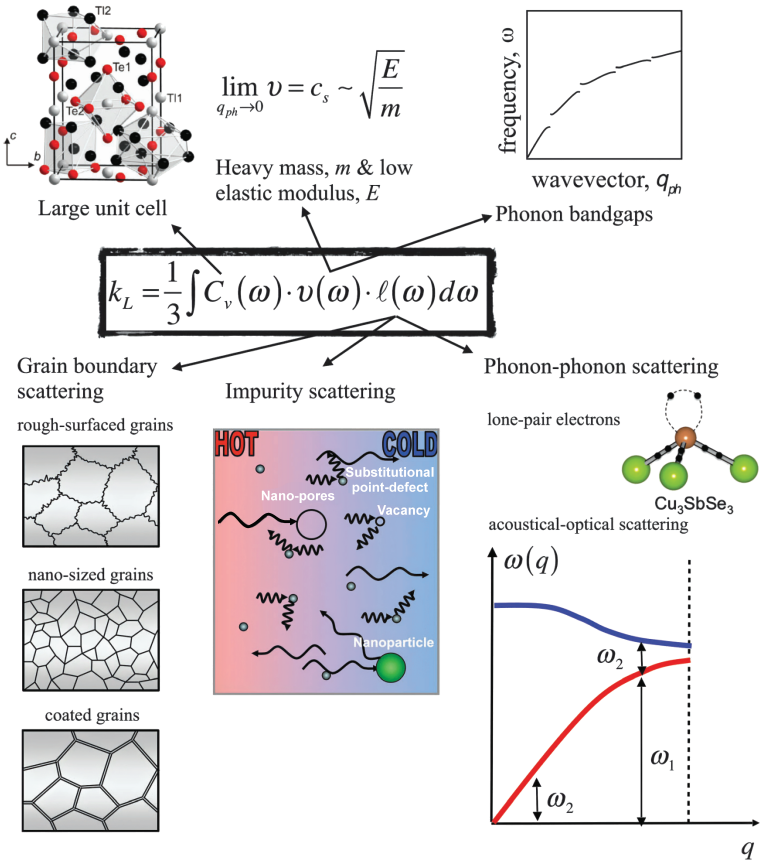

Figure 2.5 Different strategies employed for phonon engineering that are categorized into methods affecting each component of κ_{lat}, such as specific heat (C_{v}), phonon group velocity (v), and mean free path (l). The figure has been reproduced (adapted) from Ref. [84] with permission from the Royal Society of Chemistry.

The essential requirement to enhance the electrical conductivity of a material through heavy doping also leads to a significant contribution of the κ_{el} to κ. Therefore, for a variety of materials, a lot of work focuses on reducing κ_{lat}, by employing strategies to scatter the phonons in addition to the usual phonon-phonon (Umklapp) scattering, e.g. by lattice disorder, grain boundaries, solid solution formation, dislocations, point defects, nanostructuring etc. [30-35]. κ_{lat} is approximated by $\kappa_{\text{lat}} = \frac{1}{3}C_{\text{v}}vl$ [68, 84] where C_{v} is the specific heat, v is the phonon group velocity, l is the phonon mean free path (describing the scattering processes), all corresponding to a phonon frequency. A variety of strategies to reduce κ_{lat} focus on reducing either of the parameters in the stated expression of κ_{lat}, which can be visualized in Figure 2.5. The figure also shows that κ_{lat} can be reduced by mechanisms other than the previously mentioned ones. These mechanisms include impurity scattering, utilizing TE materials with large unit cell, or materials with enhanced Umklapp scattering. Besides, the accurate estimation of the electronic contribution ($\kappa_{\text{el}} = L\sigma T$) to the total thermal conductivity κ depends on a

good estimation of the Lorenz number (L). For single band transport, L depends only on η, and is calculated using [57, 67, 85]:

$$L = \left(\frac{k_B}{e}\right)^2 \frac{(1+\lambda)(3+\lambda)F_\lambda(\eta)F_{\lambda+2}(\eta) - (2+\lambda)^2 F_{\lambda+1}(\eta)^2}{(1+\lambda)^2 F_\lambda(\eta)^2} \qquad \text{Equation (2.25)}$$

Note that the scattering parameter plays a crucial role in the determination of L, therefore for the analysis of the properties, the carrier scattering mechanism must be resolved carefully to deduce the contributions from different mechanisms. For an analysis with an SPB transport (with $\lambda = 0$), the Lorentz number $L = 1.49 \times 10^{-8}\ \mathrm{V^2K^{-2}}$ and $L = 2.44 \times 10^{-8}\ \mathrm{V^2K^{-2}}$ is valid for the non-degenerate and degenerate regime (and for metals), respectively [84].

2.2.6 Optimization of thermoelectric figure-of-merit

Thermoelectric figure-of-merit, zT, can be optimized using a SPB model for the temperatures below an onset of a significant contribution from the minority carriers. zT is then given by [64, 67]:

$$zT = \frac{S^2}{L + (\psi\beta)^{-1}} \qquad \text{Equation (2.26)}$$

Here, ψ is a function that depends on η and λ (but not on microscopic material parameters), and is given as:

$$\psi = \frac{8\pi e}{3}\left(\frac{2m_0}{h^2}\right)^{1.5}(1+\lambda)F_\lambda(\eta) \qquad \text{Equation (2.27)}$$

β, a material parameter, is a measure of the thermoelectric performance of any material [86]. The β depends on microscopic material parameters such as μ_0, m_D^* and κ_{lat} [67]:

$$\beta = \frac{\mu_0 {m_D^*}^{1.5} T^{2.5}}{\kappa_{lat}} \qquad \text{Equation (2.28)}$$

The parameters μ_0, m_D^* and κ_{lat} are determined from the experimentally measured properties (S, σ, κ and R_H) using the SPB model (here, with $\lambda = 0$). These parameters are then utilized to predict the transport properties using SPB model, and calculate β along with $zT(n)$ for the temperatures, where the influence of minority carrier band is negligible [83].

2.2.7 Mixed conduction

Note that in the following text, the multiband model is discussed only for the case when a single minority band starts contributing to the transport properties. However, the equations discussed below are valid for the cases where more than one conduction or valence band contributes (e.g. energetically degenerate bands).

The transport due to single carrier type can be confirmed by one of the following ways. First, by observing the slope of T-dependent Seebeck coefficient. With increasing temperature, the reduced Fermi level η decreases and moves towards the conduction band edge (for n-type materials) and vice-versa, as visualized in Figure 2.4. At higher temperatures, $e^- - h^+$ pairs are generated by thermal excitation, and the minority carriers from the minority band start contributing to the transport properties. An influence of minority carrier band can be observed from the T-dependent Seebeck coefficient curve, which achieves a peak absolute value. This contribution of the minority carriers due to thermal activation of $e^- - h^+$ pairs is not accounted in the SPB model, and therefore, for such a case, the combined Seebeck coefficient is given by $S = \frac{S_h\sigma_h + S_e\sigma_e}{\sigma_h + \sigma_e}$. The SPB model is only applicable for temperature dependent thermoelectric transport properties before an activation of these pairs. Beyond this it is appropriate to model these properties using a multi-band transport model.

Besides, the Seebeck coefficient S of a material can be plotted as a function of its n_H (or n), called a Pisarenko plot, to examine that the material obeys single parabolic band transport or not. The plot is constructed at a given temperature point, where the single parabolic transport is valid and it is mostly plotted at room temperatures. In Figure 2.3(b), a Pisarenko plot is shown for heavily doped n-type $Mg_2Si_{0.3}Sn_{0.7}$ at 300 K. The data points lie on the orange dashed line which reflects that the m_D^* of all the samples is constant and do not vary with n_H (or n). Nevertheless, for a single dominant carrier type, it is desirable that the band structure of the TE semiconductor possesses multiple valleys in the active band(s), that are within the energetic interval of the conduction electrons, to observe a high Seebeck coefficient and electrical conductivity [64].

In the case where minority carriers contribute to the transport properties, the SPB model is not strictly valid and a multiband transport model is needed for the description of the electrical transport properties. The multiband transport model can also be implemented in multivalley situations where the microscopic material parameters should be deduced from the SPB model as a starting case. Therefore, the following equations are adapted from [67, 87] that are generally required to model experimentally measured properties.

$$n = \sum_i n_i \qquad \text{Equation (2.29)}$$

$$\sigma = \sum_i \sigma_i \qquad \text{Equation (2.30)}$$

$$R_{\mathrm{H}} = \frac{\sum_i R_{\mathrm{H},i}\sigma_i^2}{(\sum_i \sigma_i)^2} \qquad \text{Equation (2.31)}$$

$$S = \frac{\sum_i S_i\sigma_i}{\sum_i \sigma_i} \qquad \text{Equation (2.32)}$$

$$\kappa_{\mathrm{el}} + \kappa_{\mathrm{bi}} = T\sum_i L_i\sigma_i + \frac{T}{\sum_i \sigma_i}\sum_{i\neq k}\sigma_i\sigma_k(S_i - S_k)^2 \qquad \text{Equation (2.33)}$$

Here, i denotes the number of one type of bands, and k represents the band with a conduction type opposite of i (e.g. valence band, if i represents conduction band). These equations correspond to the transport coefficients which include contributions of transport coefficients of individual bands with a single carrier type. Equations for each band depend on the electrochemical potential of that carrier type i.e. $S_1 = S(\eta_1)$ and $S_2 = S(\eta_2)$, which can be written for a two band (CB+VB) model as: $\eta_2 = -\eta_1 - E_{\mathrm{g}}$. The η values obtained for each band are plugged in the Fermi integrals $F_j(\eta)$ to compute the magnitude of transport coefficients as well as the contributions of each band to this magnitude. Furthermore, the use of appropriate signs in the equations of S and R_{H} are crucial in case where transport modelling is carried out assuming both type of carriers. The equation for modelling electronic thermal conductivity κ_{el} has two terms on the right side. The first term is identical to the one used for modelling using SPB model while the second term accounts for the interaction between different bands. Note that the Lorentz number L is utilized only after determining the correct values of η, since L for each band will be different.

2.3 Material basics of Mg_2X (X: Si, Sn)

Heavily doped n-type Mg_2X (X: Si, Sn) compounds and their solid-solutions show thermoelectric figure-of-merit comparable to other high-performance thermoelectric materials. Also, these materials are inexpensive, environmentally compatible and have a low mass density. These advantages make them preferred candidates for TEG applications in the intermediate temperature range of $T = 300\ \text{K} - 800\ \text{K}$. On the other hand, the binary compounds of this material class find their application in other fields of science and engineering. For example, Mg_2Si is used to strengthen aluminum alloys, which are used in aerospace and automotive industries [88-90]. Besides, Mg_2Sn has shown to be a promising electrode material for batteries that yield high-power output [91, 92].

2.3.1 Physical properties

2.3.1.1 Crystal structure

Mg_2X materials crystallize in the cubic anti-fluorite (CaF_2) crystal structure (space group $Fm\bar{3}m$). The Mg atoms occupy eight tetrahedral sites (8c) in the interior of the lattice cell and the X atoms occupy corner and face center positions (4a) of the cubic cell (shown in Figure 2.6).

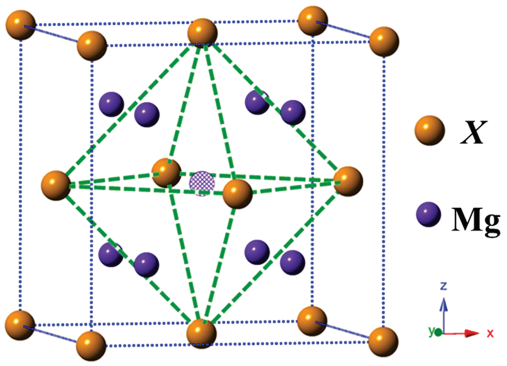

Figure 2.6 Crystal structure of Mg_2X (X = Si, Ge, and Sn) compounds. The octahedral interstitial sites (4b) can be occupied by Mg. The plot has been reprinted with permission from [93].

Besides, there are four interstitial sites corresponding to (4b) Wyckoff positions. Predominantly, Mg atoms occupy these octahedral positions (4b) in the Mg_2X lattice, and the concentration of the Mg interstitials depends on the chemical environment and their relative stability. The lattice parameters of the $Mg_2Si_{1-x}Sn_x$ lie between 6.354 Å and 6.764 Å that corresponds to binary Mg_2Si and Mg_2Sn, respectively [94]. The variation of lattice parameter

with x is in accordance with the Vegard's law. Mg_2X are low mass density compounds (varies between $2 - 3.6$ g/cm^3) compared to other state-of-the-art thermoelectric materials such as Mg_3X_2 (X: Sb, Bi) ($4.04 - 5.84$ g/cm^3) [95], $CoSb_3$ (7.64 g/cm^3) [96] and half-Heusler, particularly, TiNiSn (7.9 g/cm^3) system [97].

2.3.1.2 Electronic band structure

All Mg_2X (X: Si, Sn, Ge) materials are indirect band gap semiconductors possessing similar electronic band structure. The band gap E_g in Mg_2X decreases with increasing atomic mass of X in group 14 elements. E_g has been reported as 0.77 eV for Mg_2Si, and 0.35 eV for Mg_2Sn at 0 K [98]. For $Mg_2Si_{1-x}Sn_x$ solid solutions specifically, a change in the band structure with varying Sn content (x) is shown in Figure 2.7. Here, the valence band maximum (VBM) is located at the Γ point in the Brillouin zone while the conduction band minima (CBM) is at the X point.

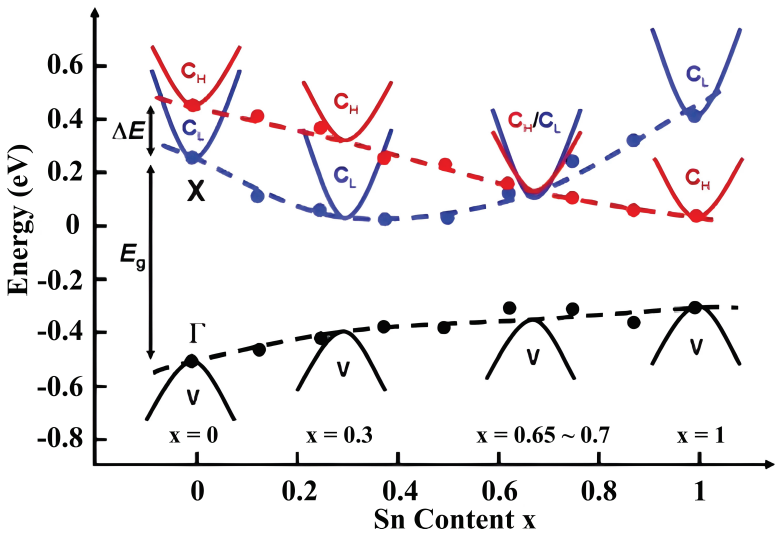

Figure 2.7 Band structure schematic showing the energy dependence of the electronic bands, both valence and conduction bands, on Sn content in $Mg_2Si_{1-x}Sn_x$ based on DFT calculations. Particularly, the energetic position of the heavy conduction band (C_H) which contain electrons with a higher m^*_{SV}, and the light conduction band (C_L) which contain electrons with a lower m^*_{SV}, vary with the Sn content. The composition of $x = 0.65 \sim 0.7$ shows a convergence of these two conduction bands. This figure has been reprinted with permission from [99].

In the past two decades, significant work has been done to optimize the TE properties of Mg_2X (X: Si, Sn) materials and their solid solutions. The studies have been focused to enhance the thermoelectric transport properties of these materials by exploiting their band structure. Initially, Fedorov *et al.* [100] and Zaitsev *et al.* [98, 101, 102] concluded that the heavily doped

n-type $Mg_2Si_{1-x}Sn_x$ solid solutions with $x = 0.6 - 0.7$ show a comparatively high thermoelectric properties compared to the n-type binary compounds. The enhancement of thermoelectric properties is due to a convergence of the conduction bands. Using experimental and computational methodologies, Liu *et al.* [99] systematically proved the observations of previous study. As shown in Figure 2.7, the band structure of Mg_2Si-Mg_2Sn possesses a light (C_L) and a heavy (C_H) conduction band that are separated by an energy offset (ΔE). This split conduction band has been a focus of many studies due to its considerable influence on the Seebeck coefficient and the electrical conductivity of these compounds [23, 103].

2.3.1.3 Synthesis of Mg_2X materials

A variety of techniques has been reported for the synthesis of Mg_2X materials. These techniques include direct melting of precursors [104, 105], induction melting of precursors [106, 107], melt spinning [108, 109], self-propagating high temperature reaction [110, 111], ball milling [53, 112-116], arc melting of precursors [117, 118], B_2O_3 encapsulation [119, 120] etc. The material synthesized using each of these stated techniques is compacted utilizing a variety of sintering techniques e.g. hot pressing, spark plasma sintering etc. Therefore, the synthesis methodology of these materials consists a synthesis step and a high temperature sintering step. Each synthesis step has some disadvantages such as prolonged synthesis durations (days to weeks), high temperature treatment of precursors, repetitive steps (including high temperature heat treatment in some cases) to achieve homogeneous samples and so on. Note that any inconsistencies in the preparation of synthesis such as improper sealing of ampoules, insufficient purging of inert gas (or evacuation) of synthesis chamber etc. might lead to the formation of unwanted phases in the material. For example, a high vapor pressure of Mg (at high temperatures) and its tendency to oxidize quite easily leads to the formation of stable oxide (MgO). Due to this reason, obtaining phase pure samples of Mg_2X and their solid solutions is a challenge. The stated disadvantages and the associated inconsistencies make the overall synthesis methodology cost ineffective.

Considering the aforementioned issues with the synthesis of these materials, mechanical alloying (MA) was employed for the experimental work conducted in this thesis. The mechanism of the synthesis of Mg_2X solid solutions was studied using mechanical alloying, which is detailed in Chapter 6. The effect of various synthesis parameters on the microstructure and TE properties was also understood. The results and analysis of this study are detailed in Chapter 6 and Chapter 8. As a result of these investigations, the optimized parameters for the synthesis of high-performance Mg_2X solid solutions were determined.

2.3.1.4 Point defects

An irregularity in the crystal lattice that has one or more dimensions of an atomic diameter order is known as a crystalline defect. Crystalline materials commonly contain a variety of defects in large concentration. These defects are classified as point defects (PD), one-, two- or three-dimensional defects based on the geometry or dimensionality of that defect. The concentrations of these imperfections in any material have observable effects on their microstructure. The concentration of defects is manipulated to control or enhance the electronic, magnetic, optical or mechanical properties [121] of materials.

Point defects arise in a perfectly arranged lattice structure of a material and can be charged in semiconductors. Depending on the density of these defects, they are known to influence the electrical and thermal transport properties. This reason makes charged point defects interesting for the studies conducted within the scope of this thesis. Therefore, the point defects are discussed here in detail while the discussion of other types of defects is neglected. In general, PD can be classified into two categories: intrinsic and extrinsic defects as shown in Figure 2.8(a).

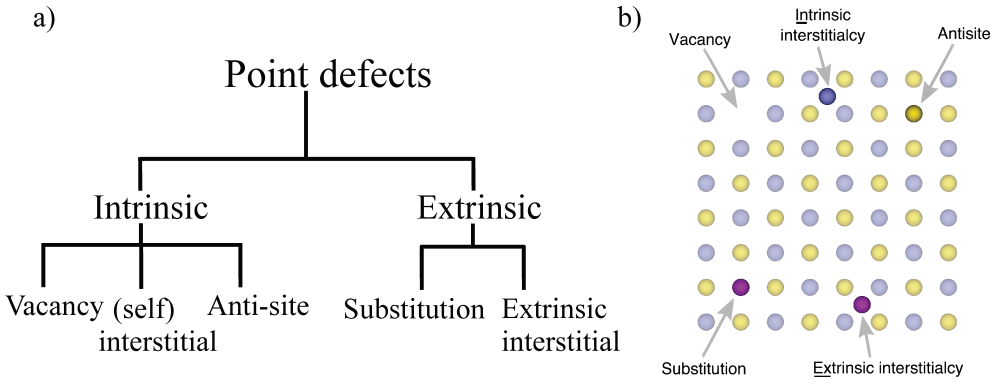

Figure 2.8 a) Classification of point defects and b) Illustration – Intrinsic (top) and Extrinsic (bottom) point defects. The figure in (b) has been re-printed under the terms of the Creative Commons Attribution-Non Commercial-No Derivatives License and requires no permission for non-commercial use [121].

Intrinsic PD consist of chemical species that are part of the base compound, therefore, they are also called native defects. They can be vacancies, self-interstitials or anti-site (only found in compounds) defects. Vacancies are voids where atoms or ions are missing from their normal site in the crystal structure. Self-interstitials are atoms or ions identical to those at the normal lattice sites but positioned in an interstitial position. The anti-site defects can be identified in an ordered alloy or compound where the atoms of one type of element are present on the lattice

site where the atoms of other element should in principle be present [122]. All intrinsic defects mentioned are visualized in the upper part of Figure 2.8(b), which depicts an orderly arrangement of atoms in a lattice. Extrinsic defects, on the other hand, which are usually referred to as impurities, are foreign chemical species introduced in the lattice sites of a bulk material. They include substitutional atoms and extrinsic interstitials. In the former type of defect, the foreign atoms replace the original atoms that normally occupy the lattice sites in a bulk material. The extrinsic interstitials are foreign atoms that occupy interstitial lattice sites of the material. These are visualized at the bottom part of Figure 2.8(b). The density of intrinsic and extrinsic point defects affects the electronic properties in any semiconductor. For this purpose, they are generally exploited to enhance their properties. A variation in the concentration of these intrinsic and extrinsic defects can cause changes in the Fermi level E_{F} [123, 124], the band gap E_{g} [125, 126] or even affect the band structure of materials in other ways [127, 128]. In all thermoelectric materials, point defects are used as a lever to achieve the desired electrical properties. Specifically, the density of (charged) native point defects have been manipulated in PbTe [129-131], Bi_2Te_3 [132-134], and other TE materials (half-Heusler [135-137], Mg_3X_2(*X*: Sb, Bi) [138, 139]) to enhance their thermoelectric performance.

Several computational studies focusing on intrinsic and extrinsic defects in binary Mg_2X materials have been conducted. The nature (charged or neutral) of different intrinsic defects and their relative stability in different growth conditions are investigated computationally. The formation energy of extrinsic defects and its dependence on the growth conditions (Mg-rich or Si/Sn-rich) have been studied for these materials as well. Liu *et al.* [93] studied the Fermi energy dependencies of the formation energies of intrinsic defects in binary Mg_2X (*X*: Si, Sn, Ge) with respect to the chemical potential of Mg, i.e. for Mg-rich and Mg-poor environments. They found Mg-interstitials (I_{Mg}) and Mg-vacancies (V_{Mg}) to be the most dominant point defects owing to their low formation energy. They demonstrated that V_{Mg} always carries two negative charges i.e. V_{Mg}^{2-}, in the entire Fermi energy range independent of the chemical environment. On the other hand, the I_{Mg} forms mainly in the Mg-rich environment and its charge depends on the position of the Fermi level. When the Fermi level is within the calculated band gap range, I_{Mg} is I_{Mg}^{2+} i.e. carries two positive charges. They also found that Sn_{Mg} (an anti-site defect) is one of the most stable defects in Sn-rich (or Mg poor) environment but its charge $(0/+1/-1)$ depends on the position of the Fermi level E_{F}. All these native defects contribute to the total carrier concentration of these materials. Accordingly, the chemical potential of Mg is often regulated by the addition of excess Mg during synthesis. As a result, Mg_2Si always shows n-type conduction while the conduction type of Mg_2Sn depends on the chemical potential

of Mg. To sum up, the chemical environment plays a crucial role for the formation of intrinsic defects in Mg_2X based materials. Moreover, Mg-related defects are charged and the most stable amongst all intrinsic defects. Correspondingly, these defects influence the conduction type and carrier concentration of Mg_2X based materials.

Computational studies were also conducted in search of suitable impurities to enhance the electrical properties of Mg_2Si and Mg_2Sn. Tani *et al.* [140, 141] carried out a systematic study using first-principles calculations considering a variety of elements namely H, Li, Na, K, Rb, Sc, Y, La, B, Al, Ga, In, N, P, As, Sb, Bi, Cu, Ag and Au to be used as extrinsic dopants in Mg_2Si and Mg_2Sn. The results showed that Li, Na and Ga (in Mg_2Si) induced p-type conduction, while Sc, Y, La, As, P, Sb, Bi and N all resulted in n-type conduction. For Ag and Cu, the site preference depends on the chemical potentials of Mg and Sn i.e. both Ag and Cu prefers to substitute Sn in Mg rich conditions and vice versa. Besides, the formation energy of Au was mostly lower compared to Ag and Cu and independent to the atomic chemical potential of Mg and Sn. Au prefers to substitute Sn over Mg for the entire range of chemical potential. The other elements (Ga (in Mg_2Sn) and In) had different conduction types, depending on the chemical potential of Mg and Si/Sn, respectively. In Mg_2Sn, the formation energies of group I(a) elements at their solubility limits were lower when substituting Mg compared to Sn, except for the H substitution on the Mg-site. Overall, the group V elements showed better solubility in both Mg-rich and Mg-poor conditions and therefore they are preferred candidates for substitution. These elements introduce n-type character in the transport properties of the material. Moreover, the heavy elements Sb/Bi as dopants also provide mass fluctuation to enhance point defect scattering of phonons. Therefore, usually Sb or Bi are substituted on the *X* site in Mg_2X (*X*: Si, Sn) binaries and solid solutions [45, 99, 142-144].

Jiang *et al.* [144] have experimentally shown that the thermoelectric properties of $Mg_2(Si,Sn)$ can be enhanced by substitution of Sb on Si/Sn sites. They also studied an interplay between Sb and I_{Mg} and V_{Mg}. In this work, they showed that the increasing Sb concentration in the material affects the concentration of V_{Mg}, and also that excess Mg facilitates the formation of I_{Mg} both of which influence the carrier concentration n of the material. A $zT \sim 1.1$ was achieved for $Mg_2Si_{0.4}Sn_{0.6-x}Sb_x$ with $x = 0.1$. Kato *et al.* have also shown that annealing Sb-doped Mg_2Si [145] and Sb-doped $Mg_2Si_{0.5}Sn_{0.5}$ [146] in different Mg partial pressure environment has a significant influence on their electrical transport properties and underlying parameters. The samples corresponding to the stated compositions were synthesized by taking excess Mg. The authors found a decrease in the carrier concentration n and the mobility μ of the material on annealing the material in Mg-poor environment. These materials recover their original carrier

concentration n on annealing them in Mg-rich environment. Kato *et al.* also found that the carrier concentration n increases with increasing Sb content in $Mg_2Si_{1-x}Sb_x$ up to $x \leq 0.1$ and decreases beyond this. They explained this as a vacancy stabilization mechanism due to defect (vacancy – dopant) association between V_{Mg} and $Sb_{Si/Sn}$. The experiments by Jiang *et al.* and Kato *et al.* suggest that the transport properties are sensitive to Mg and a further increase in Sb content beyond a certain limit promotes the formation of V_{Mg}. This interplay of Mg to Sb content suggests that there is probably a $V_{Mg} - Sb_{Si/Sn}$ association.

Overall, the chemical potential of elemental species and the chemical environment around the material governs the density of charged intrinsic and extrinsic defects as shown by computational and experimental studies. The experimentally observed variations in the thermoelectric properties due to the change in defect density qualitatively agree with the computational studies however, there are certain discrepancies that cause deviations in these investigations on comparison. These discrepancies can arise from underlying conditions or parameters; the synthesis parameters in experiments or the chemical potential inputs in the computational investigations. Therefore, the observations from both types of studies are equally important to assess the impact of native defects on the TE properties. The existing understanding of the behavior of intrinsic defects in binary Mg_2X materials is currently extrapolated to Mg_2Si-Mg_2Sn solid solutions to better understand the sensitivity and the effect of native defects on the TE properties because very limited information is available in this regard [147]. All the studies conducted within this thesis utilize Sb as a dopant on $Sb_{Si/Sn}$. All the samples were synthesized with excess Mg, which would emulate Mg-rich chemical potential. Besides this, for one study, investigated in Chapter 7, Sc was substituted on the Mg site to investigate its influence on the transport properties.

2.3.1.5 Pseudo-binary phase diagram of Mg_2Si–Mg_2Sn

The understanding of the equilibrium phase diagrams of thermoelectric materials is necessary to get a good idea of their synthesis conditions and thermochemical stability. The chemical stability of materials is quite relevant aspect because these materials are utilized for long-term high temperature applications. The understanding is helpful to further comprehend the high temperature driven evolution of the secondary phases or chemical reactions, if any, between the main phase and a secondary phase (e.g. in composites), which is occasionally added on purpose to enhance the thermoelectric performance of these materials.

Besides, assessing or constructing phase diagrams is also a starting point to identify suitable contacting solutions [148]. Nevertheless, for thermoelectric applications, it is generally

expected that these materials should be homogeneous, mechanically stable, and no structural and chemical changes shall occur at application temperatures.

There have been lots of experimental studies focused on investigating the equilibrium phase diagram of the Mg_2Si-Mg_2Sn material system that report the presence of a miscibility gap with the phase boundaries of Sn-rich and Si-rich phases. The phase boundaries of these phases are however reported differently in each study [53, 55, 149-153]. These studies also show a discrepancy in the upper temperature limit ($750\ °C - 850\ °C$) of the miscibility gap. The literature reports indicate that at $700\ °C$, the solubility limit of Sn in Mg_2Si is in the range $0.1 < x < 0.45$, where x is the Sn content while the solubility limit of Si in Mg_2Sn varies from $(1 - x) = 0.6 - 0.9$. These reports therefore suggest that both the phase boundaries and the upper temperature limit of the phase stability are disputed.

In this direction, recent work by Yi *et al.* [53] demonstrates that a single phase $Mg_2Si_{0.7}Sn_{0.3}$ is achievable at $720\ °C$ through a homogenization of binary Mg_2Si and Mg_2Sn powders by a high energy ball milling and spark plasma sintering. More specifically, the authors ball-milled the respective binaries to form the desired solid solution composition, which according to the previous reports, lies in the miscibility gap. In order to check the immiscibility of the synthesized phase, they annealed the sample for prolonged duration (3 h and 7 h at $720\ °C$) and found no phase separation, which is *not* expected from a phase diagram with a miscibility gap. This means that the composition was stable at $720\ °C$, which is in clear disagreement with the previously reported experimental [149] and theoretical [154-156] equilibrium phase diagram. Besides this, Yasseri *et al.* [152] have recently proved a complex temperature dependence of the miscibility gap. In this investigation, they concluded that $Mg_2Si_{1-x}Sn_x$ with $x = 0.5 - 0.7$ (which correspond to the compositions showing best thermoelectric performance), are stable at $T < 700\ °C$. They furthermore showed that the presence of Mg-Sn melt (at $600\ °C$) modifies the diffusion compared to a typical solid-state diffusion. Yasseri *et al.* [152] also showed that high temperature annealing leads to a decomposition of Mg_2Si-Mg_2Sn solid solution that eventually progresses in the release of elemental Si and Sn, both, due to strong Mg loss. In a separate study by Yasseri *et al.* [55] published recently, they conducted annealing experiments (at $T \leq 600\ °C$) on $Mg_2Si_{0.5}Sn_{0.5}$, also in the miscibility gap, and showed an influence of Mg partial pressure on the stability of Mg_2Si-Mg_2Sn compositions within the gap. Independent of the annealing temperatures, the investigations conducted by both Yi *et al.* and Yasseri *et al.* show a discrepancy in their results from previously published reports. Each of these investigations highlighted a potential effect of strain induced due to coherent interfaces between grains of the demixing phases, which is usually not considered when establishing an

equilibrium phase diagram. The origin of coherence strain is the lattice mismatch between the constituent binaries (Mg_2Si and Mg_2Sn) and hence Si-rich and Sn-rich solid solutions. This strain energy has a large contribution to the free energy of mixing and stabilizes a disordered system against demixing.

The discussed studies are highly relevant from the synthesis point-of-view and to understand the degradation mechanism which occurs as a result of long-term high temperature annealing. An effect of high temperature treatment on the structural, chemical and temperature dependent TE properties of samples (powder and sintered pellet, respectively) are sought. Moreover, readily available semiconductor physics-based models (SPB, 2PB etc.) that are employed to analyze transport properties also necessitate single phase character of the material. Therefore, a knowledge and understanding of the phase diagram is important.

2.3.2 An overview of TE properties of Mg_2X (*X*: Si, Sn) solid solutions

In the previous section, the different characteristics associated with the Mg_2X material system and their correlation to their thermoelectric properties have been discussed. Each of them can be (has been) used as a lever to achieve an improved thermoelectric performance of these materials. This sub-section deals with an overview of thermoelectric properties of n-type $Mg_2Si_{1-x}Sn_x$ that are reported, with an emphasis on the compositions with $x = 0.6 - 0.7$. The transport modelling results from the study of Bahk *et al.* [23] highlight that $Mg_2Si_{1-x}Sn_x$ with $x = 0.6 - 0.7$ show the best $zT_{\max}$ at ~700 K (Figure 2.9(a)). The properties were modelled using a multi-band (2CB + 1VB) model. A high TE performance results from an enhancement of the Seebeck coefficient. The convergence of the conduction bands leads to an enhanced valley degeneracy N_V (near the conduction band edge, as shown in Figure 2.9(b)), thus, results in an increase in m_D^* which therefore, leads to an enhancement of the Seebeck coefficient. Furthermore, alloying causes the mass fluctuation which leads to a decrease in κ_{lat} of these materials compared to binaries and other solid solutions of this class.

A deviation between the experimental to the modeled zT is observed for $x = 0.6, 0.7$ due to a variation in the carrier concentration n (Figure 2.9(a)). Note that n shown here is measured at 700 K assuming a SPB model with the Hall factor $r_H = 1$, which is practically ~1.1. The zT values reported by Liu *et al.* [83] fit well with the model while those reported by Søndergaard *et al.* [157] deviate from the model. One crucial difference between the cited literature is their employed synthesis route. For a ubiquitous agreement between experimental and modeled properties, a synthesis route with excellent process control and reproducibility of thermoelectric properties is necessary. This is because the synthesis routine would affect the properties of

Mg_2X solid solutions as thoroughly discussed in section 2.3. Employing a robust synthesis routine will also enable extracting reliable microscopic material parameters through band modelling.

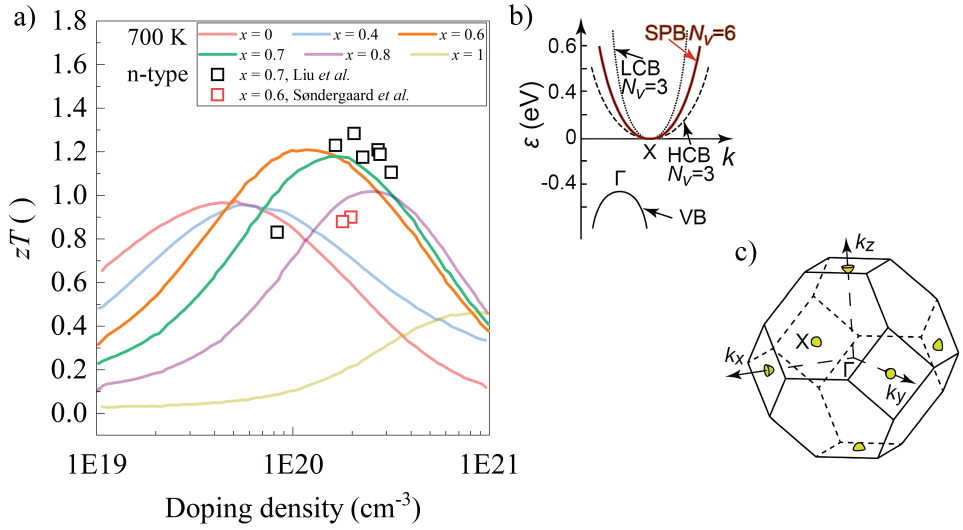

Figure 2.9 a) zT of $Mg_2Si_{1-x}Sn_x$ (with $x = 0 - 1$) as a function of doping density at 700 K. The plot has been reproduced from the results reported by Bahk *et al.* [23]. The measured n_H and the experimental zT reported by Liu *et al.* [83] ($x = 0.7$) (Bi-doped) and Søndergaard *et al.* [157] ($x = 0.6$) (Sb-doped) is shown. E vs k schematic for these compositions is shown in (b) that represents the convergence of the conduction bands responsible for an enhancement of the Seebeck coefficient, and thus, zT shown in (a). A schematic of the corresponding Brillouin zone is also shown in (c) [83]. The presented figure has been reprinted with permission from [23, 83, 157] respectively.

Besides this, the long-term stability of Mg_2X-based solid solutions at elevated temperatures is crucial for TEGs made from them to operate for longer duration. Previous studies have shown that these materials have a poor stability at high temperatures, which has been a significant challenge to overcome. The high temperature instability stems from: a high vapor pressure of Mg that leads to Mg loss [149, 158], a formation of stable secondary phases (such as MgO, Si-/Sn-rich $Mg_2Si_{1-x}Sn_x$, elemental Si and Sn) [107, 159], dopant segregation [160, 161], unstable desired phase or thermodynamically driven separation of solid solution to constituent Si-rich and Sn-rich phases [151, 152, 162] etc. In this direction, Bourgeois *et al.* [163] studied the thermal stability of $Mg_2Si_{0.75}Sn_{0.25}$ (both powder and compact) by temperature dependent *in situ* X-ray powder diffraction in Ar atmosphere where they found that the sample decomposes into another $Mg_2Si_{1-x}Sn_x$ composition, Si and MgO at 630 K. Additionally, no significant change was observed on the transport properties of $Mg_2Si_{0.75}Sn_{0.25}$ even after annealing the pellets at 875 K for a month in fused silica tubes. Andersen *et al.* [42, 164] conducted temperature

dependent *in-situ* synchrotron structural characterization on cation (Ca/Zn) and anion (Sb/Bi) doped $Mg_2Si_{0.4}Sn_{0.6}$ powder. Thermal cycling during *in-situ* synchrotron measurement on these samples caused only minor changes in the peaks corresponding to secondary phases. Yin *et al.* [42] examined the thermal stability of Sb-doped $Mg_2Si_{0.3}Sn_{0.7}$ in vacuum and air. On heating at 773 K, the material oxidizes in air whereas it experiences loss of Mg and Sn from the matrix in vacuum. They also investigated the role of coating in the prevention of material degradation and sample properties. The samples were coated with boron nitride (BN) and annealed in vacuum and air at 773 K and 823 K, respectively. Yin *et al.* found no change in the (micro-)structure and high-temperature transport properties of the coated samples when they are subject to annealing in air and vacuum at 773 K. The coated samples annealed in air at 823 K, nevertheless, showed a poor chemical homogeneity (with areas rich in Mg_2Si, and elemental Mg and Sn) and a deterioration of thermoelectric properties. Zhang *et al.* [165] also studied the effect of annealing on Sb-doped $Mg_2Si_{0.4}Sn_{0.6}$ both with and without coating. They showed that the material oxidizes when annealed at elevated temperatures in air. Moreover, the material subject to annealing in a highly pure inert atmosphere does not prevent its oxidation. Al_2O_3 coating on the sample provides resistance against degradation compared to an uncoated sample. All the cited studies show that at the elevated temperatures of annealing (or TEG operation), the Mg_2X based solid solutions are not stable and readily degrade in to Si-rich and Sn-rich $Mg_2(Si,Sn)$ or lose Mg, and form MgO. However, these investigations also show that the material degradation can be suppressed by using a suitable coating material (BN, Al_2O_3) that prevents Mg loss or oxidation. The effect of annealing on the n, m_D^* and μ of the materials (at room temperature) in different studies from Yin [42], Zhang [165] and Kato [146] can be observed from Figure 2.10. The apparent deviation also affects corresponding thermoelectric properties which are not shown here. The investigations of Yin *et al.* summarize that lowering of carrier concentration n is due to the Mg loss, which promotes formation of V_{Mg} while a lowering of the mobility μ is attributed to the formation of Mg_2Si nanostructures and other structural changes. Zhang and co-workers have also attributed a loss of n to the formation of charged Mg vacancies V_{Mg}. Particularly, Mg vacancies form localized hole states in the band structure, which trap the electrons. The authors suggest that these vacancies do not provide extra holes to the system and also do not move the Fermi level towards the valence band as inferred by the rigid band modelling approach. Annealing investigations conducted by Kato *et al.* on Sb-doped $Mg_2Si_{0.5}Sn_{0.5}$ in different Mg partial pressure environment show a variation in n and μ, which is also attributed to the variation in the V_{Mg} concentration.

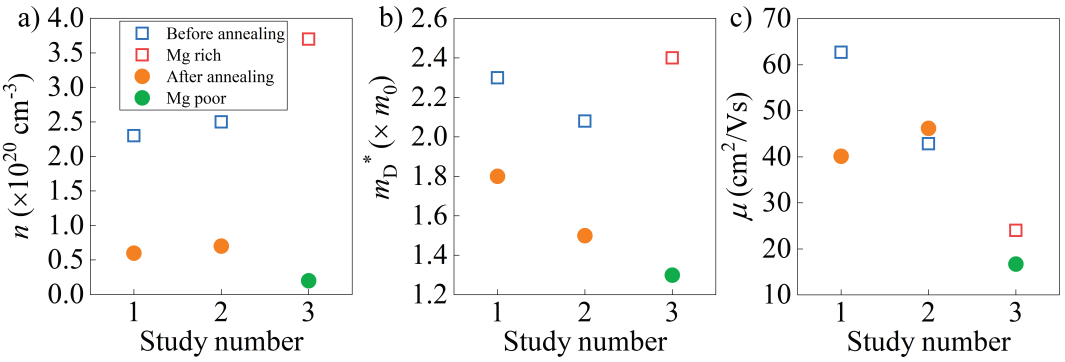

Figure 2.10 Plots showing variation in a) n, b) m_D^* and c) μ before and after annealing $Mg_2Si_{0.3}Sn_{0.7}$ [42] (study number 1), $Mg_2Si_{0.4}Sn_{0.6}$ [165] (study number 2) and $Mg_2Si_{0.5}Sn_{0.5}$ [146] (study number 3), all doped with ~0.067 at.% Sb. Note that for Kato's study the annealing was conducted in different Mg partial pressure environment (Mg-rich (10 Pa) and Mg-poor (0.1 Pa)). Some microscopic material parameters such as m_D^* for Kato's data and m_D^* and μ corresponding to Zhang's study shown here were *not* published but numerically obtained by analyzing RT thermoelectric properties from corresponding reports using a SPB model developed for the work presented in this thesis.

The transport properties measured after annealing in these reports plausibly have contributions from the effects (Mg loss, secondary phases, Si-/Sn-rich areas, MgO etc.) mentioned earlier. Based on the structural and chemical characterizations, these investigations speculate about the degradation mechanism at the annealing temperature T_{anneal} only qualitatively. More specifically, both the different stages of degradation (inhomogeneity in matrix, Mg loss, formation of secondary phases etc.) and their chronology are unclear, which would have otherwise enabled to systematically devise a mechanism. Moreover, these stages are not spatially and temporally differentiated and most probably have their combined influence on the transport properties, which is often difficult to disentangle. As a result, the thermoelectric properties measured after annealing might not be representative of a single phase. Therefore, an in-depth understanding of the different stages of the degradation of material due to a heat treatment and their correlation to the transport properties necessitates a strategy to measure these properties at operation temperatures for prolonged durations.

2.3.2.1 Thermoelectric transport properties of n-type Mg_2X based solid solutions

2.3.2.1.1 Electrical properties

The temperature dependent Seebeck coefficient S and electrical conductivity σ of Sb/Bi-doped $Mg_2Si_{0.4}Sn_{0.6}$ and $Mg_2Si_{0.3}Sn_{0.7}$ are shown in Figure 2.11 which are arguably the compositions with the best thermoelectric properties.

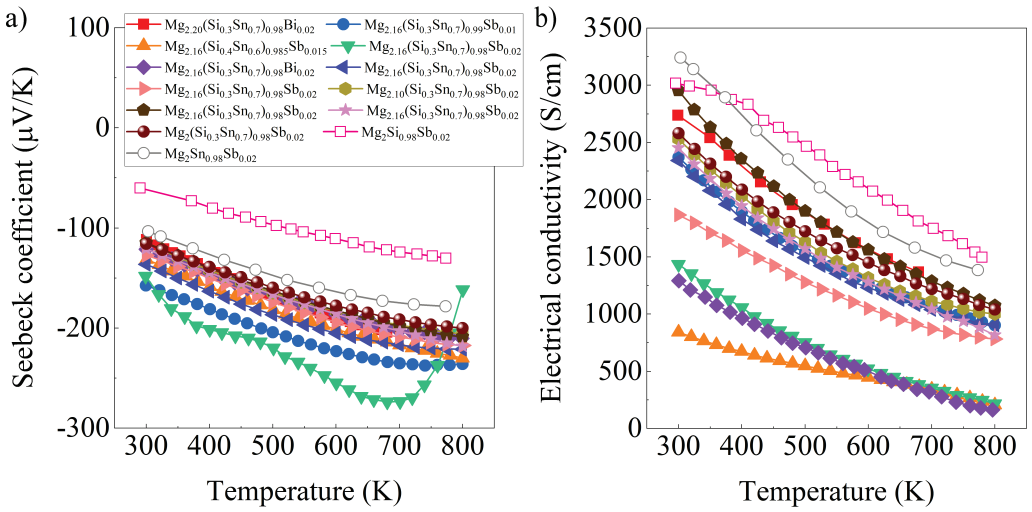

Figure 2.11 T-dependent S and σ of $Mg_2Si_{1-x}Sn_x$ with $x = 0, 0.6, 0.7$ and 1. The data is taken from the reports published by Bux *et al.* [115], Goyal *et al.* [166], Yin *et al.* [42, 44], Liu *et al.* [45, 83, 99], Zhang *et al.* [41, 43, 46] and Zhu *et al.* [167]. Each of these studies used $3 - 7$ at.% excess Mg to compensate for the Mg loss. Note that the transport properties of Sb doped compositions of both binaries are shown for comparison.

The Seebeck coefficient increases while the electrical conductivity decreases with increasing temperature, respectively, which reflects a characteristic temperature dependence of a heavily doped semiconductor. The negative Seebeck coefficient shows that the electrons are the majority carriers contributing to the transport. The plot also shows that samples with identical composition show a nearly identical temperature dependence of the electrical transport properties but with an obvious variation in their absolute values. The thermoelectric properties that are reported in different studies are not in good agreement, especially for the similar starting composition of the Mg_2X solid solution. The probable reasons can be the employed synthesis procedure, synthesis parameters (sintering time (t_{sinter}) and temperature T_{sinter}), starting Mg concentration or a difference in the type and concentration of the substituted impurity (Sb/Bi) or due to inhomogeneities in the material. The carrier concentration n at RT for some of the compositions ($\sim$0.067 at.% Sb doped (i.e. $Mg_{2-\delta}(Si_{0.3}Sn_{0.7})_{0.98}Sb_{0.02}$) in Figure 2.11) are shown in Figure 1.6(b), which shows drastic variations from one another and implies that the material synthesis is unoptimized. The synthesis of the binary and the solid solutions of Mg_2X and its optimization have been systematically studied previously. However, the optimization has only been focused on varying either the dopant concentration [44, 83, 99, 115, 166, 167], or the consolidation parameters [168, 169], in some other few cases. A systematic study to investigate an influence of different synthesis parameters, if any, on the thermoelectric properties of $Mg_2Si_{1-x}Sn_x$ (with $x = 0.6, 0.7$) is unavailable. Therefore, investigations focusing on understanding the effect of various synthesis parameters on the thermoelectric properties are

necessary. Analyzing thermoelectric properties will furthermore make it possible to establish a quantitative correlation between synthesis parameters and the properties. This would lead to an optimized set of synthesis parameters.

2.3.2.1.2 Thermal properties

The synthesis of $Mg_2Si_{1-x}Sn_x$ (with $x = 0.6, 0.7$) not only leads to an enhancement in the Seebeck coefficient values but also a lower κ_{lat} compared to their respective binaries due to a contrast of elemental mass between Si and Sn. This leads to a high figure-of-merit $zT = 1.3 - 1.4$ for these materials. The room temperature (300 K) κ_{lat} as a function of Sn content in $Mg_2Si_{1-x}Sn_x$ is shown in Figure 2.12. κ_{lat} of p-type and n-type $Mg_2Si_{1-x}Sn_x$ samples (with $x = 0.6 - 0.7$) is also shown for comparison.

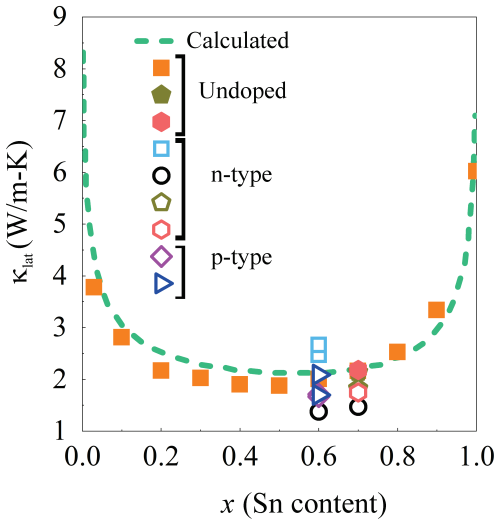

Figure 2.12 Calculated [171] (dashed green) and experimental κ_{lat} (symbols) of undoped [83, 166, 172] (with $x = 0 - 1$), n-type [83, 99, 166, 170] and p-type [114, 120] $Mg_2Si_{1-x}Sn_x$ at 300 K.

The data shows that the κ_{lat} of heavily doped samples is comparatively low than the undoped samples (except for the samples synthesized by Dasgupta *et al.* [170]). The experimental data generally agree well with the simulated values that were calculated assuming different phonon scattering mechanisms (namely Umklapp scattering, scattering due to alloy disorder, nanoparticles and GB contributions). The simulated data was obtained by plugging suitable values of the microscopic material parameters in the model which showed lowest lattice thermal conductivity for $Mg_2Si_{0.4}Sn_{0.6}$. The plot also shows that statistically the experimental κ_{lat} of $x = 0.6$ is lowest amongst all. Besides, the plot shows that the experimental data does not

perfectly agree with each other as well as with the simulated one. The possible reasons of imperfect agreement can be different employed synthesis route that causes grain size variation, different starting Mg concentration, higher density of microstructural defects (such as intrinsic and extrinsic point defects, grain boundaries, dislocations etc.), and measurement uncertainties. An optimization of the synthesis route could enable to achieve more reliable values of microscopic material parameters to simulate κ_{lat} and reduce relative deviation between experimental and calculated values.

Note that heavily doped $Mg_2Si_{0.4}Sn_{0.6}$ was chosen for the experimental investigations presented in this thesis, since this composition has shown the best thermoelectric performance. The thermoelectric PF of $Mg_2Si_{0.3}Sn_{0.7}$ is in tendency higher than of $Mg_2Si_{0.4}Sn_{0.6}$ but the modelling results show that the κ_{lat} is comparatively lower for the latter composition. As a result, the overall TE performance of both these compositions is quite identical.

Chapter 3 Summary of Research

3.1 Summary

In this chapter, the most relevant scientific questions related to the optimization of thermoelectric properties of n-type $Mg_2(Si,Sn)$ are described. In this context, the importance of highly reproducible synthesis route is emphasized and a possible effect of variation in intrinsic defect density on the thermoelectric properties is also highlighted. Furthermore, the topic of thermal stability of these materials is discussed briefly and the challenges in capturing the degradation mechanism are underscored. An overview of the problems related to the thermoelectric optimization and the issues in understanding the degradation mechanism of n-type $Mg_2(Si,Sn)$ provide a foundation to investigate composition-synthesis-microstructure-property relationships in these materials. Later, the tools, techniques and the approaches employed to address these questions are detailed in the overview section.

3.2 Scientific questions

The n-type $Mg_2Si_{1-x}Sn_x$ (with $x = 0.6 - 0.7$) shows $zT_{\max} \approx 1.3 - 1.4$ owing to a high Seebeck coefficient due to the convergence of the conduction bands and a low lattice thermal conductivity κ_{lat} due to a mass difference in their elemental constituents (Si and Sn). As previously stated, the control of the density of defects (both intrinsic and extrinsic) is crucial to achieve an optimized thermoelectric performance. A variation in the density of one or both types of defects can lead to an observable change in the electrical and thermal transport properties. The optimization studies on Mg_2X solid solutions are largely focused at determining the (extrinsic) dopant concentration to achieve the best thermoelectric properties. On comparing the thermoelectric properties of n-type $Mg_2(Si,Sn)$ (measured in different experimental studies), it is found that there is a large relative deviation (even beyond measurement uncertainty) for an identical extrinsic defect concentration. One possible reason for this deviation could be the chosen synthesis route, which leads to an inhomogeneous microstructure and prevents complete dopant incorporation in the material. In a few studies with detailed microstructural analysis, the extrinsic dopant atoms were found to be segregated at the grain boundaries. It could be possible that the dopant was added beyond the solubility limit which did not dissolve in the lattice of the grains in Mg_2Si and $Mg_2(Si,Sn)$ materials. Taking these observations into context, the observed thermoelectric properties are lower compared to the properties predicted using established semiconductor band structure models.

Beyond the stated observations, the question of particular interest is whether this lowering can be due to a sensitivity of the transport properties to the variation in the intrinsic defect density as well. In this regard, only a few studies have been focused on investigating the plausible influence of native charged point defects on the thermoelectric properties of n-type Mg_2X solid solutions. The current understanding of the influence of varying intrinsic defect density on the thermoelectric properties of Mg_2X solid solutions originates from the investigations conducted on binary Mg_2Si and Mg_2Sn materials but systematic investigations on solid solutions are scarce.

Mg_2X materials are promising candidates for TEG applications but their thermal stability has been a pressing issue which prevents them to be used for commercial purposes or real-world applications. In this regard, several annealing studies have been carried out on high performance n-type Mg_2X solid solutions at (and beyond) application temperatures to observe any changes in their thermoelectric properties. These investigations are largely focused on understanding the degradation mechanism of these materials and providing probable solutions to prevent their degradation e.g. by coating. Previous studies conclude that the degradation of thermoelectric properties of n-type Mg_2X materials and their solid solutions is driven by the formation of charged Mg vacancies. Mg vacancies form as a result of Mg loss due to its high vapor pressure at high temperatures. The formation of Mg vacancies leads to a variation in the majority charge carrier density as they are doubly charged acceptor defects. The results also show a variation in the carrier mobility μ and the density-of-states effective mass m_{D}^{*} due to high-temperature annealing but the underlying reason of this variation is not clear. The microstructure reported in some of the literature investigations suggests that the heat treatment leads to the degradation of the material due to Mg loss beyond the solubility limit of Mg vacancies. This results in the formation of secondary phases. Therefore, Mg loss beyond the solubility limit of Mg vacancies is responsible for compositional inhomogeneities in these materials. The thermoelectric properties measured after high temperature annealing are thus not representative of one single phase rather a composite that consists several phases (effective thermoelectric properties). Due to this reason, it is challenging to clearly and systematically understand the microscopic degradation mechanism of Mg_2X solid-solutions. Particularly, the observables are spatially and temporally convoluted, as several steps might have already occurred at the time of observation. The different steps of the mechanism of degradation are unknown and unclear, and a quantitative correlation of each of these steps with the thermoelectric properties of the materials is furthermore missing. Moreover, the role of intrinsic defects inducing the degradation of material properties, if any, is also discussed vaguely and controversially.

The cited issues can be addressed using a suitable and optimized synthesis method. Generally, the employed techniques for the synthesis of Mg_2X materials take days to weeks to achieve phase-pure compositions. These synthesis methods often lead to microstructure-wise inhomogeneous material and also incorporate the substituted impurities only to a limited extent. Correspondingly, a highly reproducible, convenient and fast synthesis method that allows a complete incorporation of dopants is essential.

Besides this, a systematic understanding of the role of intrinsic defects is missing i.e. the influence of variation in the intrinsic defect density on the thermoelectric properties is unclear. The manipulation of the intrinsic defect density can be experimentally controlled by using excess Mg for incorporating Mg-interstitials (I_{Mg}), while the formation of Mg-vacancies (V_{Mg}) is possible by inducing Mg-loss on purpose e.g. by tuning the sintering parameters (t_{sinter}, T_{sinter}) of the material. The intrinsic defect density can be manipulated by a long-term high temperature annealing of the material as well. Since the variation in charged intrinsic defects has a direct influence on the density of the majority charge carriers, a technique to determine the carrier density of the material is needed. Therefore, a pre-existing facility that is used to simultaneously measure the Hall coefficient R_{H} and the electrical conductivity σ at room temperature, has been extended for measuring these transport properties in the intermediate temperature range ($300\ \mathrm{K} - 723\ \mathrm{K}$).

Using the available facilities, the Seebeck coefficient, electrical conductivity and the Hall coefficient of n-type Mg_2X solid solutions can be measured at high temperatures ($T > 700\ \mathrm{K}$), thus, simulating typical TEG operation conditions. Particularly, the material would be held at a specific high temperature point in these setups and the thermoelectric properties would be measured (an *in-situ* measurement). The *in-situ* characterization of these properties can provide a direct insight on the degradation mechanism of n-type Mg_2X solid solutions. The *in-situ* measured thermoelectric properties can be then analyzed using semi-classical transport models (single- and multi-band models) based on the solutions of the Boltzmann transport equation. The modelling results can yield affected microscopic material parameters and the extent of their degradation. These results can be correlated to the changes in the microstructure of the material (e.g. intrinsic defect density), which could also allow an understanding of different stages of the degradation process and a chronology of each step of degradation process.

3.3 Overview of the thesis

In this PhD thesis, first, a general introduction to thermoelectrics and the required methodological background were provided in Chapter 1 and Chapter 2 respectively. A detailed description of the employed experimental synthesis and characterization methods is provided in Chapter 4.

Then, the Hall measurement setup is described in detail in Chapter 5, which is extended to measure the high-temperature transport properties (R_{H} and σ). In particular, a brief background on the measurement principle, different components of the Hall facility, error indicators that give an idea of the quality of measurement, and reference measurements are presented. Finally, the geometric correction factor (GCF) corresponding to the Hall coefficient R_{H} measurement was validated using finite element simulations. Using the simulation corrected GCF, the Hall coefficient measured at the presented Hall facility was corrected. The simulation corrected GCF led to a close agreement between the Hall coefficient measured at the presented facility and at different facilities of the laboratories across the globe.

In the next chapters, first in Chapter 6, the synthesis and optimization of the thermoelectric properties of high performance n-type $Mg_2(Si,Sn)$ solid solutions is discussed. This material is synthesized using a two-step synthesis method, mechanical alloying and direct current sintering press (DSP), both of which are discussed in detail. In particular, an understanding of the formation mechanism of Mg_2X (X: Si, Sn) solid solutions using mechanical alloying is presented. Later, the optimization methodology of the synthesis route is also discussed in detail. In this methodology, the synthesis parameters (such as milling time, sintering time t_{sinter}, and sintering temperature T_{sinter}) are tuned to achieve high performance thermoelectric materials and the effects of variation of each synthesis parameter on the thermoelectric properties is observed. The results show that the milling of precursors lead to the formation of Mg_2Sn phase after first few hours of milling followed by slow Si (brittle) diffusion in the Mg – Sn (ductile) rich matrix. The powder homogenizes with increasing milling time; however, it is not phase-pure after milling. This suggests that the powder needs to be treated at high temperatures. This is fulfilled by a high temperature sintering step that combines heat treatment and compaction (by the application of external mechanical pressure) to obtain a densified pellet. Analyses of these pellets show that the homogeneity and thermoelectric properties of n-type Mg_2X solid solutions are sensitive to the sintering parameters but not the milling duration. Particularly, the thermoelectric properties deteriorate with increasing t_{sinter} or T_{sinter}. However, it was not clear

if this change is due to the variation in the intrinsic defect concentration or the extrinsic defect concentration.

In Chapter 7, a substitution of Mg by a transition metal (Sc) in Mg_2X materials and their solid solutions has been attempted to further improve the thermoelectric performance of these materials. This study experimentally investigates the theoretically reported band structure modification of Mg_2X materials by Sc doping.

In Chapter 8, the mechanically alloyed powder was sintered for different durations t_{sinter} (at constant sintering temperature $T_{\mathrm{sinter}} = 973$ K) followed by the measurement of thermoelectric properties and a detailed microstructural investigation using transmission electron microscope. The temperature dependent thermoelectric properties of these samples were analyzed using a single parabolic band (SPB) model to physically interpret the reason for the observed changes, notably, in the electrical conductivity values due to a variation of sintering time t_{sinter}. The results obtained from the modelling of thermoelectric transport properties were correlated with microstructural investigations.

The effect of short-duration high temperature heat treatment on the thermoelectric properties was understood in Chapter 8. With this knowledge, n-type Mg_2X solid solutions were heat-treated for longer duration at the typical TEG operation temperatures, which is discussed in Chapter 9. The Seebeck coefficient S, the electrical conductivity σ and the Hall coefficient R_{H} were measured at a constant annealing temperature ($T_{\mathrm{anneal}} = 710$ K) (*in-situ* measurements) for a direct observation of their change and to gain an insight on the degradation mechanism of these materials. The measured thermoelectric transport properties were analyzed using SPB and two parabolic band (2PB (1CB+1VB)) models. The modelling-based analysis was carried out to understand the reason for the change in these thermoelectric properties. The analysis revealed a change in majority charge carrier density (N_{D}) which can be attributed to the loss of Mg from the sample. This analysis also leads to the determination of the extent of degradation of the microscopic material parameters, which result in the change of corresponding properties.

In Chapter 10, the *in-situ* measurement of the thermoelectric properties (S, σ and R_{H}) are conducted at even higher annealing temperatures ($T_{\mathrm{anneal}} = 773$ K and 848 K). The *in-situ* measured properties were analyzed using the established SPB and 2PB models. The change in majority charge carrier density N_{D} data was captured using exponential decay function and the rate of Mg loss was deduced corresponding to each annealing temperature. Besides this, a microscopic, multi-step model of the Mg-loss in $Mg_2(Si,Sn)$ is developed to rationalize the mechanism of degradation. The Mg loss in these materials is driven by the establishment of a

difference in Mg-chemical potential between the sample and the annealing environment. Mg-vacancies were found to be the most relevant defects for the transport of Mg atoms due to their low formation energy and low migration energy. The effective activation energy for the loss of Mg was estimated from the Arrhenius expression using the Mg loss rates (estimated from $N_{\mathrm{D}}(t)$, and $\sigma(t)$ data) corresponding to different conditions at stated annealing temperature points. A deviation was found between the kinetic parameters corresponding to the samples annealed in different setups, which were correlated with the differences in the specific annealing conditions. The effective activation energy was compared with the height of different energy barriers corresponding to each step to identify the limiting step(s) of the multi-step transport chain.

Chapter 4 Experimental methods

4.1 Summary

In this chapter, the tools and techniques utilized for the synthesis and characterization of thermoelectric materials are discussed. n-type Mg_2X material and their solid solutions were synthesized using mechanical alloying, and a high temperature sintering step. Each of these techniques are discussed in detail. Furthermore, the principles related to the structural (XRD) and chemical (SEM, TEM) characterizations and the measurement of thermoelectric properties (the Seebeck coefficient, electrical conductivity and the Hall coefficient) are discussed.

4.2 Synthesis

4.2.1 Mechanical alloying (MA)

Mechanical alloying (MA) is a solid-state technique for the synthesis of scientifically and industrially interesting materials. In this method, blended elemental or pre-alloyed material is loaded in a vial or jar along with the milling media. The milling media are the balls of same or different diameters that are usually made of the same material as the vial, e.g. stainless steel, tungsten carbide (WC), agate etc. During the milling procedure, the milling balls collide and transfer their kinetic energy to the powder material through continuous mechanical impacts that leads to a heavy deformation of powder particles. The mechanism of the synthesis of $Mg_2Si_{1-x}Sn_x$ using mechanical alloying is discussed in detail in Chapter 6. Mechanical alloying has several advantages over other synthesis procedures: it is a simple near-room temperature technique, and microstructurally, it shows better homogenization of the material compared to other synthesis techniques [113, 173-175]. The material prepared using this method shows negligible signatures of oxidation. This is because during the course of milling, the precursor elements and powder are handled under inert atmosphere. Moreover, a better dopant incorporation in the material using mechanical alloying compared to other synthesis methods has been previously reported [107, 115, 176, 177].

For the studies conducted in this work, a high energy ball mill (HEBM) (SPEX 8000D shaker mill) is employed for the mechanical alloying of precursors that promotes the synthesis of homogeneous, single phase samples in a short period of time. The precursors (Mg turnings (Merck), Si ($<$ 6 mm, ChemPure), Sn ($<$ 71 μm, Merck) and Sb granules (5 mm, Alfa Aesar) with purity $>$ 99.5 %) were weighed according to the target nominal composition. A 2 at.%

excess of Mg was added to compensate for potential Mg loss during high temperature sintering step. These precursor elements were transferred to a stainless-steel jar with a ball to powder weight ratio (BPR) of 1.6: 1. The milling process was stopped after certain time intervals to allow the cooling of the ball mill system and to ensure a proper mixing of particles. During milling, the finer particles usually cold weld together and form a lump on the jar walls. During the stated time intervals, the lump was scraped off from the jar walls using mechanical tools such as chisel, hammer, knives etc. under inert conditions. The powder was handled inside a glove box under Ar atmosphere to prevent the oxidation and contamination of powder sample. These precursor elements were milled at ~875 rpm until fine and homogeneous powders were obtained. The milling time in case of $Mg_2Si_{1-x}Sn_x$ solid solutions mainly depends on the Si:Sn ratio because Si is brittle while Mg and Sn are ductile [178, 179]. A detailed study in this regard has been reported by Kamila *et al.* [113].

4.2.2 High temperature sintering step

The final step of the synthesis is the sintering of milled powder material to produce dense pellets. A thermal treatment of powder or its compact at elevated temperatures below the melting point of the material is called sintering [180]. This heat treatment allows a change in pore shape, a shrinkage of pores and grain growth in powder samples. Sintering is largely driven by a reduction in total particle surface area. In the present case, the powder is sintered at higher temperature by combining it with an externally applied mechanical pressure and current. The sintering process can be shortly described in different stages as shown in Figure 4.1.

A stage in a sintering process can be described as an interval of geometric change in which the pore shape change is totally defined (e.g. rounding of necks in the initial stage of sintering). The stage can be alternatively defined as a time interval where a pore remains constant in shape while its size decreases (e.g. shrinkage of spherical pores during final sintering stage) [180]. The powder sample is transferred to the sintering mold, where the powder particles are in contact with each other. Thus, there is an increase in interparticle contact area even before the sintering process has started (Figure 4.1(a)). In the initial stage of sintering, neck growth occurs (Figure 4.1(b)). Neck growth means an increase in interparticle contact area, and the particles approach each other i.e. interparticle shrinkage occurs, and the relative density of a typical powder compact increases [181]. However, the different neighboring necks do not interact with each other at this stage. Besides, grain boundary forms within each neck due to mass transport by atomic diffusion at the particle surface and interfaces near the neck region. Note that at this stage the grain boundaries are confined to neck region and immobile. A significant increment in the area and energy of grain boundaries is necessary for their movement (called as grain

boundary migration) [182]. The formed neck regions become blunted as they grow and the inhibition of grain boundary migration decreases until the grain growth occurs [182]. The presence of individual pore or grain boundaries contribute to the surface energy of the material being sintering. Consequently, several pores attach to the grain boundaries at this stage owing to a comparatively low configurational energy [183] of pore-grain boundary combination compared to surface energy due to pore and the grain boundary energy. The initial stage of sintering is considered to terminate when an onset of grain growth is observed.

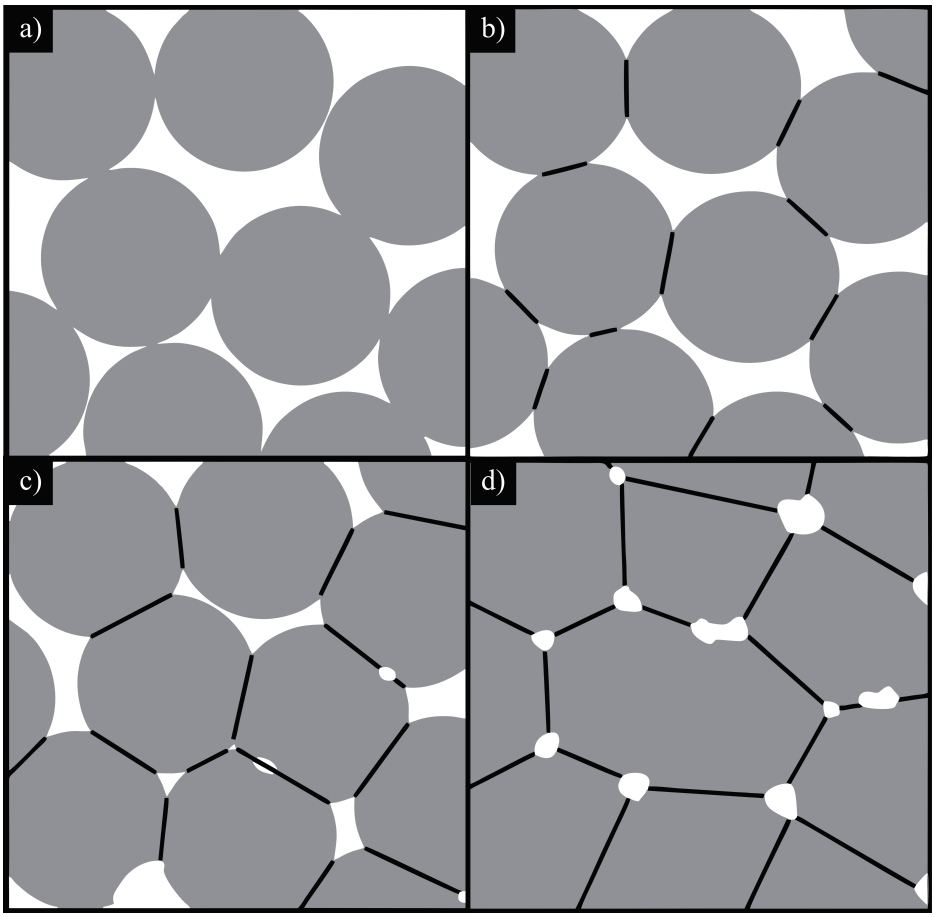

Figure 4.1 Schematic of changes occurring in a powder compact at microscale, which is subjected to high temperature sintering. (a) Loose powder particles after cold pressing. (b) Initial, (c) intermediate and (d) final stage of sintering. The figure has been reprinted (adapted) with the permission from [183, 184].

The remaining cavities between interconnected particles evolve to form pore as the sintering progresses (Figure 4.1(b)). The intermediate stage of the process has begun after the initiation of grain growth. Particularly, the particle-particle grain boundary area increases that enables grain growth, which results in large average grain size with fewer grains. The grain growth is also assisted by the grain boundary migration that occurs on the expense of grain boundary

energy. However, the grain boundary migration is impeded by the pores that are attached to these grain boundaries. Therefore, a dynamic relationship exists between the grain boundary migration and the inhibition caused due to the presence of pores at the grain boundaries. This stage is furthermore characterized by the formation (and presence) of interconnected cavities between the contact points of several particles (Figure 4.1(c) and Figure 4.2(a)). Particularly, the equilibrium dihedral angles are formed on pore surface at the intersection point with grain boundary surface [182]. As a result of this dihedral angle, a continuous channel of pores is formed along the edges of the grain boundaries (Figure 4.2(a)). The intermediate stage is also characterized by the shrinkage of these continuous channels with ongoing sintering. As a consequence, the grain growth progresses with an elimination of pore structures and the migration of grain boundaries along with the mobile pores.

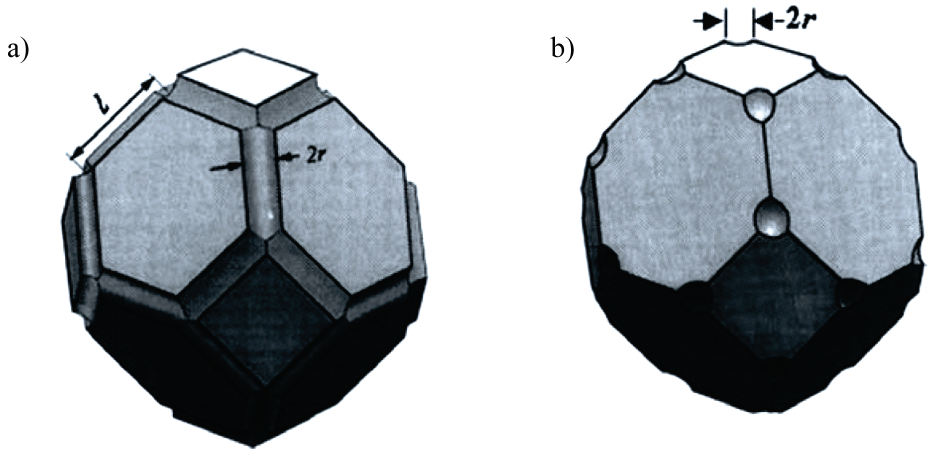

Figure 4.2 Geometrical models for (a) intermediate stage and (b) final stage sintering proposed by Coble *et al.* [182]. The plot has been reprinted (adapted) with the permission from [185].

In the final stage of sintering, generally, larger grains form at the expense of smaller grains, thus, leading to an overall grain growth, and the formed pores become smaller, more spherical and eventually pinch off as sintering progresses (Figure 4.1(d)). This stage is characterized by pore closure, pore isolation and migration (Figure 4.1(d) and Figure 4.2(b)) [186].

The driving force for sintering process is the elimination of interfacial area, i.e. first, the particle surface area followed by grain boundary area. Energetically, the surface energy is predominant in the initial stage and to some extent in the intermediate stage. With an increasing density of grain boundaries in the formed necks, the grain boundary energy acts as a driving force in the intermediate and final stage of sintering. This energy gets eliminated as a result of grain growth

in the final stage [187]. Due to sintering, the powder particles coalesce and a reduction of pore density occurs and consequently, the mechanical integrity of the samples increases.

Note that the final densification of the material is also influenced by the sintering atmosphere. In case the sintering atmosphere is a gas, then the gas gets trapped in the isolated pores which creates a counteracting gas pressure making densification close to theoretical values impossible. In case of fast diffusing gases, a full densification is possible, however, for slowly diffusing gas or inert gases, a full densification is only possible if a high external pressure is applied [185].

For this thesis, the sintering of powder samples was carried out in vacuum with continuous pumping. The basic process of DSP is similar to hot-pressing (applying external mechanical pressure and elevated temperature) with a combination of electric field $\vec{E}$ that leads to an enhanced interparticle bonding and densification. In the conventional hot pressing, the powder is indirectly heated by radiation followed by convection and conduction. Nevertheless, during the current-assisted sintering process, microscopically, the initial packing of the powder (Figure 4.1(a)) forms a network of percolating current paths. The Joule heating occurs along these paths and in certain areas, hot spots form in this network that have high local current density and eventually, the temperature of the powder rises locally. At these hotspots, the temperature rise can exceed the set process temperature such that an overheating of the powder occurs locally. This results in atomic diffusion, but melting and recrystallization can also occur, in the overall development of the microstructure. Compared to the other regions where the current density is low, the material densification sets in faster within these hotspots [188]. The sample heating rate is controlled by a feedback loop using a thermocouple. At times, several effects can occur during the sintering process. These effects can be either beneficial or detrimental to the sintering process and the sample. Some of the relevant effects include the Peltier heating and cooling, electromigration, electroplasticity and in some cases surface oxide removal [189]. Electromigration leads to a preferential diffusion of the lattice ions while electroplasticity is the plastic deformation of a material under the influence of an electric field. In electroplasticity, the electrons drifting under the influence of applied field either collide and scatter or transfer their momentum to the scattering centers. This results in an increase in the rate of atomic diffusion which help the movement of dislocations through the lattice structure [190]. As a further consequence, flow stress reduces, which is necessary for the plastic deformation (a non-reversible change in the shape). Generally, a better densification of materials results in an enhanced electrical, thermal and mechanical properties. For thermoelectric applications, particularly, a lowering of the total thermal conductivity is sought. Accordingly, different

strategies are employed to reduce the lattice component of the thermal conductivity (highlighted in 2.3.2.1.2).

The high-temperature sintering of powder samples was conducted using a DSP 510 SE, Dr. Fritsch GmbH. For the sintering, the mechanically alloyed powder material is transferred in the graphite mold/die (Ø ≈ 13.3 mm) and placed in a sintering chamber. The sintering chamber was evacuated ($\sim 10^{-5}$ bar) and a mechanical pressure of 67 MPa was externally applied on the sintering mold. The powder samples were heated at a rate of 1 K s^{-1} to reach the target sintering temperature. After the completion of high-temperature sintering procedure, the graphite mold with the powder compact is allowed to passively cool down to the room temperature, without externally applied mechanical pressure. This is done because a continuous application of external pressure during the cooling step has mostly led to broken compacted pellets. A variation in T_{sinter} and t_{sinter} affects the thermoelectric properties of $Mg_2Si_{1-x}Sn_x$. This is because some precursors either remain unalloyed during mechanical alloying or because they can easily sublimate because of their higher vapor pressure (e.g. Mg) at high temperatures compared to other precursors. This would affect the (local) stoichiometry which might lead to an inhomogeneous sample. The influence of a variation in the synthesis parameters on the TE properties has been investigated and discussed in Chapter 6 and Chapter 8.

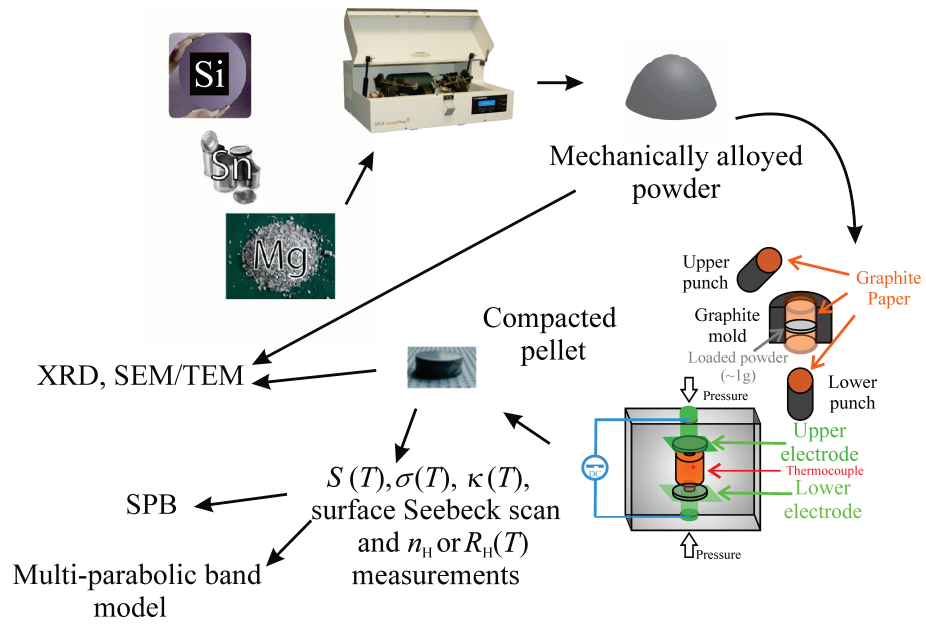

Figure 4.3 Work flow of the synthesis route, characterization and the analysis of the n-type Mg_2X (*X*: Si, Sn) and their solid solutions prepared using high-energy ball milling. There are two synthesis steps: mechanical alloying (by HEBM) and DSP. The sintered materials are characterized for structural, chemical and thermoelectric properties.

A complete workflow of the experiments, characterizations and analysis is visualized in Figure 4.3. The method of synthesizing n-type Mg_2X (X: Si, Sn) and their solid solutions were discussed in detail in the last section. In the next section, the characterization techniques are described in detail.

4.3 Characterization

The pellets obtained after the high temperature sintering step were wet ground with ethanol using SiC (carborundum) paper to prepare them for structural, chemical characterization and thermoelectric transport property measurements. The Archimedes' method was used to determine the mass density ρ of the compacted pellets.

4.3.1 Structural and chemical characterization

The milled powders and the compacted pellets were analyzed using X-ray diffraction (XRD) and scanning electron microscope (SEM). A transmission electron microscope (TEM) was utilized for a further detailed analysis of the compacted pellets (Chapter 8). These techniques were employed to investigate the structural purity, homogeneity and chemical purity of the samples, respectively. Each characterization technique is described briefly in the following section.

4.3.1.1 X-ray diffraction (XRD)

The phase purity of n-type Mg_2X solid solutions was investigated by using X-ray diffraction. It is a commonly used instrument for the identification of phase(s) in a material. The principle of X-ray diffraction is based on Bragg's law which is given by:

$$n\lambda = 2d'\sin\theta \qquad \text{Equation (4.1)}$$

Here, n, λ, d' and θ are the order of reflection, the wavelength of the incident X-ray, the interplanar spacing of the crystal, and the angle of incidence and reflection of the incident X-ray, respectively. The Bragg's law needs to be satisfied for observing diffraction which means that the orientation of crystallographic planes should not be arbitrary with respect to the incident X-ray beam.

During the measurement, the electrons of atoms in the sample, which are exposed to the incident X-rays, physically interact with the incoming X-rays. The electrons of the atoms in the material scatter this incident X-ray and produce a pattern in accordance with the Bragg's law stated above. This pattern is recorded and analyzed to determine crystal structure i.e. the phase of

material. Out of all the diffracted X-rays, only those ones that are in-phase (mutually reinforce one another) form a diffracted beam. The diffracted beam that makes an exit angle equal to the angle of incidence, θ, is shown in Figure 4.4(a). The essential components of an XRD system are: an X-ray source (a sealed X-ray tube), an X-ray detector, a goniometer, as shown in Figure 4.4(b), and electronics for counting detector pulses in synchronization with the position of the goniometer [191].

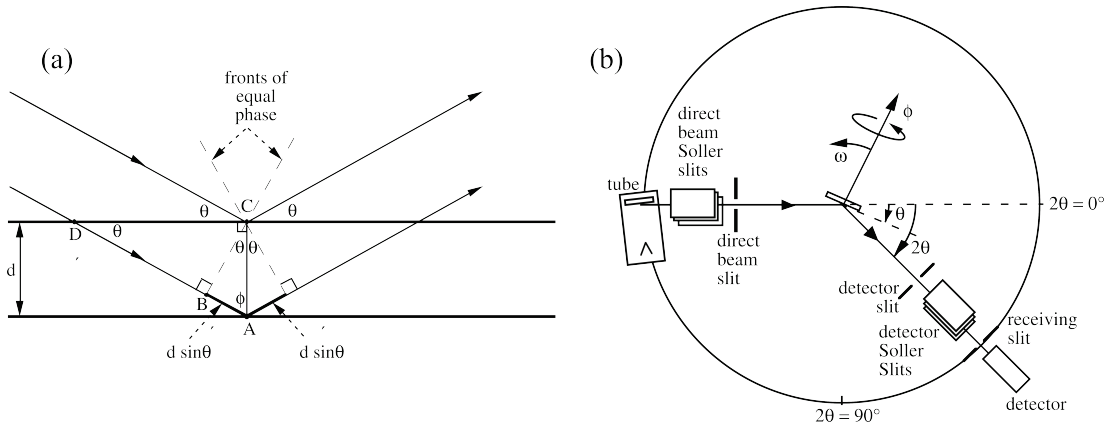

Figure 4.4 (a) A scheme highlighting two atomic planes separated by a spacing, d', with incident and diffracted waves (Bragg's law) and (b) a schematic of the D5000 diffractometer setup [192]. The figures have been reprinted (adapted) with the permission from [191].

The X-ray tube contains an electron source (cathode), and a metal target (anode). The tube is evacuated and the cathode is maintained at a voltage of $U = 30 - 50$ kV while the anode is at the ground potential to create a potential difference. A current of $I \approx 3$ A is passed through the cathode, a tungsten filament, which causes a thermionic emission of electrons. Due to a high electric potential difference maintained in this tube, the emitted electrons accelerate towards the anode, and generate X-rays on collision. The electrons collide with the anode and lose their kinetic energy, and a part of this lost energy is emitted as X-rays. Since most of the kinetic energy is lost in the form of heat ($\approx 98\,\% - 99\,\%$), the anode is always water cooled to prevent its melting. Based on the energy of accelerated electrons, they produce characteristic X-rays and a continuous X-ray spectrum at sufficiently higher voltage magnitudes. The characteristic X-rays are used for the purpose of characterizing a material. Here, the employed XRD system is based on the Debye-Scherrer method. This method utilizes monochromatic radiation on a polycrystalline sample, which comprises a distribution of the crystallographic planes, thus, fulfilling the Bragg's law. For the Debye-Scherrer method, a goniometer is required for the precise mechanical movements of both, the detector and the specimen, with

respect to the X-ray source. A Bragg-Brentano geometry-based goniometer is implemented in the XRD system used here as shown in Figure 4.4(b). In addition to the source tube and the detector, and the supportive electronics, there are other necessary components of the XRD system that improve the quality of measurement which include filters and collimators. A filter, e.g. Ni foil, for X-rays coming out from the metal target, or a monochromator, e.g. Ge or graphite, are used for the primary purpose of suppressing the undesired part of the spectrum and to decrease the background radiation (fluorescent radiation and incoherent scattered radiation originating from the specimen) that also comes along the characteristic X-rays from the specimen. X-rays pass through a collimator before being incident on the sample. A similar collimator is also present on the detector side to reduce the divergence of the diffracted beams. The diffracted X-rays (from the specimen) are absorbed by the detector which generates a current pulse. The diffractometer used here contains a scintillation detector. A scintillation detector is mainly an optically active material (mostly NaI) that makes a flash of light on interaction with X-rays. This light leads to the generation of an electron pulse by the photocathode (in a photomultiplier) of the detector. The electrical circuits (pulse height analyzer and scalars) count the electric pulses per second and this information is transferred to the acquisition software for further analysis [193]. This software provides relevant information about d', the diffraction angle 2θ etc. and display it as diffractograms i.e. counts per second (a measure of intensity) as a function of the diffraction angle 2θ. The diffractograms of powder sample or the cylindrical pellets were measured by utilizing two XRD systems namely Siemens D5000 Bragg–Brentano diffractometer and a Bruker D8 advance diffractometer with a secondary monochromator. The setups were operated at an acceleration voltage of $U \approx 40$ kV and Cu-Kα radiation (1.5406 Å) in the range of $2\theta = 20° - 80°/120°$ with a step size of $0.01°$. The powder samples or the cylindrical pellets each were placed on a sample holder or fixed with a polymer (plasticine), respectively. The samples were carefully leveled with the sample holder to prevent any geometry related errors with the measurement. Using the software DIFFRAC.SUITE EVA V4.0, the analysis of diffractogram was performed to identify different phases in the material synthesized for the experiments presented in this thesis.

4.3.1.2 Scanning electron microscopy (SEM)

The scanning electron microscopy is utilized to study the surface morphology, grain size/shape, inclusions, precipitates, dendrites, grain boundaries, compositional contrast, surface topography etc. that are present in any material. Moreover, using the capabilities of energy dispersive X-ray spectroscopy (EDS), a quantitative elemental analysis can be easily performed either pointwise or over extended surface regions of the sample.

During an SEM investigation, the interaction of the electron beam with a sample surface leads to the generation of different signals in the form of secondary electrons (SE), back-scattered electrons (BSE), and characteristic X-rays. These signals are processed for an image generation and its analysis. The electrons of the electron beam penetrate the sample surface by a few microns and generate stated types of signals. A schematic illustration of the volume of the electron-sample interaction, resulting signals, and information produced from the signals coming from different depths of the specimen is shown in Figure 4.5.

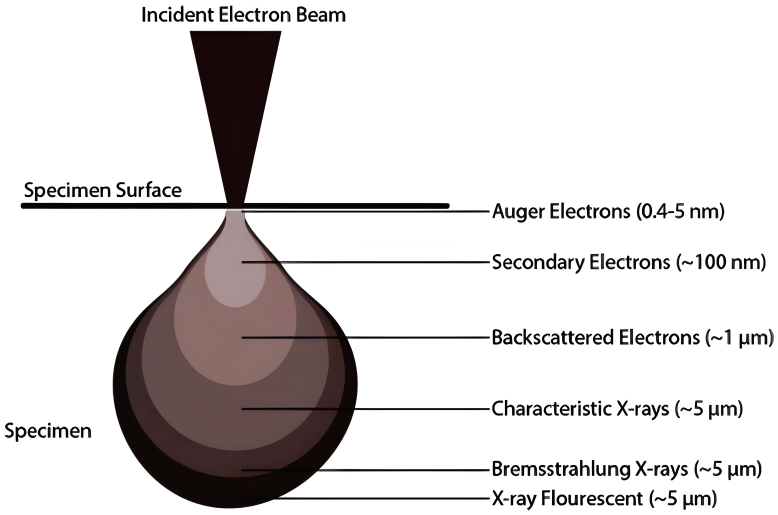

Figure 4.5 A schematic illustration of the interaction volume (teardrop shaped) between a focused electron beam and a solid sample showing a variety of generated signals. The figure has been reprinted (adapted) with the permission from [195].

Commonly, SE and BSE images are acquired and the EDS analysis is conducted to obtain chemical information of the sample on a micron scale, respectively. Each of these modes have been utilized for investigating samples produced for this thesis which are briefly described in the following section.

Backscattered electrons (BSE)

During the electron beam-specimen interaction, the beam electrons that scatter elastically can be deflected with a scattering angle ranging between $0° - 180°$ and eventually leave the specimen [194]. These electrons are called backscattered electrons. The BSE constitute a significant portion of the total energy of the incident beam. The contrast shown by an image formed due to these electrons is called compositional or atomic number (Z) contrast. This means that a heavier element can be correlated with the brighter spots in the image of the specimen while the lighter ones would be comparatively dark.

Secondary electrons (SE)

In addition to the BSE, some electrons are also ejected from the specimen itself and these electrons are called secondary electrons. The secondary electrons are loosely bound outer shell electrons of atoms, which reside near the sample surface. When these loosely bound electrons are struck by the electrons of the incident beam, an inelastic scattering event occurs, which results in a knock-out of secondary electrons. If adequate energy is transferred, these loosely bound electrons are ejected out of the specimen and collected by the SE detector. Generally, the surface morphology and topographic features of samples are investigated using secondary electrons. The morphological features include grain shape, precipitate size, the phase distribution of specific physical features, while the topographic features include distribution and arrangement of physical features at sample surface, defects, crack voids etc. This is feasible due to the low energy of the SE, which are emitted from the top surface of the sample. The sample features facing towards the detector generate higher intensity compared to those away from the detector.

Energy dispersive X-ray spectroscopy (EDS)

The electron beam-sample interaction results in the generation of characteristic X-rays and background X-rays (white radiation/background radiation/continuum), collectively forming an X-ray signal. This X-ray signal is collected using an X-ray detector and analyzed. The characteristic X-rays form the basis for microchemical analysis since they are unique for each element which produces them. The analysis provides a complete information of the elements and their concentrations in the investigated areas of the sample. The EDS detectors are the most commonly used X-ray detectors in the SEM.

The SEM instrument Zeiss Ultra 55 SEM with a Zeiss QBSE detector equipped with an Oxford energy dispersive X-ray (EDS) detector (PentaFETx3) was used for investigating Mg_2X samples (both powder and pellets), with high energy electrons (10 or 15 keV) under vacuum. Some samples were prepared by embedding/mounting them in a polymer stub before preparing them for the SEM investigation. The embedding process was initiated by placing the samples (powder or pellet) on the metal surface (~25 mm in diameter) of the embedding machine sample holder (Struers CitoPress-30). A thermosetting resin (POLYFAST) powder made of Bakelite with carbon fillers was put on top of the sample. The amount of resin powder depends on the required thickness of the stub. This resin powder was mounted on the mounting cylinder (with sample) and pushed towards the heater where they were heated at $T = 180$ °C for 4 min at an applied pressure $p = 200$ bar. For the brittle samples, time and pressure were lowered to

2 min and 50 bar respectively to prevent any damage to the sample. This step was followed by a cooling step of 3 min before the solid embed was taken out of the embedding system. Both embedded and the non-embedded samples are prepared for the SEM investigation by wet-grinding on SiC paper using ethanol. The sample pellets are grinded on papers with different Grits (1200, 2500 and 4000) in an increasing order starting from the grit 1200. At each stage of grinding/polishing, the direction of scratches on the ground/polished surface should be carefully observed. Ideally, the scratches should be in one direction, and no scratches must be present from the previous grinding/polishing step. The polishing is usually carried out to enhance the features of sample surface, observing grains and most importantly, a removal of any scratches left (from the previous grinding step). The pellets and the polymeric stub with embedded powders (or pellets) were polished using disks with a diamond solution of size 3 μm using Buehler EcoMet 250 system. As a last step, the polished sample surface is first cleaned and then sonicated using ethanol.

4.3.1.3 Transmission electron microscopy (TEM)

The TEM is a sophisticated and powerful electron-optical instrument for the nano- and the microstructural characterization of different types of materials. For a TEM investigation, the specimen must be very thin ($\sim$50 nm) so that the electron beam transmits through the specimen even if some part of the incident electron beam either scatters or gets absorbed. The electron-specimen interaction results in different types of signals. These signals include transmitted electrons, backscattered electrons, secondary and Auger electrons, visible light (due to cathodoluminescence), X-ray signals and heat generated by the electron beam during exposure. Some of these signals are shown in a schematic in Figure 4.6.

The transmitted electrons include unscattered, elastically scattered and inelastically scattered electrons. Generally, the experiments that are conducted using TEM include conventional imaging (bright-field and dark-field imaging), electron diffraction (SAED), convergent-beam electron diffraction (CBED), phase-contrast imaging (HR-TEM), high-angle annular dark-field imaging (HAADF or Z-contrast imaging) and electron energy-loss spectroscopy (EELS). These analyses largely utilize the transmitted electrons while the X-ray signals are used for EDS analysis to analyze chemical composition of the samples. During a TEM investigation, other generated signals are furthermore not utilized for the analysis except visible light signals, which are used to investigate optical properties. The experiments stated above are used for imaging the specimen and extracting information at atomic resolution (down to the angstrom or even sub-angstrom level). In high-resolution mode, the crystallographic information of specimen at

the nanoscale can be obtained by electron diffraction as well. Overall, the samples can be investigated to extract information such as the presence of different types of defects and secondary phase particles, the arrangement of atoms and chemical information of the specimen by electronic excitations from small areas of the specimen.

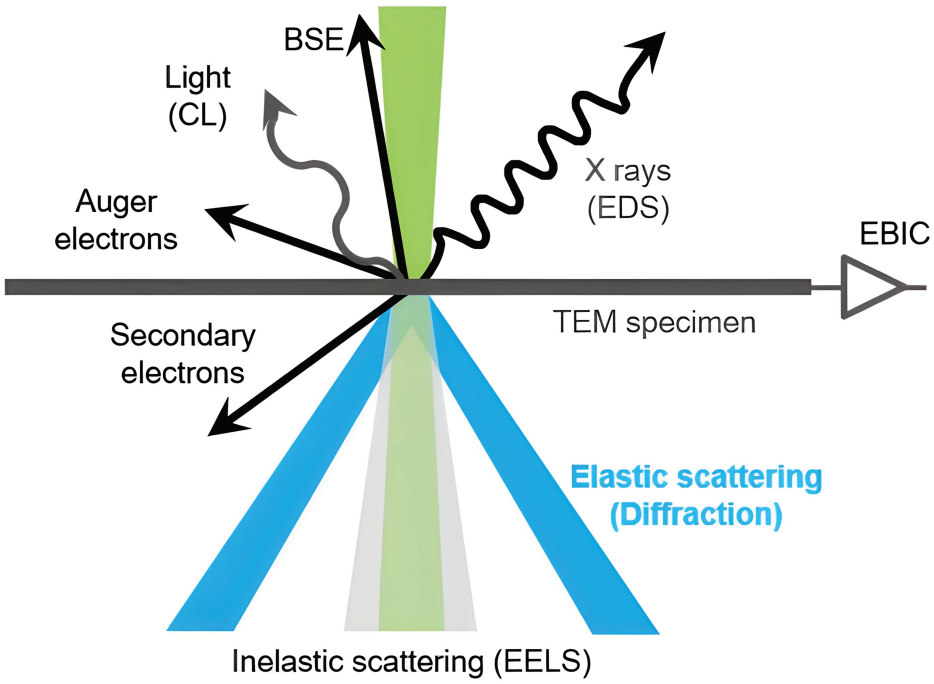

Figure 4.6 A schematic illustration of electron beam-specimen interaction in a TEM column showing a variety of signals generated. The image has been taken from [196].

TEM systems are made up of different components: electron gun, electron accelerator, condenser-lens system, specimen stage, imaging system, vacuum system. The electron gun generates an electron beam, similar to an SEM, but with a kinetic energy high enough to pass through the thin areas of the sample. This gun consists of a negatively charged electrode (cathode) which is held at high negative potential (kV) with respect to the ground potential. There are different types of electron sources which are based on different processes such as thermionic, Schottky and field emission. The TEM instrument used for the present work has a field emission gun (FEG) as an electron source. The FEG has an added advantage over other sources of electron beam such as a possibility of operation at RT and extended usage lifetime.

The Mg_2X samples were investigated using a Philips Tecnai F30 STEM at an acceleration voltage $U = 300$ keV. The microscope is equipped with a Gatan MSC 794 CCD camera and a windowless EDAX Apollo XLTW SDD-detector for the EDS analysis. The imaging and

analysis of the samples prepared for the present work was conducted in dark-field, bright-field, and HAADF modes (both before and after EDS measurements). Additionally, EDS (point scans, maps and line scans) and SAED measurements were also conducted in different areas of the sample. Particular details about sample preparation and instrument calibration are provided in the materials and methods section of Chapter 8. The TEM measurements and the data analysis were carried out by Dr. Klemens Kelm while the interpretation and correlation of microstructural data with the TE properties were conducted by the author of this thesis.

Each technique described above in this section is used for analyzing the structural and chemical features of the samples prepared for this work. The equilibrium phase diagram of Mg_2Si-Mg_2Sn solid solutions shows a miscibility gap which can lead to the occurrence of certain microscopic features during synthesis that cannot be resolved from X-ray diffractograms and thus, necessitates the use of SEM or TEM.

4.3.2 Characterization of thermoelectric transport properties

4.3.2.1 Seebeck coefficient and electrical conductivity measurements

The temperature dependent thermoelectric properties, both S and σ, were measured using an in-house developed measurement facility (HT-$S\sigma$) utilizing a four-probe technique. The measurement system is capable of accurately measuring the transport properties in the temperature range of $T = 300\ \text{K} - 1000\ \text{K}$. The sample holder is made of Shapal (AlN), and is equipped with two gradient heaters, as shown in Figure 4.7.

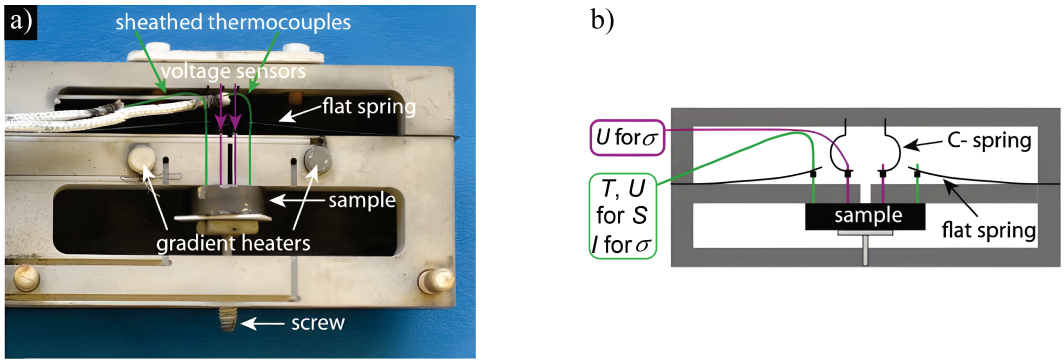

Figure 4.7 (a) Mounted sample in the sample holder and (b) system of the mechanical and electrical connections for the HT-$S\sigma$ facility. Note that the sheath of thermocouples acts as current feed for electrical conductivity measurement. This image has been reprinted with the permission from [197].

The advantage of two heaters is that the Seebeck coefficient S of the sample can be measured by varying the heat/temperature gradient in both directions. Each heater is a bifilar winded filament that gets heated by supplying electrical power. The sample is mounted and fixed in the sample holder using a headless screw and a 'T'-piece. Samples with dimensions from 10 to 30 mm in length, and 0.1 to 8 mm in thickness (d) can be easily measured. The samples can be measured in either vacuum or inert gas atmosphere. There are two type N thermocouples that record temperatures on each end of the sample. When the sample is heated by the gradient heaters at respective ends, these thermocouples also measure the thermally induced voltage from the sample. These thermocouples are sheathed which makes them advantageous compared to the ceramic tube coated thermocouples. The thermocouple sheath provides a better mechanical flexibility facilitating easy thermocouple assembly and exchange. The sheath is made of Inconel which prevents the chemical contamination of the measuring junction. The individual wires of the thermocouple (within the Inconel sheath) are insulated from each other by a ceramic filling. Flat tungsten-rhenium alloy springs allow the thermocouples to be strongly pressed on to the sample for a better thermal coupling of sample and the thermocouples. The tungsten-rhenium alloy has a large Young's modulus at elevated temperatures and enables accurate measurement of the thermovoltage, and correspondingly an accurate determination of the Seebeck coefficient. Additional potential probes (for the determination of σ) are pressed on the sample by two C-shaped springs. This entire sample holder is enclosed in a few mm thick graphite enclosure that allows homogenization of the thermal environment and serves as a radiation shield. This sample holder is connected to a vacuum flange by molybdenum rods. The flange covers the edge of the quartz tube which contains the sample holder.

The properties are measured in the following manner: first, the electrical conductivity is measured at a desired temperature point, and for this purpose, the furnace temperature is set and allowed to stabilize. Following this, an alternating current (AC) is passed through the sheath of the thermocouples acting as current leads and the voltage is measured across the tungsten carbide potential probes. σ is calculated using the relation $\sigma = \frac{I}{2\pi s' UC}$, where s' is the spacing between the tips, C is a geometric correction factor (GCF), which accounts for finite sample size, its geometry and spacing between the tips [197].

The thermovoltage is measured using the thermocouples that are made of different types of wire material (Nisil and Nicrosil). Accordingly, the measured thermovoltage has a contribution of the Seebeck coefficient of each thermocouple wire as well. Note that the thermovoltage across same type of wire material (in a thermocouple) are recorded. As mentioned earlier, the setup is equipped with two gradient heaters which are used to develop a small ΔT for the

Seebeck coefficient measurement. In such condition, consecutive measurements of thermovoltage and temperatures are carried out. To record the voltage and temperature for a number of data points, the first heater is switched on for 60 s creating a ΔT with respect to the second heater, which is inactive. Later, the first heater is switched off to allow the system to relax and during this time, temperature and voltage developed are recorded, and later used for analysis. This step is repeated with the second heater while keeping the first heater switched off. Instead of a single $U - T$ pair, the developed voltages (U_A and U_B) and temperatures corresponding to each consecutive measurement (where heater 1 then heater 2 are active) are used for further analysis. Specifically, the slope of U_A versus U_B is employed to determine the Seebeck coefficient by using the expression: $S(\bar{T}) = S_{TC}(\bar{T})/(1 - \partial U_B/\partial U_A) + S_A(\bar{T})$, with $S_{TC} = S_B - S_A$ is the Seebeck coefficient of thermocouples while S_A and S_B are the Seebeck coefficient of the Nisil and Nicrosil wires probing the voltage drop (U_A and U_B), respectively. Mean temperature, $\bar{T}$, is determined by averaging the temperature points of thermovoltage measurement.

The sample properties were measured in the temperature range RT – 723 K/773 K. Particularly, these measurements were made at many intermediate temperature points (within the stated range) during heating and cooling (collectively called as a thermal cycle). Generally, a good measurement reproducibility was observed in temperature dependent thermoelectric properties of n-type Mg_2X solid solutions (Figure 4.8). The thermoelectric transport properties measured during cooling are analyzed using semiconductor transport models.

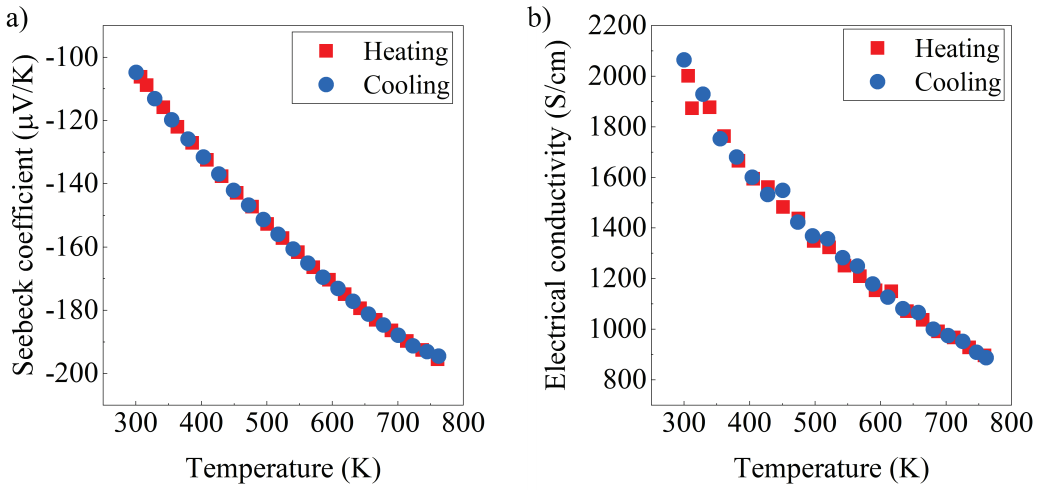

Figure 4.8 Temperature dependence of (a) the Seebeck coefficient S and (b) the electrical conductivity σ of $Mg_{2.06}Si_{0.385}Sn_{0.6}Sb_{0.015}$ while heating up and cooling down the sample.

All measurements have their respective uncertainties and therefore it is crucial to discuss the various sources of uncertainty for both the Seebeck coefficient S and the electrical conductivity σ measurements. The uncertainty in the electrical conductivity σ could stem from a combination of noisy voltage readings affecting resistance measurements, from geometrical uncertainties of the sample or probe spacing which can affect s' or C, respectively. The electrical conductivity σ calculation utilizes a GCF and therefore for a proper positioning of the tips, a uniform spacing between them, sample preparation and the measurement of geometrical dimensions are crucial factors. If the spacings between the tips are not same for all four tips, the GCF equation does not hold valid.

On the other hand, uncertainties in the Seebeck coefficient measurement stem from inaccuracies in the voltage U readings, since, these readings are usually quite small in magnitude and can be affected by noise. A further uncertainty can occur during the analysis of measurement signals when voltage signals are interpolated with respect to time. This uncertainty originates due to the spurious thermal offset voltages. The equation stated above does not require that the thermal offset voltage (of U_{B} and U_{A}) should be same, rather, they should be constant over time. Any change in the said voltage offset affects the Seebeck coefficient, that might be identified by observing a deviation in the correlation coefficient between U_{B} versus U_{A} from unity. Moreover, a comparatively severe uncertainty comes from the thermal contact resistance between the sample, the thermocouples, and a part of the sample holder pressed onto the sample. Such thermal contact resistances can cause an error in the temperature readings (but not the measured Seebeck voltage U_{Seebeck} readings), which can thus, lead to incorrectly determined Seebeck coefficient values [197].

The uncertainty in the measurement of both the Seebeck coefficient S and the electrical conductivity σ is $\pm 5\ \%$ which is confirmed by measuring NIST standard reference material 3451, a low temperature standard material for the Seebeck coefficient, and measurements on a high temperature reference material (β-$FeSi_2$) proposed in [198, 199]. The measurement uncertainties of the HT-$S\sigma$ setup is comparable to that obtained in an international round robin test [200, 201]. Note that the round robin test was conducted to understand the discrepancy in measurements and the development of standard testing procedures. The temperature dependent Seebeck coefficient and conductivity measurements for the thesis were performed by Mr. P. Blaschkewitz, DLR.

4.3.2.2 Hall measurement

The carrier concentration n is one of the fundamental parameters for the optimization of thermoelectric performance. A measurement setup based on the principle of the Hall effect is the commonly utilized technique for the determination of the carrier density of any conducting material. In principle, a current (I) is passed through a conducting sample placed in a homogeneous magnetic field (B), which exerts a force on the moving charge carriers transversely to their direction of flow, called the Lorentz force. As a result, the carriers accumulate at one side of the material, and likewise produce an opposite charge on the other side, thus, forming a dipole. This exerted force is given by the relation $F = qvB$, where q is the electric charge, and v is the electron velocity. The accumulation of charge at opposite ends leads to the formation of an electric field and induces an electric potential difference that can be measured. This 'induced' electric potential difference is called the Hall voltage (U_{H}), which is used to calculate the Hall coefficient (R_{H}). Therefore, the developing potential difference across a current-carrying conductor (transverse to the current), of thickness d, placed in a magnetic field perpendicular to the current flow (Figure 4.9) is called the Hall voltage.

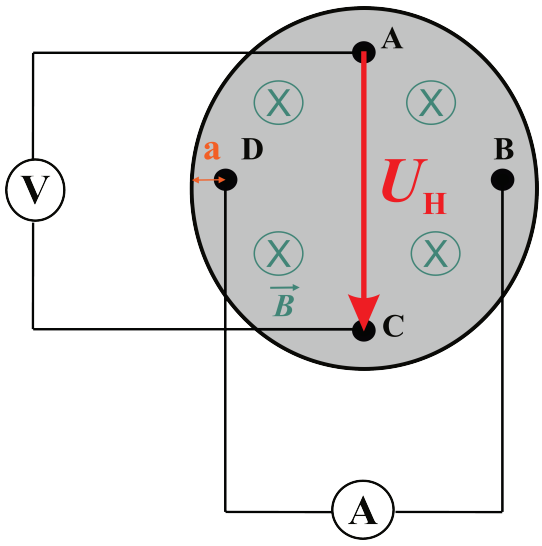

Figure 4.9 Schematic sketch of the sample holder for the measurement of Hall voltage in a van der Pauw geometry.

The Hall coefficient of thermoelectric samples was measured at RT using an in-house developed facility with a van der Pauw configuration. In this configuration, the sample and the sample holder geometry are different from the traditional bar shaped geometry. For a successful measurement of the Hall coefficients in a van der Pauw configuration, there are a few pre-requisites, which are: the sample must be flat with a uniform thickness, it should possess no

voids, and the measurement probes must be sufficiently small in their diameter. In the van der Pauw configuration, the measurement probes are sometimes parallel to each other, and they should lie perpendicular to each other at the sample surface in a geometry, as shown in Figure 4.9. Nevertheless, the measurement probes should ideally be located at the periphery of the sample. While the same geometry (of the sample holder) can be utilized for a square shaped geometry, it is convenient if a cylindrical geometry is used for the measurement. The same cylindrical geometry is shown in Figure 4.9 with contacts A, B, C and D near the sample periphery.

For a van der Pauw geometry, the Hall coefficient can be calculated as: $R_{\mathrm{H,AC}} = \frac{U_{\mathrm{AC}}}{I_{\mathrm{BD}}}\frac{d}{B}$. According to this expression, plugging in the voltage signals and other parameters would yield the value of Hall coefficient. In principle, when a constant current I_{BD} is passed through a conducting specimen (diameter D, thickness d) in a constant magnetic field with flux B (perpendicular to the sample surface), an electric potential difference U_{AC} is generated which is perpendicular to the direction of applied current and the magnetic field. In the present facility, nevertheless, the Hall coefficient is determined by measuring the change of voltage as a function of change in the flux of magnetic field i.e. $(\partial U_{\mathrm{H}}/\partial B)$ (the slope). The slope corresponding to a constant current value is utilized as an input to deduce the Hall coefficient at any temperature point. The voltage signals are measured across two configurations (U_{AC} and U_{BD}) for the sake of averaging.

For the measurement of the Hall coefficient on the presented setup, a minimum sample diameter should be $D > 9.5$ mm since the diagonal contact distance is 8.2 mm, while the thickness (d) should be around 1 mm for a good signal-to-noise ratio. The diameter is not an input parameter to deduce the Hall coefficient if the contacts lie perfectly at the edge, it is nevertheless needed to use it in a geometry correction factor, given as: $GCF = -8a/\pi D$, that corrects the error arising due to geometry. The GCF is a correction term utilized in the calculation of the Hall coefficient, since, in the present setup, the probes are not exactly on the sample edge, rather near the sample edge as shown in Figure 4.9. The corresponding deviation (a) of the probes from the specimen periphery is highlighted by 'a' in the figure. Further details of the Hall measurement system, data acquisition routine, analysis of the raw measurement data, the stated calculation etc. are discussed in detail in Chapter 5. For heavily doped thermoelectric materials, n_{H} (at RT) is calculated from R_{H} by the expression $n_{\mathrm{H}} = \frac{1}{R_{\mathrm{H}}e}$ assuming a single carrier type.

4.3.2.3 Thermal conductivity measurement

The thermal conductivity is a measure of the ability of a material to conduct heat. As previously stated, for a material to have high zT, its thermal conductivity should in principle be as low as possible. For the studies conducted within the framework of this thesis, the laser flash method is used to measure the thermal diffusivity (α) of the sample. The temperature dependent diffusivity values are utilized to calculate the thermal conductivity (as discussed later in the text). The laser flash method is a transient technique of measurement and it possesses features such as easy sample preparation, short measurement duration with high accuracy [202]. It is a non-contact and non-destructive technique for the measurement of the thermal diffusivity of materials [203]. It was first introduced by Parker *et al.* [204]. A schematic with a mounted sample is shown in Figure 4.10. In laser flash method, heat is supplied to the sample in the form of a pulse (from a laser source) that results in transient (amplitude signal output) change in the sample temperature (as shown in Figure 4.10).

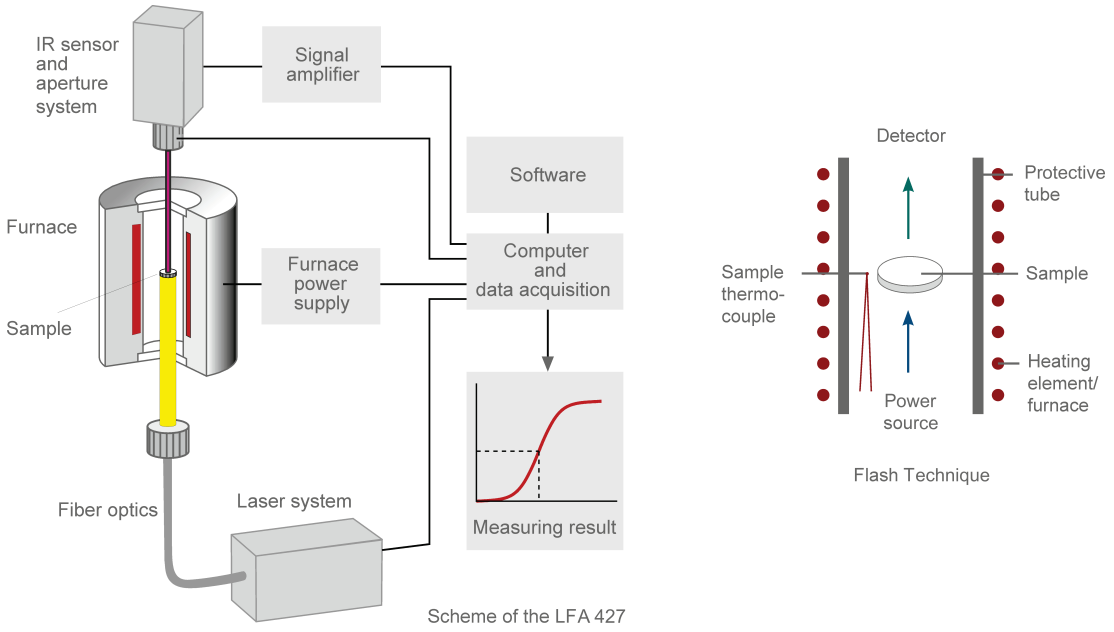

Figure 4.10 Schematic illustration of the laser flash method for thermal diffusivity measurement. The right sub-figure shows a zoom-in of the furnace where the sample is placed. These images are reprinted from [205].

The curve resulting from instantaneous heating of the sample is shown in Figure 4.11. The heat wave propagates through the sample and the detector on the rear side of the sample tracks the time dependent rise in temperature at the sample surface. The signal reaches a maximum and, at the very end, the signal shows a decrease with time because the heat is lost from the sample to the surroundings (in furnace) which can be visualized in Figure 4.11.

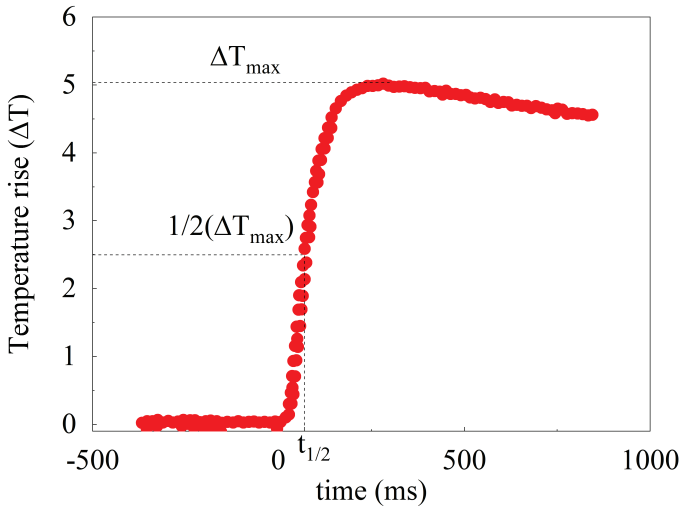

Figure 4.11 Plot showing signal measured from the rear side (facing the detector) of the sample that corresponds to a temperature rise at the sample surface, as a function of time. The plot has been reconstructed from [206].

The time-dependent temperature response curve shows the speed of a rise in sample temperature, where a fast temperature rise on the rear side of sample corresponds to a rapid transfer of heat. This allows a determination of the thermal diffusivity of sample. An adiabatic model is utilized to explain the rise of temperature (time axis intercept) until it reaches a maximum. The time corresponding to $^1/_2\,(\Delta T_{\max})$ (i.e. half of the maximum temperature ($\Delta T_{\max}$) during a temperature rise) is called half-time ($t_{1/2}$). The half-time is plugged in the diffusivity equation, $\alpha = 0.1388\frac{d^2}{t_{1/2}}$, where the constant value (0.1388) is a factor for the adiabatic case; the employed software takes the sample geometry and non-adiabatic conditions into account. Since α and κ are directly related to the sample thickness (d) by $\alpha \propto \kappa \propto d^2$, so, d should be measured with care [204].

The thermal diffusivity of the cylindrical pellets prepared for this thesis were measured by Netzsch LFA 427 and LFA 467HT *HyperFlash*® apparatuses [205]. The cylindrical pellets with a diameter of ~12.7 mm were measured from RT to 723 K/773 K with a step width of 25 K or 50 K. Thermal conductivity was calculated from the measured diffusivity by the relation: $\kappa = \alpha c_{\mathrm{p}}\,\rho$, and the c_{p} value was calculated from the Dulong-Petit limit for the specific heat at constant volume ($C_{\mathrm{V}}^{\mathrm{DP}}$) by using the expression $c_{\mathrm{p}} = C_{\mathrm{v}}^{\mathrm{DP}} + \frac{9E_{\mathrm{t}}^2 T}{\beta_{\mathrm{T}}\,\rho}$, where E_{t} and β_{T} are the coefficient of thermal expansion and the isothermal compressibility at different temperatures, respectively [207]. The uncertainty in α measurements is $\pm 8\,\%$. The

measurements of the temperature dependent thermal diffusivity were carried out by Mr. P. Blaschkewitz, DLR.

4.3.2.4 Analysis of thermoelectric transport properties

The thermoelectric properties were analyzed using single band and multiband models assuming parabolic bands. These models consist the equations of transport coefficients that are solutions to the Boltzmann transport equation. The models were scripted and the calculations were performed in MATLAB® as the equations contain infinite integrals that needs to be solved numerically.

Chapter 5 Establishing and analysis of high temperature Hall measurements

5.1 Summary

Herein, a detailed description of the facility used for the measurement of the Hall coefficient (R_H) and electrical conductivity (σ) is presented. The Hall coefficient R_H is used to determine carrier concentration n, which is one of fundamental parameters to optimize the TE performance of any material. The facility uses a van der Pauw technique for the measurement of the Hall coefficient and electrical conductivity. The capability of this facility is extended for measuring these properties at elevated temperatures (300 K – 723 K). A schematic and a circuit diagram of this facility is presented and the function of each component of this facility is briefly discussed. Room temperature reference measurements are carried out on $Mg_2(Si,Sn)$ samples (with different types of conductivity (both p-type and n-type)) in different Hall facilities at laboratories across the globe that allowed a comparison of measurement uncertainties between these facilities. Moreover, the temperature dependent measurements of the Hall coefficient and the electrical conductivity were carried out on a p-type $FeSi_2$ specimen in the Hall facilities at DLR and the Department of Chemistry, Aarhus University, Denmark. The measurement data acquired on each of these setups was compared and discussed. The geometry correction factor associated with the van der Pauw technique is validated by the finite element modelling (FEM) using ANSYS.

In a separate technical report (accessible under [208]), the following information is provided:

- Flowcharts of the pre-existing data acquisition routine (including central routine, temperature loop, sub-routines for the measurement of the Hall voltage and voltage for electrical conductivity) and their detailed description.
- Flowcharts of the data analysis routine along with the sub-routines for the checks to assess the quality of the Hall measurement before and after analyzing the raw signals.
- Furthermore, there were issues related to the measurement of electrical conductivity which are highlighted in the technical report. In this regard, a description of different experiments conducted to resolve these issues and the solutions to this problem are discussed there as well.

5.2 Purpose and relevance

Thermoelectric properties of materials are governed by their carrier concentration n, as shown in Figure 1.5. Correspondingly, n is tuned by manipulating the (intrinsic and extrinsic) point defect concentration in any material for achieving optimized thermoelectric properties. The Hall effect is a commonly used method for the determination of the carrier concentration of a material. The carrier concentration can be directly calculated using the measured Hall coefficient R_{H} ($n \propto 1/R_{\mathrm{H}}$) for the temperature regime where only majority carrier contributes to the thermoelectric properties. The electrical conductivity σ of the same material can be simultaneously measured with the same measurement facility. Moreover, a temperature dependent measurement of these transport properties could provide useful insight on the contributions of different bands in a semiconductor with complex band structure as is typical for many TE materials. This is possible by plugging these transport parameters in well-established models (discussed in 2.2 of Chapter 2) for the physical interpretation of carrier transport phenomena in semiconductors. In addition to this, the Hall mobility μ_{H} can be calculated from the measured properties which provides an insight on the relevant mechanisms of carrier scattering. In the coming section, the pre-conditions and principles of the van der Pauw technique is discussed in detail.

5.3 Theoretical background of van der Pauw method

The van der Pauw geometry of the sample holder is utilized for the measurement of these properties as shown in Figure 5.1(c-e). This configuration can be utilized for an arbitrarily shaped sample; however, a cylindrical specimen is shown here that represents the shape of the sintered pellets. For a simultaneous measurement of the Hall coefficient R_{H} and the electrical conductivity σ, van der Pauw geometry utilizes four probes while a traditional sample holder geometry utilizes five (or six) probes. Figure 5.1(a) and Figure 5.1(b) also shows a traditional sample geometry for the Hall coefficient R_{H} and the conductivity σ measurement for comparison. There are some pre-conditions for the van der Pauw technique: the sample should be homogeneous, conducting and of uniform thickness d [209]. The sample shape is less important but there should be no isolated holes (or pores) in the material. Moreover, the contacts should be at the circumference of specimen but can otherwise be located arbitrarily, and should be small in diameter compared to the sample diameter (D). In this section, the measurement principles and the expressions to deduce the electrical conductivity σ and the Hall coefficient R_{H} are briefly described.

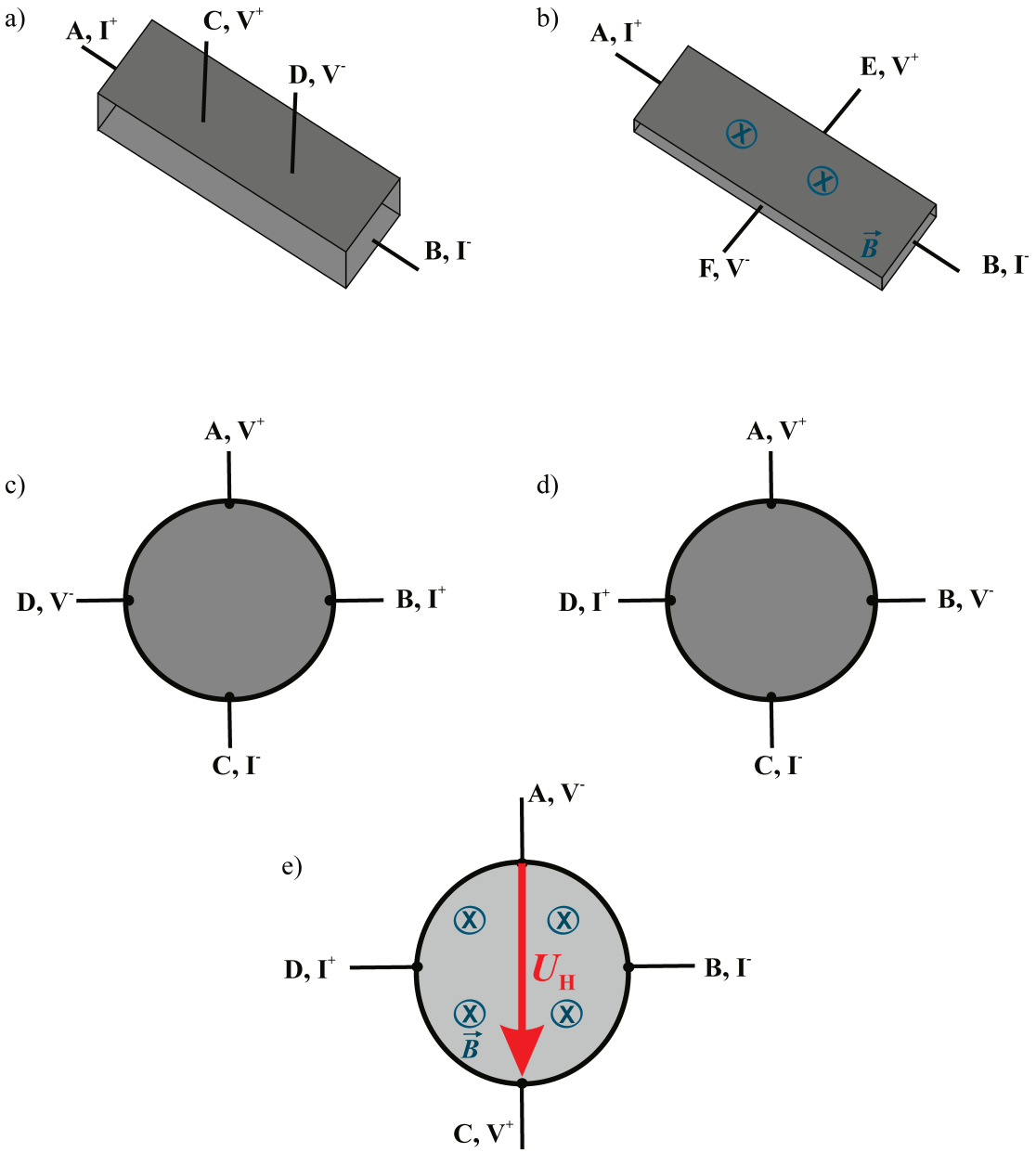

Figure 5.1 Different specimen and contact geometries for the measurement of both the Hall voltage U_H and measured voltage (U_σ) corresponding to the electrical conductivity of a specimen using the traditional and the van der Pauw method, respectively. Probe positions for electrical conductivity σ measurement with the traditional and the van der Pauw method is shown in (a), (c) and (d) respectively. The Hall coefficient R_H measurement using the traditional and the van der Pauw technique is shown in (b) and (e). The direction of the magnetic field ($\vec{B}$) is represented by ⊗ meaning that the field is perpendicular and inwards the plane (away from the reader) with respect to the specimen in (b) and (e).

5.3.1 The electrical conductivity

Van der Pauw [209, 210] showed that the electrical conductivity of an arbitrarily shaped specimen with a constant thickness can be determined from Equation (5.1) using conformal mapping under the stated pre-conditions. For a round specimen, as shown in the panels (c) and (d) of Figure 5.1, passing a current from contact B to C (or D to C), induces a voltage (U_σ) that can be measured between contacts A and D (or A and B), respectively. The corresponding resulting resistance is given simply by: $R_1 = R_{\mathrm{BC,AD}} = U_{\mathrm{AD}}/I_{\mathrm{BC}}$ (and $R_2 = R_{\mathrm{DC,AB}} = U_{\mathrm{AB}}/I_{\mathrm{DC}}$). R_1 and R_2 are resistances calculated from the voltage signals that are measured in the configurations shown in (Figure 5.1(c) and Figure 5.1(d)). The different configurations of the measurement probes are based on the selection of these probes to pass current and measure voltages as shown in respective figures. Due to symmetry, interchanging the current source and voltmeter or reversing the polarity of current source and the voltmeter (in the shown configurations) will yield the same result. The two resistances fulfill the van der Pauw relationship expressed as [209, 210]:

$$e^{(-\pi R_1\, d\sigma)} + e^{(-\pi R_2\, d\sigma)} = 1 \qquad \text{Equation (5.1)}$$

Equation (5.1) is numerically solved using root finding functions that are available in different high-level programming languages (e.g. MATLAB, Python). The solution yields the value of electrical conductivity. Besides, for a simplified calculation (without need of root finding functions), σ can also be written as expressed in Equation (5.2) [209, 210]. Note that the equation utilizes factor f is a factor which is a function of the ratio R_1/R_2.

$$\frac{1}{\sigma} = \rho = \frac{\pi d}{ln2}\frac{R_1 + R_2}{2} f\left(\frac{R_1}{R_2}\right) \qquad \text{Equation (5.2)}$$

Equation (5.2) is useful for quick manual estimates of conductivity, f (as given in Figure 5 of the paper from van der Pauw [210]), is not so different from unity if the resistance values (in the shown configurations) were not too different ($R_1 \approx R_2$). It was, e.g., used to calculate conductivity σ values at room temperature while conducting handwaving tests manually. Note that these tests were conducted to find the origin of large deviation in the electrical conductivity σ values measured at the HT Hall and HT-$S\sigma$ facilities (discussed in detail in the technical report) [208].

5.3.2 The Hall coefficient

In a van der Pauw geometry, the Hall coefficient R_H is determined by utilizing the same four contact probes used for the electrical conductivity σ measurement. However, in this case, the probes that are diagonal to each other are utilized for the measurement of the Hall voltage (U_H), which is induced when current is passed through a specimen in a magnetic (B) flux perpendicular to the surface of the specimen as shown in Figure 5.1(e). The Hall coefficient is calculated by the expression $R_{H,AC} = \frac{U_{AC}}{I_{BD}} \frac{d}{B}$. In the facility at DLR, the measurement is repeated to confirm the reproducibility of the measured values. The R_H for this (other) configuration is given as $R_{H,BD} = \frac{U_{BD}}{I_{AC}} \frac{d}{B}$, and in ideal pre-conditions stated above, the $R_{H,AC} = R_{H,BD}$.

The stated conditions of the measurement of these transport properties are used in our lab to our advantage, by readily using the cylindrical pellet obtained after sintering since no specific sample geometry is required. This makes the van der Pauw technique compatible with the facilities used for the Seebeck coefficient and thermal diffusivity measurements. This also reduces the inhomogeneity issues that can occur while shaping the sample geometry. The measurement of both the Hall coefficient R_H and the electrical conductivity σ using this technique is carried out in the plane of the cylindrical specimen disk i.e. perpendicular to the sample pressing direction. Therefore, for materials with a directional dependence of transport properties (e.g. single crystals, polycrystalline textured materials, Bi_2Te_3 etc.), anisotropy needs to be taken into account [211]. Using a sample holder with a bar-shaped geometry is advantageous in this case as the current flow can be aligned to the crystal axes in 1D (valid only for thin samples), however, in a van der Pauw based geometry, current flow is aligned in 2D. In the presented Hall facility, bulk samples of thickness ($d \approx 1-2$ mm), and diameter ($D \geq 10-15$ mm) can be utilized. Ideally, a sample with $D = 12.5$ mm and $d = 1$ mm thickness would yield good signal-to-noise ratio, given the other measurement conditions are kept unchanged. The ease of van der Pauw geometry has been utilized in the design of a few different setups [211-217] for measuring temperature dependent Hall coefficient R_H and electrical conductivity σ, while a few utilize the traditional bar shaped geometry [215, 217, 218] as well.

The facilities to measure the Hall coefficient R_H and the Hall mobility μ_H at high temperatures are scarcely available. As a result, thermoelectricians have achieved only a limited understanding of the carrier transport at higher temperatures. Therefore, a setup with a capability of measuring temperature dependent transport properties is essential for advancing the field and a further development of thermoelectric devices.

5.4 Components of the measurement system

In this section, the function of each component of the Hall measurement facility is briefly described. The basic schematic of the Hall measurement system is shown in Figure 5.2(a) along with a corresponding circuit diagram highlighting the connections in Figure 5.2(b). Moreover, a pictorial representation of the Hall measurement system is shown in Figure A.1 of Appendix A.

a)

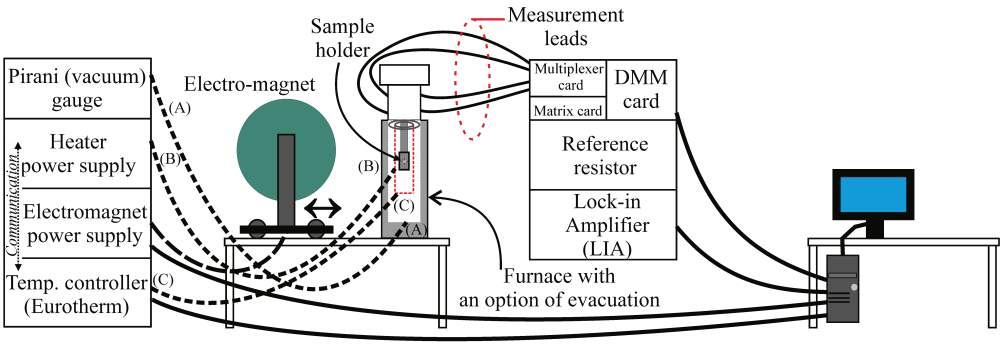

b)

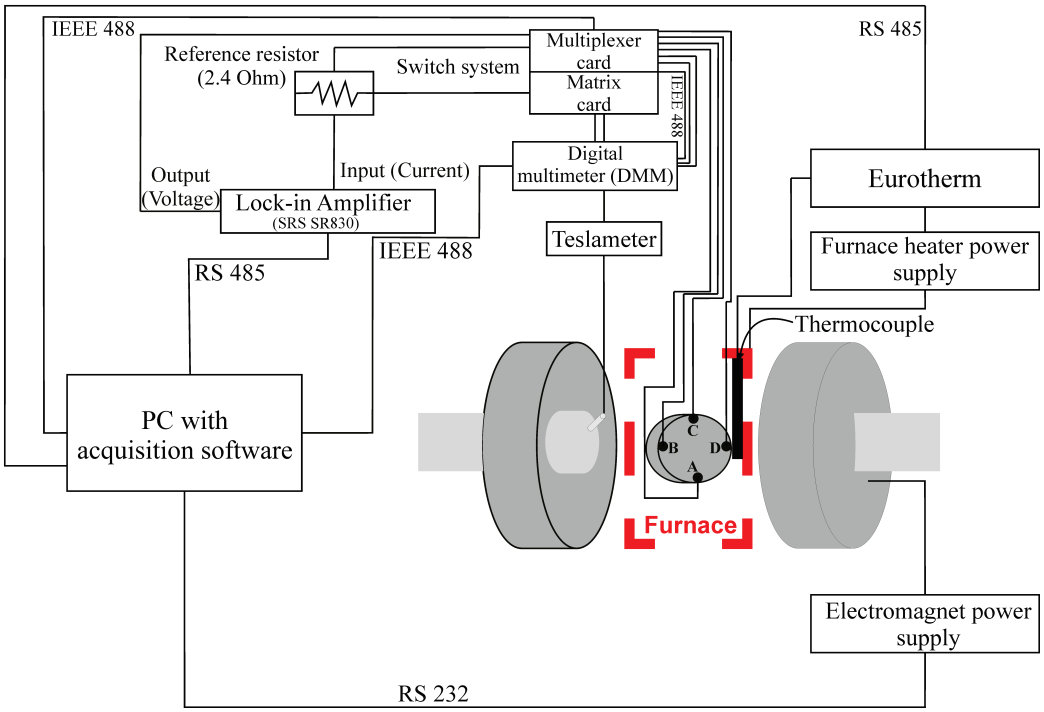

Figure 5.2 a) Schematic of the Hall measurement system, and the corresponding b) electrical circuit of the measurement system.

5.4.1 The magnet

The setup utilizes an electromagnet that comprises a pair of Helmholtz coils (copper) (Figure 5.2(a)) for the generation of a uniform B-field. The distance between the pole caps of the electromagnet is 11 cm and the diameter of each pole cap is 18 cm. This ensures a perpendicular and homogeneous B-field, which is essential for R_{H} measurement at the sample position (placed in the center of the gap between the pole caps). Moreover, a sufficiently large distance between the pole caps allows for the accommodation of a heating vessel in which the sample holder is rested. The details of the sample holder are described in the coming section (5.4.2). The magnitude of the B-field developed from this electromagnet lies in the range $B \approx \pm 0.5$ T. During the measurement routines, the magnitude of the B-field is varied stepwise by the acquisition routine (discussed briefly after the end of section 5.7 and in detail in the technical report [208]) that controls the power supply of the electromagnet. The magnitude of the B-field is calibrated by a magnetometer with respect to the current supplied from the electromagnet power unit. Therefore, in the data analysis routine, a calibrated curve of the change of B-field with (measurement) time is utilized for analyzing raw signals from each measurement since the B-field settings were unchanged during all measurements.

5.4.2 Sample holder

Figure 5.3 shows the sample holder where the probes of four thermocouples are positioned in a van der Pauw geometry. A direct contact between the probes and the specimen is maintained by pressing the specimen on the probe tips with the help of a ceramic stub. The ends of this stub are screwed on the sample holder which keeps the specimen fixed in this position. A ceramic piston acts as a base for the sample so that the sample is immovable with respect to the probes during the measurement. This piston also helps in maintaining the van der Pauw geometry of thermocouple probes: Beneath the piston, the thermocouples are loaded individually with compression springs, which gives them mechanical flexibility such that their tips are pressed onto the specimen. Furthermore, the ceramic springs between the ceramic components allow a good fixing of the ceramic stub on the sample holder.

Note that Figure 5.3(c) shows an arrangement of probes for U_{H} measurement through the AC configuration only but the same arrangement is utilized for measurement across the BD configuration, with an interchange of probe channels for I and U_{H} during the measurement. The same arrangement is used for U_{σ} measurement across different configurations. The only difference between the schematic in Figure 5.3(c) and in Figure 5.1(e) is the placement of

probes which is not exactly at the edges in the present setup. An influence of asymmetry in probe arrangement and non-edge contacts on the measurement is discussed in section 5.9.1.

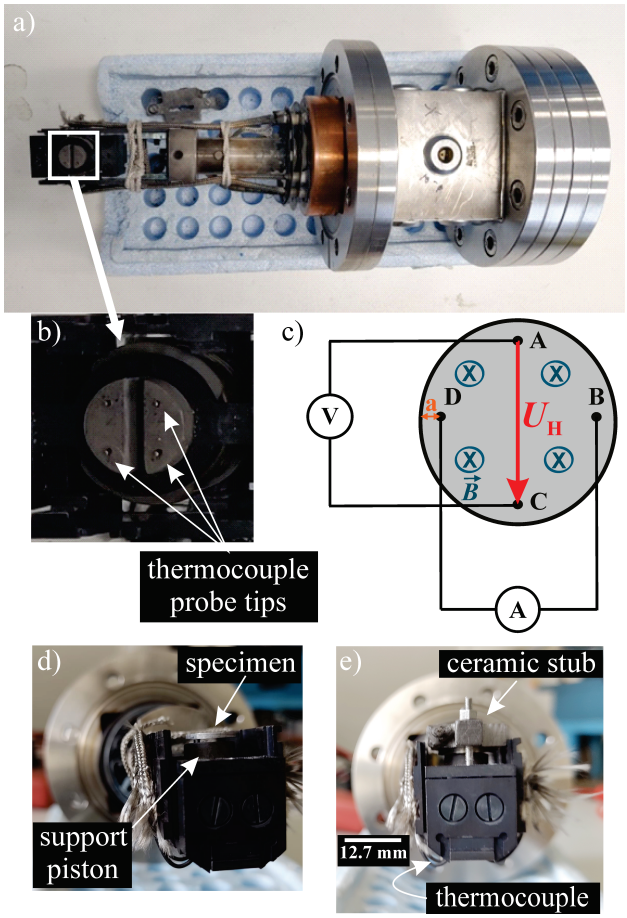

Figure 5.3 a) The sample holder integrated on the measuring head of the Hall facility. The sample holder is zoomed-in showing thermocouple probes in b), while c) shows the schematic of the van der Pauw configuration for the Hall measurement (for comparison). The probe-to-edge distance, a, indicates that the probes do not exactly lie on the sample edges. The specimen is d) mounted on the sample holder, and e) pressed on the thermocouple tips with help of a ceramic stub. The specimen is supported by a ceramic piston on the other face of specimen.

5.4.3 Controlled recipient

The sample holder resides in a stainless-steel cylindrical vessel furnace so that the sample can be heated to higher temperatures. This vessel is evacuated with continuous pumping using a rotary vane vacuum pump to prevent sample oxidation during *T*-dependent measurements. The vessel diameter is designed such that it easily accommodates the sample holder, and the vessel occupies the area between pole caps of the magnet. Note that the electromagnet and the vessel both are connected to cooling water supply to prevent their overheating.

5.4.4 Thermocouples

The furnace temperature is probed and controlled by using a type-N thermocouple. Both voltages (U_{H} and U_{σ}) and the sample temperature are measured on the sample surface by type-N thermocouple probes as well. The probes are 1 mm in diameter and tapered to 0.5 mm at the tip. These thermocouples are sheathed with Inconel to prevent them against corrosion during high temperature measurements. During a measurement, two probes are utilized for measuring the voltage drop while other two probes are utilized to supply current. The current is supplied *via* the Inconel sheath as it is electrically conductive. Moreover, each of the thermocouples is surrounded by a high-temperature braided sleeve to avoid the contact between the thermocouple and the electrically conductive components of the sensor head. This is because both current and voltage signals can transmit through the thermocouple sheath. The same configuration can be used for T-dependent measurement of the Seebeck coefficient. Overall, these thermocouples provide better mechanical strength and flexibility to be utilized as signal probes over those (e.g. non-sheathed, soft-metal based contacts etc.) that have been typically used in other systems that employ van der Pauw geometry [211, 213-215]. This is mainly because no medium (e.g. silver paste) is used to contact the measuring probes to the sample, and sheathing allows the supply of current and simultaneous voltage measurements.

5.4.5 The heater

The sample and a significant fraction of the sample holder is placed in a cylindrical ring (outer diameter $d = 6.5$ cm, and a length of 10 cm) made of carbon-fiber reinforced carbon (CFC) composite material. This heater is connected to the power supply with a type-N thermocouple in its proximity for probing temperatures, which is displayed and stabilized by a T-controller (Eurotherm®). The desired temperature is set by the acquisition program, and current is supplied to the heater which heats up the furnace by resistive heating. The heater power supply is connected to the T-controller to monitor and control the supply.

5.4.6 Measurement power supply and measurement of electrical signals

A lock-in amplifier (LIA) acts as a current source (signal generator, reference oscillator) for electrical measurements and amplifies the voltage measured on the sample. The AC is passed through the sample *via* a reference resistor (RR) box, with a highly accurate value of $R = 2.4\ \Omega$, and a corresponding voltage signal is recorded. The measurement signal is amplified with respect to a reference signal of known phase and frequency. This means that signals with other frequencies are filtered out and the overall noise in the measured signal is reduced.

Besides, the sensitivity of the LIA is in the range of nanovolts (nV), and such sensitivity is required to measure highly conductive samples.

5.4.7 Switch system and multimeter

The switch system consists of a multiplexer and a matrix card that are responsible for an interconnection of channels for the measurement of voltage and supply of current, respectively. During the measurement cycle, the switch system is controlled by an acquisition routine implemented on a computer (discussed in the technical report [208]). The switch system enables voltage measurement across different channels without a need to swap cables manually. The four thermocouples are connected to the multiplexer card which initiates and measures the sample temperature (on the surface). The sample temperature is measured by a digital multimeter (DMM) in the form of a voltage signal using the thermocouples on the sample surface. The DMM is also connected to the multiplexer card and acquisition computer. During acquisition, the measurement routine commands the DMM to measure voltages and temperatures. Besides, the measurement routine also commands the LIA to supply current. The channels for measuring voltage are closed with the help of multiplexer card while the matrix card closes channels for supplying current. The analog signals are converted into digital signals by an analog-to-digital converter in the multimeter. The magnetometer is also connected to the DMM, and its probe is used for measuring the magnitude of B-field at the pole cap during the measurement. As mentioned earlier in 5.4.1, the magnetometer is used for calibration but not utilized permanently in the Hall facility.

5.4.8 Electrical connections

The electrical connections are visualized in Figure 5.2(b), and in more detail in Figure A.1 of Appendix A. The control computer is connected to the power supply of the electromagnet *via* an RS 232 interface, which enables the program to set current on the power supply to achieve a desired magnitude of B-field. The Eurotherm® is connected to the computer *via* an RS 485 interface. The thermocouples at the sample holder are connected to the switch system. When a measurement is initiated or executed, the switch system commands the DMM card to make a voltage measurement across closed channels on the multiplexer which correspond to a particular configuration. The switch system and the DMM are connected to the computer *via* daisy chain method using an IEEE 488 interfacing. In network communication, daisy-chaining is one of common methods of signal propagation along a network. In such method, the components are connected in series [219, 220]. The LIA is connected to the computer *via* a RS 485 interface.

5.5 Geometric correction factors

The necessity of the correction factor arises from the fact that the measurement probes are positioned not exactly at the edge of the sample, as shown in Figure 5.3. The GCF for the calculation of R_{H} was derived by van der Pauw and is given by Equation (5.3). The measured and the true (or real) R_{H} are related by Equation (5.4) [210]:

$$GCF_{R_{\mathrm{H}}} = \frac{\Delta R_{\mathrm{H}}}{R_{\mathrm{H,real}}} = \frac{-8a}{\pi D} \qquad \text{Equation (5.3)}$$

$$\Delta R_{\mathrm{H}} = R_{\mathrm{H,meas}} - R_{\mathrm{H,real}} \qquad \text{Equation (5.4)}$$

This expression shows that $GCF_{R_{\mathrm{H}}}$ depends on the probe to edge distance (a) and the diameter D of specimen. The probe-to-edge distance 'a' is further expressed as: $a = (D - 8.2)/2$, where 8.2 (in mm) is the diagonal distance between two thermocouples. Note that non-ideal contacts lead to a small R_{H} value, and therefore this factor overcomes discrepancy due to this contact configuration. The final equation can be expressed as: $R_{\mathrm{H,real}} = R_{\mathrm{H,meas}}/1 + (-8a/\pi D)$. Another geometric correction factor, GCF_{σ}, corresponding to measured conductivity signals, is also required because of the same stated reason that leads to a deviation in the measured value (σ_{meas}) from the true (or real) value (σ_{real}). In a van der Pauw configuration, the relative deviation is given as $\Delta\sigma/\sigma_{\mathrm{real}}$. The true value can be determined after plugging Equation (5.6) in Equation (5.5) [210, 221]:

$$GCF_{\sigma} = \frac{\Delta\sigma}{\sigma_{\mathrm{real}}} = \frac{-2a^2}{D^2 \ln(2)} \qquad \text{Equation (5.5)}$$

$$\Delta\sigma = \sigma_{\mathrm{meas}} - \sigma_{\mathrm{real}} \qquad \text{Equation (5.6)}$$

The true value of conductivity can be expressed as: $\sigma_{\mathrm{real}} = \sigma_{\mathrm{meas}}/1 + (-2a^2/D^2 \ln(2))$. This expression is utilized in the program that automates the data analysis.

5.6 Measurement acquisition routine

The acquisition routine measures voltage (both U_{H} and U_{σ}) drop on the sample (output voltage signals), detects currents driven through the sample, temperature readings etc. The user supplies desired measurement parameters on the graphical user interface (GUI) of the acquisition routine. Some of the relevant parameters are: temperature steps, B-field: number of points in a specified range (from -0.5 T to $+0.5$ T), number of sweep cycles (one sweep refers to a variation of magnitude of B-field (from -0.5 T to $+0.5$ T)), and thickness (d) and diameter (D) of the samples etc. for R_{H} and σ measurements. The program also computes electrical conductivity values using corresponding voltage and current values that are measured and supplied respectively.

The raw data output files are later utilized for the analysis of the measured signals. The acquisition routine is scripted in MS Visual Basic which was developed by ex-colleague Dr. Gabriele Karpinski and later updated by Dr. Hendrik Kolb. A detailed description of the data acquisition routine is given in the technical report [208].

5.7 Data analysis routine

A data analysis routine was developed for the analysis of raw voltage signals (both U_{H} and U_{σ}). A detailed description of the data analysis routine is given in the technical report [208]. Broadly, for the analysis, the program files are copied in the folder containing the raw data files. The code/name of the measured specimen is a necessary input to the central routine program code (named 'Hall Program') to run the analysis. The main function of the data analysis routine is to sort raw signals, check for inconsistencies and filter such signals out, out of which some aspects are discussed in the coming section. The true values of the Hall coefficient and the electrical conductivity are calculated (by the program) from the filtered raw signals after employing the values of $GCF_{R_{\mathrm{H}}}$ (Equation (5.3)) and GCF_{σ} (Equation (5.5)). The data analysis software is designed and scripted in MATLAB® by the author of this thesis. This program was developed for a time-efficient analysis of the raw signals to deduce the transport properties for ≥ 100 samples (from the author and department colleagues) throughout the Ph.D. work.

A constant set of measurement conditions were implemented for the Hall measurements at the presented facility. During the measurement, the magnitude of B-field is varied between -500 mT to $+500$ mT at an interval of 250 mT. The voltage signal is measured at five different values of the magnitude of B-field i.e. -500, -250, 0, $+250$, $+500$ mT, and back (which is referred to here as a sweep cycle). So, each sweep cycle has two sweeps. Therefore, in total, the voltage measurement is measured in ten (10) sweep cycles at each temperature point, and the total number of sweeps are $n = 20$. Furthermore, the voltage signals are measured twenty times at each value of the magnitude of B-field. This routine is followed for the measurement at one or more temperature points. During the data analysis, briefly, these twenty voltage values are averaged out at each magnitude of B-field which gives five values of voltages, each corresponding to one value of the magnitude of B-field (e.g. $+250$ mT) in a sweep of a sweep cycle. In principle, the five values (each corresponding to one value of magnitude of B-field) should follow a linear trend, which is expected on varying the magnitude of B-field (as explained in the coming sub-sections). These voltages U_{H} are linearly fitted with respect to a change in the magnitude of B-field to determine slope, $\left(\frac{\partial U_{\mathrm{H}}}{\partial B}\right)$, which is plugged in the equation expressed in section 5.3.2, to calculate the Hall coefficient. The aforementioned text gives a

brief overview of the acquisition routine and the data analysis routine that gives a necessary base for a clearer understanding of the discussion in the upcoming sections.

5.8 An assessment of the quality and reliability of the Hall coefficient measurements

An evaluation of raw signal quality is a necessary step to obtain reliable transport properties. In this section, these aspects are discussed for the measurement signals corresponding to the Hall coefficient. On the other hand, the electrical conductivity measurements had some issues before the extension of the HT Hall facility for high temperature operations. Specifically, σ values (at RT) measured at the HT-$S\sigma$ and HT Hall facilities showed a large relative deviation ($\geq 50\ \%$) with lower values measured at the HT Hall facility. In this regard, a variety of experiments were conducted that led to the main reason for the observed discrepancy in the electrical conductivity values. The details of each experiment, the results and the corresponding interpretation is discussed in the technical report [208]. Finally, the issues were identified and resolved which lowered the relative deviation between the electrical conductivity values measured at the HT-$S\sigma$ and HT Hall facilities to $\mathrm{R.D.} \leq 8\ \%$, as discussed in the coming sections.

5.8.1 Hall voltage – ideal and real measurement

A change in the measured Hall voltage with a change in the magnitude of B-field, both as a function of time is shown by the means of a 2Y-plot, which is visualized in Figure 5.4(a) and Figure 5.4(b). The data corresponding to a change of the Hall voltage with the change in the magnitude of B-field is extracted for further analysis (as described in the last paragraph of the previous section). The extracted data is shown in Figure 5.4(c) and Figure 5.4(d) which enables to make a preliminary conclusion about the quality of the measurement signal. Particularly, a change of the Hall voltage U_{H} signal with respect to the variation in the magnitude of B-field should be linear. A linear fitting of the Hall voltage U_{H} versus the magnitude of B-field gives the slope. This slope is obtained for each sweep at each temperature point which is utilized for the calculation of the Hall coefficient R_{H}. Besides, the variation of the magnitude of B-field from negative to positive and back to negative should in principle, decrease (increase) to increase (decrease) and decrease (increase) the Hall voltage. The measured voltage signal is displayed on the lock-in amplifier (LIA).

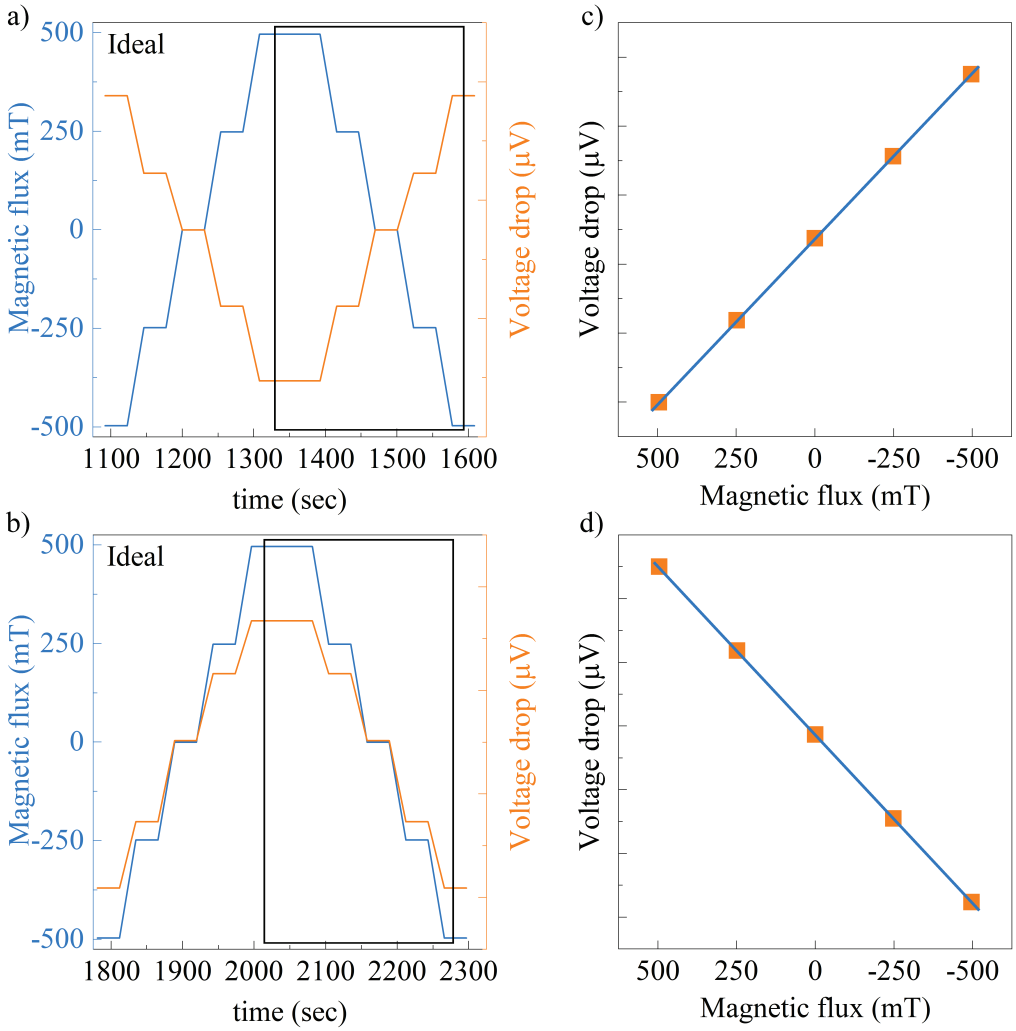

Figure 5.4 Schematic change of the Hall voltage U_H with a change in the magnitude of B-field with respect to time t, with the direction of voltage drop in a) one direction, and b) in other direction. Note that the direction of voltage drop depends on the phase difference between the measured and the reference signal, explained in detail in relevant section below. c) & d) show U_H as a function of the magnitude of B-field from the black rectangular box in a) and b), respectively. Note that the U_H data shown here is synthetic data which is referred to as ideal.

Note that LIA extracts and displays only those signals (from the measured voltage), which have the same frequency as the reference signal. Besides this, the phase between signals must not change with time as it will influence the measured signal (and the signal amplitude displayed on the LIA). LIA maintains a constant phase difference between the measured and the reference signal. LIA uses a phase-locked loop that locks the phase of the reference signal to the phase of the measurement signal, and this loop also ensures that the phase shift is always constant [222]. The phase of the reference oscillator can be tuned by the user manually as well. An automated phase difference set by the LIA affects the sign (+ or −) of the amplitude of the

signal displayed. This is exemplified by the two types of ideal signals that are shown in Figure 5.4(a) and Figure 5.4(b). Here, the voltage drop has a positive or a negative slope because the LIA found a phase difference between the measured voltage signal and the reference oscillator signal (current) near 0° or 180° respectively. And so, the voltage drop shows either an increase or decrease with respect to the magnitude of B-field.

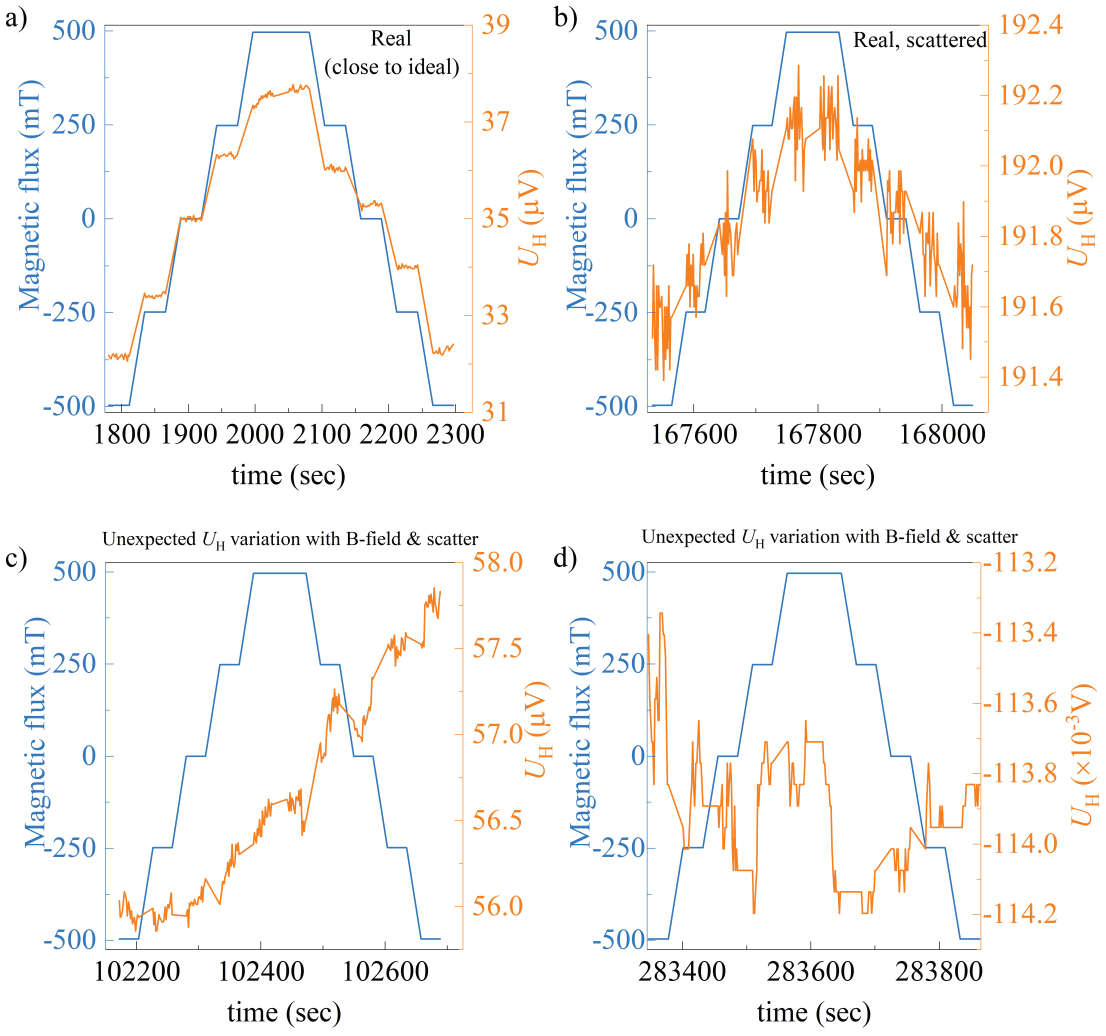

Figure 5.5 2Y-plots showing a change of U_H and the magnitude of B-field with respect to time t. The plots show a) real (close to ideal), b) real (scattered) conditions while c) and d) show poor signal output with respect to change in the magnitude of B-field.

As said, the LIA is based on the principle of phase sensitive detection (PSD) which ensures that the signal is not lost in the interfering signals. The LIA filters the signal using a reference frequency and phase, thus, ignoring other signals. Therefore, ideally, the magnitude of U_H at a

particular magnitude of B-field should remain constant as shown by the illustration in Figure 5.4(a) and (b). However, the recorded signals are mostly not ideal and, in some cases, quite far from ideal. The raw signals can be correspondingly roughly classified based on two aspects, first, the scatter (low or high) in voltage signal at a particular magnitude of B-field, and second, whether the variation in voltage signal due to the varying magnitude of B-field is linear or not. For one's understanding the classification as a good signal (close to ideal or scattered) or a poor signal can be exemplarily visualized in Figure 5.5. The good signals can be observed to vary in a manner, which is similar to the ideal signals but with some degree of scatter compared to the ideal signals at each magnitude of B-field. The poor signals, on the other hand, are qualitative different from the expectation and change partially non-systematically with the varying magnitude of B-field, as shown in Figure 5.5(c) and Figure 5.5(d). The probable reason for poor signal quality can be at the specimen level or the measurement system level or at times both. Note that in the Figure 5.4 and Figure 5.5, only one sweep cycle is shown to highlight the issue of signal quality and reliability. However, the measurement is performed usually by selecting multiple sweep cycles to obtain statistically robust slope values from the raw signals and correspondingly reliable R_{H} values.

5.8.2 Error indicators

In the previous section, some preliminary analysis was shown in order to assess the quality of measurement. Besides observing the raw signals, other parameters are quantified which are useful in recognizing issues related to U_{H} measurement. These indicators are the Hall voltage at zero magnitude of B-field ($B = 0$ T), $U_{\mathrm{H},B=0}$, the correlation coefficient $R_{\mathrm{C.C.}}$ and the standard deviation of the slope values $s\left(\frac{\partial U_{\mathrm{H}}}{\partial B}\right)$. $U_{\mathrm{H,B=0}}$ is actually expressed as $(U_{\mathrm{H,B=0}})_{\mathrm{T}} = \frac{1}{i}\sum_1^i U_{\mathrm{H,B=0}}$, where $U_{\mathrm{H,B=0}}$ is the measurement value at $B = 0$ T for each sweep of the magnitude of B-field, indexed by i and T is the measurement temperature. The correlation coefficient $R_{\mathrm{C.C.}}$ is the degree of association between two variables, which here are U_{H} (dependent (on B) variable) and the magnitude of B-field (independent variable) [223]. $R_{\mathrm{C.C.}} = \pm 1$ or the values close to unity shows that the U_{H} and B are well correlated while the values deviating away from these values reflect poor correlation. $s\left(\frac{\partial U_{\mathrm{H}}}{\partial B}\right) = \sum_{i=1}^{n} \left|\frac{\partial U_{\mathrm{H}}}{\partial B} - \mathrm{M}\right|^2 /(n-1)$ is the standard deviation of the slopes ($\frac{\partial U_{\mathrm{H}}}{\partial B}$), and their mean (M), $\mathrm{M} = \frac{1}{n}\sum_{i=1}^{n}(\frac{\partial U_{\mathrm{H}}}{\partial B})_i$, and here, n = number of slope values corresponding to each sweep (at each temperature point). $s\left(\frac{\partial U_{\mathrm{H}}}{\partial B}\right)$ is computed after each filtering step in the data analysis program, as described in detail in the technical report [208].

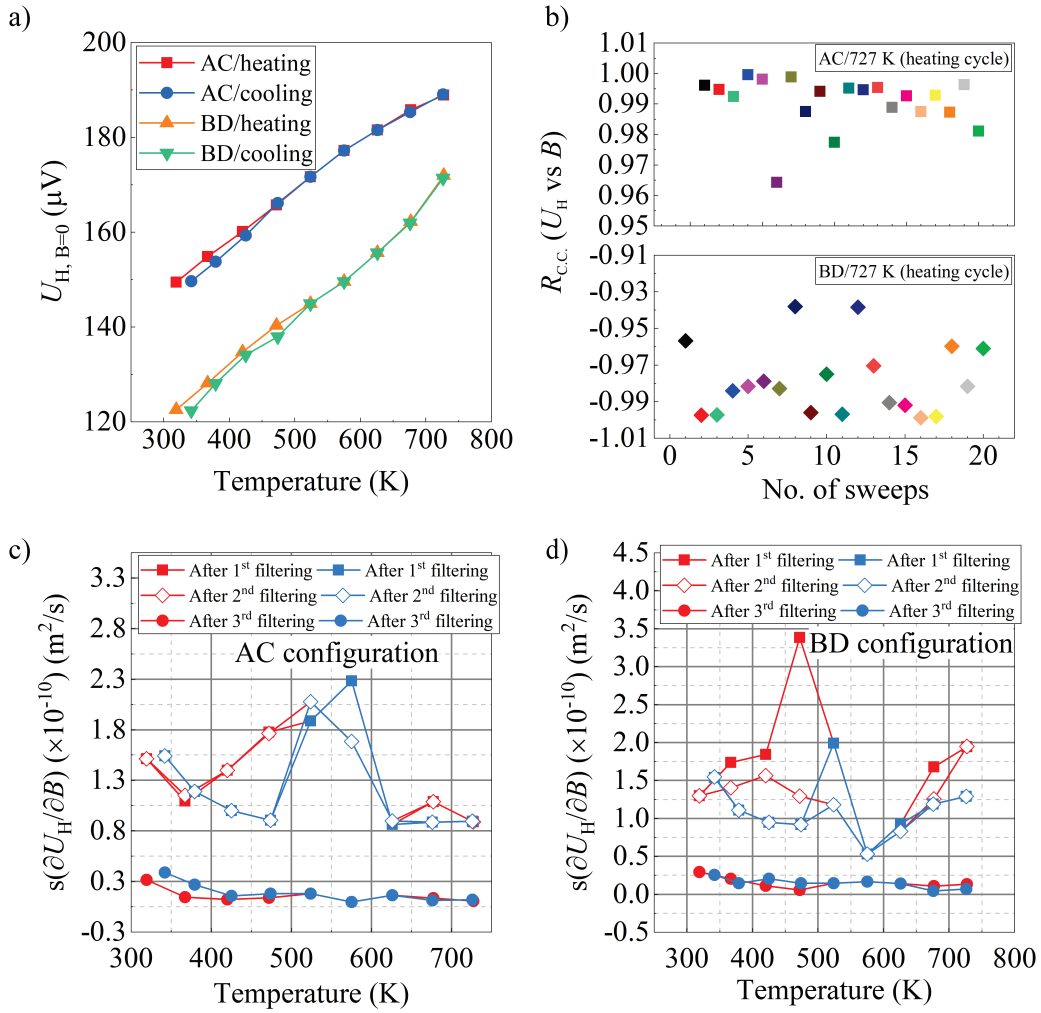

Figure 5.6 a) $U_{\mathrm{H},B=0}$, b) $R_{\mathrm{C.C.}}$ of U_{H} and B, and the c) $s\left(\frac{\partial U_{\mathrm{H}}}{\partial B}\right)$ ($\approx 10^{-10}$) across AC and BD configurations. The standard deviation is calculated after each filtering step (elaborated in the technical report [208]) of the data analysis program. The red and the blue data points in (c) and (d) correspond to heating and cooling temperatures respectively.

The $U_{\mathrm{H,B=0}}$ should ideally be zero since the U_{H} measurement probes (which are perpendicular to the current I flow) should lie on a line of symmetry. However, due to a non-ideal positioning of the thermocouple probes, a small signal is measured even at $B = 0$ T, which can be observed from different sweeps in Figure 5.5(a) and Figure 5.5(b). This anomaly is used here as an error indicator to check if the measurement runs as expected or not, particularly, an abrupt change in $U_{\mathrm{H},B=0}$ at any temperature point can be indicative of a problem with the measurement. The $U_{\mathrm{H},B=0}$ is shown in the Figure 5.6(a) for a T-dependent measurement (discussed in detail in section 5.9.2) on a p-type $FeSi_2$ specimen. $U_{\mathrm{H},B=0}$ increases with increasing measurement temperature. This agrees with the behavior of a typical doped semiconductor, for which the resistivity of material increases with increasing temperature.

Besides, the $R_{\text{C.C.}}$ between U_{H} and the magnitude of B-field is also plotted to observe the quality of the obtained slopes. In particular, the values close to ± 1 show a good correlation, and values towards zero show poor correlation. $R_{\text{C.C.}}$ is also utilized in one of the filtering steps to efficiently filter out the slope values that show a value lower than 0.90 (please refer to the technical report [208]). This coefficient is particularly helpful to sort out slopes corresponding to bad signal sweeps and use relatively good signals for analyzing the data since not always all sweeps are bad.

The standard deviation, $s\left(\frac{\partial U_{\text{H}}}{\partial B}\right)$, is another statistical parameter that is utilized as an error indicator. The slope values of heavily doped semiconductor specimens have been usually observed to be of the order of 10^{-9} or lower (in m^2/s). The calculation of slope corresponding to each sweep, the mean and standard deviation corresponding to the Hall voltage measurement at each temperature point is briefly described in the last paragraph of the previous section. $s\left(\frac{\partial U_{\text{H}}}{\partial B}\right)$ is calculated thrice in the data analysis routine to observe the changes in the order and its magnitude as shown in Figure 5.6(c) and Figure 5.6(d). The $s\left(\frac{\partial U_{\text{H}}}{\partial B}\right)$ is computed, first, immediately after the linear fitting of U_{H} versus the magnitude of B-field, and the rest are calculated each after subsequent filtering steps. A detailed description of different filtering steps together with the flowcharts of the sub-functions where these filtering steps have been implemented are provided in the technical report [208].

5.8.3 A Comparison of the measurements of the Hall coefficient and the electrical conductivity at room temperature

The Hall coefficient and electrical conductivity values of a few specimens (both p- and n-type $Mg_2(Si,Sn)$) were measured on the presented Hall facility (at RT). The stoichiometry of these specimens is listed in Table 5.1. Note that the p-type specimens (Li-doped) were prepared using induction melting and the n-type specimen (Sb-doped) was prepared using MA and the DSP.

Table 5.1 Sample code and composition for the specimens measured at different facilities.

Sample code	Composition
1	$Mg_{1.96}Li_{0.04}Si_{0.2}Sn_{0.8}$
2	$Mg_{2.05}Li_{0.04}Si_{0.2}Sn_{0.8}$
3	$Mg_{2.06}Li_{0.04}Si_{0.2}Sn_{0.8}$
4	$Mg_{2.07}Li_{0.04}Si_{0.2}Sn_{0.8}$
5	$Mg_{2.06}Si_{0.385}Sn_{0.6}Sb_{0.015}$

The Hall carrier concentration is calculated from the Hall coefficient using the expression: $|R_H| = \pm 1/n_H e$, which is a reasonable assumption at room temperature for this class of materials. The sign of R_H depends on the transport of the type of carriers (electrons or holes). The room temperature transport properties of these samples were also measured on other Hall facilities at the Department of Metallurgical Engineering and Materials Science, IIT Bombay, India and the Department of Experimental Physics, JLU Gießen, Germany. The transport properties measured at different facilities were compared (Figure 5.7(a) and Figure 5.7(c)) to quantify the measurement uncertainty and to test the reliability of measurement.

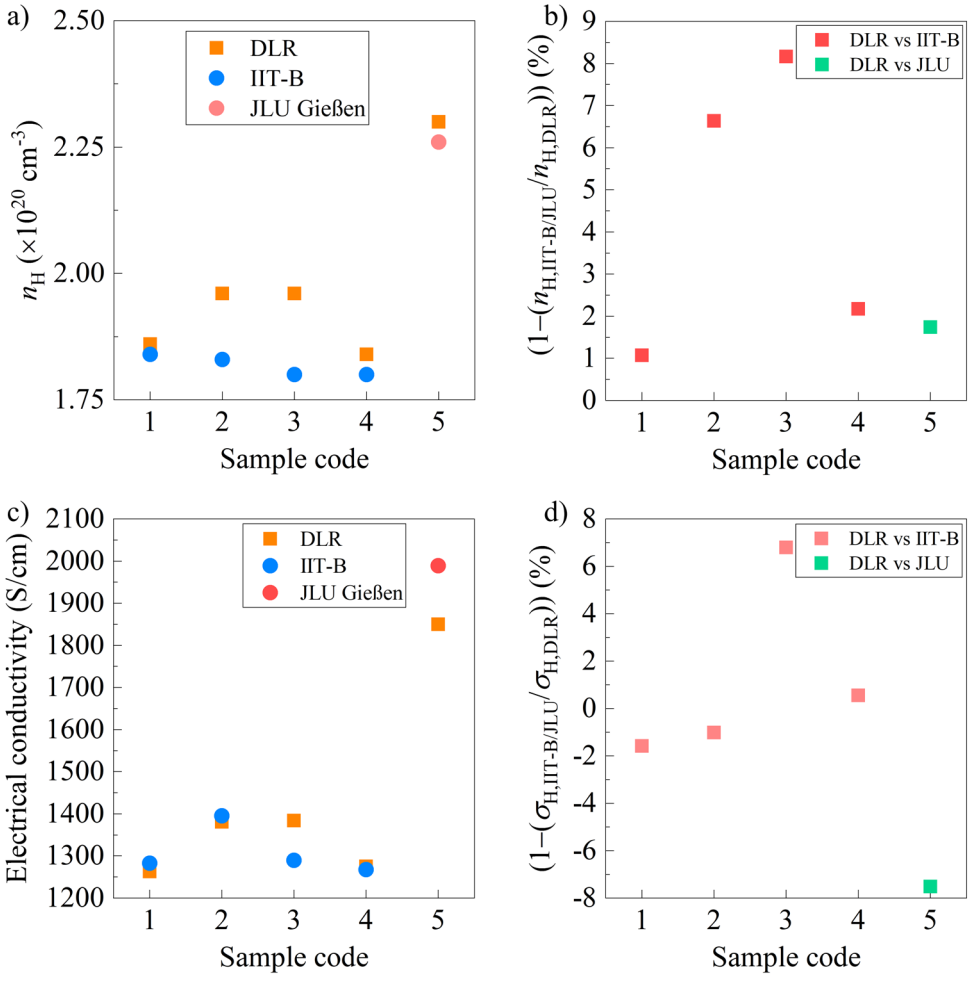

Figure 5.7 RT a) Hall carrier concentration & c) electrical conductivity of five different samples (both p-type and n-type) measured on the Hall facilities at DLR, IIT Bombay and JLU Gießen with van der Pauw configuration of the sample holder, and the corresponding relative deviation in b) n_H & d) σ measurement. Note that the n_H and σ measurements were carried out at relatively low temperature ($T \approx 277$ K) in the Hall facility at JLU Gießen.

The comparison shows that both n_H and σ values are in good agreement with a relative deviation of $< \pm 8$ % (Figure 5.7(c) and Figure 5.7(d)). A relative deviation of $< \pm 2$ % was found between the n_H values of heavily doped $Mg_{2.06}Si_{0.385}Sn_{0.6}Sb_{0.015}$ specimen, which was measured on the facilities at DLR and JLU. Comparing the results obtained from different measurement systems is reasonable since the sample holder of each of these setups is based on the van der Pauw method. Nevertheless, beyond the van der Pauw geometry of sample holder, other sample holder geometries should also give same results. The facility at IIT Bombay utilizes an electromagnet that generates a maximum magnitude of B-field of $B = \pm 0.6$ T and the measurement utilizes a DC current unlike the presented DLR facility, which utilizes an AC measurement signal. The in-house developed Hall facility at the JLU works in the temperature range between 1.5 K -277 K with a maximum magnitude of B-field of 10 T, and therefore, the measurement of n_H and σ is at a lower temperature (~ 277 K) instead of 300 K (RT). The carrier concentration of n-type Mg_2(Si,Sn) materials does not fluctuate between the range of 277 K (JLU facility) and 300 K (DLR facility) [83, 224, 225]. Due to this fact, the comparison of Hall carrier concentration n_H data measured at both facilities is feasible. The room temperature electrical conductivity value of n-type specimen nevertheless shows an observable deviation on comparison. For this specimen, a higher value of conductivity is measured at the JLU facility. A lower value of conductivity measured the Hall facility at DLR is not unexpected as the carrier scattering increases with temperature. This is observed, especially for Mg_2(Si,Sn) materials, as shown in Figure 5(b) of Chapter 8. A linear extrapolation of the temperature dependent electrical conductivity data (300 K – 419 K) to 277 K leads to a decrease in relative deviation from 7.5 % to 5.3 %. A temperature dependent electrical conductivity plot (1.5 K – 773 K) for this n-type sample is shown in Figure A.3 of Appendix A. The Hall carrier concentration is constant for heavily doped semiconductors, so, any variation in temperature will lead to a change in the electrical conductivity.

5.9 Results and discussion

A dimensionless parameter that corrects the measured values, which are often different from true values owing to differences in the probe positioning with respect to the sample geometry, is called geometric correction factor. In this section, the validity of geometric correction factor is investigated by comparing the experimental and simulated Hall voltages. Note that the Hall voltages were measured at different probe positions in a simulation environment. Lastly, a temperature dependent reference measurement of the Hall coefficient and the electrical conductivity is discussed.

5.9.1 Utilizing GCF equations and their validation

The arrangement of thermocouple probes for the measurement of the Hall coefficient and the electrical conductivity is shown in Figure 5.3(c). In case of the specimens with larger diameter ($D \geq 11$ mm), these probes do not lie exactly on the edges but only close to the edge. Therefore, the utilization of the generic equations of the Hall coefficient and electrical conductivity (expressed in section 5.3.2 and Equation (5.1)) will lead to a deviation between the calculated and the real values. Thus, van der Pauw gave a set of equations (GCF) accounting for the inconsistencies in the measurement of each transport property due to the specimen geometry. The GCF for computing real values of the Hall coefficient and electrical conductivity are expressed in Equation (5.3), Equation (5.4), Equation (5.5) and Equation (5.6), respectively. The corrected value of the Hall coefficient depends on the GCF (Equation (5.3)), which is implemented in the data analysis routine. It is not clearly known whether the GCF is applicable for all the values of probe-to-edge distance (a) or when does the implicit assumptions used to derive the given expression breaks down. The relative offset, a/D, is a crucial parameter for the GCF, therefore, GCF obtained by using Equation (5.3) was validated by simulating the measurement. The FEM software ANSYS, Inc. (versions 19.1) with the mechanical APDL module has been utilized for simulating the experimental environment, and measuring the Hall voltage U_{H} under the influence of an applied magnitude of B-field. The simulation part was carried out by Dr. Prasanna Ponnusamy, who was a Ph.D. colleague in the department at DLR, while the interpretation of the results of the simulation was done by the author of this thesis.

For the modelling of the Hall voltage U_{H} using ANSYS, a van der Pauw arrangement of four probes was constructed, which is similar to the sample holder in the present facility (Figure 5.8(a)). The Hall voltage U_{H} was obtained by applying the current on two probes under a magnetic field magnitude of $B = 0.8$ T. The model was tested with a value of $B = 0$ T which resulted in an output voltage of $V = 0$ V. The sample thickness was kept constant with a value $d = 1$ mm. The effect of sample thickness on the resistivity measurements in a van der Pauw geometry was studied by Kasl *et al*. [226]. They concluded that top/bottom contacts in combination with a finite sample thickness d lead to significantly incorrect measurements when thickness is $2d \geq D$, whereas in our experiments, the samples thickness is low, in the range $10d \leq D \leq 5d$. It can be therefore argued that the effect of sample thickness in our case is negligible and so, the effect of using a sample thickness different than that of an actual sample can be ignored. Besides, note the difference in the (initial) modelling arrangement and the sample holder of the current Hall facility (Figure 5.3(c)). Particularly, in the beginning of the

simulation, the probes are fixed at the edges of the sample to determine the real values of the Hall coefficient R_H. In the later stages of simulation, the probe positions are varied, which is explained in the later part of this section. Under an applied magnitude of B-field, the Hall voltage U_H is measured by two thermocouples probes as shown in the Figure 5.8(a). The probes for passing current I signals during the simulation are on the opposite surface of the specimen (not shown in Figure 5.8(a)). The corresponding schematic of the position of different probes on the specimen is shown in Figure 5.8(b). The applied magnitude of B-field is perpendicular to the specimen and the direction of the flow of current through the specimen.

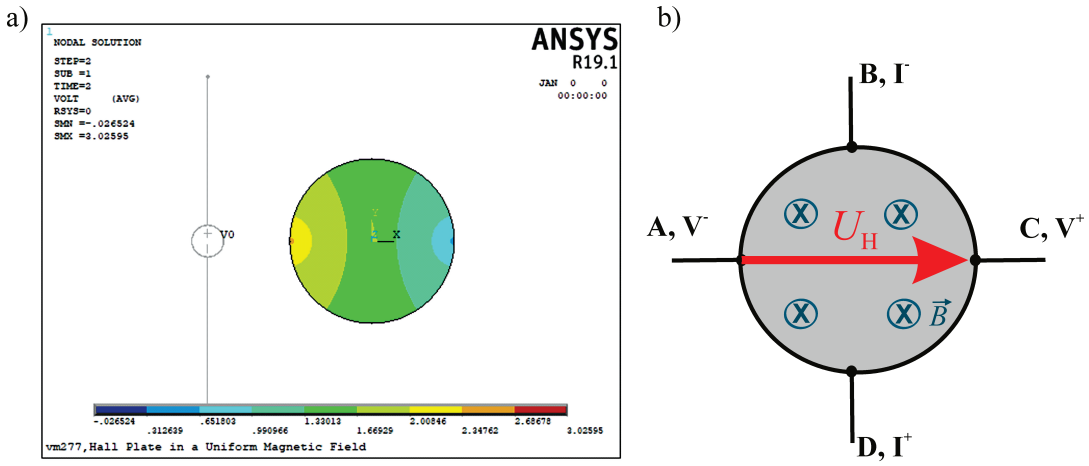

Figure 5.8 a) Construction of the model in ANSYS, Inc. for a FEM of the sample holder with the color indicating the potential field forming U_H, (b) a schematic to show the position of the probes and the direction of B-field.

For the given cylindrical geometry, Hall voltage U_H was simulated for a material of known Hall coefficient R_H, and pre-defined values of current I and thickness d. For a constant value of current, the applied magnitude of B-field and thickness d, the Hall voltage U_H translates directly to R_H. Therefore, the $R_{H,real}$ of the material with the contacts on the edges (real case) was simulated, and it was compared with $R_{H,FEM}$, which was also simulated when the contacts are off from the edge (non-ideal case). For a comparison with the GCF derived by van der Pauw [210], Equation (5.3) can be re-expressed here: $GCF_{R_H} = \frac{\Delta R_H}{R_{H,real}} = \frac{-8}{\pi}\left(\frac{a}{D}\right)$, where $\Delta R_H = R_{H,meas} - R_{H,real}$. Note that van der Pauw [210] has used this expression for the correction of the Hall coefficient R_H considering the individual shift of each probe i.e. $GCF = \frac{-2}{\pi}\left(\frac{a}{D}\right)$, while here, a shift of all four probes is considered, which is representative of the sample holder design. Here, a and D are related to each other due to fixed probe positions, i.e. a is directly influenced by a chosen value of diameter D, and a variation of the relative offset, $\frac{a}{D}$, can lead to a

discrepancy in the R_H values. Therefore, the ratio of $R_{H,meas}/R_{H,real} = 1 + (-8a/\pi D) = P$, and the ratio $R_{H,FEM}/R_{H,real} = Q$ are calculated. Note that Q is computed after obtaining the respective values by FEM simulation. Both P and Q are compared to investigate the validity of the equation of GCF reported by van der Pauw [210]. For comparison, in one case, the ratio $\frac{a}{D}$ is varied symmetrically, which means that all four probes were uniformly varied to obtain $R_{H,FEM}$. Whereas, in the other case, the ratio $\frac{a}{D}$ is varied asymmetrically. An asymmetric variation means that the ratio $\frac{a}{D}$ for only one of the probes was varied while for the other three probes, this ratio is kept constant ($\frac{a}{D} = 0.01$). For this case, e.g. the ratio of R_H can be re-expressed as: $R_{H,meas}/R_{H,real} = 3\frac{-2}{\pi}(0.01) + \frac{-2}{\pi}\left(\frac{a}{D}\right)$, where $\frac{a}{D}$ is varied. The symmetric and the asymmetric cases, and the corresponding change in the relative offset to determine the ratio are shown in Figure 5.9(a) and Figure 5.9(b), respectively. Besides, the discrepancy in R_H (corrected using the traditional GCF equation and the ANSYS simulated values) is deduced by computing relative deviation $\text{R.D.}\% = (P - Q)/P$.

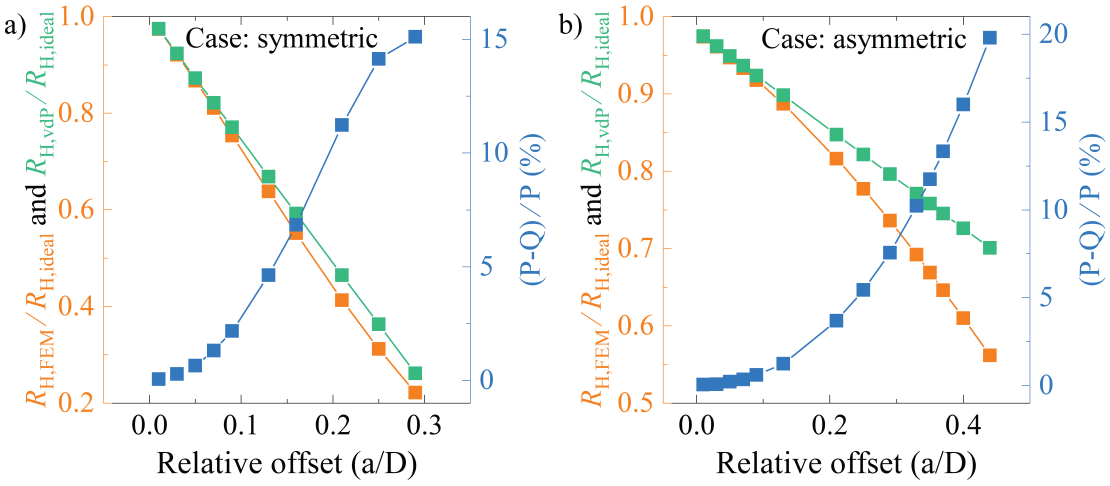

Figure 5.9 P and Q with respect to (a/D) for a) symmetric and b) asymmetric case. The relative deviation between P and Q for the respective cases is shown in blue.

The results show that Q deviates from P as the value of $\frac{a}{D}$ increases and this deviation makes the correction factor proposed by van der Pauw (expressed in Equation (5.3)) less accurate. Particularly, considering a sample diameter $D = 12.7$ mm, and $a = 2.25$ mm, which corresponds to the present sample holder, the relative offset comes out to be $\frac{a}{D} \approx 0.135$. Figure

5.9(a) shows that for $\frac{a}{D} \approx 0.135$, the (relative) deviation $\mathrm{R.D.} > 5\ \%$. Considering this value (of $5\ \%$) as the limit of the deviation, the usage of GCF proposed by van der Pauw is less reliable for $\frac{a}{D} > 0.135$ and $\frac{a}{D} > 0.241$ for the symmetric and asymmetric case, respectively. Moreover, P (van der Pauw expression) is higher in magnitude compared to Q (FEM validated) for all the values of $\frac{a}{D}$, and this difference is observed for both the cases (symmetric and asymmetric). For the reference measurement carried out in the temperature range from $300\ \mathrm{K} - 723\ \mathrm{K}$ (as discussed in the next section), the value of $\frac{a}{D}$ was utilized to determine the relative deviation between the Hall coefficient calculated from the van der Pauw derived GCF and the FEM calculated values. The FEM corrected value of GCF was employed to calculate the Hall coefficient. Besides, the FEM computational modelling can get affected due to chosen computational parameters (meshing, probe diameter etc.). Particularly, a discrepancy in the calculated values of P and Q while optimizing FEM simulation was observed. Therefore, to neglect the effects of simulation parameters that could lead to inaccuracies in the output values, the probe diameter was kept constant with $D = 0.02$ mm, and a converged meshing was used in the mechanical APDL module.

A validation of the geometric correction factors related to the determination of true values of electrical conductivity should, in principle, be performed. Nevertheless, the values of electrical conductivity measured in the setups employing different measurement principles and equations for calculating it, has shown small error uncertainty (at room temperatures and high temperatures, discussed in the next section). Therefore, the need of a validation of corresponding factors was less and thus, not performed.

5.9.2 A comparison of the measurement of the Hall coefficient and the electrical conductivity on a reference specimen at high temperatures

The temperature dependent measurement of the Hall coefficient and the electrical conductivity was simultaneously carried out in the presented setup and a Hall facility at the Department of Chemistry, Aarhus University, Denmark [211]. Each of these measurements were compared and the accuracy of the Hall measurement setup was examined. For this purpose, a p-type β-$FeSi_2$ sample was utilized. The temperature dependent thermoelectric properties (S, σ and R_H, σ) of p-type β-$FeSi_2$ sample is visualized in Figure A.4 and Figure A.5 of Appendix A. β-$FeSi_2$ was chosen because it has been recently shown [197, 198] that this material fulfills the criterion of a high temperature reference material for the Seebeck coefficient measurement, which is related to R_H, as discussed in section 2.2.4.

5.9.2.1 Hall coefficient

The temperature dependent Hall coefficient measured in both setups and the relative deviation between the measured data are shown in Figure 5.10. Note that $|R_H|$ is shown here. The measured values showed a good agreement with an overall relative deviation of R. D. ≤ 8 %. The Hall coefficient value calculated using GCF (given by van der Pauw, Equation (5.3)) led to a relative deviation of R. D. ≈ 6.3 % lower compared to the values computed by utilizing FEM simulation corrected GCF. In relation to $Q(= 0.5815)$, $P(= 0.6206)$ is over-estimated, which is a major cause of observed deviation. This allows for a correction of the values obtained from P with Q, which led to a better agreement between temperature dependent transport properties obtained from the DLR setup and the Aarhus setup as shown in Figure 5.10(a).

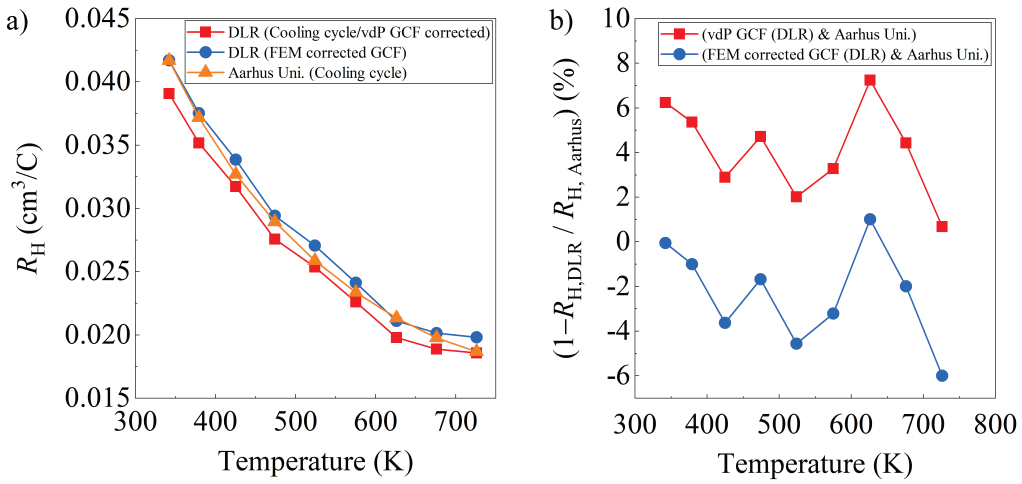

Figure 5.10 T-dependence of a) R_H and b) relative deviation in the measurement. The red and blue curve in sub-figure (b) shows a relative deviation $(1-(R_{H,DLR}/R_{H,Aarhus}))$ between the R_H measured at the HT Hall setup at DLR (with GCF according to van der Pauw's original work and the improved FEM derived values) and Aarhus University, respectively.

Note that the comparison between R_H calculated after correcting the GCF (by FEM simulation) and the data measured on the Aarhus setup holds legitimate since the Aarhus setup has the measurement probes exactly at the sample edges [211], which do not need a correction of the geometry unlike the DLR setup. The agreement in the absolute values gets better, which can be observed by a lowering of the relative deviation. This means that the values measured at the present setup are close to the true values of the Hall coefficient. Besides, the comparative RT measurements shown in Figure 5.7 of the sub-section 5.8.3 have also been corrected by using

FEM corrected GCF, and the new results are shown in Figure A.2 in the section A.2 of Appendix A. The relative deviation between the RT Hall carrier concentrations is also lowered.

5.9.2.2 Electrical conductivity

The temperature dependent electrical conductivity of the same sample (p-type β-$FeSi_2$) was measured simultaneously (along with R_H) in the Hall facilities at the Aarhus University and DLR (Figure 5.11).

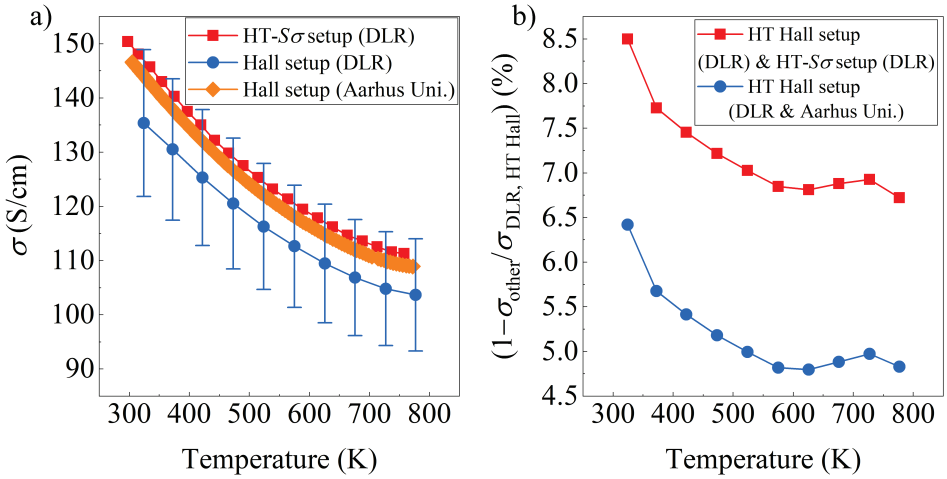

Figure 5.11 Temperature dependent a) electrical conductivity measured on HT-$S\sigma$ setup, Hall setup at DLR and Aarhus University, respectively, and b) relative deviation $(1-(\sigma_{others}/\sigma_{DLR,HT\ Hall})$ between the measurement data conducted at different (HT-$S\sigma$ and Aarhus University) facilities.

The electrical conductivity of this sample was also measured at HT-$S\sigma$ setup, and compared with the conductivity data measured on other two facilities, as shown in Figure 5.11. The temperature dependence of electrical conductivity values measured on each stated facility is identical. The relative deviation (Figure 5.11(b)) in the data obtained from the DLR HT Hall facility and HT-$S\sigma$ facility lies between $6\,\% - 8\,\%$. The relative deviation between the electrical conductivity data measured on the HT Hall facility at DLR and Aarhus University is even lower ($4\,\% - 6\,\%$). Note that the relative deviation between the measurement data was calculated by fitting the HT-$S\sigma$ data and Aarhus University data by a 3rd order polynomial equation.

Therefore, the overall relative deviation in the Hall coefficient and the electrical conductivity measurements using the Hall facility at DLR and other facilities is $R.D. < 8\,\%$.

5.10 Conclusion

A pre-existing facility to simultaneously measure the Hall coefficient (R_{H}) and electrical conductivity (σ) was extended to operate at higher temperatures (300 K – 723 K). The facility is based on the van der Pauw (vdP) method which is discussed in detail. The details of the measurement acquisition routine and the data analysis routine are briefly discussed. The data analysis routine was developed to automate the analysis of the measured signals. This routine has the ability to handle the signals with relatively poor quality as well. The slopes ($\partial U_{\mathrm{H}}/\partial B$) are calculated from the plot of the measured Hall voltage (U_{H}) versus the magnitude of B-field. Several error indicators are discussed which are beneficial in quantifying the errors associated with the acquired raw signals. These include the measured Hall voltage offset at zero magnitude of magnetic field, the correlation coefficient and the standard deviation of slopes.

The geometric correction factor (GCF) (proposed by van der Pauw) was validated by finite element simulations, which depicts the probe positioning in the sample holder of current facility. GCF is a function of probe-to-edge distance (a) and sample diameter (D), which is expressed as: $\frac{a}{D}$. The Hall coefficient was simulated by systematically varying $\frac{a}{D}$, particularly, the position of one (asymmetric case) or all (symmetric case) probes was varied. A ratio of the R_{H} (simulated asymmetrically and symmetrically) and real R_{H} value (also simulated by positioning the measuring probes exactly on the sample edge, real case) was computed. For the same values of $\frac{a}{D}$, these ratios were computed using the equation proposed by van der Pauw and compared with the ratios of FEM determined R_{H} values. Computed ratios were observed to deviate with increasing $\frac{a}{D}$. Considering the limit of the relative deviation of ~5 % between these 'ratios', the GCF equation (proposed by van der Pauw) is insufficient for $\frac{a}{D} > 0.135$ and $\frac{a}{D} > 0.241$ for the symmetric and asymmetric cases, respectively. Besides, a reference measurement comparing the Hall coefficient and the electrical conductivity, both at room (300 K) and high temperature range (300 K – 723 K), carried out on the presented Hall facility and other facilities (of different international research groups) showed a good agreement with a relative deviation of ≤ 8 %.

Chapter 6 Understanding the synthesis mechanism of optimized n-type $Mg_2Si_{0.4}Sn_{0.6}$ and tuning the synthesis parameters

6.1 Summary

It was mentioned in the introductory chapters (sub-section 2.3.1.3 and section 3.2) that the synthesis of high performance Mg_2X solid solutions is challenging due to several reasons such as a high vapor pressure of Mg at typical synthesis temperatures, low dopant solubility, a tendency of the precursors to oxidize, and inhomogeneity; achieving a homogeneous phase requires a prolonged treatment of precursors at high temperatures. To overcome these challenges, mechanical alloying was employed for the synthesis of these materials. The previously *unknown* mechanism of the formation of $Mg_2(Si,Sn)$ using mechanical alloying was understood. Mechanically alloyed powder was characterized at different time intervals using advanced techniques of microstructure analysis. Mg-Sn (ductile) rich matrix forms rapidly after a few hours ($1-2$ h) of milling of precursors followed by slow Si (brittle) diffusion in the ductile matrix, over a longer following period (35 h). The results show that a phase-pure material was not formed at the end of milling but powder with particles of different Si:Sn ratio was obtained. A high-temperature treatment of milled powders was necessary to achieve phase-pure samples. The effect of a variation of synthesis parameters (t_{milling}, t_{sinter} and T_{sinter}) on the TE properties was investigated as well. The carrier density (at RT) was sensitive to varying sintering parameters (both t_{sinter} and T_{sinter}), which led to observable changes in TE properties of the samples, however, these properties remain largely unaffected by varying t_{milling}. Optimized TE properties were comparable to the best reports in the literature, and finally a maximum TE performance $zT = 1.3$ was achieved for the sample sintered at $973\ \mathrm{K}/20$ min.

6.2 CRediT (Contributor Roles Taxonomy) author statement

Aryan Sankhla: Conceptualization, Methodology, Validation, Formal analysis, Investigation, Writing – original draft, Visualization. **Akash Patil:** Methodology, Validation, Investigation. **Hasbuna Kamila:** Validation. **Mohammad Yasseri:** Validation. **Nader Farahi:** Validation. **Eckhard Mueller:** Writing – review & editing, Supervision. **Johannes de Boor:** Conceptualization, Methodology, Writing – review & editing, Supervision, Project administration, Funding acquisition.

ACS APPLIED ENERGY MATERIALS
Cite This: ACS Appl. Energy Mater. 2018, 1, 531−542
Article
www.acsaem.org

Mechanical Alloying of Optimized $Mg_2(Si,Sn)$ Solid Solutions: Understanding Phase Evolution and Tuning Synthesis Parameters for Thermoelectric Applications

Aryan Sankhla,*[,†,§] Akash Patil,[†,§] Hasbuna Kamila,[†] Mohammad Yasseri,[†,‡] Nader Farahi,[†] Eckhard Mueller,[†,‡] and Johannes de Boor*[,†]

[†]Institute of Materials Research, Linder Hoehe, German Aerospace Center (DLR), D-51170 Koeln, Germany
[‡]Institute of Inorganic and Analytical Chemistry, Justus Liebig University of Giessen, D-35392 Giessen, Germany

Supporting Information

Downloaded by DLR BIBLIO INFORMATIONSWESEN at 02:13:22:204 on June 26, 2019
from https://pubs.acs.org/doi/10.1021/acsaem.7b00128.

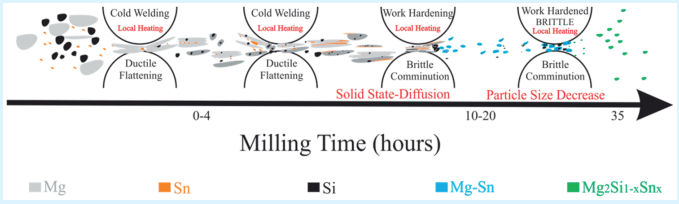

ABSTRACT: Mechanical alloying by high energy ball milling is an attractive solid-state technique for synthesizing a diverse range of stable and metastable materials. We have studied the synthesis of n-type thermoelectric $Mg_2Si_{0.4}Sn_{0.6}$ solid solution, aiming for a fundamental understanding of the mechanisms underlying this synthesis technique. The investigations on powders by XRD and SEM show that milling leads to welding of Mg and Sn but fracturing of Si. This fractured Si diffuses into the ductile matrix on longer milling times resulting in a phase mixture close to the nominal starting composition after 35 h of milling. However, phase pure material was only achievable after sintering; hence, the synthesis of $Mg_2(Si,Sn)$ is a two-step process. Furthermore, a thorough study on the effect of varying synthesis parameters on the thermoelectric properties was performed. This was done by systematically varying the milling and consolidation parameters. No strong influence of milling time on the thermoelectric properties was observed, and just 2 h of milling followed by compaction was sufficient to obtain a pellet with optimal thermoelectric properties. Moreover, increasing sinter temperature/time deteriorated carrier concentration, hence degrading the electronic properties. Thus, optimized thermoelectric properties were obtained for the powder consolidated at 973 K/20 min. $Mg_2Si_{0.4}Sn_{0.6}$ synthesized by mechanical alloying achieved a thermoelectric figure-of-merit $zT_{max} \sim 1.4$.

KEYWORDS: *mechanical alloying, phase formation, n-type $Mg_2Si_{0.4}Sn_{0.6}$, thermoelectric properties, magnesium silicide stannide, high energy ball milling, sintering profile optimization*

INTRODUCTION

Thermoelectrics (TE) is a principle of reversible coupling between heat and charge flow.[1] Thermoelectric materials are used in solid-state devices either to harvest waste heat for power generation or for cooling applications. These solid-state thermoelectric generators (TEGs) have been utilized in lunar and planetary landers in deep space probe for extraterrestrial flight missions and commercially, for example, for cathodic protection against corrosion of gas pipelines and in thermogenerators.[2,3] To secure a place in the market, they should be inexpensive, environmentally benign and have high conversion efficiency. Fulfilling these requirements could pave the way for their application in automotive and aviation industries since two-third of the generated energy from primary sources, for example fossil fuels, is released as waste heat.[4,5] The conversion efficiency of a TEG is governed by figure−of−merit (zT) of the employed materials, which is given by $zT = S^2\sigma T/\kappa$; where S, σ, T, and κ are Seebeck coefficient, electrical conductivity, absolute temperature and the total thermal conductivity, respectively. The latter comprises electronic (κ_{el}), bipolar (κ_{bip}), and lattice (κ_{lat}) contributions. Ideally, to have maximum zT, a TE material should obey the concept of PGEC (phonon glass electron crystal); i.e., it concomitantly should possess the electronic properties of an ideal crystalline (heavily doped) semiconductor and the thermal properties of a glass. However, it is observed that the interlink between the electronic parameters (S, σ, κ_{el}, and κ_{bip}), as well as a significant contribution from the lattice, makes it challenging to achieve $zT_{avg} \sim 1.0$ for mid-temperature materials.[5] Among the various promising materials for intermediate temperatures (500−800

Received: November 8, 2017
Accepted: January 9, 2018
Published: January 9, 2018

ACS Publications © 2018 American Chemical Society

DOI: 10.1021/acsaem.7b00128
ACS Appl. Energy Mater. 2018, 1, 531−542

Table 1. Synthesis Conditions, zT_{max}, and Room Temperature Carrier Concentration n_H and Mobility μ_H of the $Mg_2Si_{0.4}Sn_{0.6}$ Samples

sample name	milling time (h), sintering temperature/time (K/min)	density (g cm^{-3})	zT_{max}	n_H ($\times 10^{20}$) (cm^{-3})	μ_H (cm^2 V^{-1} s^{-1})
MS-2-973/20	2, 973/20	3.02 (98.6%)	1.35 ± 0.18 (729 K)	2.3	54
MS-4-973/20	4, 973/20	2.93 (95.7%)	1.37 ± 0.19 (726 K)	2.0	51
MS-20-973/20	20, 973/20	2.97 (97.0%)	1.38 ± 0.19 (759 K)	2.1	51
MS-50-973/20	50, 973/20	2.95 (96.4%)	1.28 ± 0.17 (726 K)	2.2	52
MS-20-923/20	20, 923/20	3.02 (98.6%)	1.28 ± 0.17 (779 K)	2.4	50
MS-20-1023/20	20, 1023/20	2.94 (96.0%)	1.18 ± 0.16 (759 K)	1.9	50
MS-20-973/5	20, 973/5	2.98 (97.3%)	1.34 ± 0.18 (756 K)	2.3	50
MS-20-973/10	20, 973/10	2.98 (97.3%)	1.31 ± 0.18 (759 K)	2.1	47
MS-20-973/30	20, 973/30	3.03 (99.0%)	1.21 ± 0.16 (760 K)	1.9	48

K) such as PbTe,[6] TAGS,[7] Skutterudites,[8] Zn_4Sb_3,[9] and half-Heuslers,[10] magnesium silicide (Mg_2Si) based solid solutions (especially $Mg_2Si_{1-x}Sn_x$[11]) have attracted a fair amount of attention in the past decade. This is due to their confirmed excellent thermoelectric properties $zT_{max} \sim 1.3-1.5$,[11,12] low density, elemental abundance, and environmental compatibility.[13]

A variety of synthesis routes have been examined such as melting of the elements,[11,14] self-propagating high temperature synthesis (SHS),[15] solid-state reaction,[16] or a combination of these techniques as steps[17] followed by a sintering process to obtain a pellet. Furthermore, high energy ball milling has been utilized to synthesize Mg_2Si and its solid solutions.[18−20] For the high temperature liquid synthesis route, precise Mg content control is challenging due to its high vapor pressure.[16,21] Mechanical alloying overcomes disadvantages of conventional synthesis mechanisms such as undesired material loss due to significant differences in the melting temperatures of the elements or chemical interaction of the melt with the crucibles/ampules leading to off-stoichiometry and contamination. Furthermore, MgO formation is often observed[21−23] which is detrimental to the electrical conductivity of the material.[24] Besides the $Mg_2(Si,Sn)$ system, high energy ball milling has become a very popular technique for the synthesis of various thermoelectric materials.[19,25−29]

Several attempts to synthesize $Mg_2Si_{1-x}Sn_x$ by mechanical alloying in the past have resulted in the formation of either multiphase or impure materials.[30−35] Only recently, high energy ball milling combined with a compaction step has been employed successfully to obtain n-type Mg_2Si as well as n- and p-type $Mg_2(Si,Sn)$.[19,20,36,37] So, on the basis of the previous reports it is clear that high energy ball milling is an efficient and attractive synthesis route; however, an understanding of $Mg_2Si_{1-x}Sn_x$ phase formation and its underlying mechanism is still missing. Therefore, a detailed phase formation analysis to comprehend the synthesis mechanism was performed. We decided to study the formation of $Mg_2Si_{0.4}Sn_{0.6}$ because this composition has shown the best thermoelectric properties for this material class.[16,38,39]

The sintering parameters play a crucial role in obtaining phase pure and homogeneous samples; they furthermore heavily influence the TE properties of the material. For the $Mg_2Si_{0.4}Sn_{0.6}$ system there is first no detailed analysis available correlating sintering parameters with the TE properties, and second it remains unclear how sensitive the material is to the variation in these parameters. Instead, the previously reported sintering parameters differ and cause ambiguity.[17,40−43] We have therefore systematically studied the changes that occur during sintering, and their effect on the TE properties was observed.

EXPERIMENTAL SECTION

The magnesium tin silicide solid solution was synthesized using commercially available starting elements [Mg turnings (Merck), Si (<6 mm, Chempure), Sn (<71 μm, Merck), and Sb (5 mm, Alfa Aesar)], all with purity >99.5%. A high energy mechanical alloying mill (SPEX 8000D Shaker Mill) was employed with stainless steel vials and balls. The elements were weighed according to the desired composition $Mg_2Si_{1-x-y}Sn_xSb_y$ ($x = 0.6$, $y = 0.015$). Magnesium was taken 3 at. % in excess to compensate for possible Mg loss. There were two sets of experiments performed. In the first set, a specific amount of powder (1.25 g) was removed for the analysis of the sample (XRD, SEM, and particle size analysis); thus, as the milling progressed, the ball-to-powder ratio (BPR) increased, see Supporting Information (Table S1). In the second set, the effect of milling time (rather than BPR) with constant BPR and $t_{milling}$ = 2, 4, 20, 50 h was investigated. All the samples were sintered at 973 K for 20 min.

In order to obtain homogeneous samples with optimum thermoelectric properties, different combinations of sintering parameters were tested. The powder mechanically alloyed for 20 h was utilized for this optimization study as this duration has been reported frequently in the literature.[20,36,37,44] The powder handling during synthesis was done under argon to prevent oxidation and contamination. The sample powder was sintered at three different temperatures/constant time (923 K/20 min, 973 K/20 min, and 1023 K/20 min) combinations with constant temperature/different sintering times (973 K/5 min, 973 K/10 min, 973 K/20 min, 973 K/30 min) to study the effect of varying sintering parameters. Powder samples were sintered utilizing a direct-current sintering press (DSP 510 SE) from Dr. Fritsch GmbH. Sintering was performed using a graphite mold Ø12.7 mm under vacuum (~10^{-5} bar) at a heating rate of 1 K s^{-1}. The density measurement for all the pellets was done using the Archimedes method. The relative densities of the obtained pellets were >95% of the theoretical value (3.06 g cm^{-3}).

X-ray diffraction was performed on powders and sample pellets utilizing a Siemens D5000 Bragg−Brentano diffractometer with a secondary monochromator. The specifics used in the system were Cu Kα radiation (1.5406 Å) in the 2θ range 20−80° with a step size of 0.01°. Scanning electron micrographs (SEMs) were taken using a Zeiss Ultra 55 equipped with an energy dispersive X-ray (EDX) detector. A laser-assisted particle size analyzer (Beckman Coulter IS3320) was used to analyze the particle size distribution of powder samples. The homogeneity of sample pellets was studied by an in-house developed surface-scanning Seebeck microprobe.[45] Also, the temperature dependent electronic transport properties were measured utilizing an in-house developed facility utilizing a four-probe technique.[46,47] The thermal diffusivity (α) of the pellets was obtained using the Netzsch LFA 427 apparatus. The thermal conductivity (κ) was obtained using the relation $\kappa = \alpha\rho c_p$, where ρ and c_p are sample density and heat capacity. The c_p value was obtained from the Dulong−Petit limit for c_V^{DP} follows: $c_p = c_V^{DP} + \frac{9E_t^2T}{\beta_T\rho}$. $E_t \sim 2 \times 10^{-5}$ K^{-1} and $\beta_T \sim 2.07 \times$

DOI: 10.1021/acsaem.7b00128
ACS Appl. Energy Mater. 2018, 1, 531−542

10^{-11} Pa^{-1} are the linear coefficient of thermal expansion and isothermal compressibility, respectively.[48] The measurements were performed in a temperature range from 300 to 773 K under vacuum. The measurement uncertainties for S, σ, and κ are ±5%, ±5%, and ±8%, respectively. For better visibility of the TE data, the error bars are shown for one sample only. The room temperature Hall coefficient R_H for different samples was determined using an in-house facility in a van der Pauw configuration under a varying magnetic field of maximum 0.5 T.[49] The Hall carrier concentration n_H was estimated from R_H assuming a single carrier type $n_H = \frac{1}{R_H \times e}$. Measurement uncertainties for n_H and mobility μ_H are ±10%.

The synthesis conditions and representative data for different samples are summarized in Table 1.

XRD patterns of the powders milled for different durations are presented in Figure 1. The formation of multiphase material with

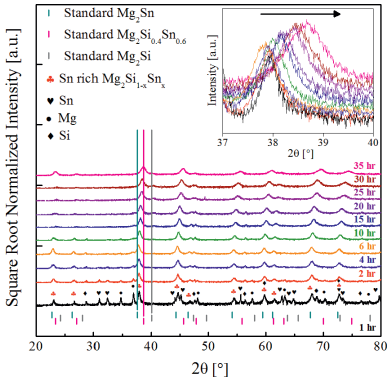

Figure 1. X-ray patterns show the formation of the desired phase with increasing milling time. A shift of the prominent (220) peak with increasing milling time can be observed from the inset [$2\theta \sim 37°$–$39°$] signifying that the material system is close to the desired phase after 35 h of milling.

compositions close to Mg_2Sn takes place within the first hour, while the formation of Si-rich $Mg_2(Si,Sn)$ is not observed. The participation of starting elements in the phase formation is visualized by the diminishing elemental peaks. However, the consumption time of the starting elements is different: while Sn has basically disappeared after $t_{milling}$ = 15 h, elemental Si still persists in the pattern at least until $t_{milling}$ = 25 h, asserting that incorporation of Si in the material system to form the Mg–Si–Sn phase takes place after a longer milling time. A gradual shift of the $Mg_2(Si,Sn)$ peaks toward higher 2θ (~37°→ 39° for the 220 peak) with increasing ball milling time signifies decreasing lattice constant (Figure 1, inset). Any impurity peaks corresponding to phases originating from the milling vial or grinding media were not found.

The median of the particle size distribution decreases with increasing milling time (Figure 2). Initially (up to $t_{milling} \approx 6$ h), a strong decrease in particle size is observed, mainly due to fracturing of the starting elements. The curve corresponding to powder milled from 4 h to longer milling times has an increasing fraction of particles in the sub-10 μm region, which is not observed for the shorter milled powders, and is further followed by a plateau between 10 and 25 h (the particle size distributions for exemplary powder samples are provided in Figure S1 in the Supporting Information). This is because the system tends to form a dynamic equilibrium between the reduction in particle size and reagglomeration. On continuous milling, the ductile phase particles get work hardened. Later, this work hardened system undergoes progressive brittle cracking and/or further fragmentation of

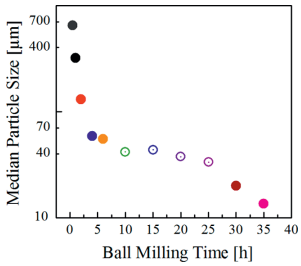

Figure 2. Particle size median versus ball milling time. Particle size decreases with longer milling time. Curve shows a plateau from 10 to 25 h attributed to a dynamic equilibrium existing between cold welding of ductile phase particles (here Mg–Sn) and comminution of brittle phase particles (Si particles).

fragile components leading to a decrease in particle size for $t_{milling}$ > 25 h.

The SEM analysis was performed on the cross-section of the powder particles milled for $t_{milling}$ = 4, 20, and 35 h as shown in Figure 3. The observations from 4 h milled powder suggest that individual particles comprise different starting particles cold welded together. The EDAX analysis suggests that the Mg particles preferentially tend to interact with Sn particles. The area on which the EDAX mapping and line scans were done shows that the Si particles get trapped within the Mg–Sn-rich particle matrix. Further investigations on 20 h milled powder particles show significant size reduction in comparison to the 4 h milled powder. The line scans performed on the Mg–Si/(Mg–Sn)–Si interfaces on the particles show that the Si concentration in the corresponding rich area decreases and the Mg and Sn concentrations become significantly larger in comparison to the 4 h milled sample. Similarly, the investigations on 35 h milled powder suggested less Si-rich areas on the powder particle compared to a 20 h milled powder sample; although the Si-rich region had atomic fraction(s) almost comparable to those for 20 h samples, some areas appeared to be diffusing into the Mg–Sn matrix. The additional line scans corresponding to $t_{milling}$ = 4, 20, and 35 h are also provided in the Supporting Information (Figures S2–S4).

DISCUSSION

The combined analysis of SEM, XRD, and particle size gave us an understanding of the phase formation of $Mg_2Si_{1-x}Sn_x$ using high energy ball milling which is depicted in Figure 4. The cold welding and fracturing depends to a large extent on the deformation characteristics of the starting materials. Mg and Sn are ductile elements with lower shear modulus, Young's modulus, and bulk modulus compared to those of the more brittle silicon.[50,51] During the complete process of mechanical alloying first the ductile Mg and Sn dominantly experience plastic deformation (repeated cold welding and flattening) resulting in the formation of *fresh* interfaces. These new interfaces act as centers for the other elements to cold weld. On the other hand, the silicon particles are initially subject to comminution and mostly get trapped within these flattened Mg and Mg–Sn constituents. Additionally, the Si requires either a higher impact energy from the balls or a longer impact time to diffuse into the complete Mg–Sn-rich particle matrix due to higher values of moduli. Thus, the reaction time toward the desired phase gets prolonged (compared to, e.g., Mg and Sn only, see ref 31).

With increasing milling time, the Sn-rich $Mg_2Si_{1-x}Sn_x$ particles get work hardened, which increases the brittleness of

DOI: 10.1021/acsaem.7b00128
ACS Appl. Energy Mater. 2018, 1, 531–542

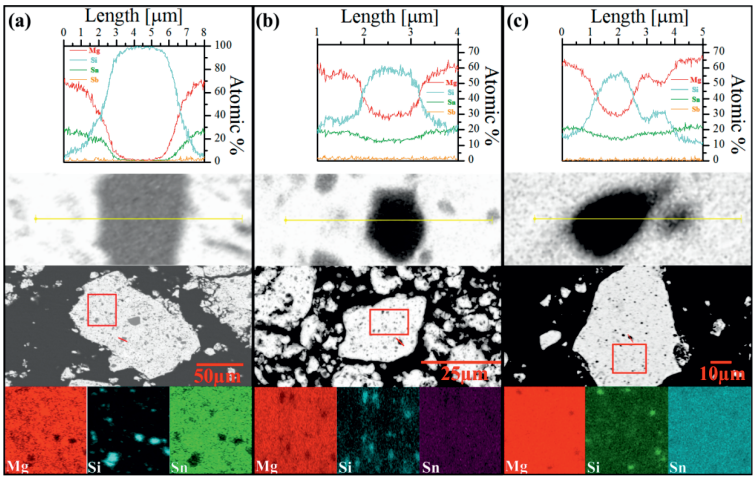

Figure 3. Electron micrographs, EDAX line scans, and elemental mapping of (a) 4 h, (b) 20 h, and (c) 35 h milled powders.

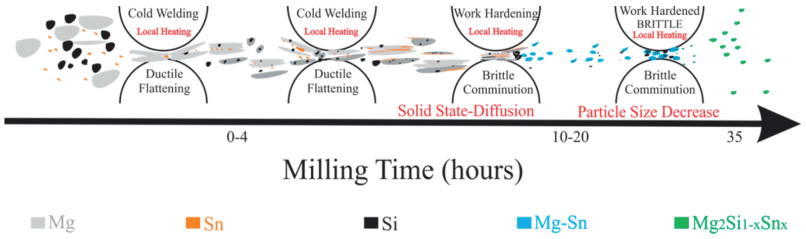

Figure 4. Formation mechanism of the $Mg_2Si_{1-x}Sn_x$ phase through high energy mechanical alloying.

the system together with the progressing Si incorporation. From this stage, the size of powder particles decreases further. Simultaneously, the Si particles get completely diffused into the Mg–Sn-rich matrix leading to the formation of $Mg_2Si_{1-x}Sn_x$ solid solution with $0 < x < 1$. This is in agreement with previous reports on mechanical alloying of Mg_2X (X: Si, Sn, and Ge) based materials[19,31,52] where the formation of Mg_2Sn comprising ductile–ductile constituents was found to be faster than that of Mg_2Si (ductile–brittle system). Moreover, the experimental and theoretical values of the formation enthalpy of Mg_2Sn, −80.75 and −80 kJ/mol (at 298 K), respectively, are higher than those of Mg_2Si, −68 kJ/mol, −64.8 kJ/mol (at 298 K), respectively,[31,53,54] which suggests the formation of Mg_2Sn to be thermodynamically more favorable. Therefore, the observed faster (Mg–Sn) formation is also expected from a thermodynamic point of view. The cross-section image of the 4 h milled powders (in Figure 3a) and the line scan on the highlighted region of particle show a clear gradient in the atomic fraction. The brighter region is Mg–Sn-rich whereas the dark gray area is Si-rich. The gradient in atomic fraction curve is more evident at the Mg–Sn/Si interface suggesting that the diffusion of Si into Mg–Sn-rich matrix has not started yet. On longer milling, the particles appear to be smaller and of uniform size. The SEM analysis on a 20 h milled powder particle shows fewer gray areas suggesting that less Si particles are occluded by the ductile phase. The EDAX line scans on these powder particles show an increase in atomic fraction of Mg and Sn in the Si-rich particle compared to 4 h milled powder particles (Figure 3b). This indicates an onset but slow diffusion of silicon into the Mg–Sn matrix. This also implies that the intermetallic Mg_2Si formation at the Mg–Si interface readily takes place, but the interdiffusion of ductile–brittle constituents requires prolonged mechanical force for the reaction to proceed. This is also supported by a previous report.[31] In addition to this, Aizawa et al. found Si particles trapped in a ductile matrix sustain lower strain when milled for longer time even while experiencing the same mechanical stress/force. This is because Si particles become mobile together with plastically deformed ductile constituents and experience a lower flow stress.[52]

However, on longer milling ($t_{milling} \geq 25$ h), the short-range diffusion in the ductile matrix was evident from the diminishing Si peaks from the X-ray pattern and lowering of Si-rich areas from the EDAX maps on 35 h milled powder. The dark Si-rich regions had atomic fractions comparable to those found on the 20 h sample as evident from EDAX maps. Furthermore, the increase in the atomic fraction of Mg and Sn in Si-rich area(s)

DOI: 10.1021/acsaem.7b00128
ACS Appl. Energy Mater. 2018, 1, 531–542

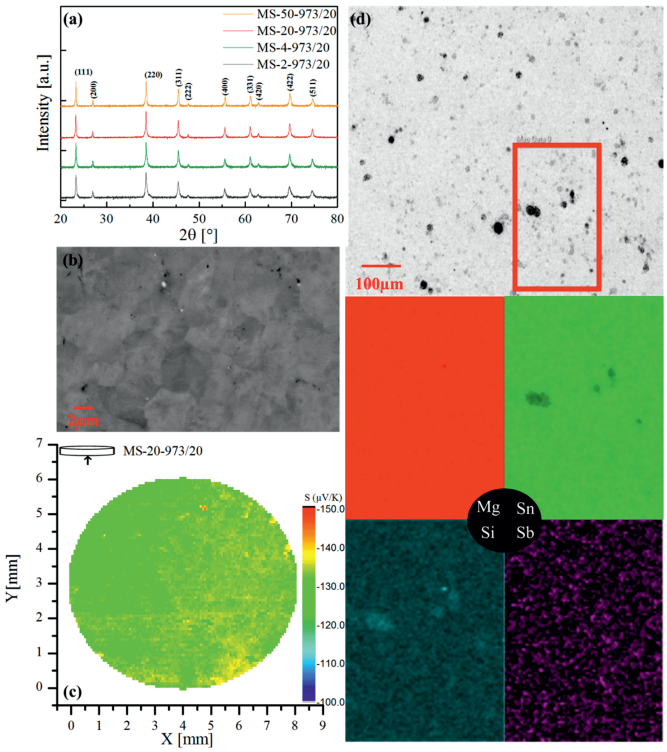

Figure 5. (a) XRD for samples with identical compaction parameters but different milling times, (b) microstructure, (c) surface Seebeck scan, and (d) EDAX mapping of the compacted pellet MS-20-973/20.

observed from the line scans on dark (~2 μm scan length) and light (at ~3–4 μm scan length) gray areas asserts *slow* diffusion of Si in the Mg–Sn matrix as (Figure 3c). This also confirms that the Si diffusion into the Mg–Sn-rich particle matrix took place almost completely. Thus, this led to formation of desired the $Mg_2Si_{1-x}Sn_x$ composition (with varying x). This is evident from the X-ray pattern of 35 h milled samples having convoluted peaks at $2\theta \sim 37.5°$ as shown in Figure 1. However, a single phase sample is achieved only after a high temperature sintering step (see Figure S6 in the Supporting Information).

Effect of Milling Time on Thermoelectric Parameters. In order to determine the minimum milling time required to obtain phase pure material after sintering, the starting elements were mechanically alloyed for different times ($t_{milling}$ = 2, 4, 20, and 50 h). The ball-to-powder ratio was kept almost constant for all the powders (1.6:1 for $t_{milling}$ = 2, 20, and 50 h and 2.2:1 for $t_{milling}$ = 4 h). Please note that the previously discussed powders were obtained with a strongly increasing ball-to-powder ratio and the times are therefore not directly comparable. The X-ray data asserts that a phase pure sample was obtained after sintering the powder material milled for 2 h (Figure 5a) already. Accordingly, samples from longer milled powder are also phase pure, and the XRD patterns are almost identical. The diffractograms of the sample pellets were indexed with a standard $Mg_2Si_{0.4}Sn_{0.6}$ pattern (ICSD PDF number 01-089-4254) confirming the formation of desired solid solution phase (fcc, space group $Fm\bar{3}m$). Also, the samples show no MgO impurity, which is often observed for other synthesis procedures. The SEM and EDAX mapping on the MS-20-973/20 sample showed that the sample was homogeneous. The grain boundaries were quite visible, and the grain sizes were in the range 4–6 μm. We found that the sample had evenly distributed elemental constituents, though Si-rich areas in the matrix are visible (Figure 5b,c). The obtained pellet was dense with little porosity. The surface Seebeck scans performed on the top and bottom surfaces of the sample revealed the homogeneity of the sample. The sample was found to be homogeneous in terms of room temperature Seebeck values (top surface, 132.1 ± 2.6 $\mu V\ K^{-1}$, and bottom surface, 132.2 ± 2.6 $\mu V\ K^{-1}$). The values are in agreement with the room temperature data of the integral temperature dependent measurements.

The transport properties of samples obtained from the second set of synthesis in the temperature range 350–735 K are shown in Figure 6. The lattice thermal conductivity plus the

DOI: 10.1021/acsaem.7b00128
ACS Appl. Energy Mater. 2018, 1, 531–542

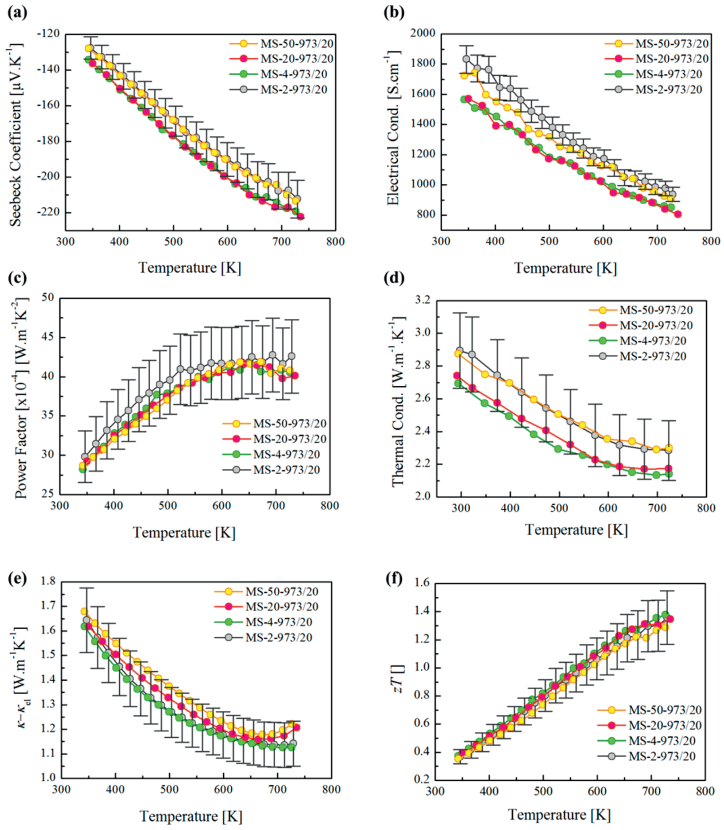

Figure 6. Temperature dependent (a) Seebeck coefficient, (b) electrical conductivity, (c) power factor, (d) thermal conductivity, (e) lattice thermal conductivity, and (f) figure-of-merit of differently long (2, 4, 20, and 50 h) milled powder samples. Fluctuations in the electronic properties can be observed, but no systematic trend with increasing milling time. In particular, $\kappa - \kappa_{el}$ remains almost unchanged.

bipolar contribution ($\kappa - \kappa_{el}$) was calculated using $\kappa_{lat} + \kappa_{bip} = \kappa - \kappa_{el} = \kappa - L\sigma T$, where κ_{el} is the electronic contribution to the thermal conductivity and the Lorenz number (L) was calculated using the Seebeck coefficient values.[55] The Seebeck coefficient shows n-type behavior signifying electron dominated transport. Correspondingly, the electrical conductivity decreases with increasing temperature. Thus, all the samples show degenerate semiconducting behavior. The high values of Seebeck coefficient −125 μV K^{-1} and electrical conductivity 1560−1700 S cm^{-1} at 350 K are attributed to the high carrier concentration combined with a large density of states carrier effective mass due to the band convergence at this composition.[11,16]

At higher temperatures (~730 K), the Seebeck coefficient increases (−225 μV K^{-1}), and electrical conductivity correspondingly decreases to 800−930 S cm^{-1} due to acoustic phonon scattering and alloy scattering of the charge carriers. Small and non-systematic differences can be observed between the samples, which can be attributed to small variations in carrier concentration (±10%), see Table 1. Nevertheless, the power factor lies in the same range for all the samples with maximum value of 39−42 [×10^{-4}] W m^{-1} K^{-2} within the temperature region 600−700 K.

The total thermal conductivity expectedly decreased with increasing temperature for all the samples. The bipolar effect observed in the calculated ($\kappa - \kappa_{el}$) plot was stronger for the MS-20-973/20 and MS-50-973/20 samples at temperature values >650 K. The results for the lattice thermal conductivity indicate no significant effect of ball milling time. The observed small differences in the total thermal conductivity are due to the electronic contribution of the thermal conductivity of the respective samples. The zT_{max} values of all of the samples are tabulated in Table 1 ($zT_{max} \sim 1.4$). It is now thus demonstrated that the thermoelectric properties remain unaffected by milling for higher times. The room temperature carrier concentration values summarized in Table 1 were calculated from the Seebeck

DOI: 10.1021/acsaem.7b00128
ACS Appl. Energy Mater. 2018, 1, 531−542

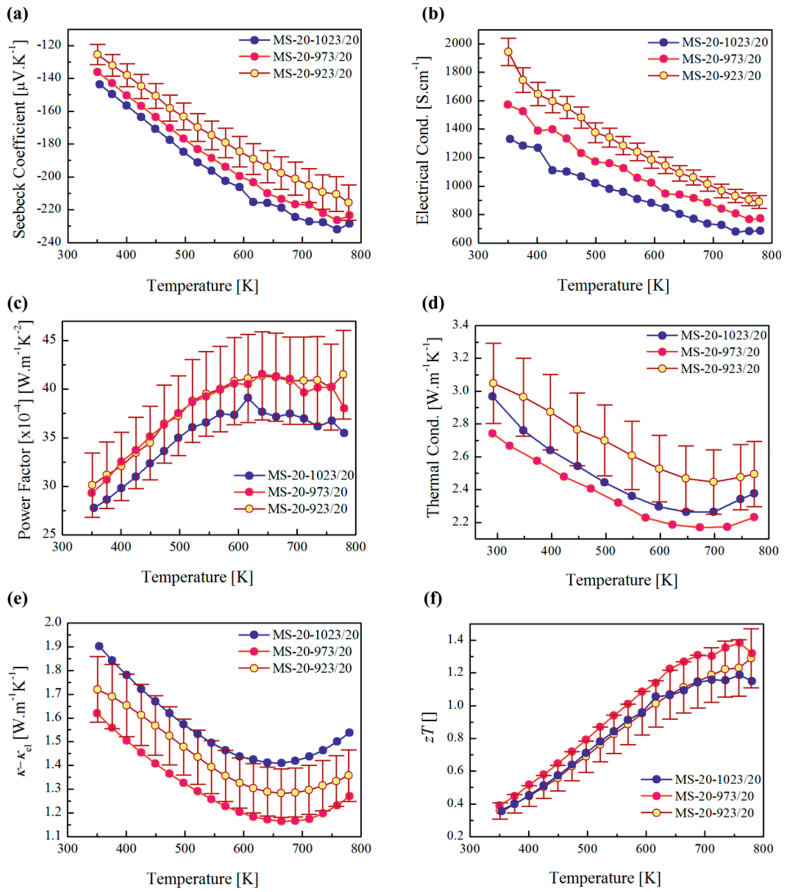

Figure 7. Temperature dependent (a) Seebeck coefficient, (b) electrical conductivity, (c) power factor, (d) thermal conductivity, (e) lattice thermal conductivity, and (f) figure-of-merit of powder sintered at different temperatures (923, 973, 1023 K) for t_{sinter} = 20 min. The nomenclature of the sample is MS-20-T_{sinter}/t_{sinter}.

coefficient values using a single parabolic band (SPB) model. We have employed an average value for the density of states effective mass ($m_D^* = 2.3m_0$) after conducting room temperature Hall measurements on several samples of the present study. The assumption of a constant m_D^* is reasonable due to the relatively narrow carrier concentration interval; the value is furthermore in agreement with previous reports.[39,56]

The calculated Hall mobility (μ_H) is also tabulated (Table 1) and ranges 50 ± 5 cm^2 V^{-1} s^{-1}. The values of n_H and μ_H are comparable to those reported by Farahi et al.[17] for $Mg_2Si_{0.3}Sn_{0.665}Bi_{0.035}$ and Liu et al.[16] for $Mg_{2.14}Si_{0.39}Sn_{0.6}Sb_{0.009}$ samples. The observed differences in electrical conductivity are mainly due to differences in n_H.

This also indicates that high energy mechanical alloying does not cause a visible reduction in the carrier mobility of the $Mg_2Si_{1-x}Sn_x$ solid solutions compared to high temperature synthesis routes. This is in contrast to the observed mobility values reported for $(Bi,Sb)_2(Se,Te)_3$ solid solutions and bulk Si samples, which decreased on mechanical alloying.[57,58] Furthermore, the expected decrease of lattice thermal conductivity with higher milling time was not observed. The grain size of the MS-2-973/20 sample was 4−7 μm comparable to that of MS-20-973/20 (4−6 μm) which could be a possible reason for no observable difference in the lattice thermal conductivity values (please refer to Figure S5 in Supporting Information). The zT_{max} values show that high performance $Mg_2(Si,Sn)$ can be synthesized after only 2 h of mechanical alloying.

Effect of Sintering Parameters on Thermoelectric Properties. As discussed above, a sintering step is necessary to obtain phase pure $Mg_2(Si,Sn)$. Powder compaction is sensitive

DOI: 10.1021/acsaem.7b00128
ACS Appl. Energy Mater. 2018, 1, 531−542

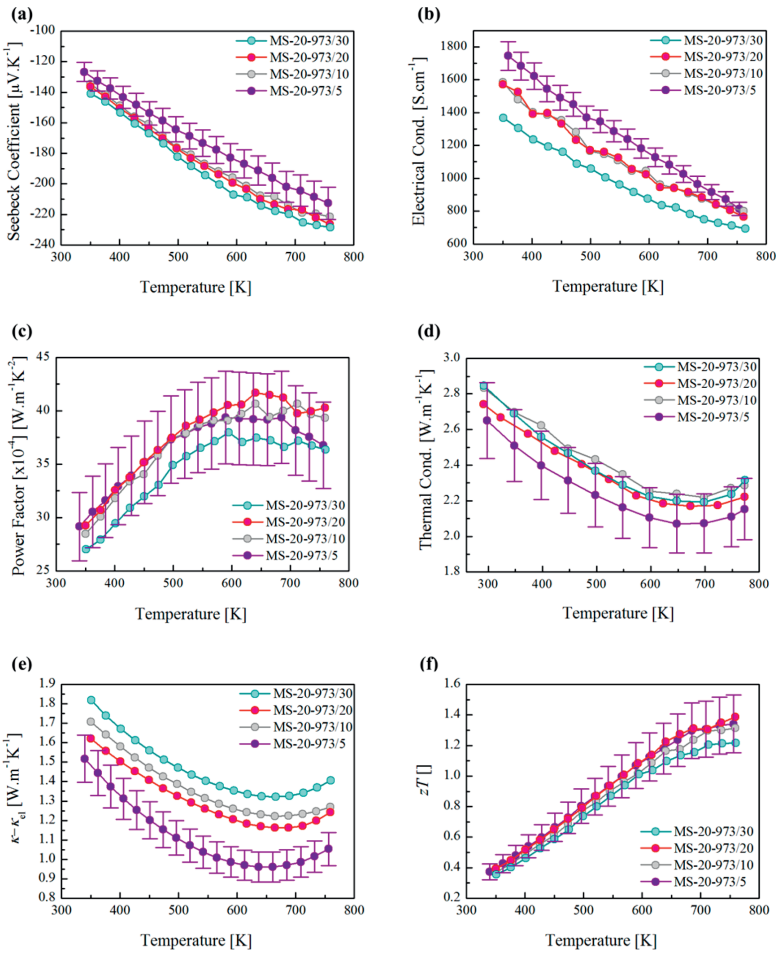

Figure 8. Temperature dependent thermoelectric transport data: (a) Seebeck coefficient, (b) electrical conductivity, (c) power factor, (d) thermal conductivity, (e) lattice thermal conductivity, and (f) figure-of-merit of the samples sintered at T_{sinter} = 700 °C for varying t_{sinter} (5, 10, 20, and 30 min). The nomenclature of the sample is MS-20-700/t_{sinter}.

to sintering parameters, namely, to ramp up/down temperature, holding time, pressure (or load), sintering atmosphere, etc. We have studied the effect of sintering parameters in two sets of experiments, adjusting sintering temperature in the first set while varying sinter holding time in the second. The various combinations are listed in Table 1. The pressure was kept constant for all the experiments (67 MPa) since no strong influence of sintering pressure on the TE properties was observed for this class of materials.[59]

Effect of Sintering Temperature at Constant Time. The transport properties of the samples sintered for 20 min at different temperatures (MS-20-923/20, MS-20-973/20, and MS-20-1023/20) were acquired after sintering the powder obtained by mechanical alloying for 20 h, see Figure 7.

The Seebeck coefficient increased, and electrical conductivity vice versa experienced a reduction with increase in temperature. The relatively high PF value of MS-20-923/20 is due to slightly higher carrier concentration than that of MS-20-973/20 and MS-20-1023/20 samples. The results for κ differ due to different electrical conductivities and differences in the lattice thermal conductivity which do not follow a discernible trend. The bipolar contribution is clearly visible above 600 K and comparable for all samples. In summary, MS-20-973/20 displays the best performance with zT_{max} = 1.38 ± 0.19.

DOI: 10.1021/acsaem.7b00128
ACS Appl. Energy Mater. 2018, 1, 531−542

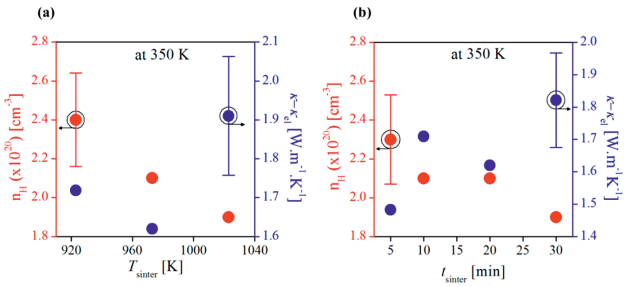

Figure 9. Plots showing change in carrier concentration (n_H) and lattice thermal conductivity ($\kappa - \kappa_{el}$) on varying (a) sintering temperature (t_{sinter} 20 min) and (b) sintering time (T_{sinter} 973 K).

Effect of Sintering Time at Constant Temperature. This study was performed to identify the required sinter holding time after determining the appropriate sinter temperature. The thermoelectric data is presented in Figure 8.

The electronic properties and lattice thermal conductivity were affected similarly to those in the varying temperature study. The (absolute) Seebeck coefficient values show a slight increase with increasing time of compaction, while the inverse trend is observed for the electrical conductivity data. This is in line with the observed decreasing carrier concentration, see Table 1. The samples compacted under a holding time of 5 and 30 min thus have slightly lower PF values. The loss of charge carriers at higher holding time could be attributed to the migration of antimony to the grain boundaries. The lattice thermal conductivity shows an overall increase with increasing sintering time, and the bipolar contribution is roughly comparable for all samples. Although the overall thermoelectric performances of the 5, 10, and 20 min samples are comparable, we chose 20 min as the preferred sintering time due to the better sample homogeneity (see Seebeck scan in Figure 5 and Figure S7 in Supporting Information).

The effect of sintering temperature and time on carrier concentration and $\kappa - \kappa_{el}$ of different samples is summarized in Figure 9. The carrier concentration decreases with increasing sintering temperature, affecting electrical conductivity (and with it κ_{el}) and the Seebeck coefficient which have an opposing dependence on the carrier concentration. For our samples we find that increasing sintering time decreases the carrier concentration out of the optimum range thus leading to lower power factor values. The $S^2\sigma$ values of MS-20-923/20 and MS-20-973/20 (41.5×10^{-4} W m^{-1} K^{-1}) were comparable to the literature values.[21] Similarly, the effect of sinter holding time is shown in Figure 9b.

The increasing sintering time affected n_H leading to slightly lower power factor values for both the 5 and 30 min sintered samples. The observed effect of sintering time and sintering temperature is presumably a consequence of dopant segregation at the grain boundaries. Dopant segregation would lead to a decrease of the dopant-induced free carriers and hence a change in the electronic properties. This is in agreement with our experimental observations and matches with our data (see Table 1). Previous experimental reports have furthermore proven that heavy dopants (such as Sb, Bi) can indeed migrate and settle at the grain boundaries.[17] We observe a small overall increase in lattice thermal conductivity with increasing sintering time and temperature. The reason for that remains to be found but is not an obvious grain growth. The absolute value of $\kappa - \kappa_{el}$ for the samples (1.5−1.8) is comparable to those reported by Farahi et al. for $Mg_2Si_{0.365}Sn_{0.6}Bi_{0.035}$ (1.39 W m^{-1} K^{-1} at 320 K),[17] and calculated values by Tan et al. for $Mg_2Si_{0.365}Sn_{0.625}$ showed $\kappa - \kappa_{el} \sim 1.62$ W m^{-1} K^{-1} (at 300 K).[60] Overall, it was observed that 2 h of milling is enough to obtain a phase pure pellet. The thermoelectric properties are almost unaffected by increasing the milling time. The thermoelectric performance of the best samples is found to be competitive with some other previously reported studies for the same material[21,39] utilizing different synthesis procedures. The ambiguity that arose as a result of reports of different sintering conditions for $Mg_2Si_{0.4}Sn_{0.6}$ material(s)[17,40,42,61] is resolved by a detailed study on varying time and temperature in different combinations. The increase in sintering temperature and time was observed to affect the carrier concentration and lattice thermal conductivity of different samples leading to changes in the thermoelectric properties. Nevertheless, the zT_{max} of different samples was found to vary between 1.2 and 1.4 suggesting that the thermoelectric properties of Mg_2X solid solutions are quite robust with respect to the synthesis parameters. This is in contrast to the other material system, where the thermoelectric properties were found to be more sensitive to the compaction parameters, e.g., $CoSb_3$ based Skutterudites,[62] Zn_4Sb_3,[63] and $AgSn_mSbTe_{2+m}$ materials.[64]

CONCLUSION

The formation mechanism of $Mg_2Si_{0.4}Sn_{0.6}$ by mechanical alloying was investigated. Initially, Sn-rich $Mg_2(Si,Sn)$ is formed followed by the slow incorporation of Si driving the composition toward the desired $Mg_2Si_{0.4}Sn_{0.6}$ phase. This is supported by the XRD peak shift toward higher angles and an increasing homogenization as observed from the cross-sectional SEM images of the powder. However, we also find that within the observed milling time no phase pure $Mg_2Si_{0.4}Sn_{0.6}$ was obtained by high energy mechanical alloying only, but rather a somewhat broad phase mixture. In order to obtain a phase pure pellet, a high temperature sintering step is required. We have therefore shown that the $Mg_2Si_{0.4}Sn_{0.6}$ material synthesis is a two-step process involving high energy mechanical alloying and high temperature pressing of the mechanically alloyed powder. We have found the same phenomenon experimentally also for other ternary compositions of (Mg_2Si,Sn) in contrast to previous reports on binary Mg_2X (X: Si, Sn, Ge). Investigations on the phase pure samples synthesized by mechanical alloying

DOI: 10.1021/acsaem.7b00128
ACS Appl. Energy Mater. 2018, 1, 531−542

for different milling times ($t_{milling}$ = 2, 4, 20, 50 h) led to the conclusion that 2 h of mechanical alloying is sufficient and no significant influence of milling time on the TE properties was found. On the other hand, systematic effects of the sintering parameters were observed: An increase in sintering time and temperature led to a shift of the carrier concentration and hence caused changes in the electronic properties. We found no significant increase in grain size with increasing sintering time and temperature. In contrast to the electronic properties the thermal conductivity reacted only to a small extent on the sintering parameters and showed only a minor increase with increasing sintering time and temperature. This also suggests that the grain size is in a range where the thermal conductivity is less sensitive to small changes due to change in the synthesis parameters. In summary, we found the optimum thermoelectric properties for sintering at 973 K for 20 min. We also found that the synthesis route has a good reproducibility and is relatively robust against small changes of the synthesis parameters. Mechanical alloying is thus a sound and attractive technique that can be utilized for high performance Mg_2X based solid solutions.

■ ASSOCIATED CONTENT

Supporting Information

The Supporting Information is available free of charge on the ACS Publications website at DOI: 10.1021/acsaem.7b00128.

Tabulated change in BPR, exemplary particle size analysis for powders milled for different milling times, EDAX line scans on powder particles, microstructure of sample obtained after 2 h of milling, and additional room temperature surface Seebeck scans on the samples (MS-20-700/10 and MS-20-700/20) (PDF)

■ AUTHOR INFORMATION

Corresponding Authors

*E-mail: Aryan.Sankhla@dlr.de.
*E-mail: Johannes.deBoor@dlr.de.

ORCID

Aryan Sankhla: 0000-0002-1527-6902
Johannes de Boor: 0000-0002-1868-3167

Author Contributions

§A.S. and A.P. contributed equally.

Notes

The authors declare no competing financial interest.

■ ACKNOWLEDGMENTS

We would like to gratefully acknowledge the endorsement from the DLR Executive Board Member for Space Research and Technology and the financial support from the Young Research Group Leader Program. The authors would like to thank P. Blaschkewitz (DLR) for his untiring support with the thermoelectric measurements. The authors would also like to thank C. Stiewe and R. Sottong for their help in sample preparation for SEM characterization. The authors acknowledge Pawel Ziolkowski for his help in providing and conducting Seebeck scans on sample surface. The authors (A.S., and H.K. and N.F.) would like to acknowledge financial support by the DAAD (Fellowships 247 and 241, respectively). Also, financial support of one of the authors (M.Y.) is provided by the DFG via the GRK (Research Training Group) 2204 "Substitute Materials for Sustainable Energy Technologies".

■ REFERENCES

(1) Brantut, J.-P.; Grenier, C.; Meineke, J.; Stadler, D.; Krinner, S.; Kollath, C.; Esslinger, T.; Georges, A. A Thermoelectric Heat Engine with Ultracold Atoms. *Science* **2013**, *342*, 713−715.

(2) Tsynaeva, A. A. Cathode Protection Systems of Cross-country Pipelines. *Procedia Eng.* **2015**, *111*, 777−782.

(3) Beretta, D.; Massetti, M.; Lanzani, G.; Caironi, M. Thermoelectric Characterization of Flexible Micro-Thermoelectric Generators. *Rev. Sci. Instrum.* **2017**, *88*, 015103.

(4) Alam, H.; Ramakrishna, S. A Review on the Enhancement of Figure of Merit from Bulk to Nano-Thermoelectric Materials. *Nano Energy* **2013**, *2*, 190−212.

(5) Snyder, G. J.; Toberer, E. S. Complex Thermoelectric Materials. *Nat. Mater.* **2008**, *7*, 105−114.

(6) Gelbstein, Y.; Dashevsky, Z.; Dariel, M. P. The search for mechanically stable PbTe based thermoelectric materials. *J. Appl. Phys.* **2008**, *104*, 033702.

(7) Cook, B. A.; Kramer, M. J.; Wei, X.; Harringa, J. L.; Levin, E. M. Nature of the Cubic to Rhombohedral Structural Transformation in $(AgSbTe_2)_{15}(GeTe)_{85}$ Thermoelectric Material. *J. Appl. Phys.* **2007**, *101*, 053715.

(8) Tang, Y.; Gibbs, Z. M.; Agapito, L. A.; Li, G.; Kim, H.-S.; Nardelli, M. B.; Curtarolo, S.; Snyder, G. J. Convergence of Multi-Valley Bands as the Electronic Origin of High Thermoelectric Performance in $CoSb_3$ Skutterudites. *Nat. Mater.* **2015**, *14*, 1223−1228.

(9) Snyder, G. J.; Christensen, M.; Nishibori, E.; Caillat, T.; Iversen, B. B. Disordered Zinc in Zn_4Sb_3 with Phonon-Glass and Electron-Crystal Thermoelectric Properties. *Nat. Mater.* **2004**, *3*, 458−463.

(10) Chen, S.; Ren, Z. Recent Progress of Half-Heusler for Moderate Temperature Thermoelectric Applications. *Mater. Today* **2013**, *16*, 387−395.

(11) Zaitsev, V. K.; Fedorov, M. I.; Gurieva, E. A.; Eremin, I. S.; Konstantinov, P. P.; Samunin, A. Y.; Vedernikov, M. V. Highly Effective $Mg_2Si_{1-x}Sn_x$ Thermoelectrics. *Phys. Rev. B: Condens. Matter Mater. Phys.* **2006**, *74*, 045207.

(12) Zaitsev, V. Thermoelectrics on the Base of Solid Solutions of Mg_2B^{IV} Compounds (B^{IV} = Si, Ge, Sn). *Thermoelectrics Handbook: Macro to Nano*; CRC Press, 2005; pp 29-1−29-12.

(13) de Boor, J.; Dasgupta, T.; Saparamadu, U.; Müller, E.; Ren, Z. F. Recent Progress in p-Type Thermoelectric Magnesium Silicide Based Solid Solutions. *Materials Today Energy* **2017**, *4*, 105−121.

(14) Dasgupta, T.; Stiewe, C.; de Boor, J.; Müller, E. Influence of Power Factor Enhancement on the Thermoelectric Figure of Merit in $Mg_2Si_{0.4}Sn_{0.6}$ Based Materials. *Phys. Status Solidi A* **2014**, *211*, 1250−1254.

(15) Zhang, Q.; Su, X.; Yan, Y.; Xie, H.; Liang, T.; You, Y.; Tang, X.; Uher, C. Phase Segregation and Superior Thermoelectric Properties of $Mg_2Si_{1-x}Sb_x$ ($0 \le x \le 0.025$) Prepared by Ultrafast Self-Propagating High-Temperature Synthesis. *ACS Appl. Mater. Interfaces* **2016**, *8*, 3268−3276.

(16) Liu, W.; Tan, X.; Yin, K.; Liu, H.; Tang, X.; Shi, J.; Zhang, Q.; Uher, C. Convergence of Conduction Bands as a Means of Enhancing Thermoelectric Performance of n-Type $Mg_2Si_{1-x}Sn_x$ Solid Solutions. *Phys. Rev. Lett.* **2012**, *108*, 166601.

(17) Farahi, N.; Prabhudev, S.; Botton, G. A.; Salvador, J. R.; Kleinke, H. Nano- and Microstructure Engineering: An Effective Method for Creating High Efficiency Magnesium Silicide Based Thermoelectrics. *ACS Appl. Mater. Interfaces* **2016**, *8*, 34431−34437.

(18) Liu, W.; Kim, H. S.; Chen, S.; Jie, Q.; Lv, B.; Yao, M.; Ren, Z.; Opeil, C. P.; Wilson, S.; Chu, C.-W.; Ren, Z. n-Type Thermoelectric Material $Mg_2Sn_{0.75}Ge_{0.25}$ for High Power Generation. *Proc. Natl. Acad. Sci. U. S. A.* **2015**, *112*, 3269−3274.

(19) Bux, S. K.; Yeung, M. T.; Toberer, E. S.; Snyder, G. J.; Kaner, R. B.; Fleurial, J.-P. Mechanochemical Synthesis and Thermoelectric Properties of High Quality Magnesium Silicide. *J. Mater. Chem.* **2011**, *21*, 12259−12266.

(20) Mao, J.; Kim, H. S.; Shuai, J.; Liu, Z.; He, R.; Saparamadu, U.; Tian, F.; Liu, W.; Ren, Z. Thermoelectric Properties of Materials Near

DOI: 10.1021/acsaem.7b00128
ACS Appl. Energy Mater. 2018, 1, 531−542

the Band Crossing Line in Mg_2Sn−Mg_2Ge−Mg_2Si System. *Acta Mater.* **2016**, *103*, 633−642.
(21) Liu, W.; Tang, X.; Li, H.; Yin, K.; Sharp, J.; Zhou, X.; Uher, C. Enhanced Thermoelectric Properties of n-Type $Mg_{2.16}(Si_{0.4}Sn_{0.6})_{1-y}Sb_y$ due to Nano-sized Sn-rich Precipitates and an Optimized Electron Concentration. *J. Mater. Chem.* **2012**, *22*, 13653−13661.
(22) Dasgupta, T.; Stiewe, C.; Hassdorf, R.; Zhou, A. J.; Boettcher, L.; Mueller, E. Effect of Vacancies on the Thermoelectric Properties of $Mg_2Si_{1-x}Sb_x$ ($0 \le x \le 0.1$). *Phys. Rev. B: Condens. Matter Mater. Phys.* **2011**, *83*, 235207.
(23) Zhang, L.; Xiao, P.; Shi, L.; Henkelman, G.; Goodenough, J. B.; Zhou, J. Suppressing the Bipolar Contribution to the Thermoelectric Properties of $Mg_2Si_{0.4}Sn_{0.6}$ by Ge Substitution. *J. Appl. Phys.* **2015**, *117*, 155103.
(24) de Boor, J.; Dasgupta, T.; Kolb, H.; Compere, C.; Kelm, K.; Mueller, E. Microstructural Effects on Thermoelectric Efficiency: A Case Study on Magnesium Silicide. *Acta Mater.* **2014**, *77*, 68−75.
(25) May, A. F.; Fleurial, J.-P.; Snyder, G. J. Thermoelectric Performance of Lanthanum Telluride Produced via Mechanical Alloying. *Phys. Rev. B: Condens. Matter Mater. Phys.* **2008**, *78*, 125205.
(26) May, A. F.; Toberer, E. S.; Saramat, A.; Snyder, G. J. Characterization and Analysis of Thermoelectric Transport in n-Type $Ba_8Ga_{16-x}Ge_{30+x}$. *Phys. Rev. B: Condens. Matter Mater. Phys.* **2009**, *80*, 125205.
(27) Li, D.; Zhao, H.; Li, S.; Wei, B.; Shuai, J.; Shi, C.; Xi, X.; Sun, P.; Meng, S.; Gu, L.; Ren, Z.; Chen, X. Atomic Disorders Induced by Silver and Magnesium Ion Migrations Favor High Thermoelectric Performance in α-MgAgSb-Based Materials. *Adv. Funct. Mater.* **2015**, *25*, 6478−6488.
(28) Shuai, J.; Wang, Y.; Liu, Z.; Kim, H. S.; Mao, J.; Sui, J.; Ren, Z. Enhancement of Thermoelectric Performance of Phase Pure Zintl Compounds $Ca_{1-x}Yb_xZn_2Sb_2$, $Ca_{1-x}Eu_xZn_2Sb_2$, and $Eu_{1-x}Yb_xZn_2Sb_2$ by Mechanical Alloying and Hot Pressing. *Nano Energy* **2016**, *25*, 136−144.
(29) Poudel, B.; Hao, Q.; Ma, Y.; Lan, Y.; Minnich, A.; Yu, B.; Yan, X.; Wang, D.; Muto, A.; Vashaee, D.; Chen, X.; Liu, J.; Dresselhaus, M. S.; Chen, G.; Ren, Z. High-Thermoelectric Performance of Nanostructured Bismuth Antimony Telluride Bulk Alloys. *Science* **2008**, *320*, 634−638.
(30) Riffel, M.; Schilz, J. Mechanically Alloyed $Mg_2Si_{1-x}Sn_x$ Solid Solutions as Thermoelectric Materials. *Fifteenth International Conference on Thermoelectrics*; 1996; pp 133−136.
(31) Clark, C. R.; Wright, C.; Suryanarayana, C.; Baburaj, E. G.; Froes, F. H. Synthesis of Mg_2X (X = Si, Ge, or Sn) Intermetallics by Mechanical Alloying. *Mater. Lett.* **1997**, *33*, 71−75.
(32) You, S.-W.; Kim, I.-H.; Choi, S.-M.; Seo, W.-S.; Kim, S.-U. Solid-State Synthesis and Thermoelectric Properties of $Mg_2Si_{1-x}Sn_x$. *J. Electron. Mater.* **2013**, *42*, 1490−1494.
(33) You, S.-W.; Kim, I.-H.; Choi, S.-M.; Seo, W.-S. Thermoelectric Properties of Bi-doped $Mg_2Si_{1-x}Sn_x$ Prepared by Mechanical Alloying. *J. Korean Phys. Soc.* **2013**, *63*, 2153−2157.
(34) You, S.-W.; Kim, I.-H.; Choi, S.-M.; Seo, W.-S. Thermoelectric Properties of Sb-doped $Mg_2Si_{1-x}Sn_x$ Prepared by Mechanical Alloying and Hot Pressing. *Journal of Ceramic Processing Research* **2014**, *15*, 398−402.
(35) Hu, X.; Barnett, M. R.; Yamamoto, A. Synthesis of Al-doped $Mg_2Si_{1-x}Sn_x$ Compound Using Magnesium Alloy for Thermoelectric Application. *J. Alloys Compd.* **2015**, *649*, 1060−1065.
(36) Saparamadu, U.; Mao, J.; Dahal, K.; Zhang, H.; Tian, F.; Song, S.; Liu, W.; Ren, Z. The Effect of Charge Carrier and Doping Site on Thermoelectric Properties of $Mg_2Sn_{0.75}Ge_{0.25}$. *Acta Mater.* **2017**, *124*, 528−535.
(37) de Boor, J.; Saparamadu, U.; Mao, J.; Dahal, K.; Müller, E.; Ren, Z. Thermoelectric Performance of Li doped, p-type $Mg_2(Ge,Sn)$ and Comparison with $Mg_2(Si,Sn)$. *Acta Mater.* **2016**, *120*, 273−280.
(38) Liu, W.; Chi, H.; Sun, H.; Zhang, Q.; Yin, K.; Tang, X.; Zhang, Q.; Uher, C. Advanced Thermoelectrics Governed by a Single Parabolic Band: $Mg_2Si_{0.3}Sn_{0.7}$, a Canonical Example. *Phys. Chem. Chem. Phys.* **2014**, *16*, 6893−6897.
(39) Gao, P.; Berkun, I.; Schmidt, R. D.; Luzenski, M. F.; Lu, X.; Bordon Sarac, P.; Case, E. D.; Hogan, T. P. Transport and Mechanical Properties of High-ZT $Mg_{2.08}Si_{0.4-x}Sn_{0.6}Sb_x$ Thermoelectric Materials. *J. Electron. Mater.* **2014**, *43*, 1790−1803.
(40) Zheng, L.; Zhang, X.; Liu, H.; Li, S.; Zhou, Z.; Lu, Q.; Zhang, J.; Zhang, F. Optimized Nanostructure and Thermoelectric Performances of $Mg_2(Si_{0.4}Sn_{0.6})Sb_x$ Solid Solutions by In Situ Nanophase Generation. *J. Alloys Compd.* **2016**, *671*, 452−457.
(41) Søndergaard, M.; Christensen, M.; Borup, K. A.; Yin, H.; Iversen, B. B. Thermal Stability and Thermoelectric Properties of $Mg_2Si_{0.4}Sn_{0.6}$ and $Mg_2Si_{0.6}Sn_{0.4}$. *J. Mater. Sci.* **2013**, *48*, 2002−2008.
(42) Bellanger, P.; Gorsse, S.; Bernard-Granger, G.; Navone, C.; Redjaimia, A.; Vivès, S. Effect of Microstructure on the Thermal Conductivity of Nanostructured $Mg_2(Si,Sn)$ Thermoelectric Alloys: An Experimental and Modeling Approach. *Acta Mater.* **2015**, *95*, 102−110.
(43) Liu, W.; Tang, X.; Sharp, J. Low-Temperature Solid State Reaction Synthesis and Thermoelectric Properties of High-Performance and Low-Cost Sb-doped $Mg_2Si_{0.6}Sn_{0.4}$. *J. Phys. D: Appl. Phys.* **2010**, *43*, 085406.
(44) Liu, Z.; Shuai, J.; Mao, J.; Wang, Y.; Wang, Z.; Cai, W.; Sui, J.; Ren, Z. Effects of Antimony Content in $MgAg_{0.97}Sb_x$ on Output Power and Energy Conversion Efficiency. *Acta Mater.* **2016**, *102*, 17−23.
(45) Platzek, D.; Karpinski, G.; Drasar, C.; Mueller, E. Seebeck Scanning Microprobe for Thermoelectric FGM. *Mater. Sci. Forum* **2005**, *492*−*493*, 587−592.
(46) de Boor, J.; Stiewe, C.; Ziolkowski, P.; Dasgupta, T.; Karpinski, G.; Lenz, E.; Edler, F.; Mueller, E. High-Temperature Measurement of Seebeck Coefficient and Electrical Conductivity. *J. Electron. Mater.* **2013**, *42*, 1711−1718.
(47) de Boor, J.; Müller, E. Data Analysis for Seebeck Coefficient Measurements. *Rev. Sci. Instrum.* **2013**, *84*, 065102.
(48) Borup, K. A.; de Boor, J.; Wang, H.; Drymiotis, F.; Gascoin, F.; Shi, X.; Chen, L.; Fedorov, M. I.; Mueller, E.; Iversen, B. B.; Snyder, G. J. Measuring Thermoelectric Transport Properties of Materials. *Energy Environ. Sci.* **2015**, *8*, 423−435.
(49) van der Pauw, L. A Method of Measuring Specific Resistivity and Hall Effect of Discs of Arbitrary Shape. *Philips Res. Rep* **1958**, *13*, 1−9.
(50) Gale, W. F. *Mechanical Properties of Metals and Alloys A2. Smithells Metals Reference Book*, 8th ed.; Totemeier, T. C., Ed.; Butterworth-Heinemann: Oxford, 2004; pp 22-1−22-162.
(51) Hopcroft, M. A.; Nix, W. D.; Kenny, T. W. What is the Young's Modulus of Silicon? *J. Microelectromech. Syst.* **2010**, *19*, 229−238.
(52) Aizawa, T.; Song, R. Mechanically Induced Reaction for Solid-State Synthesis of Mg_2Si and Mg_2Sn. *Intermetallics* **2006**, *14*, 382−391.
(53) Song, R. B.; Aizawa, T.; Sun, J. Q. Synthesis of $Mg_2Si_{1-x}Sn_x$ Solid Solutions as Thermoelectric Materials by Bulk Mechanical Alloying and Hot Pressing. *Mater. Sci. Eng., B* **2007**, *136*, 111−117.
(54) Jung, I.-H.; Kang, D.-H.; Park, W.-J.; Kim, N. J.; Ahn, S. Thermodynamic Modeling of the Mg−Si−Sn System. *CALPHAD: Comput. Coupling Phase Diagrams Thermochem.* **2007**, *31*, 192−200.
(55) Kim, H.-S.; Gibbs, Z. M.; Tang, Y.; Wang, H.; Snyder, G. J. Characterization of Lorenz Number with Seebeck Coefficient Measurement. *APL Mater.* **2015**, *3*, 041506.
(56) Jiang, G.; He, J.; Zhu, T.; Fu, C.; Liu, X.; Hu, L.; Zhao, X. High Performance $Mg_2(Si,Sn)$ Solid Solutions: a Point Defect Chemistry Approach to Enhancing Thermoelectric Properties. *Adv. Funct. Mater.* **2014**, *24*, 3776−3781.
(57) Bux, S. K.; Blair, R. G.; Gogna, P. K.; Lee, H.; Chen, G.; Dresselhaus, M. S.; Kaner, R. B.; Fleurial, J.-P. Nanostructured Bulk Silicon as an Effective Thermoelectric Material. *Adv. Funct. Mater.* **2009**, *19*, 2445−2452.
(58) Hu, L.; Zhu, T.; Liu, X.; Zhao, X. Point Defect Engineering of High-Performance Bismuth-Telluride-Based Thermoelectric Materials. *Adv. Funct. Mater.* **2014**, *24*, 5211−5218.
(59) de Boor, J.; Compere, C.; Dasgupta, T.; Stiewe, C.; Kolb, H.; Schmitz, A.; Mueller, E. Fabrication Parameters for Optimized Thermoelectric Mg_2Si. *J. Mater. Sci.* **2014**, *49*, 3196−3204.

DOI: 10.1021/acsaem.7b00128
ACS Appl. Energy Mater. 2018, 1, 531−542

(60) Tan, X. J.; Liu, W.; Liu, H. J.; Shi, J.; Tang, X. F.; Uher, C. Multiscale Calculations of Thermoelectric Properties of n-Type $Mg_2Si_{1-x}Sn_x$ Solid Solutions. *Phys. Rev. B: Condens. Matter Mater. Phys.* **2012**, *85*, 205212.
(61) Søndergaard, M.; Christensen, M.; Borup, K. A.; Yin, H.; Iversen, B. B. Gravity-Induced Gradients in Thermoelectric $Mg_2Si_{0.9925-x}Sn_xSb_{0.0075}$. *Acta Mater.* **2012**, *60*, 5745−5751.
(62) Liu, W.-S.; Zhang, B.-P.; Li, J.-F.; Zhao, L.-D. Thermoelectric Property of Fine-Grained $CoSb_3$ Skutterudite Compound Fabricated by Mechanical Alloying and Spark Plasma Sintering. *J. Phys. D: Appl. Phys.* **2007**, *40*, 566.
(63) Pedersen, B. L.; Birkedal, H.; Iversen, B. B.; Nygren, M.; Frederiksen, P. T. Influence of Sample Compaction on the Thermoelectric Performance of Zn_4Sb_3. *Appl. Phys. Lett.* **2006**, *89*, 242108.
(64) Falkenbach, O.; Schmitz, A.; Dankwort, T.; Koch, G.; Kienle, L.; Müller, E.; Schlecht, S. Influence of Mechanochemical Syntheses and Compacting Methods on the Thermoelectric Properties of Nanostructured $AgSn_mSbTe_{2+m}$ (TAST-m). *Semicond. Sci. Technol.* **2014**, *29*, 124009.

DOI: 10.1021/acsaem.7b00128
ACS Appl. Energy Mater. 2018, 1, 531−542

Chapter 7 Attempt to modify the electronic band structure in Mg_2X (X: Si, Sn) for an optimization of thermoelectric properties

7.1 Summary

In a quest to improve the TE performance, Bourgeois *et al.* [163] computationally studied the effect of the substitution of different transition elements in Mg_2X materials. They concluded that substituting Mg with scandium can modify the electronic band structure by increasing the density-of-states (DOS) near the conduction band (CB) edge and shifting the Fermi level towards the CB edge. Increasing DOS could lead to a large DOS mass m_D^*, thus enhancing the Seebeck coefficient and corresponding TE performance of Mg_2X solid solutions. Accordingly, $Sc_xMg_{2-x}Si_{0.4}Sn_{0.6}$ with $x = 0.01, 0.05$ were prepared using mechanical alloying and characterized using XRD and SEM. The results showed that the synthesized samples were phase pure while the microstructure analysis revealed the presence of scandium silicide phases. The effect of Sc on the TE properties can be observed only if the formation of scandium silicide phases is prevented. Therefore, $Sc_xMg_{2-x}Sn$ with $x = 0.01, 0.05$ were synthesized. XRD and SEM investigations showed the presence of scandium stannide phases (Sc_5Sn_3 and $ScSn_2$) and unreacted tin. The formation of scandium stannide phases agrees with the Sc-Sn equilibrium phase diagram. The observed unreacted tin is not unexpected as the Mg loss is plausibly strong at sintering temperature, such that the Mg concentration taken for the synthesis of Mg_2Sn is not sufficient to form a phase pure material. Note that 7.5 % excess Mg was used for the formation of undoped and Sc-doped Mg_2Sn, which resulted in a nominal stoichiometry of $Mg_{2.15}Sn$. Temperature dependent thermoelectric properties of scandium-added (but not substituted) $Sc_xMg_2Si_{0.4}Sn_{0.6}$ and Sc_xMg_2Sn showed semiconductor behavior with intrinsic charge carrier activation. Thus, Sc was found to be inefficient as a dopant on the Mg site in Mg_2X materials.

7.2 CRediT (Contributor Roles Taxonomy) author statement

Aryan Sankhla: Conceptualization, Methodology, Validation, Formal analysis, Investigation, Writing – original draft, Visualization. **Mohammad Yasseri:** Validation, Investigation. **Hasbuna Kamila:** Resources, Validation. **Eckhard Mueller:** Writing – review & editing, Supervision. **Johannes de Boor:** Conceptualization, Methodology, Writing – review & editing, Supervision, Project administration, Funding acquisition.

Journal of Applied Physics ARTICLE scitation.org/journal/jap

Experimental investigation of the predicted band structure modification of Mg_2X (X: Si, Sn) thermoelectric materials due to scandium addition

Cite as: J. Appl. Phys. **125**, 225103 (2019); doi: 10.1063/1.5089720
Submitted: 22 January 2019 · Accepted: 16 May 2019 ·
Published Online: 11 June 2019

View Online Export Citation CrossMark

Aryan Sankhla,[1,a)] Mohammad Yasseri,[1,2] Hasbuna Kamila,[1] Eckhard Mueller,[1,2] and Johannes de Boor[1,a)]

AFFILIATIONS

[1]Institute of Materials Research, Linder Hoehe, German Aerospace Center (DLR), D-51170 Koeln, Germany
[2]Institute of Inorganic and Analytical Chemistry, Justus Liebig University of Giessen, D-35392 Giessen, Germany

Note: This paper is part of the special topic on Advanced Thermoelectrics.
[a)]**Authors to whom correspondence should be addressed:** Aryan.Sankhla@dlr.de and Johannes.deBoor@dlr.de

ABSTRACT

Modification of the electronic band structure via doping is an effective way to improve the thermoelectric properties of a material. Theoretical calculations from a previous study have predicted that Sc substitution on the Mg site in Mg_2X materials drastically increase their Seebeck coefficient. Herein, we experimentally studied the influence of scandium substitution on the thermoelectric properties of $Mg_2Si_{0.4}Sn_{0.6}$ and Mg_2Sn. We found that the thermoelectric properties of these materials are unaffected by Sc addition, and we did not find hints for a modification of the electronic band structure. The SEM-energy dispersive X-ray analysis revealed that the scandium does not substitute Mg but forms a secondary phase (Sc-Si) in $Mg_2Si_{0.4}Sn_{0.6}$ and remains inert in Mg_2Sn, respectively. Thus, this study proves that scandium is an ineffective dopant for Mg_2X materials.

Published under license by AIP Publishing. https://doi.org/10.1063/1.5089720

INTRODUCTION

Solid state devices fabricated from thermoelectric materials, which use waste heat to generate electrical power, are an effective way to increase the energy efficiency of various micro-/macrodevices.[1] They are currently being utilized in the automotive industry.[2] Furthermore, thermoelectric generators serve as an energy source where usual electric power supply is impossible, such as in space-probes.[3] Significant progress has been made in the past two decades in increasing the thermoelectric efficiency. This progress is achieved by exploiting fundamental concepts such as electronic band structure modification (carrier pocket engineering, band convergence, and resonant dopant levels), the scattering of phonons at nano-/microscale, size effect/quantum confinement, and self-optimization of carrier concentration.[4–8] These modifications have been applied to various thermoelectric material classes including magnesium silicides and its solid solutions (Mg_2X; X: Si, Sn, and Ge).[9,10] This promising class of material is very attractive, comprising features that include precursor abundance, lightweight, high thermoelectric performance ($zT \sim 1.1$–1.5), and environmental compatibility. The common strategies to increase the performance of thermoelectric materials such as the optimization of dopant concentration, alloying, and synthesizing solid solutions resulting in mass fluctuation to lower the thermal conductivity have already been applied successfully.[11–13] Apart from them, there have been attempts to modify the band structure by introducing various impurity atoms, with the aim to increase the thermoelectric performance of these materials further. In the quest for suitable/novel dopants, different theoretical and experimental studies have been performed. However, the theoretical studies do not provide a complete picture until an experimental confirmation is achieved. A lot of work has been dedicated to the X site in Mg_2X materials; however, only few impurity elements have been tried on the Mg site. Zhang *et al.* doped Co on the Mg site in $Mg_2(Si_{0.3}Sn_{0.7})_{1-y}Sb_y$ which resulted in the formation of CoSi as a secondary phase and

Published under license by AIP Publishing.

Journal of Applied Physics ARTICLE scitation.org/journal/jap

the samples behaved as intrinsic semiconductors.[14] Similarly, Sakamoto *et al.* and Zhao attempted doping Al, Cu, and Zn on the magnesium site in Mg_2Si materials, respectively.[14,15] Meng *et al.* doped yttrium (Y) possibly on the Mg site to observe an enhancement in the thermoelectric properties.[16] However, most of the previous studies did not give a clear picture on the influence of dopant substitution on the thermoelectric properties of the Mg_2X material (s). This is because often the dopant(s) tend(s) to form secondary phase(s) in a matrix or their role as an impurity is not fully understood, as they are co-doped with other impurity atoms (usually Sb or Bi). The notion of band structure modification and, in particular, resonant states in thermoelectric materials to increase their efficiency was introduced in the last decade.[17,18] Since then, several research groups have succeeded in exploiting this concept by the introduction of suitable dopants such as Tl in PbTe, Al in PbSe, V in $Hf_{0.75}Zr_{0.25}NiSn$, and recently Sn in As_2Te_3.[18–21] Bourgeois *et al.* reported in a density functional theoretical (DFT) study that transition metals could be prospective dopants on the Mg site. In particular, scandium (Sc) substitution could cause a shift in the Fermi level toward the conduction band and modify the density of states near the Fermi level, resulting in an increase in the Seebeck coefficient.[22] Moreover, Meng *et al.* also attempted doping scandium in Mg_2Si but were unable to make a proper conclusion on the effect of Sc on the thermoelectric properties of Mg_2Si.[16] In this study, we present experimental results and discuss the implications of doping scandium on the magnesium site (tetrahedral sites) in Mg_2X based materials.

MATERIAL AND METHODS

The scandium doped solid solutions of magnesium tin silicide ($Mg_2Si_{0.4}Sn_{0.6}$) and binary magnesium stannide (Mg_2Sn) were synthesized using commercially available starting elements [Mg turnings (Merck), Si (<6 mm, Chempure), Sn (<71 μm, Merck), Sc pieces (Chempure), and Sb (5 mm, Alfa Aesar)], all with purity >99.5%. A high energy ball mill (SPEX 8000D Shaker Mill) was used with stainless steel vials and balls. The elements were weighed according to the desired compositions with stoichiometries $Sc_xMg_{2-x}Si_{0.4}Sn_{0.6}$, $Sc_xMg_{2-x}Sn$ (x = 0.01, 0.05) and $Sc_xMg_{2.06-x}Sn_{1-y}Sb_y$ (x = 0.05, y = 0.03), respectively. The elemental precursors of $Sc_xMg_{2-x}Si_{0.4}Sn_{0.6}$ were mechanically alloyed for 20 h and 12 h for $Sc_xMg_{2-x}Sn$ and $Sc_xMg_{2.06-x}Sn_{1-y}Sb_y$ compositions, respectively. The powder handling during the synthesis was done under argon (Glove box; MBraun MB200) to prevent oxidation and contamination. The temperature/holding time to sinter the powder samples was 973 K/20 min for $Sc_xMg_{2-x}Si_{0.4}Sn_{0.6}$ samples and 873 K/10 min. for $Sc_xMg_{2-x}Sn$ and $Sc_xMg_{2.06-x}Sn_{1-y}Sb_y$ samples, respectively. A systematic study of optimal sintering temperature vs Si:Sn content can be found in Ref. 23. The powder samples were sintered by a direct-current sintering press (DSP 510 SE) from Dr. Fritsch GmbH. The sintering was performed using a graphite mold Ø12.7 mm under vacuum (~10^{-5} bar) at a heating rate of 1 K s^{-1}. The density of the compacted samples was measured using Archimedes' method. The relative densities of the pellets were >95% of the theoretical values ($Mg_2Si_{0.4}Sn_{0.6}$: 3.06 g cm^{-3} and Mg_2Sn: 3.59 g cm^{-3}), respectively. The XRD measurements on the samples were done utilizing a Siemens D5000 Bragg-Brentano diffractometer with a secondary monochromator. The parameters used were CuK_α radiation (1.5406 Å) in the 2θ range 20°–80° with a step size of 0.01°. The SEM analysis was done by a Zeiss Ultra 55 system equipped with an energy dispersive X-ray (EDS) detector. Moreover, the temperature dependent electronic properties were measured utilizing an in-house developed facility utilizing a four-probe technique.[24,25] The thermal diffusivity (α) of the pellets was obtained using a Netzsch LFA 467HT apparatus. The thermal conductivity (κ) was obtained using the relation $\kappa = \alpha\rho C_P$, where ρ and C_P are sample density and heat capacity, respectively. The C_P value was obtained from the Dulong-Petit limit for c_V^{DP}: $C_p = c_V^{DP} + \frac{9E_t^2T}{\beta_T\rho}$, $E_t^{Mg_2Si_{0.4}Sn_{0.6}}$ 1.7 10 ^{5} K ^{1} and $\beta_T^{Mg_2Si_{0.4}Sn_{0.6}}$ 2.07 10 ^{11} Pa ^{1}, and $E_t^{Mg_2Sn}$ 2.97 10 ^{5} K ^{1} and $\beta_T^{Mg_2Sn}$ 2.4 10 ^{11} Pa ^{1} are the linear coefficient of thermal expansion and the isothermal compressibility for $Mg_2Si_{0.4}Sn_{0.6}$ and Mg_2Sn, respectively.[26,27] We found that the samples doped with Sc were more fragile than samples without Sc. The measurement error uncertainties for S, σ, and κ are ±5%, ±5%, and ±8%, respectively. The error bars are shown for one sample only for better visibility of the thermoelectric data. The room temperature Hall coefficient (R_H) of different samples was determined using an in-house facility in a van der Pauw configuration under a varying magnetic field of maximum ±0.5 T. The Hall carrier concentration n_H was estimated from R_H assuming a single carrier type. The measurement uncertainties for n_H are ±10%.

RESULTS

The $Sc_{0.01}Mg_{1.99}Si_{0.4}Sn_{0.6}$ and $Sc_{0.05}Mg_{1.95}Si_{0.4}Sn_{0.6}$ samples are phase pure XRD-wise with no presence of secondary phases. The diffractograms of these samples were indexed by the ICSD standard pattern for $Mg_2Si_{0.4}Sn_{0.6}$ (ICSD PDF number 01-089-4254) confirming the formation of the desired phase (fcc, space group *Fm3m*) [Fig. 1(a)]. The $Sc_{0.01}Mg_{1.99}Sn$, $Sc_{0.05}Mg_{1.95}Sn$, and $Sc_{0.05}Mg_{2.01}Sn_{0.97}Sb_{0.03}$ samples were indexed by the ICSD standard pattern for Mg_2Sn (ICSD PDF number 01-071-9596 65-2997) Fig. 1(b). The main phase was determined to be Mg_2Sn with the presence of elemental peaks of Sn and some peaks of scandium stannide phases (Sc_5Sn_3 and $ScSn_2$) in the XRD patterns of $Sc_{0.01}Mg_{1.99}Sn$, $Sc_{0.05}Mg_{1.95}Sn$, and $Sc_{0.05}Mg_{2.01}Sn_{0.97}Sb_{0.03}$ samples, respectively.

We have tabulated the lattice constants (Table I) of the $Mg_2Si_{0.4}Sn_{0.6}$ and Mg_2Sn samples doped with scandium. We find no change in the values of the lattice constants with increasing dopant concentration. The constant lattice parameter suggests no dopant incorporation to the parent compound.

EDS mappings were performed on the samples with compositions $Sc_{0.05}Mg_{1.95}Si_{0.4}Sn_{0.6}$ and $Sc_{0.05}Mg_{1.95}Sn$ as shown in Fig. 2. In Fig. 2(a), it is observed that the scandium in the sample reacts with silicon to form a Sc-Si based the secondary phase. In the latter sample, the scandium largely remains unreacted as an elemental impurity, as seen in Fig. 2(b). Moreover, the EDS point analysis on the $Sc_{0.05}Mg_{1.95}Sn$ sample revealed the presence of $ScSn_2$ islands which agree with the XRD pattern. For both sample types, Sc is thus observed only outside of the matrix phase. This is in agreement with the constancy of the lattice constant vs Sc content. Moreover, the secondary phase present in $Sc_{0.05}Mg_{1.95}Si_{0.4}Sn_{0.6}$ and $Sc_{0.05}Mg_{1.95}Sn$ was determined by the backscattered image contrast, and area-wise quantified to be 2.2% and 1.4%, respectively.[28]

Published under license by AIP Publishing.

Journal of Applied Physics ARTICLE scitation.org/journal/jap

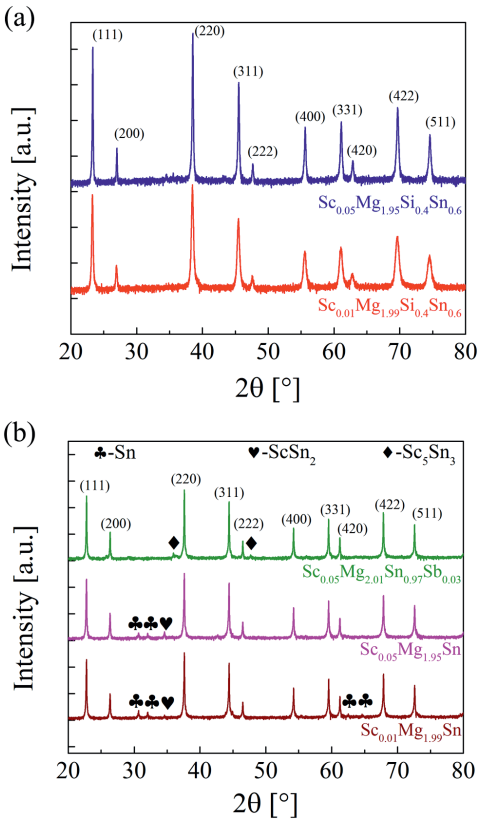

FIG. 1. XRD patterns of (a) $Sc_{0.01}Mg_{1.99}Si_{0.4}Sn_{0.6}$ and $Sc_{0.05}Mg_{1.95}Si_{0.4}Sn_{0.6}$ and (b) $Sc_{0.01}Mg_{1.99}Sn$, $Sc_{0.05}Mg_{1.95}Sn$, and $Sc_{0.05}Mg_{2.01}Sn_{0.97}Sb_{0.03}$ samples.

TABLE I. List of sample compositions, their lattice constants, and relative sample densities.

Composition	Lattice constant (Å)	Relative sample density (%)
$Sc_{0.01}Mg_{1.99}Si_{0.4}Sn_{0.6}$	6.528	97.8
$Sc_{0.05}Mg_{1.95}Si_{0.4}Sn_{0.6}$	6.528	98.4
$Sc_{0.01}Mg_{1.99}Sn$	6.692	98.6
$Sc_{0.05}Mg_{1.95}Sn$	6.692	100.8
$Sc_{0.05}Mg_{2.01}Sn_{0.97}Sb_{0.03}$	6.692	97.7

The temperature dependence of Seebeck coefficient and electrical conductivity data for all the samples shown in Fig. 3 follows the trend corresponding to an intrinsic semiconductor. We observe a slight lowering of the Seebeck coefficient with an increase in dopant concentration and a subtle increase in the electrical conductivity near room temperature. The change in Seebeck coefficient/electrical conductivity near room temperature could be possibly due to the presence of secondary phases, as observed from the SEM/EDS data (as both Sc_5Si_3 and ScSi have quite high electrical conductivity[29]).

We observe from Fig. 3(c) that the thermal conductivity for all the samples shows a similar trend with first a decrease with temperature and then an increase due to the bipolar effect of intrinsic charge carriers at temperatures around 500 K. Mainly as a result of the increased electrical conductivity, the zT_{max} (~0.19) values get almost doubled with an increase of Sc concentration in $Sc_xMg_{2-x}Si_{0.4}Sn_{0.6}$.

As observed from the SEM, the formation of scandium silicide secondary phase in $Sc_{0.05}Mg_{1.95}Si_{0.4}Sn_{0.6}$ prevented an evaluation of the influence of scandium in the parent compound. The Si-Sc phase diagram points out that there could be a formation of Sc_5Si_3 and ScSi phases for Si-Sc.[30] Thus, to observe an effect of scandium on the thermoelectric properties of Mg_2X materials, we investigated the binary Mg_2Sn compound and doped it with different concentrations of scandium. The temperature dependent transport data can be observed from Fig. 4. It can be seen that the undoped sample has a positive Seebeck coefficient at room temperature, while the samples with Sc exhibit a negative Seebeck coefficient. This, together with the temperature dependence of the electrical conductivity, indicates that all three samples have mixed conduction with the Sc samples having a higher number of electrons. This could be due to very inefficient doping of Sc or due to a change of the intrinsic defect concentrations, induced by the addition of Sc or the change in Sc:Mg ratio.[10] In order to check for any modification of the electronic band structure of Sc (even if not acting as an efficient dopant), we co-doped the 2.5% Sc-doped Mg_2Sn sample with 3% Sb and compared it with the 3% Sb-doped Mg_2Sn sample. The electronic transport properties for both of these samples were found to be almost identical. This suggests that there is no influence of Sc doping on the thermoelectric properties of Mg_2X based materials. Thus, this experimental observation contradicts the theoretical work on Mg_2X claiming Sc being a prospective dopant.[22] We utilized high energy ball milling as the synthesis technique for $Mg_2(Si,Sn)$ and Mg_2Sn, which is known for its high dopant efficiency in comparison to other techniques.[11,31]

DISCUSSION

The band structure simulations for scandium doped Mg_2X materials suggest that scandium (Sc) is a potential dopant. However, taking other aspects into account such as formation enthalpies, phase diagram analysis, etc., it is observed that for Sc-doped $Mg_2(Si,Sn)$ materials, scandium favorably reacts with silicon rather than substituting magnesium. This is in accordance with quite high formation enthalpies of ScSi [-117.2 kJ mol^{-1} (at 298 K) and -87.1 ± 2.1 kJ mol^{-1} (825–1045 K)] and of Sc_5Si_3 [-161.1 kJ mol^{-1} (at 298 K) and -102.8 ± 3.2 kJ mol^{-1} (835–895 K)].[32]

Published under license by AIP Publishing.

Journal of Applied Physics ARTICLE scitation.org/journal/jap

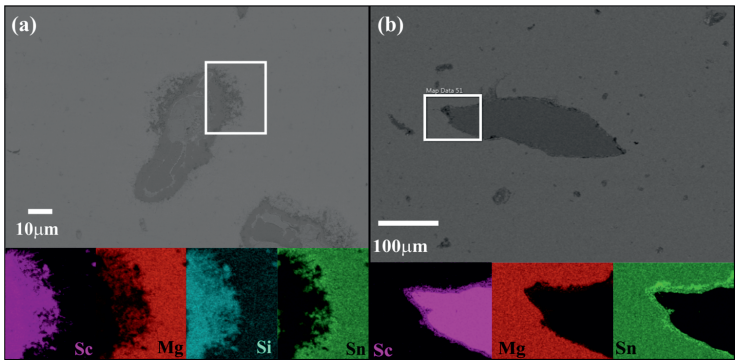

FIG. 2. EDS mapping on (a) $Sc_{0.05}Mg_{1.95}Si_{0.4}Sn_{0.6}$ and (b) $Sc_{0.05}Mg_{1.95}Sn$ samples. In the sample with composition $Sc_{0.05}Mg_{1.95}Si_{0.4}Sn_{0.6}$, a region with the presence of scandium and silicon can be seen clearly. On further point analysis, it reveals a composition close to Sc_5Si_3 and some excess unreacted silicon. In the sample with composition $Sc_{0.05}Mg_{1.95}Sn$, scandium stays unreacted and can be observed as a secondary phase.

This also suggests that the formed Sc-Si phase would probably be Sc_5Si_3.[30] Qualitatively, the Sc-Si phases have a higher room temperature electrical conductivity values than Mg_2X materials which possibly explains the subtle variations in the properties at near room temperature of Sc-doped $Mg_2Si_{0.4}Sn_{0.6}$ materials.[29] However, this cannot be quantified since these secondary phases are not present continuously throughout the samples. We doped binary Mg_2Sn (without Si) with Sc to avoid the formation of scandium silicide phase as in $Mg_2(Si,Sn)$. Even though the Sn-Sc phase diagram indicates the existence of Sc_5Sn_3 and $ScSn_2$ phases, these phases have lower formation energy (Sc_5Sn_3: -56.04 kJ mol^{-1} and $ScSn_2$: -44.9 kJ mol^{-1})[33] than Sc-Si phases. Therefore, it was previously unclear whether scandium substitutes Mg in Mg_2Sn, forms a Sn-Sc secondary phase or remains inert. The $Sc_xMg_{2-x}Sn$ samples

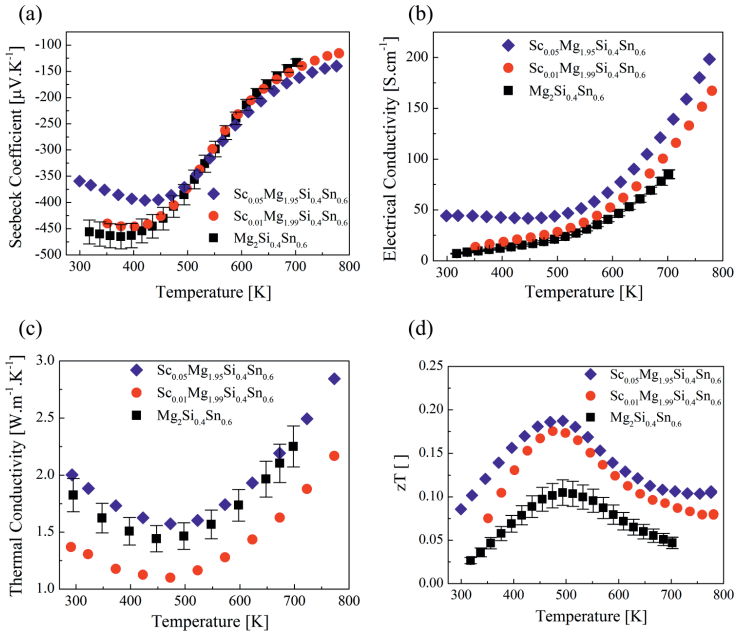

FIG. 3. Temperature dependent (a) Seebeck coefficient, (b) electrical conductivity, (c) thermal conductivity, and (d) figure-of-merit (zT) of undoped, $Sc_{0.01}Mg_{1.99}Si_{0.4}Sn_{0.6}$, and $Sc_{0.05}Mg_{1.95}Si_{0.4}Sn_{0.6}$ samples.

Published under license by AIP Publishing.

Journal of Applied Physics ARTICLE scitation.org/journal/jap

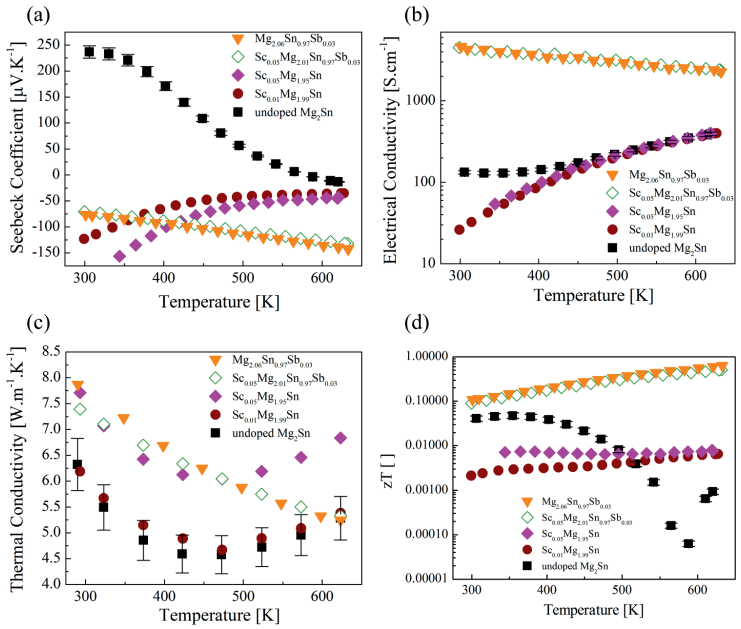

FIG. 4. Temperature dependent (a) Seebeck coefficient, (b) electrical conductivity, (c) thermal conductivity, and (d) figure-of-merit (zT) of undoped, $Sc_{0.01}Mg_{1.99}Sn$, $Sc_{0.05}Mg_{1.95}Sn$, $Sc_{0.05}Mg_{2.01}Sn_{0.97}Sb_{0.03}$, and $Mg_{2.06}Sn_{0.97}Sb_{0.03}$ samples, respectively. The Y-axis of the electrical conductivity and estimated zT plots has a logarithmic scale for better visualization of the data.

show a weak n-type character at room temperature. This n-type character of the samples could possibly be a result of either elemental Sc that has a Seebeck coefficient between −6 and −10 μV K^{-1}[34,35] or due to a change in the intrinsic defect concentration that leads to a change in character from a p-type to an n-type material. A similar effect was observed by Liu *et al.* in their study on the Ga doping in p-type $Mg_2Si_{0.3}Sn_{0.7}$ material.[36] This weak n-type nature of these samples can be a combination of both the aforementioned effects. We also carried out room temperature Hall measurements (n_H) on both Sc-doped $Mg_2Si_{0.4}Sn_{0.6}$ and Sc-doped Mg_2Sn samples to observe an effect of scandium addition to the stoichiometry. The values are tabulated in Table II. However, we found negligible change to the magnitude of n_H for these "doped" samples in comparison with the carrier concentration of their respective undoped samples. The $Sc_{0.05}Mg_{2.01}Sn_{0.97}Sb_{0.03}$ sample showed poor mechanical strength and the Hall measurement was, therefore, not feasible on this sample. We estimated n_H for this sample from the Seebeck coefficient by employing a single parabolic band (SPB) model in the following manner. First, we obtained a density-of-states effective mass m_D^*=2.0m_0 for $Mg_{2.06}Sn_{0.97}Sb_{0.03}$ using the experimental value of the Seebeck coefficient to obtain the reduced chemical potential η from $S = \frac{k}{e}\left(\frac{2F_1(\eta)}{F_0(\eta)} - \eta\right)$ and then m_D^* was obtained from $n = 4\pi\left(\frac{2m_D^* k_B T}{h^2}\right)^{\frac{3}{2}} F_{0.5}(\eta)$. $F_j(\eta)$ are the Fermi integrals and n is related to the experimentally obtained Hall carrier concentration n_H by $n = n_H.r_H$ with $r_H = \frac{3}{2}.F_{0.5}(\eta)\frac{F_{-0.5}(\eta)}{2F_0^2(\eta)}$. These equations assume an SPB with mobility limited by acoustic phonon scattering [scattering parameter ($\lambda = 0$)]. Finally, the obtained value of m_D^*=2.0m_0 was used to estimate n of $Sc_{0.05}Mg_{2.01}Sn_{0.97}Sb_{0.03}$ from the measured S value and the above equations.

TABLE II. Sample compositions, Seebeck coefficient at room temperature, theoretical carrier concentration, and Hall carrier concentration of scandium and antimony doped Mg_2X (X: Si, Sn) samples. The value marked with an asterisk was estimated using a single parabolic band model using the room temperature Seebeck coefficient values of that sample.

Composition	Seebeck coefficient (μV K^{-1})	Theoretical n (10^{19}) (cm^{-3})	n_H (10^{19}) (cm^{-3})
$Mg_2Si_{0.4}Sn_{0.6}$			
Undoped $Mg_2Si_{0.4}Sn_{0.6}$	−425	…	0.2
$Sc_{0.01}Mg_{1.99}Si_{0.4}Sn_{0.6}$	−401	14.3	0.22
$Sc_{0.05}Mg_{1.95}Si_{0.4}Sn_{0.6}$	−343	71.8	0.56
Mg_2Sn			
Undoped Mg_2Sn	243	…	0.57
$Sc_{0.01}Mg_{1.99}Sn$	−125	13.3	0.59
$Sc_{0.05}Mg_{1.95}Sn$	−218	66.7	0.47
$Sc_{0.05}Mg_{2.01}Sn_{0.97}Sb_{0.03}$	−69	107	44*
$Mg_{2.06}Sn_{0.97}Sb_{0.03}$	−74	39	38

Published under license by AIP Publishing.

Journal of Applied Physics ARTICLE scitation.org/journal/jap

The theoretical carrier concentration was calculated assuming that one scandium atom substitutes one magnesium atom and one antimony atom substitutes one tin atom in the lattice of the complete crystal of the compound(s), respectively, both effectively providing one additional electron. The total number of atoms in a crystal was estimated from the lattice constant corresponding to the most significant peak in the XRD pattern of each sample. The theoretical carrier concentration of $Mg_{2.06}Sn_{0.97}Sb_{0.03}$ sample was estimated using the literature values of the lattice constant for Mg_2Sn.[37] Thus, the Hall measurements confirm no influence of scandium substitution.

On the other hand, the thermal conductivity of $Sc_xMg_{2-x}Sn$ (x: 0.01 and 0.05) samples show a difference of ~15%–18%, with $Sc_{0.05}Mg_{1.95}Sn$ having higher room temperature values. This could be qualitatively understood from the XRD and the EDS data of $Sc_{0.05}Mg_{1.95}Sn$ sample that has a higher Sc content as a secondary phase than Mg_2Sn[38] and $Sc_{0.01}Mg_{1.99}Sn$. However, zT is not affected much and has a value of ~0.008 for $Sc_{0.05}Mg_{1.95}Sn$.

CONCLUSION

In this study, we have investigated the effect of scandium doping on Mg_2X thermoelectric materials. The presence of secondary phases was ascertained by EDS analysis on scanning electron micrographs of the samples. These EDS mappings reveal that elemental scandium forms an Sc-Si phase when added to $Mg_2Si_{0.4}Sn_{0.6}$ and remains mostly unreacted in Mg_2Sn samples. The thermoelectric data suggest that scandium in $Mg_2Si_{0.4}Sn_{0.6}$ does not act as a dopant. The zT value for $Sc_{0.05}Mg_{1.95}Si_{0.4}Sn_{0.6}$ was $zT_{max} \sim 0.19$. An addition of Sc to Mg_2Sn samples turns the samples into n-type, but the carrier concentration remains far below the optimum range. The thermoelectric properties of Sb-doped and Sb, Sc co-doped samples reveal no significant difference on comparison. Thus, the current study strongly suggests that Sc is not a suitable dopant for Mg_2X materials.

ACKNOWLEDGMENTS

We would like to gratefully acknowledge the endorsement from DLR Executive Board Members for Space Research and Technology and the financial support from Young Research Group Leader Program. The authors would like to thank P. Blaschkewitz (DLR) for his untiring support with the thermoelectric measurements. The authors (A.S. and H.K.) would like to acknowledge financial support by the DAAD (Fellowship No. 247). Also, financial support of one of the authors (M.Y.) is provided by the DFG via the GRK (Research Training Group) 2204 "Substitute Materials for Sustainable Energy Technologies."

REFERENCES

[1]G. J. Snyder and E. S. Toberer, Nat. Mater. **7**, 105 (2008).
[2]X. Liu, Y. D. Deng, Z. Li, and C. Q. Su, Energy Convers. Manage. **90**, 121 (2015).
[3]T. M. Tritt and M. A. Subramanian, MRS Bull. **31**, 188 (2006).
[4]J. Mao, Z. Liu, and Z. Ren, npj Quantum Mater. **1**, 16028 (2016).
[5]W. Liu, X. Tan, K. Yin, H. Liu, X. Tang, J. Shi, Q. Zhang, and C. Uher, Phys. Rev. Lett. **108**, 166601 (2012).
[6]K. Biswas, J. He, I. D. Blum, C.-I. Wu, T. P. Hogan, D. N. Seidman, V. P. Dravid, and M. G. Kanatzidis, Nature **489**, 414 (2012).
[7]Y. Pei, A. F. May, and G. J. Snyder, Adv. Energy Mater. **1**, 291 (2011).
[8]J. P. Heremans, B. Wiendlocha, and A. M. Chamoire, Energy Environ. Sci. **5**, 5510 (2012).
[9]J. de Boor, T. Dasgupta, U. Saparamadu, E. Müller, and Z. F. Ren, Mater. Today Energy **4**, 105 (2017).
[10]X. Liu, L. Xi, W. Qiu, J. Yang, T. Zhu, X. Zhao, and W. Zhang, Adv. Electron. Mater. **2**, 1500284 (2016).
[11]A. Sankhla, A. Patil, H. Kamila, M. Yasseri, N. Farahi, E. Mueller, and J. de Boor, ACS Appl. Energy Mater. **1**, 531 (2018).
[12]P. Gao, I. Berkun, R. D. Schmidt, M. F. Luzenski, X. Lu, P. Bordon Sarac, E. D. Case, and T. P. Hogan, J. Electron. Mater. **43**, 1790 (2014).
[13]N. Farahi, S. Prabhudev, G. A. Botton, J. R. Salvador, and H. Kleinke, ACS Appl. Mater. Interfaces **8**, 34431 (2016).
[14]Q. Zhang, W. Liu, C. Liu, K. Yin, and X. F. Tang, J. Electron. Mater. **43**, 2188 (2014).
[15]T. Sakamoto, T. Iida, A. Matsumoto, Y. Honda, T. Nemoto, J. Sato, T. Nakajima, H. Taguchi, and Y. Takanashi, J. Electron. Mater. **39**, 1708 (2010).
[16]Q. S. Meng, W. H. Fan, R. X. Chen, and Z. A. Munir, J. Alloys Compd. **509**, 7922 (2011).
[17]D. Bilc, S. D. Mahanti, E. Quarez, K.-F. Hsu, R. Pcionek, and M. G. Kanatzidis, Phys. Rev. Lett. **93**, 146403 (2004).
[18]J. P. Heremans, V. Jovovic, E. S. Toberer, A. Saramat, K. Kurosaki, A. Charoenphakdee, S. Yamanaka, and G. J. Snyder, Science **321**, 554 (2008).
[19]J. W. Simonson, D. Wu, W. J. Xie, T. M. Tritt, and S. J. Poon, Phys. Rev. B **83**, 235211 (2011).
[20]B. Wiendlocha, J.-B. Vaney, C. Candolfi, A. Dauscher, B. Lenoir, and J. Tobola, Phys. Chem. Chem. Phys. **20**, 12948 (2018).
[21]Q. Zhang, H. Wang, W. Liu, H. Wang, B. Yu, Q. Zhang, Z. Tian, G. Ni, S. Lee, K. Esfarjani, G. Chen, and Z. Ren, Energy Environ. Sci. **5**, 5246 (2012).
[22]J. Bourgeois, J. Tobola, B. Wiendlocha, L. Chaput, P. Zwolenski, D. Berthebaud, F. Gascoin, Q. Recour, and H. Scherrer, Funct. Mater. Lett. **06**, 1340005 (2013).
[23]H. Kamila, A. Sankhla, M. Yasseri, N. P. Hoang, N. Farahi, E. Mueller, and J. de Boor, Mater. Today Proc. **8**, 546 (2019).
[24]J. D. Boor and E. Müller, Rev. Sci. Instrum. **84**, 065102 (2013).
[25]J. de Boor, C. Stiewe, P. Ziolkowski, T. Dasgupta, G. Karpinski, E. Lenz, F. Edler, and E. Mueller, J. Electron. Mater. **42**, 1711 (2013).
[26]K. A. Borup, J. de Boor, H. Wang, F. Drymiotis, F. Gascoin, X. Shi, L. Chen, M. I. Fedorov, E. Müller, B. B. Iversen, and G. J. Snyder, Energy Environ. Sci. **8**, 423 (2015).
[27]*Non-Tetrahedrally Bonded Elements and Binary Compounds I*, edited by O. Madelung, U. Rössler, and M. Schulz (Springer, Berlin, 1998), p. 1.
[28]M. Yasseri, N. Farahi, K. Kelm, E. Mueller, and J. de Boor, Materialia **2**, 98–103 (2018).
[29]O. Thomas, C. S. Petersson, and F. M. d'Heurle, Appl. Surf. Sci. **53**, 138 (1991).
[30]H. Okamoto, J. Phase Equilib. **13**, 679 (1992).
[31]J. Mao, H. S. Kim, J. Shuai, Z. Liu, R. He, U. Saparamadu, F. Tian, W. Liu, and Z. Ren, Acta Mater. **103**, 633 (2016).
[32]G. M. Lukashenko, R. I. Polotskaya, and V. R. Sidorko, J. Alloys Compd. **179**, 299 (1992).
[33]A. Iddaoudi, N. Selhaoui, M. Ait Amar, S. Kardellass, R. Karioui, and L. Bouirden, Calphad **41**, 71 (2013).
[34]M. V. Vedernikov, Adv. Phys. **18**, 337 (1969).
[35]N. V. Morozova, V. V. Shchennikov, and S. V. Ovsyannikov, J. Appl. Phys. **118**, 225901 (2015).
[36]W. Liu, K. Yin, X. Su, H. Li, Y. Yan, X. Tang, and C. Uher, Intermetallics **32**, 352 (2013).
[37]H. Kasai, L. Song, H. L. Andersen, H. Yin, and B. B. Iversen, Acta Crystallogr. Sect. B **73**, 1158 (2017).
[38]B. W. Jolliffe, R. P. Tye, and R. W. Powell, J. Less Common Met. **11**, 388 (1966).

Published under license by AIP Publishing.

Chapter 8 Influence of sintering duration on the transport properties and the critical role of Mg

8.1 Summary

The variation in sintering time (t_{sinter}) and temperature (T_{sinter}) (at a constant mechanical pressure of 67 MPa) led to an observable variation in the temperature dependent TE properties of Mg_2X solid solutions as discussed in Chapter 6. A variation of the carrier density n at RT with increasing t_{sinter} was also observed which qualitatively explains the variation in respective TE properties. The reason of a variation in n with increasing t_{sinter} was unclear. It was important to identify the reason of this observation as this was related to an optimization of the synthesis route of $Mg_2(Si,Sn)$. Consequently, three samples with identical composition $Mg_{2.06}Si_{0.385}Sn_{0.6}Sb_{0.015}$ were synthesized using identical synthesis steps and parameters but with different t_{sinter} (i.e. at 10 min, 20 min and 40 min). The microstructure of the samples sintered for 20 min and 40 min was investigated using TEM which revealed the presence of Mg-depleted grain boundaries (GBs) and local compositional inhomogeneity in different regions (both matrix and GBs). The 40 min sintered sample showed stronger variations in the Mg:Sn ratio compared to the 20 min sintered sample. The elemental concentration of Si was nearly identical in all regions of the sample, and importantly no dopant loss was observed. The analysis of the transport properties using the SPB model revealed a loss of n and mobility μ, and a lowering of lattice thermal conductivity κ_{lat} ($\sim$20%) with increasing t_{sinter}. A variation in the said parameters as well as the local compositional inhomogeneity were both linked to the Mg loss. Nevertheless, the TE performance of all these samples was similar. This study shows that the transport properties are quite sensitive to slight variation in the Mg content while the TE performance of Mg_2X material behaves relatively robustly to these changes and the TE devices made from these materials can accommodate some Mg loss.

8.2 CRediT (Contributor Roles Taxonomy) author statement

Aryan Sankhla: Conceptualization, Validation, Data curation, Analysis, Writing – original draft. **Hasbuna Kamila:** Validation. **Klemens Kelm:** Investigation, Data curation, Writing: Reviewing & Editing. **Eckhard Mueller:** Supervision, Writing – Reviewing & Editing. **Johannes de Boor:** Conceptualization, Methodology, Validation, Supervision, Writing – Reviewing & Editing, Project administration.

Acta Materialia 199 (2020) 85–95

Contents lists available at ScienceDirect

Acta Materialia

journal homepage: www.elsevier.com/locate/actamat

Full length article

Analyzing thermoelectric transport in n-type $Mg_2Si_{0.4}Sn_{0.6}$ and correlation with microstructural effects: An insight on the role of Mg

Aryan Sankhla[a,*], Hasbuna Kamila[a], Klemens Kelm[a], Eckhard Mueller[a,b], Johannes de Boor[a,*]

[a] German Aerospace Center (DLR), Institute of Materials Research, Koeln D-51147, Germany
[b] Institute of Inorganic and Analytical Chemistry, Justus Liebig University of Giessen, Giessen D-35392, Germany

ARTICLE INFO

Article history:
Received 5 May 2020
Revised 14 July 2020
Accepted 15 July 2020
Available online 21 July 2020

Keywords:
Sintering
Transmission electron microscopy (TEM)
Electronic band structure
Analytical modeling

ABSTRACT

Fundamental material parameters governing the carrier transport in thermoelectric materials are affected by microstructural characteristics. We have investigated the effects of compaction duration on microstructure and the thermoelectric properties of Sb doped $Mg_2Si_{0.4}Sn_{0.6}$. The transport properties show drastic changes with increasing compaction duration from 10 min to 40 min. A TEM-EDS analysis on samples sintered for 20 min and 40 min highlights Mg depleted grain boundaries and local compositional inhomogeneities but gives no indications for dopant loss. The transport properties were analyzed using a single parabolic band (SPB) model, and the observed changes can be attributed to carrier (n) loss, diminished carrier mobility (μ_0) and a reduction in lattice thermal conductivity (κ_{lat}). Comparatively stronger carrier scattering in longer sintered sample is a combined effect of increasing electron-phonon interaction (higher E_{Def}) and local compositional inhomogeneities in the material which are both linked to Mg depletion. The transport behavior of these samples can be fully captured by the SPB model only after the addition of grain boundary scattering in conjunction to acoustic phonon and alloy scattering. Furthermore, compensation between a lower κ_{lat} and μ_0 of the longer sintered sample led to a similar $zT_{max} = 1.3 \pm 0.18$ and an only marginally reduced performance parameter β. While it is evident that Mg deficiency modifies the transport properties, the thermoelectric performance is only mildly affected and a $Mg_2(Si,Sn)$ based TE device can therefore withstand some Mg loss without a deterioration of its performance.

© 2020 Acta Materialia Inc. Published by Elsevier Ltd. All rights reserved.

1. Introduction

The rapid consumption of fossil fuels has severely exhausted the natural energy reservoirs which forewarns mankind to reduce their usage and suppress their effects, such as greenhouse gas emissions, which further impacts our environment. On the other hand, the continuously increasing global energy requirements raises a critical need for green alternatives. The direct thermal-to-electric conversion technology is one potential alternative which could provide a reliable, robust and scalable solution to the global energy requirements. Semiconducting thermoelectric materials, the basic building blocks of thermoelectric devices, enable us to generate electrical energy from the scavenged heat. The efficiency of thermoelectric devices essentially depends on the performance of these materials, which is quantified by a figure-of-merit (zT); defined as $zT = S^2\sigma(\kappa_{lat} + \kappa_e)^{-1}T$, where S, σ, κ_{lat}, κ_e and T represent the Seebeck coefficient, electrical conductivity, lattice and electronic thermal conductivity and the absolute temperature, respectively [1]. An optimized thermoelectric material should have a high power factor ($PF = S^2\sigma$) and a low thermal conductivity (κ).

State-of-the-art thermoelectric materials include PbTe [2], $CoSb_3$-based skutterudites [3], half-Heusler compounds [4], Zintl-phases (such as Mg_3Sb_2 [5,6]), and Mg_2X (X: Si,Sn) and its solid solutions [7,8] comprising $zT_{max} = 1.3 - 1.5$ in the intermediate temperature range ($500K - 900K$). As reported previously for Mg_2Si based solid solutions [9,10] and other material classes [11-15] an interplay of synthesis parameters and microstructural features has a major role in the optimization of thermoelectric properties. The fabrication of thermoelectric materials usually involves a synthesis step and a high temperature compaction step. Both of these steps comprise inter-dependent parameters (such as duration, temperature, pressure, inert environment etc.) which affect thermoelectric properties in a complicated manner. As a result, it becomes impor-

* Corresponding authors.
E-mail addresses: Aryan.Sankhla@dlr.de (A. Sankhla), Johannes.deBoor@dlr.de (J. de Boor).

https://doi.org/10.1016/j.actamat.2020.07.045
1359-6454/© 2020 Acta Materialia Inc. Published by Elsevier Ltd. All rights reserved.

tant to observe and analyze the individual effects of both the synthesis route employed and the high-temperature compaction step, separately. The compaction step includes parameters such as duration, temperature and applied pressure. Each of them has their own effects and can govern n, μ and the κ_{lat}. At elevated temperatures, chemical kinetics can administer n through either enhanced dopant solubility or by various degradation mechanisms (for example oxidation, segregation etc.). Besides, both the μ and κ_{lat} are affected due to evolved microstructural features (such as concentration and quality of grain boundaries, dislocations etc.) and the number, amount and dispersion of secondary phase(s) formed during high temperature steps, respectively. In particular, the variations in the sintering parameters have led to significant changes in the thermoelectric properties of materials such as Bi_2Te_3 [16], $CoSb_3$ [17], ZnSb [18] and its alloys [19] and half Heusler compounds [20] etc.

The Mg_2X (X: Si, Sn) solid solutions are attractive candidates because of their low mass density, environmental compatibility, and economic precursor elements. Furthermore, compared to their respective binaries (Mg_2Si and Mg_2Sn), n-type $Mg_2Si_{0.4}Sn_{0.6}$ possesses superior thermoelectric properties because of both a degeneracy of the conduction bands and lower lattice thermal conductivity as a result of alloy scattering [21]. Beyond this, $Mg_2Si_{0.4}Sn_{0.6}$ is technologically more developed compared to any other Mg_2X (X: Si, Sn) solid-solutions, where progress in both contact material development [22,23] and prediction of thermoelectric performance under operation conditions have been made [24].

Previous reports on Mg_2Si [25] and their solid solutions [9] have shown that either a change in synthesis routine and/or variation in optimized synthesis parameters, affect both carrier scattering and lattice thermal conductivity, which can be attributed to formation of intrinsic charged defects and/or secondary phase such as MgO. Moreover, in our previous study on the optimization of n-type $Mg_2Si_{0.4}Sn_{0.6}$, we have discussed that the thermoelectric properties are not drastically affected by the duration of mechanical alloying. However, varying the high-temperature compaction duration leads to a deterioration of the properties [10,26]. In particular, we observed pronounced differences in the carrier concentration and lattice thermal conductivity which led to corresponding changes in the thermoelectric properties of the samples. The observed changes matched qualitatively the consequences of carrier loss and we therefore postulated the segregation of dopant atoms to be the underlying cause of these changes. Additionally, past studies on Mg_2X [27] and their solid solutions [28] have reported that substituted dopant (Bi) tend to segregate to the grain boundaries which led to a deterioration in carrier concentration and the electrical transport properties. Nevertheless, a thorough analysis of the transport data of the samples sintered for different duration in conjunction with a microstructural investigation, in order to find the actual cause of change in properties is fundamentally beneficial and highly desired. There have been attempts to link transport properties of Mg_2(Si,Sn) to its microstructure which report quite different fundamental materials parameters such as effective mass (m_D^*), lattice thermal conductivity and carrier concentration [29–31]. The dependence of these parameters on the synthesis protocol and thermal history (annealing or sintering parameters) are often overlooked. For a proper comparison and conclusive interpretation of the effect of sintering duration, it is necessary to prepare the material utilizing the same synthesis route and compaction step. Besides this, the thermoelectric measurements from the same set of apparatuses, a physics model-based approach for both the extraction and a comparison of fundamental parameters that are unaffected by carrier concentration, is sought.

Subsequently, we have synthesized Sb-doped $Mg_2Si_{0.4}Sn_{0.6}$ using high-energy mechanical alloying and tuned the duration of the high temperature compaction step. We analyzed the high temperature transport properties using a single parabolic band (SPB) model and correlated them with the microstructure of the respective samples. The chosen composition $Mg_2Si_{0.4}Sn_{0.6}$ does not necessarily suffer from thermodynamically induced de-mixing based on our recent study [32] at temperatures >600 °C which makes it thermally and chemically stable for these investigations.

The $zT(T)$ of all the samples is qualitatively similar as a result of the interplay between power factor and thermal conductivity. However, a systematic analysis using SPB model shows that the carrier mobility along with the carrier concentration and the lattice thermal conductivity decrease with an increase in compaction duration. We attribute the observed changes in the transport properties to an increased electron-phonon interaction (higher E_{Def}) and increasing relevance of grain boundary scattering (higher E_B). The microstructural features can be held responsible for variation in these parameters. As a result, we observe both a higher amount of scattering that leads to differences in the carrier mobility, and changes in κ_{lat} for sample sintered for longer duration. The hypothesized Sb segregation to the grain boundaries causing a lowering of thermoelectric properties was not observed from the microstructure.

2. Materials and methods

2.1. Synthesis

The desired composition $Mg_2Si_{1-x-y}Sn_xSb_y$ ($x = 0.6$, $y = 0.015$) was synthesized using commercially available precursors [Mg turnings (Merck), Si (<6 mm, ChemPure), Sn (<71 μm, Merck) and Sb (5 mm, Alfa Aesar)], all with purity >99.5%. An excess of Mg (2 at.%) is added to compensate for potential loss during the synthesis process. A high energy ball mill (SPEX 8000D Shaker Mill) was used with stainless steel vials and balls as the milling media. All the precursor elements were milled for the duration of 20 h. During the complete synthesis process, the powder was handled under argon (Glove box; MBraun MB200) to prevent oxidation and contamination. Three samples were sintered at a temperature of 973 K, each with a holding time of 10, 20 and 40 min respectively. The sintering was conducted utilizing a direct-current sintering press (DSP 510 SE) from Dr. Fritsch GmbH, using a graphite mold Ø13.3 mm under vacuum (~10^{-5} bar) at a heating rate of 1 Ks^{-1} and under an external pressure/load of 67 MPa on the mold. The density of all the pellets was measured using the Archimedes method. The XRD measurements on the sintered pellets were conducted utilizing a Siemens D5000 Bragg-Brentano diffractometer with a graphite secondary monochromator. The diffractograms were collected in the 2θ range 20°−80° with a step size of 0.01° using CuK_α radiation (1.5406 Å).

2.2. TEM measurement

The microstructure analysis on the sample pellets was done using a transmission electron microscope (Philips Tecnai F30 STEM, Eindhoven) at an acceleration voltage of 300 keV. The microscope is equipped with a Gatan MSC 794 CCD-camera and a windowless EDAX Apollo XLTW SDD-detector for the EDS analysis. Three pellets, each with a diameter of 3 mm, were drilled out from half the radius of each sintered sample. Each of these pellets was ground to a thickness of 100 μm. In the center, each pellet had a thickness of $40-60$ μm left after dimple grinding. Finally, the samples were etched by Ar^+–ion beam (Gatan PIPS 691 Polisher), operated at 4 keV and a beam incidence angle of 7°. The elemental quantifications from the EDS analysis performed in the form of line-scans and maps have been done using the Cliff–Lorimer method using respective binaries for the instrumental calibration. The Mg/Sn ratio in a binary Mg_2Sn was varying from one area to

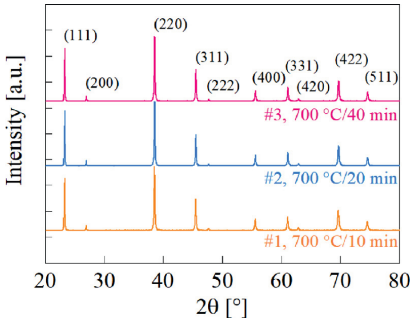

Fig. 1. XRD patterns of the samples sintered for different durations (10, 20 and 40 min) at 973 K. All samples are phase pure and crystallize in the anti-fluorite (fcc) structure.

the other, which prevented us from measuring proper experimental k–factors. The k-factor ($k_{Sn,\ Mg}$) is a sensitivity factor which correlates the composition (w_{Sn} and w_{Mg} in wt.%) of two-elements (for example: Mg and Sn) in a sample to their experimentally measured x-ray intensities (I_{Sn} and I_{Mg}) (above background) by [33]: $w_{Sn}/w_{Mg} = k_{Sn.Mg}I_{Sn}/I_{Mg}$. Thus, we relied on the k-factors supplied by the instrument manufacturer. To our experience, this results in a systematic error of 5 – 10% in the concentrations of the respective elements.

2.3. Thermoelectric measurements

The temperature dependent Seebeck coefficient and electrical conductivity were measured on an in-house developed facility utilizing a four-probe technique [34,35]. The thermal diffusivity (α) of the pellets was obtained using a Netzsch LFA 467HT apparatus. The thermal conductivity (κ) was obtained using the relation $\kappa = \alpha\rho C_P$, where ρ and C_P are the sample density and the heat capacity respectively. The C_P value was obtained from the Dulong-Petit limit for c_V^{DP}:$C_p = c_V^{DP} + \frac{9E_t^2T}{\beta_T\rho}$, $E_t^{Mg_2Si_{0.4}Sn_{0.6}} \sim 1.7 \times 10^{-5}\ K^{-1}$ and $\beta_T^{Mg_2Si_{0.4}Sn_{0.6}} \sim 2.07 \times 10^{-11}$ Pa^{-1} are the linear coefficient of thermal expansion and isothermal compressibility of $Mg_2Si_{0.4}Sn_{0.6}$, respectively [22,36]. The measurement error uncertainties for S, σ and κ are $\pm$ 5%, $\pm$ 5% and $\pm$ 8%, respectively. The error bars are shown for only one sample for a better visibility of the thermoelectric data. The room temperature Hall coefficient (R_H) for different samples was determined using an in-house facility in a van der Pauw configuration. The measurement signals were acquired at different (but constant) magnetic field intensities with a maximum of $\pm$ 0.5 T. The Hall carrier concentration n_H was estimated from R_H assuming a single carrier type $n_H = 1/R_He$. The measurement uncertainties for n_H and mobility μ_H are $\pm$ 10%.

3. Results

The X-ray diffractograms (Fig. 1) were indexed with a standard $Mg_2Si_{0.4}Sn_{0.6}$ pattern (ICSD PDF number 01–089–4254) confirming the formation of a pure phase (anti-fluorite (fcc) structure and $Fm\bar{3}m$ space group). No MgO reflections are observed from the X-ray diffractograms of individual samples. The sample density decreases from sample #1 to #3 indicating porosity in the samples with increasing time of sintering (please refer to Table S1 in supplementary information).

The white wavy lines/ripples present in all the TEM images corresponding to samples #2 and #3 are due to topological structuration of upper and lower sample surfaces using ion-beam etching. This preparation step results in a contrast during sample imaging as a result of thickness variation. Thus, the difference in image contrast due to these ripples is purely due to sample preparation and not representative of compositional variations in the sample. Mechanical alloying, as employed here, favors formation of planar defects (such as grain boundaries, lattice dislocations etc.) in the material. A high density of grain boundaries in both the samples can be observed from Fig. 2. The boundaries of the grains with different shape and size are brighter compared to the bulk for both samples (Fig. 2b and 2d), indicating the presence of heavy element(s) at these boundaries. We also found a higher pore density at/near grain boundaries compared to the matrix in both samples. The overall pore density was higher in sample #3 compared to sample #2 (please refer to Figs. S1 and S2 in supplementary information). Few dislocations are observed close to the grain boundaries for both the samples (Fig. 2a and 2c). We have observed more dislocation arrays (Fig. 2c (inset)) in sample #3 compared to sample #2. A high dislocation density (~ 10^{12} cm^{-2}) has been experimentally proven to scatter phonons efficiently thus, reducing the lattice thermal conductivity of thermoelectric materials [37,38].

An EDS quantification mapping conducted on an area of the sample #2 ((Fig. 3a), almost identical to Fig. 2a) suggests uniform distribution of Mg, Si and Sn with slight local oxygen enrichment. Few regions in the mapped area provide signals corresponding to both silicon and oxygen indicating formation of SiO_2 or other silicides (Fig. S3 in supplementary information). The silicon might have been left unreacted during the high temperature sintering step. The observed change in brightness between grain boundaries and the matrix in the dark field images were not observed in EDS maps. This is due to the fact that the dark-field HAADF images are much more sensitive to variations in composition than the EDS mapping. The line scan conducted on a grain boundary of sample #2 which appeared to be very bright in HAADF contrast shows a slight increase in the atomic concentration of Sn in concert with a slight decrease in Mg content around 33–37 nm. Thus, this suggests Sn-enrichment at some of the grain boundaries. However, the form of existence of Sn either as (Mg-poor) Sn-rich Mg_2(Si,Sn) region, a precipitated Sn-rich Mg_2(Si,Sn) phase, a defect structure (substituting Mg) or even a thin layer of elemental Sn is unclear. A similar EDS quantification analysis on a grain boundary of sample #3 (as shown in Fig. 4) was conducted. For sample #3, we did not find Sn enrichment at the grain boundary but some fluctuation in the signals of Mg and Sn in both grains. To complement these and complete the picture, a summary of the results of the two samples is provided in the supplementary information where we also show compositional variation (variation in Mg:X ratio) between different scanned areas (variation in the elemental concentration of matrix and at/near grain boundaries) of both samples #2 and #3, individually (Please refer to Fig. S4 in supplementary information). Moreover, the EDS data from different areas of both samples showed compositional variation when compared with the starting nominal composition.

We have also observed signals corresponding to Mg and O in some regions of the mapped area of both the samples #2 and #3 which suggest formation of MgO. However, the presence of MgO in these regions could be either on the surface of pores or as MgO inclusions. Importantly, we did not observe the presence of the dopant Sb at the grain boundaries in both the samples.

4. Thermoelectric properties

The temperature dependent electrical transport properties of all three samples are typical of a highly degenerate semiconductor; however, the effect of the minority charge carriers is prominent in sample #3 at higher temperatures. Besides, the electrical transport properties of sample #1 and sample #2 are quite sim-

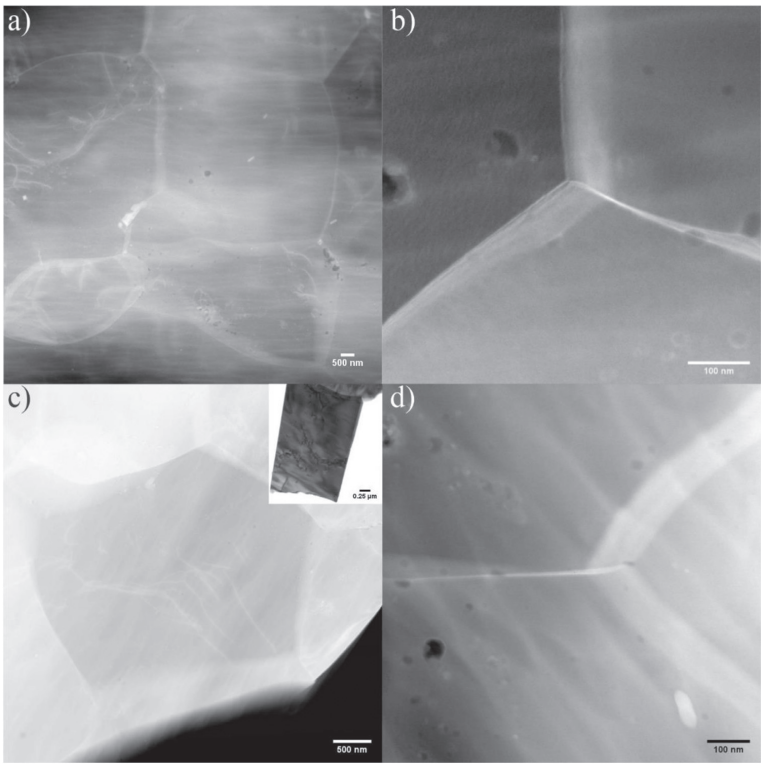

Fig. 2. HAADF dark field images of the sample #2 (700 °C/20 min) (a, b) and sample #3 (700 °C/40 min) (c, d). The TEM analysis conducted on an area of sample #2, (a) at low magnification showing numerous grains as well as their grain boundaries and (b) grain boundaries at higher magnification. The TEM analysis on sample #3 shows (c) polygonal grains with hairy dislocation structures within the grains. A low magnification in the inset shows presence of dislocation arrays. (d) A high magnification image on an area where the grains share common grain boundaries show high concentration of pores at/near the grain boundaries. Please note that the wavy ripples on the sample surface arise due to thickness variation caused by sample preparation and are not a characteristic of the material.

ilar. The Seebeck coefficient of all the samples has negative values indicating n-type conduction. An increase in the Seebeck coefficient and a corresponding decrease of the electrical conductivity of sample #3 compared to the other samples indicate loss of charge carriers with an increase in sintering duration (Fig. 5a and 5b). However, the observed difference in the electrical conductivity of sample #3 and other samples is larger compared to the difference in the Seebeck coefficient of these samples. This suggests that not only the carrier concentration but also carrier mobility is affected. As a result, a reduction in the power factor of the longer sintered sample compared to other samples was observed (Fig. 5c). To investigate the role of the Sb concentration we also synthesized $Mg_{2.1}Si_{0.2925}Sn_{0.7}Sb_{0.0075}$ samples using identical sintering parameters (700 °C/20 min and 700 °C/40 min) and compared their electrical properties. The concurrent increase in the Seebeck coefficient ($8-10\%$) and decrease in the electrical conductivity ($25-30\%$) of the longer-sintered sample compared to short-time sintered sample indicate that the carrier mobility was also affected along with the loss of charge carriers (please refer to Fig. S5 in the supplementary information) similar to the highly doped samples. This confirms that the observed change of the thermoelectric properties with an increase in sintering duration is largely independent of the dopant concentration and a mechanism other than Sb loss was responsible for the change in transport properties.

Besides this, the temperature dependent thermal conductivity of the samples showed a decrease in the absolute values with an increase in sintering duration. The total thermal conductivity of sample #3 from $300K-650K$ was $\sim 15-20\%$ lower compared to the other two samples as observed from Fig. 5d. The estimated $zT(T)$ (Fig. 5f) of all the samples was unaffected as a result of countermotion of electrical and thermal properties and showed $zT_{max} = 1.3 \pm 0.18$ (as summarized in Table 1).

5. Discussion

The EDS line scan on the grain boundary of sample #2 (Fig. 2c) suggest they are Mg-poor/Sn-rich. However, unlike sample #2, we did not observe significant variation in Mg:*X* ratio from the EDS line scan of grain boundary (Fig. 4) in sample #3. One reason of not observing a variation in the EDS line scan could be due to selection of the grain boundary for analysis in sample #3 and the fact that not all the grain boundaries are both qualitatively and (elemental) concentration-wise identical. This could be confirmed from EDS scans on different grain boundaries of sample #3 (Fig. S4b in supplementary information). We further observed local compositional inhomogeneities in different scanned areas (at/near grain boundaries and matrix) of both samples #2 and #3 (Fig. S4 in supplementary information). The elemental analysis furthermore revealed a strong deviation in the elemental composition of dif-

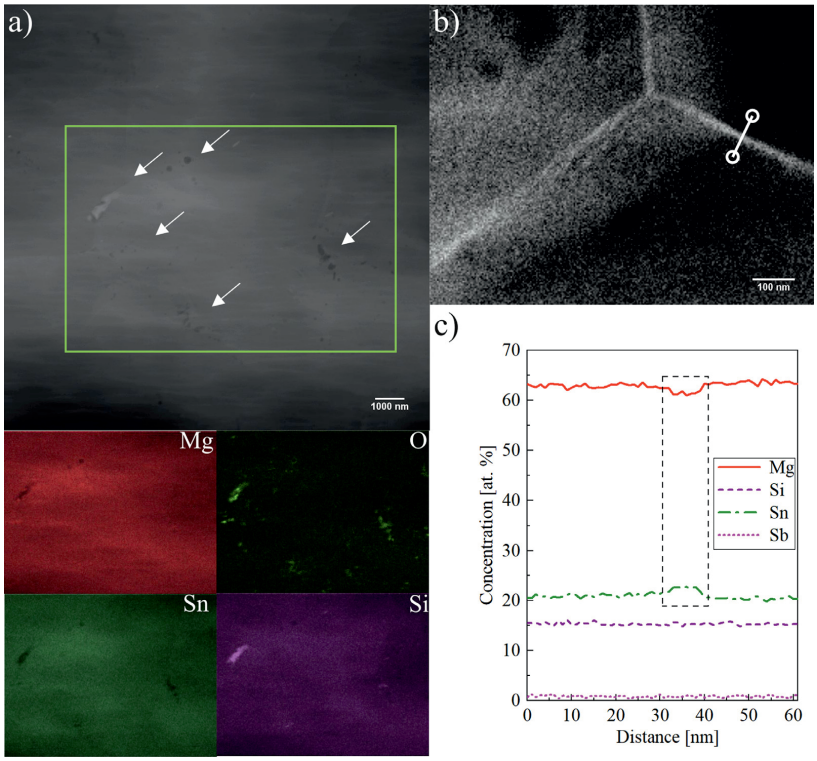

Fig. 3. HAADF image of an area on sample #2 (700 °C/20 min) (a) EDS mapping on a selected area (marked in green) of the image, almost identical to the area shown in Fig. 2a. The Si containing inclusions (mainly SiO_2), MgO inclusions and pores are shown by white arrows. The presence of pores can also be confirmed from Fig. 2a. (b) Magnified HAADF image of an area with bright grain boundaries and (c) EDS line scan on one of these grain boundaries reveal that these are rich in Sn and poor in Mg. The brightness and contrast of HAADF image in (a), and Mg map has been adjusted for better visibility.

Table 1
Synthesis conditions, room temperature carrier concentration n_H, mobility μ_H, density of states effective mass m_D^* and figure-of-merit zT_{max} of the $Mg_2Si_{0.385}Sn_{0.6}Sb_{0.015}$ samples.

Sample	$n_H \times 10^{20}(cm^{-3})$	μ_H (cm^2/Vs)	$m_D^*(m_0)$	zT_{max}
#1, 700 °C/10 min	2.1	47	2.4	1.32 ± 0.18
#2, 700 °C/20 min	2.0	49.2	2.4	1.34 ± 0.18
#3, 700 °C/40 min	1.5	41	2.4	1.34 ± 0.18

ferent areas of both the samples when compared to the nominal. Even considering an uncertainty in the (calibration of the) k-factors, we found the grain boundaries of both samples to be Mg deficient when compared with the nominal (Fig. S4). A lowering of the Mg content would not be surprising and could be attributed to its high vapor pressure during high temperature compaction step for longer duration. This will also favor local de-mixing of phase of the solid-solution [32].

Also, a higher pore density observed for sample #3 might be related to the Mg loss mechanism. Beyond this, we find a higher density of dislocation arrays in sample #3 (700 °C/40 min) compared to sample #2, see Fig. 2c (inset). This is not visible in the HAADF images (Fig. 3 and Fig. 4) because those are less sensitive to dislocation arrays than the dark field images. The dislocations have strain field energies associated with them and these strain energies might further impact the local bonding in the vicinity of dislocations. As a consequence, the bonds might weaken or break to reduce these strain energies and relax the lattice. Furthermore, the theoretical study by Liu et al. and the experimental analysis by Kasai et al. on binary Mg_2Si and Mg_2Sn show that the bonding is weaker between Mg and Sn compared to Mg and Si [39,40]. These reports suggest that the Mg-Sn bond has a higher probability to break which along with a higher number of dislocations might be a plausible reason for the observed local compositional inhomogeneities in sample #3. Besides this, we can rule out Sb loss/migration to the grain boundaries as the relevant reason for the observed changes in the thermoelectric properties based on the following estimation. The number of resulting Sb monolayers that would have been observed at the grain boundaries due to an assumed segregation can be estimated using a cubic grain model and the observed change in carrier concentration. Assuming one Sb atom substitutes one Si atom in the complete crystal lattice and contributes an extra electron, the difference in the Hall carrier concentration of sample #1 (700 °C/10 min) and sample #3

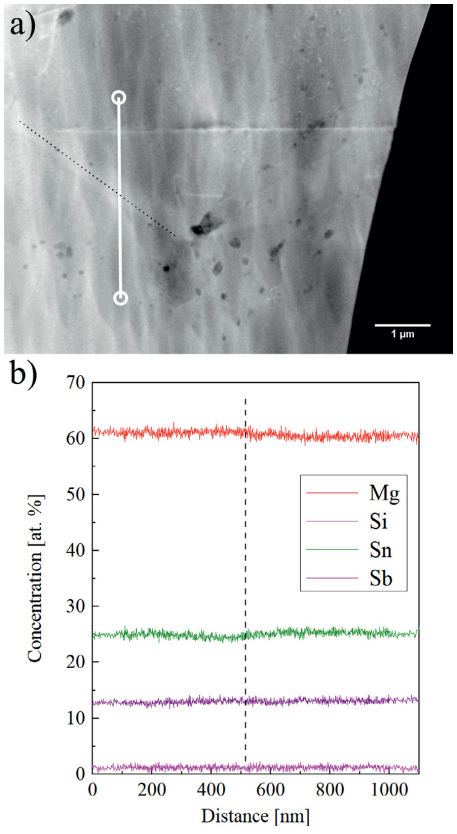

Fig. 4. (a) A low magnification HAADF image on sample #3 (700 °C/40 min) shows an area with grain boundaries (below and in parallel to the black-dotted line), and (b) An EDS line scan conducted on the grain boundary.

(700 °C/40 min) would correspond to six Sb monolayers which would have been observed at the grain boundaries. For a detailed description of the estimation of Sb monolayers, please refer to Fig. S6 and the subsequent calculation in the supplementary information.

Since we find no Sb migration to grain boundaries, the lowering in the carrier concentration can be attributed to Mg loss. Liu et al. have calculated the formation energies of charged intrinsic defects as a function of change in the Fermi level for binary Mg_2Si and Mg_2Sn materials, both in Mg-rich and Mg-poor conditions [39]. They report that for both the binaries, both Mg vacancies (electron acceptor defects) and Mg interstitials (electron donor defects) are the most favorable defects independent of the chemical environment. For n-Mg_2X (X: Si,Sn), Mg-vacancies are the most favorable defects regardless of a small variation in the Fermi level. Extrapolating this knowledge from the binaries, we learn that for a constant Fermi level (fixed extrinsic doping i.e. here: identical Sb-content), when going from the Mg-rich to the Mg-poor side of the Mg_2X homogeneity range, the formation energy of Mg vacancies in $Mg_2(Si,Sn)$ solid solutions gets lower. Therefore, we hypothesize that longer sintering duration leads to Mg loss and formation of Mg vacancies which partially compensate the electrons due to extrinsic doping. We have estimated the equivalent Mg-deficiency (δ) from the loss in carrier concentration (see supplementary information for a detailed calculation) for each sample (Fig. 6). We find a minor but observable (calculated) difference in δ between samples #2 and #3. This is not in contradiction with the findings of the TEM-EDS analysis which did not find a clear difference in overall Mg content as EDS is insensitive to small changes in elemental concentration as estimated here.

The transport data of all three samples was investigated for changes in the fundamental material properties using a single parabolic band model. The governing equations are as follows:

$$S = \frac{k_B}{e}\left(\frac{2F_1(\eta)}{F_0(\eta)} - \eta\right) \quad (1)$$

$$n = 4\pi\left(\frac{2m_D^* k_B T}{h^2}\right)^{1.5} F_{0.5}(\eta) \quad (2)$$

$$n_H = \frac{n}{r_H},\ r_H = \frac{1.5F_{0.5}(\eta)(0.5)F_{-0.5}(\eta)}{F_0^2(\eta)} \quad (3)$$

$$\mu_H = \mu_0 \frac{F_{-0.5}(\eta)}{2F_0(\eta)} \quad (4)$$

$$\sigma = n_H e \mu_H \quad (5)$$

Here k_B is the Boltzmann's constant, $F_i = \int_0^\infty \frac{\varepsilon^i d\varepsilon}{1+exp[\varepsilon-\eta]}$, the Fermi integral of order i, and the reduced chemical potential η is given by $\eta = \frac{E_F}{k_B T}$, where E_F is the Fermi energy. For the calculation, we have assumed a scattering parameter of $\lambda = 0$ which corresponds to the energy dependence of scattering with acoustic phonons (AP) and alloy scattering (AS). The room temperature Hall carrier concentration (n_H), the Hall mobility (μ_H) and the density of states effective mass (m_D^*) of all three samples obtained using the SPB model have been summarized in Table 1.

As we didn't find indications of dopant loss and the observed change of the thermoelectric properties is independent of dopant concentration, we argue that the differences between the samples are linked to their Mg content. In that sense, it is plausible that samples #1 and #2 are Mg-rich (due to the excess Mg used for the synthesis) whereas sample #3 is comparatively Mg-poor, which is also observed from Fig. 6. During the first 20 min of compaction, the samples only lose excess Mg whereas compacting for longer duration causes a change in the actual matrix composition. As a result, we deduce that sample #3 had less Mg-interstitials and more Mg-vacancies and hence a lower electron concentration which led to a 10% increase in the absolute Seebeck coefficient compared to other samples (Fig. 5a). Also, an indistinct difference in the Seebeck coefficient of sample #1 and #2 is possibly due to variation in remaining elemental Mg (but not within the matrix) in the samples. Kato et al. also report the effect of annealing Sb doped Mg_2Si under different Mg-vapor pressure on their Seebeck coefficient [41]. The room temperature Seebeck coefficient of $Mg_2Si_{0.99}Sb_{0.01}$ increased from $-75.5\ \mu VK^{-1}$ to $-84\ \mu VK^{-1}$ (10% increase), and of $Mg_2Si_{0.98}Sb_{0.02}$ increased from $-61.9\ \mu VK^{-1}$ to $-80\ \mu VK^{-1}$ (20% increase), after annealing under Mg-poor (0.1 Pa) conditions; as at starting point the samples had been annealed in Mg-rich (10 Pa) conditions. The predicted temperature dependence of the Seebeck coefficient (lines in Fig. 5a) assuming a constant carrier concentration agrees with the experimental Seebeck coefficient reasonably well until the bipolar effect sets in. Moreover, a constant m_D^* justifies the utilization of SPB model and indicates that the electronic band structure is not significantly different between the samples and can be used to predict the transport properties of highly doped $Mg_2Si_{0.4}Sn_{0.6}$ solid solutions. Although a multi band model would be a better representation of the material system in general, the samples are treated as having one effective band. This is in line

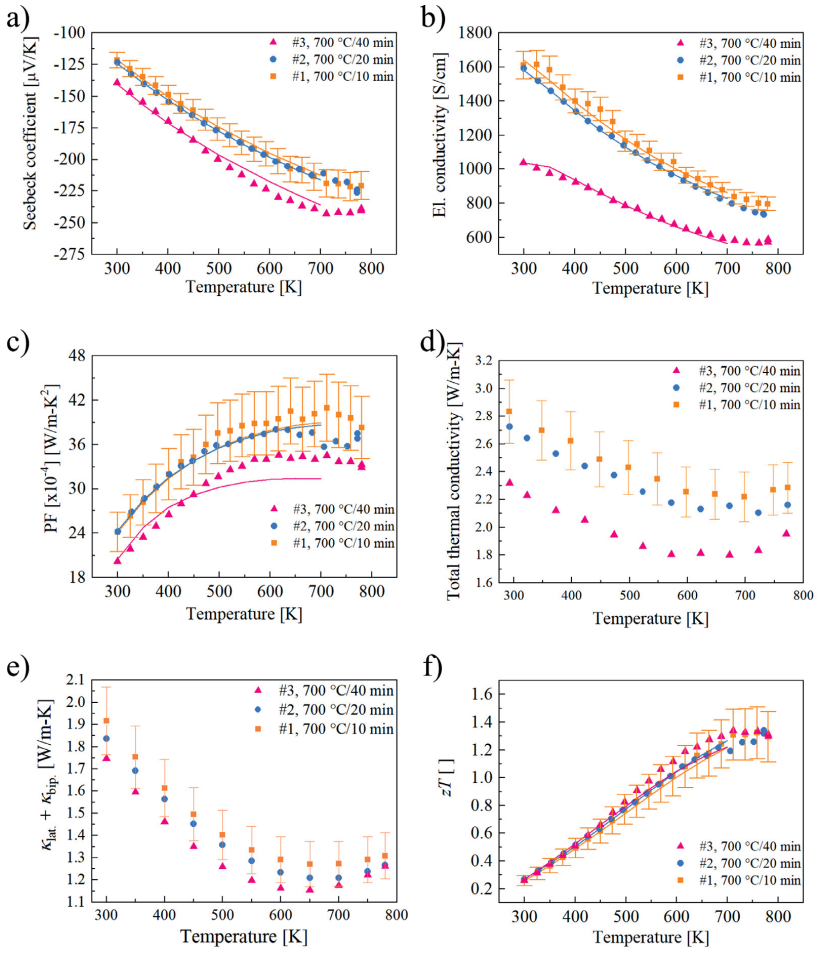

Fig. 5. The experimental (filled symbols) and predicted (solid lines) temperature dependent (a) Seebeck coefficient (b) electrical conductivity (c) power factor (d) total thermal conductivity (e) lattice (and bipolar) thermal conductivity and (f) figure-of-merit (zT) of the $Mg_2Si_{0.385}Sn_{0.6}Sb_{0.015}$ samples prepared using mechanical alloying and sintered at 973 K for 10 min (sample #1), 20 min (sample #2) and 40 min (sample #3) respectively.

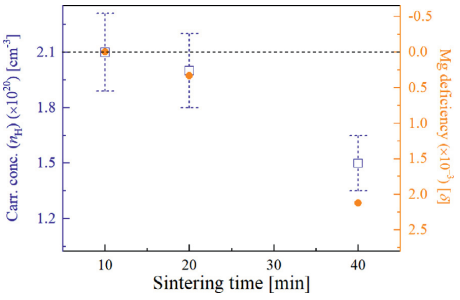

Fig. 6. Room temperature Hall carrier concentration and the equivalent Mg deficiency (δ) in $Mg_{(2+x)-\delta}Si_{0.385}Sn_{0.6}Sb_{0.015}$ versus sintering time. Here, we assume no Mg loss for the carrier concentration of sample #1 ($\delta = 0$). This is reasonable because the difference between the carrier concentration estimated from the nominal composition and the measured carrier concentration is negligible.

with previous studies on $Mg_2Si_{1-x}Sn_x$ [7,42,43] and due to the convergence of the two relevant conduction bands, and a relatively high carrier concentration of the composition under investigation making the effect of minority charge carriers insignificant.

As the experimental Hall mobility is affected by carrier concentration, the mobility parameter (μ_0) was used to determine the differences in the carrier mobility of different samples using Matthiessen's rule [9]:

$$\frac{1}{\mu_0} = \frac{1}{\mu_0^{AP}} + \frac{1}{\mu_0^{AS}} \tag{6}$$

Acoustic phonon scattering mobility (μ_0^{AP}) is described by the following equation:

$$\mu_0^{AP} = \frac{\pi\sqrt{8}e\hbar^4\rho v_l^2}{4E_{Def}{}^2(m_s)^{2.5}(k_BT)^{1.5}} \tag{7}$$

$\hbar$ is the reduced Planck's constant, ρ is the theoretical mass density, v_l is the longitudinal velocity of sound $v_l = 5824\ m^2s^{-1}$, E_{Def}

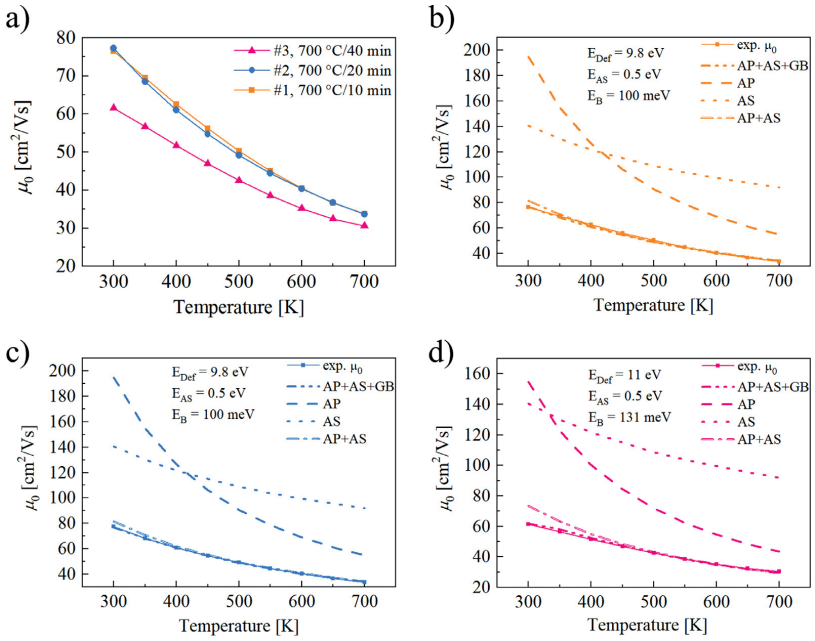

Fig. 7. Temperature dependence of (a) mobility parameter from experimental Hall mobility for samples #1-#3, and comparison between experimental and calculated mobility assuming different scattering mechanisms (AP: scattering by acoustic phonons, AS: alloy scattering, GB: grain boundary scattering) for (b) sample #1 (700 °C/10 min) (c) sample #2 (700 °C/20 min) and (d) sample #3 (700 °C/40 min). Consideration of grain boundary scattering (GB) as a further scattering mechanism is required to capture the temperature dependence at lower temperature (300 K-400 K), in particular for sample #3. Note also that a higher value of the deformation potential and barrier height are required to fit the experimental mobility parameter of sample #3.

is the deformation potential which characterizes the interaction between charge carriers and phonons. The single valley effective mass (m_s) is calculated from $m_s = m_D^*/N_v^{2/3}$, $N_v = 6$. Furthermore, the mobility due to alloy scattering is described by:

$$\mu_0^{AS} = \frac{16e\hbar^4 N_0}{3(2)^{1.5}\pi x(1-x)E_{AS}^2(m_s)^{2.5}(k_B T)^{0.5}} \quad (8)$$

N_0 is the number of atoms per unit volume, x is the Sn fraction and E_{AS} is the alloy scattering potential. The acoustic phonon scattering is more relevant at high temperatures ($\mu^{AP} \propto T^{-z}$, $z > 1$) and the alloy scattering ($\mu^{AS} \propto T^{-0.5}$) at lower temperature. For the prediction of electrical conductivity and the mobility parameter, we have assumed a constant alloy scattering parameter ($E_{AS} = 0.5$ eV). This is because the synthesis routine employed in the present case is identical to the one utilized in our previous study [44], and it is highly unlikely that E_{AS} changes for different compositions of $Mg_2(Si,Sn)$ solid-solutions. Furthermore, μ_0^{AS} has only a weak temperature dependence but we observe differences in the electrical conductivity between sample #1/#2 and #3 over the whole temperature range and have therefore adjusted E_{Def} to capture the $\sigma(T)$ and $\mu_0(T)$.

Samples #1 and #2 show almost identical values and the same temperature dependence of the mobility parameter whereas sample #3 shows values lower by ~ 20% and a weaker temperature dependence Fig. 7a). Since the microstructure analysis showed no signatures of Sb segregation, we can assume that the effect of Sb is essentially identical in all the samples. Thus, we predicted the temperature dependence of the mobility parameter using Eqs. (6)–(8), which led to an agreement to the experimental μ_0 with $E_{Def} = 9.8$ *eV* and $E_{AS} = 0.5$ *eV* for samples #1 and #2 (Fig. 7b and 7c), respectively.

A lowering in the Hall mobility while going from Mg-rich (samples #1 and #2) to Mg-poor (sample #3) stoichiometry, and also an imperfect agreement between the experimental and modeled μ_0 at near room temperature (300 K – 400 K) (Figs. 7, S7 and S8 in supplementary information) clearly affirm an additional scattering mechanism. Aside from this, based on the TEM-EDS analysis, we have observed different types of grain boundaries in both samples #2 and #3. Potentially, the observed Mg deficient grain boundaries and/or their Sn decoration could affect their scattering behavior; differently in each sample. Considering this, we have modelled the mobility and the electrical conductivity with the addition of grain boundary scattering Eq. (9) as a further scattering mechanism [45]. This is plausible because previous reports have shown that grain boundary scattering can be a relevant phenomenon especially under Mg loss and/or when MgO is observed [25,41], and other scattering mechanisms (for example: ionized impurity scattering and point defect scattering) have either entirely different temperature dependencies or have not been previously observed for this material system.

$$\mu_{GB} = Be\left(\frac{1}{2\pi m_s k_B T}\right)^{1/2} \exp\left(\frac{-E_B}{k_B T}\right) \quad (9)$$

where B is the grain size and E_B is the barrier height. We kept $B = 5$ μm constant, since we have observed from our previous study that the grain size is unaffected on sintering for either longer duration or at higher temperature [10]. On tuning, we found a barrier height ($E_B = 100$ meV) that fitted the experimental μ_0 for samples #1 and #2 quite well (Fig. 7b and 7c). For sample #3, we

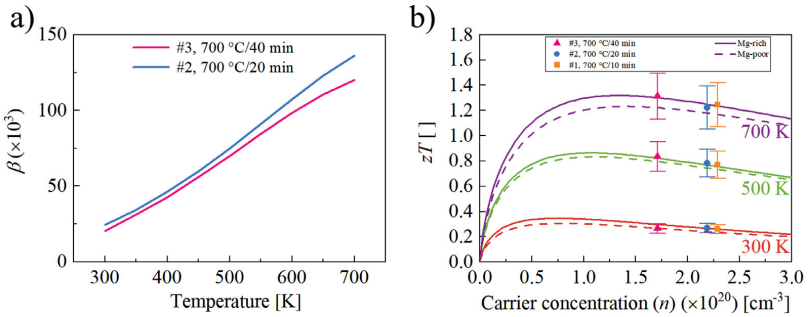

Fig. 8. (a) Temperature dependent β parameter of samples #2 and #3 and (b) experimental data (symbols) as well as SPB prediction for the figure of merit (zT) vs. carrier concentration (n) of sample #1 and #2 (solid lines) and sample #3 (dashed lines) at 300 K, 500 K, and 700 K. The error bars (not shown) for the carrier concentration are smaller than the symbols.

found that the scattering parameters of samples #1 and #2 were not able to predict the experimental μ_0 (Fig. S8 in the supplementary information), and a higher $E_{Def} = 11$ eV was used to model the mobility (Fig. 7d, Fig. S8a and S8b). A higher deformation potential is indicative of a stronger interaction between phonons and charge carriers, and corresponds to lower carrier mobility. Furthermore, an increase in the deformation potential suggests that the lattice disordering in the system increases which could be attributed to a high Mg deficiency in sample #3 (Fig. 6). Also, the higher density of dislocations observed from the gray scale images of sample #3 (Fig. 2c (inset)) could be related to an increase in E_{Def}. The predicted data showed close agreement with the experimental mobility parameter near room temperature for sample #3 (Fig. 7d) only after adding grain boundary scattering with a higher value of the barrier height of $E_B = 131$ meV. Thus, a comparatively higher E_B suggests that a change of the grain boundaries of sample #3 can be linked to Mg deficiency leading to higher scattering in sample #3. Moreover, as previously mentioned, a high pore density at/near the grain boundaries of sample #3 might be related to Mg loss mechanism which could further affect scattering of charge carriers. The analysis also reveals that subtle lowering in Mg content reduces both μ and n significantly. Kato and co-workers [41] have also reported a lowering in carrier mobility besides a reduction in carrier concentration for Sb-doped Mg_2Si samples under Mg-pressure controlled annealing. They observed a minimum of $\sim$ 30% loss in mobility at room temperature for a reduction in Mg ($\delta \sim 10^{-4}$ and $\sim 10^{-3}$, where δ is equivalent Mg deficiency as mentioned) individually for both $Mg_2Si_{0.99}Sb_{0.01}$ and $Mg_2Si_{0.98}Sb_{0.02}$ compositions. However, as mentioned, the loss in carrier mobility of sample #3 is roughly 20% ($\delta \sim 10^{-3}$) compared to the other samples.

The contribution of the lattice and bipolar thermal conductivity to the total thermal conductivity (shown in Fig. 5e) were computed using the Wiedemann-Franz law, $\kappa_{lat} + \kappa_{bi} = \kappa - \kappa_e = \kappa - L\sigma T$, where the Lorenz number $L = (\frac{k_B}{e})^2 \frac{3F_0(\eta)F_2(\eta) - 4F_1{}^2}{F_0(\eta)^2}$ was calculated from the Fermi integrals ($F_i(\eta)$). The lattice thermal conductivity showed a similar trend for all the samples with sample #3 having a lower magnitude. This could be qualitatively interpreted to be due to the presence of pores, dislocations or different quality of the grain boundaries as mentioned. Moreover, a comparably significant bipolar effect at temperatures >600 K was observed for sample #3 as a consequence of the reduced carrier concentration. The analysis of the transport properties shows that sintering the samples for longer duration affects not only carrier concentration, mobility and the lattice thermal conductivity but also a more fundamental material constant: the electron-phonon interaction (E_{Def}). Our analysis shows that the change of the material parameters is mainly due to Mg loss but not Sb loss. Although a change in E_{Def} might appear surprising at a first glance, it has been shown before that E_{Def} is affected by strain [46–48], which could here be related to the changed microstructure. Moreover, the value of E_{Def} is used as an effective fitting parameter and we cannot totally exclude that the observed changes in the mobility might also be due to a different v_l, which is assumed to be constant for the modeling. However, the changes mainly counteract in their effect on the figure of merit, so the Mg-poor sample is as good as the Mg-rich sample indicating that the thermoelectric performance of Mg_2(Si,Sn) is relatively robust against small changes in the sintering conditions [49].

The figure of merit zT can also be written as $zT = \frac{S^2}{L + (\psi\beta)^{-1}}$ where $\psi = \frac{8\pi e}{3}(\frac{2m_0k_B}{h^2})^{1.5}F_0(\eta)$ and the material parameter $\beta = \frac{(\frac{m_b^*}{m_0})^{1.5}\mu_0 T^{2.5}}{\kappa_{lat}}$. The materials β parameter is indicative of the performance of thermoelectric materials independent of the carrier concentration [50–52]. For the prediction of $zT(n)$, we took the average of lattice thermal conductivity (κ_{lat}) of samples #1 and #2 at different temperatures up to 700 K where the SPB model is approximately valid, and the $\mu_0(T)$ of sample #2 was taken since both samples #1 and #2 showed almost identical values and temperature dependence. In spite of a lower mobility (Fig. 7a) but due to the reduced lattice thermal conductivity (Fig. 5e), sample #3 exhibits only moderately inferior (~7 – 15%) β parameter compared to sample #2 (Fig. 8a). Curves of $zT(n)$ as predicted using a SPB model are shown in Fig. 8b. The $zT(n)$ curves of both Mg-rich and Mg-poor samples show minor differences at all temperatures due to subtle differences in their respective β parameter. The (predicted) optimum carrier concentration increases from 1.33 × 10^{20} cm^{-3} (Mg rich) to 1.39 × 10^{20} cm^{-3} (Mg poor) at 700 K, with an increase in sintering duration. Generally, a stronger electron phonon interaction (increase in E_{Def}) shifts the range of optimum carrier concentration towards higher values of n, and also broadens optimum range of n. As a result of lowering in $\mu_0(T)$ (due to higher E_{Def}), the figure of merit decreases. On the other hand, a lowering in κ_{lat} shifts optimum carrier concentration to lower values along with a narrow range of optimum carrier concentration consequently leading to a higher figure of merit. For Mg-poor sample, a compensation between a comparatively low $\mu_0(T)$ (due to higher E_{Def}) and lower values of κ_{lat} leads to optimum carrier concentration, quite similar to Mg-rich samples. Besides this, we have assumed a constant (Hall) carrier concentration for each sample for the temperatures 300 K, 500 K and 700 K respectively. As observed from Fig. 8b, the experimental and the predicted data of samples #1 and #2 are in close agreement whereas we observe

a discrepancy in the data of sample #3 at 500 K and 700 K. The observed discrepancy arises potentially from using the room temperature value of m_D^* ($= 2.4m_0$), also at higher temperatures. The observed discrepancy due to different m_D^* can be verified from a deviation between the predicted and experimental Seebeck coefficient of sample #3 at high temperatures as observed from Fig. 5a. Assuming constant m_D^* for the complete temperature range might not be fully correct since a systematic increase in m_D^* with temperature has been previously reported for n-type Mg_2Si [25,27]. We therefore conclude from Fig. 8 that even after observing the differences between the parameters n, μ and κ_{lat} of Mg-rich and Mg-poor samples which affect their corresponding thermoelectric properties, their overall performance (zT and β parameter) is fairly similar. Overall, the predicted $zT(n)$ shows a broad range of optimum thermoelectric performance with a zT_{max} ~ 1.3 for a carrier concentration ($\approx 1.3 \times 10^{20}$ cm^{-3}) at 700 K.

6. Conclusions

In this study, we have investigated the effect of sintering duration on the microstructure and thermoelectric properties of Sb-doped $Mg_2Si_{0.4}Sn_{0.6}$. The TEM-EDS analysis conducted on 700 °C/20 min and 700 °C/40 min annealed samples revealed local compositional inhomogeneities in each sample. The grain boundaries in each sample were found to be Mg deficient but no Sb (dopant) loss was observed. For the thermoelectric properties, we observe a decrease in carrier concentration, a significant reduction of the carrier mobility and a lowering in the lattice thermal conductivity with increasing sintering time when analyzing the corresponding changes in the temperature dependence of S, σ and κ. An in-depth analysis of the electrical properties by employing a single parabolic band model indicates that the reduced carrier mobility can be attributed to an increased electron-phonon interaction (increased deformation potential E_{Def}) and increasing local compositional inhomogeneity, which can be both linked to ongoing Mg loss. Based on previous reports and the observed microstructural changes we also deduce that the observed change in the carrier concentration and lattice thermal conductivity can be explained by increasing Mg deficiency. Interestingly, the thermoelectric performance of $Mg_2(Si,Sn)$ is mainly unaffected by the variation of the sintering time and the changes in the fundamental material parameter, with $zT_{max} = 1.3 \pm 0.18$ for all samples. This is due to the counteracting effects of both reduced carrier mobility and lattice thermal conductivity on zT_{max}. In essence, this indicates that while Mg loss changes the material properties substantially, the material performance is relatively robust against these changes and $Mg_2(Si,Sn)$-based TEGs can accommodate a certain loss of Mg without significant degradation.

Declaration of Competing Interest

The authors declare that they have no known competing financial interests or personal relationships that could have appeared to influence the work reported in this paper.

Acknowledgments

We would like to gratefully acknowledge the endorsement from DLR Executive Board Members for Space Research and Technology and the financial support from the Young Research Group Leader Program. The authors would like to thank P. Blaschkewitz (DLR) for his untiring support with the thermoelectric measurements. The authors (A.S. and H.K.) would like to acknowledge financial support by the DAAD (Fellowship No. 247), while JdB is partially funded by the Deutsche Forschungsgemeinschaft (DFG, German Research Foundation), project number 396709363.

Supplementary materials

Supplementary material associated with this article can be found, in the online version, at doi:10.1016/j.actamat.2020.07.045.

References

[1] G.J. Snyder, E.S. Toberer, Complex thermoelectric materials, Nat. Mater. 7 (2) (2008) 105–114.
[2] Y. Pei, X. Shi, A. LaLonde, H. Wang, L. Chen, G.J. Snyder, Convergence of electronic bands for high performance bulk thermoelectrics, Nature 473 (7345) (2011) 66–69.
[3] Y. Tang, Z.M. Gibbs, L.A. Agapito, G. Li, H.-S. Kim, Marco B. Nardelli, S. Curtarolo, G.J. Snyder, Convergence of multi-valley bands as the electronic origin of high thermoelectric performance in $CoSb_3$ skutterudites, Nat. Mater. 14 (12) (2015) 1223–1228.
[4] X. Yan, W. Liu, H. Wang, S. Chen, J. Shiomi, K. Esfarjani, H. Wang, D. Wang, G. Chen, Z. Ren, Stronger phonon scattering by larger differences in atomic mass and size in p-type half-Heuslers $Hf_{1-x}Ti_xCoSb_{0.8}Sn_{0.2}$, Energy Environ. Sci. 5 (6) (2012) 7543–7548.
[5] J. Zhang, L. Song, M. Sist, K. Tolborg, B.B. Iversen, Chemical bonding origin of the unexpected isotropic physical properties in thermoelectric Mg_3Sb_2 and related materials, Nat. Commun. 9 (1) (2018) 4716.
[6] K. Imasato, S.D. Kang, S. Ohno, G.J. Snyder, Band engineering in Mg_3Sb_2 by alloying with Mg_3Bi_2 for enhanced thermoelectric performance, Mater Horiz. 5 (1) (2018) 59–64.
[7] T. Dasgupta, C. Stiewe, J. de Boor, E. Mueller, Influence of power factor enhancement on the thermoelectric figure of merit in $Mg_2Si_{0.4}Sn_{0.6}$ based materials physica status solidi (a), App. mater. sci. 211 (6) (2014) 1250–1254, doi:10.1002/pssa.201300196.
[8] A. Sankhla, M. Yasseri, H. Kamila, E. Mueller, J. de Boor, Experimental investigation of the predicted band structure modification of Mg_2X (X: Si, Sn) thermoelectric materials due to scandium, J. Appl. Phys. 125 (22) (2019) 225103.
[9] H. Kamila, G.K. Goyal, A. Sankhla, P. Ponnusamy, E. Mueller, T. Dasgupta, J. de Boor, Systematic analysis of the interplay between synthesis route, microstructure, and thermoelectric performance in p-type $Mg_2Si_{0.2}Sn_{0.8}$, Mater. Today Phys. 9 (2019) 100133.
[10] A. Sankhla, A. Patil, H. Kamila, M. Yasseri, N. Farahi, E. Mueller, J. de Boor, Mechanical alloying of optimized $Mg_2(Si,Sn)$ solid solutions: understanding phase evolution and tuning synthesis parameters for thermoelectric applications, ACS Appl. Energy Mater. 1 (2) (2018) 531–542.
[11] J. Camut, I. Barber Rodriguez, H. Kamila, A. Cowley, R. Sottong, E. Mueller, J. de Boor, Insight on the Interplay between Synthesis Conditions and Thermoelectric Properties of α-MgAgSb, Mater. 12 (11) (2019) 1857.
[12] J.R. Sootsman, J. He, V.P. Dravid, S. Ballikaya, D. Vermeulen, C. Uher, M.G. Kanatzidis, Microstructure and Thermoelectric Properties of Mechanically Robust PbTe-Si Eutectic Composites, Chem. Mater. 22 (3) (2010) 869–875.
[13] X. Su, H. Li, Y. Yan, G. Wang, H. Chi, X. Zhou, X. Tang, Q. Zhang, C. Uher, Microstructure and thermoelectric properties of $CoSb_{2.75}Ge_{0.25-x}Te_x$ prepared by rapid solidification, Acta Mater. 60 (8) (2012) 3536–3544.
[14] M.H. Aguirre, D. Logvinovich, L. Bocher, R. Robert, S.G. Ebbinghaus, A. Weidenkaff, High-temperature thermoelectric properties of Sr_2RuYO_6 and Sr_2RuErO_6 double perovskites influenced by structure and microstructure, Acta Mater. 57 (1) (2009) 108–115.
[15] C.S. Birkel, J.E. Douglas, B.R. Lettiere, G. Seward, Y. Zhang, T.M. Pollock, R. Seshadri, G.D. Stucky, Influence of Ni nanoparticle addition and spark plasma sintering on the TiNiSn–Ni system: structure, microstructure, and thermoelectric properties, Solid State Sci. 26 (2013) 16–22.
[16] G. Delaizir, G. Bernard-Granger, J. Monnier, R. Grodzki, O. Kim-Hak, P.D. Szkutnik, M. Soulier, S. Saunier, D. Goeuriot, O. Rouleau, J. Simon, C. Godart, C. Navone, A comparative study of Spark Plasma Sintering (SPS), Hot Isostatic Pressing (HIP) and microwaves sintering techniques on p-type Bi_2Te_3 thermoelectric properties, Mater. Res. Bull. 47 (8) (2012) 1954–1960.
[17] W.S. Liu, B.P. Zhang, J.F. Li, L.D. Zhao, Thermoelectric property of fine-grained $CoSb_3$ skutterudite compound fabricated by mechanical alloying and spark plasma sintering, J. Phys. D Appl. Phys. 40 (2) (2007) 566–572.
[18] D. Eklöf, A. Fischer, Y. Wu, E.W. Scheidt, W. Scherer, U. Häussermann, Transport properties of the II–V semiconductor ZnSb, J. Mater. Chem. A 1 (4) (2013) 1407–1414.
[19] B.L. Pedersen, H. Birkedal, B.B. Iversen, M. Nygren, P.T. Frederiksen, Influence of sample compaction on the thermoelectric performance of Zn_4Sb_3, Appl. Phys. Lett. 89 (24) (2006) 242108.
[20] J.P.A. Makongo, X. Zhou, D.K. Misra, C. Uher, P.F.P. Poudeu, Correlation between processing conditions, microstructure and charge transport in half-Heusler alloys, J. Solid State Chem. 201 (2013) 280–287.
[21] W. Liu, X. Tan, K. Yin, H. Liu, X. Tang, J. Shi, Q. Zhang, C. Uher, Convergence of conduction bands as a means of enhancing thermoelectric performance of n-Type $Mg_2Si_{1-x}Sn_x$ Solid Solutions, Phys. Rev. Lett. 108 (16) (2012) 166601.
[22] N.H. Pham, N. Farahi, H. Kamila, A. Sankhla, S. Ayachi, E. Mueller, J. de Boor, Ni and Ag electrodes for magnesium silicide based thermoelectric generators, Mater. Today Energy 11 (2019) 97–105.
[23] S. Ayachi, G. Castillo Hernandez, N.H. Pham, N. Farahi, E. Mueller, J. de Boor, Developing Contacting Solutions for $Mg_2Si_{1-x}Sn_x$-Based Thermoelectric Generators: cu and $Ni_{45}Cu_{55}$ as Potential Contacting Electrodes, ACS Appl. Mater Interf. 11 (43) (2019) 40769–40780.

[24] P. Ponnusamy, J. de Boor, E. Mueller, Using the constant properties model for accurate performance estimation of thermoelectric generator elements, Appl. Energy 262 (2020) 114587.

[25] J. de Boor, T. Dasgupta, H. Kolb, C. Compere, K. Kelm, E. Mueller, Microstructural effects on thermoelectric efficiency: a case study on magnesium silicide, Acta Mater. 77 (2014) 68–75.

[26] H. Kamila, A. Sankhla, M. Yasseri, N. Pham, N. Farahi, E. Mueller, J. de Boor, Synthesis of p-type $Mg_2Si_{1-x}Sn_x$ with x= 0-1 and optimization of the synthesis parameters, Mater. Today-Proc. 8 (2019) 546–555.

[27] S.K. Bux, M.T. Yeung, E.S. Toberer, G.J. Snyder, R.B. Kaner, J.-.P. Fleurial, Mechanochemical synthesis and thermoelectric properties of high quality magnesium silicide, J. Mater. Chem. 21 (33) (2011) 12259–12266.

[28] N. Farahi, S. Prabhudev, G.A. Botton, J.R. Salvador, H. Kleinke, Nano- and microstructure engineering: an effective method for creating high efficiency magnesium silicide based thermoelectrics, ACS Appl. Mater Interf. 8 (50) (2016) 34431–34437.

[29] R. Vracar, G. Bernard-Granger, C. Navone, M. Soulier, M. Boidot, J. Leforestier, J. Simon, Microstructure and thermoelectrical investigations of an N-type magnesium–silicon–tin alloy, J. Alloys Compd. 598 (2014) 272–277.

[30] G. Bernard-Granger, C. Navone, J. Leforestier, M. Boidot, K. Romanjek, J. Carrete, J. Simon, Microstructure investigations and thermoelectrical properties of an N-type magnesium–silicon–tin alloy sintered from a gas-phase atomized powder, Acta Mater. 96 (2015) 437–451.

[31] J. Chen, W. Xue, S. Li, G. Zhang, G. Cai, H. Zhao, Enhanced thermoelectric properties in N-type $Mg_2Si_{0.4-x}Sn_{0.6}Sb_x$ synthesized by alkaline earth metal reduction, RSC Adv. 9 (7) (2019) 4008–4014.

[32] M. Yasseri, A. Sankhla, H. Kamila, R. Orenstein, D.Y.N. Truong, N. Farahi, J. de Boor, E. Mueller, Solid solution formation in Mg_2(Si,Sn) and shape of the miscibility gap, Acta Mater 185 (2020) 80–88.

[33] G. Cliff, G.W. Lorimer, The quantitative analysis of thin specimens, J. Microsc. 103 (2) (1975) 203–207.

[34] J. de Boor, C. Stiewe, P. Ziolkowski, T. Dasgupta, G. Karpinski, E. Lenz, F. Edler, E. Mueller, High-Temperature Measurement of Seebeck Coefficient and Electrical Conductivity, J. Electron. Mater. 42 (7) (2013) 1711–1718.

[35] J. de Boor, E. Mueller, Data analysis for Seebeck coefficient measurements, Rev. Sci. Instrum. 84 (6) (2013) 065102.

[36] K.A. Borup, J. de Boor, H. Wang, F. Drymiotis, F. Gascoin, X. Shi, L. Chen, M.I. Fedorov, E. Mueller, B.B. Iversen, G.J. Snyder, Measuring thermoelectric transport properties of materials, Energy Environ. Sci. 8 (2) (2015) 423–435.

[37] S.I. Kim, K.H. Lee, H.A. Mun, H.S. Kim, S.W. Hwang, J.W. Roh, D.J. Yang, W.H. Shin, X.S. Li, Y.H. Lee, G.J. Snyder, S.W. Kim, Dense dislocation arrays embedded in grain boundaries for high-performance bulk thermoelectrics, 348(6230) (2015) 109–114.

[38] Z. Chen, B. Ge, W. Li, S. Lin, J. Shen, Y. Chang, R. Hanus, G.J. Snyder, Y. Pei, Vacancy-induced dislocations within grains for high-performance PbSe thermoelectrics, Nat. Commun. 8 (1) (2017) 13828.

[39] X. Liu, L. Xi, W. Qiu, J. Yang, T. Zhu, X. Zhao, W. Zhang, Significant Roles of Intrinsic Point Defects in Mg_2X (X = Si, Ge, Sn), Thermoelectric Mater. 2 (2) (2016) 1500284.

[40] H. Kasai, L. Song, H.L. Andersen, H. Yin, B.B. Iversen, Multi-temperature structure of thermoelectric Mg_2Si and Mg_2Sn, Acta Crystallogr. Sect. B 73 (6) (2017) 1158–1163.

[41] D. Kato, K. Iwasaki, M. Yoshino, T. Yamada, T. Nagasaki, Significant effect of Mg-pressure-controlled annealing: non-stoichiometry and thermoelectric properties of $Mg_{2-\delta}Si_{1-x}Sb_x$, Phys. Chem. Chem. Phys. 20 (40) (2018) 25939–25950.

[42] W. Liu, H. Chi, H. Sun, Q. Zhang, K. Yin, X. Tang, Q. Zhang, C. Uher, Advanced thermoelectrics governed by a single parabolic band: $Mg_2Si_{0.3}Sn_{0.7}$, a canonical example, Phys. Chem. Chemi. Phys. 16 (15) (2014) 6893–6897.

[43] G.K. Goyal, S. Mukherjee, R.C. Mallik, S. Vitta, I. Samajdar, T. Dasgupta, High thermoelectric performance in $Mg_2(Si_{0.3}Sn_{0.7})$ by enhanced phonon scattering, ACS Appl. Energy Mater. 2 (3) (2019) 2129–2137.

[44] H. Kamila, P. Sahu, A. Sankhla, M. Yasseri, H.N. Pham, T. Dasgupta, E. Mueller, J. de Boor, Analyzing transport properties of p-type Mg_2Si–Mg_2Sn solid solutions: optimization of thermoelectric performance and insight into the electronic band structure, J. Mater. Chem. A 7 (3) (2019) 1045–1054.

[45] J.Y.W. Seto, The electrical properties of polycrystalline silicon films, J. Appl. Phys. 46 (12) (1975) 5247–5254.

[46] F. Murphy-Armando, S. Fahy, Giant enhancement of n-type carrier mobility in highly strained germanium, Nanostructures 109 (11) (2011) 113703.

[47] J.L. Lan, B. Zhan, Y.C. Liu, B. Zheng, Y. Liu, Y.H. Lin, C.W. Nan, Doping for higher thermoelectric properties in p-type BiCuSeO oxyselenide, Appl. Phys. Lett. 102 (12) (2013) 123905.

[48] Z. Liu, Y. Wang, J. Mao, H. Geng, J. Shuai, Y. Wang, R. He, W. Cai, J. Sui, Z. Ren, Lithium Doping to Enhance Thermoelectric Performance of with Weak Electron–Phonon Coupling, Adv. Energy Mater. 6 (7) (2016) 1502269.

[49] J. de Boor, T. Dasgupta, E. Mueller, in: Thermoelectric Properties of Magnesium Silicide–Based Solid Solutions and Higher Manganese Silicides, Materials Aspect of Thermoelectricity, CRC Press, 2016, pp. 173–232.

[50] V.I. Fistul', in: Transport Phenomena in Heavily Doped Semiconductors, Heavily Doped Semiconductors, Springer New York, Boston, MA, 1969, pp. 77–205.

[51] A.F. May, G.J. Snyder, Introduction to Modeling Thermoelectric Transport At High temperatures, Materials, Preparation, and Characterization in Thermoelectrics, CRC press, 2017 11-1-11-18.

[52] A.F. Ioffe, Semiconductor Thermoelements and Thermoelectric Cooling, Infosearch limited, London, 1957.

Chapter 9 Analyzing the effect of *in-situ* annealing on the thermoelectric properties of n-type $Mg_2Si_{0.4}Sn_{0.6}$

9.1 Summary

The study discussed in Chapter 8, and other literature reports suggest that the transport properties in Mg_2X materials are sensitive to Mg variation. If this is the case, then the TE properties of these materials could be affected due to the variation of the Mg content at operation temperatures as well. As a result, this could eventually lower the materials performance and inhibit their long-term usage. Consequently, an influence of thermal treatment on the TE properties of this material was investigated by simulating the operation environment of corresponding TEGs. Two samples with an identical composition $Mg_{2.06}Si_{0.385}Sn_{0.6}Sb_{0.015}$ were prepared using mechanical alloying (20 h) and sintering (at 973 K/20 min with an axial pressure of 67 MPa). Room temperature TE properties of these samples were nearly identical as well. S, σ and R_H of these samples were simultaneously measured *in-situ* during annealing (at $T = 710$ K) in HT Hall and HT-$S\sigma$ facilities, respectively. The samples showed no de-mixing even after annealing for $\sim$275 h and $>$ 1100 h of annealing, respectively. The measured properties were analyzed using SPB and 2PB models which revealed a loss of majority charge carriers. This loss is due to Mg loss in the material which leads to a formation of compensating p-type intrinsic defects. Further analysis showed a reduction of mobility and a lowering of DOS mass m_D^* at RT, which could be due to Mg loss or a lifted degeneracy of the CBs. The corresponding rate of Mg loss was determined as well. *In-situ* measurement of transport properties and their analysis using band structure models give a new insight on the degradation of Mg_2X materials at high temperatures. Besides, the previously unknown phase width of this composition (with respect to Mg) at elevated temperature (710 K) was established using a simple defect chemistry model.

9.2 CRediT (Contributor Roles Taxonomy) author statement

Aryan Sankhla: Conceptualization, Data curation, Validation, Analysis, Writing – original draft. **Hasbuna Kamila**: Discussions & suggestions on the study, Writing: Reviewing & Editing. **Harshita Naithani**: Discussions & suggestions on the study, Writing: Reviewing & Editing. **Eckhard Mueller**: Supervision, Writing: Reviewing & Editing. **Johannes de Boor**: Conceptualization, Methodology, Validation, Supervision, Writing – Reviewing & Editing, Project administration.

Materials Today Physics 21 (2021) 100471

Contents lists available at ScienceDirect

Materials Today Physics

journal homepage: https://www.journals.elsevier.com/materials-today-physics

On the role of Mg content in $Mg_2(Si,Sn)$: Assessing its impact on electronic transport and estimating the phase width by in situ characterization and modelling

A. Sankhla [a, *], H. Kamila [a], H. Naithani [a], E. Mueller [a, b], J. de Boor [a, c, **]

[a] Institute of Materials Research, German Aerospace Center (DLR), Germany
[b] Institute of Inorganic and Analytical Chemistry, Justus Liebig University of Giessen, Giessen, Germany
[c] Institute of Technology for Nanostructures (NST), Faculty of Engineering, University of Duisburg-Essen, Germany

ARTICLE INFO

Article history:
Received 30 April 2021
Received in revised form
22 June 2021
Accepted 24 June 2021
Available online 6 July 2021

Keywords:
$Mg_2Si_{1-x}Sn_x$
In-situ annealing
Modelling transport properties
Mg-related defects
Carrier transport

ABSTRACT

Carrier transport in $Mg_2Si_{1-x}Sn_x$ thermoelectrics was experimentally found to be highly sensitive to high temperature heat treatment and in particular the role of the precise Mg content has been discussed controversially. Considering this, electrical transport properties of Sb doped $Mg_2Si_{0.4}Sn_{0.6}$ were measured in-situ during annealing at 710 K. We measured two quasi-identical samples: sample 1, for the Seebeck coefficient and the electrical conductivity (σ) measurement in helium, and sample 2 for Hall coefficient and σ measurement in vacuum, respectively. Both samples largely remain single phase and did not show de-mixing after annealing for ~276 hours and ~1100 hours respectively. The observed experimental data can be modelled using a single- and two parabolic band model and a continuous reduction in majority carriers is identified, which can be linked to Mg loss. Thorough analysis furthermore reveals mobility loss and a lowering of the density of states effective mass which could both be due to ongoing Mg loss or due to a lifted degeneracy of conduction bands in $Mg_2Si_{0.4}Sn_{0.6}$ at room temperature. Finally, we can link the change in carrier concentration to a change in Mg-related defects and identify a phase width $\Delta\delta$ in $Mg_{2-\delta}Si_{0.4}Sn_{0.6}$.

© 2021 Elsevier Ltd. All rights reserved.

1. Introduction

Solid state power generation devices, fabricated using thermoelectric materials, directly convert heat to electricity and are a potentially sustainable and scalable solution to global energy requirements. The performance of any material to be used in a thermoelectric device is characterized by its thermoelectric figure-of-merit (zT), $zT = (S^2\sigma/\kappa)T$, where S is the Seebeck coefficient, σ is the electrical conductivity, κ is the total thermal conductivity (comprising contributions from lattice thermal conductivity (κ_{lat}), electronic thermal conductivity (κ_{ele}) and bipolar thermal conductivity (κ_{bip})) and T is the absolute temperature, respectively [1]. An efficient thermoelectric material should have a high power factor ($PF = S^2\sigma$) and a low (total) thermal conductivity.

Thermoelectric devices work at elevated temperatures in the range of 300 K–1100 K, and their thermal stability at operating temperatures is a significant challenge to overcome. Therefore, it is important to understand the impact of heat treatment on the material for prolonged duration at operation temperatures. Previous reports on different materials [2–9] studied effects of heat treatment by comparing phase constitution, microstructure and corresponding thermoelectric properties before and after heat treatment, and speculate on degradation mechanism qualitatively. Such studies have also been carried out for Mg_2X materials [10,11] which are an attractive class of thermoelectrics featuring a low mass density, environmental compatibility, economic precursor elements and high thermoelectric performance [12–14]. However, there is no report of direct observation of change in materials properties during annealing which could provide us a better insight into degradation mechanism and affected parameters.

We therefore carried out annealing experiments utilizing n-type $Mg_2Si_{0.4}Sn_{0.6}$ and measured electrical transport properties in-situ during the complete annealing duration. We specifically chose this composition since it possesses better thermoelectric

* Corresponding author.
** Corresponding author.
E-mail addresses: Aryan.Sankhla@dlr.de (A. Sankhla), Johannes.deBoor@dlr.de (J. de Boor).

https://doi.org/10.1016/j.mtphys.2021.100471
2542-5293/© 2021 Elsevier Ltd. All rights reserved.

properties, due to band convergence and low lattice thermal conductivity, compared to the binary end members (Mg_2Si and Mg_2Sn) [15–18]. Our in-situ measured transport properties showed a degradation with increasing annealing duration and a saturation after 210 h of annealing. The room temperature Hall carrier concentration of sample 1 decreased by an order of magnitude after annealing compared to prior annealing. Previous studies on Mg_2X and its solid solutions report that the thermochemical stability, and the thermoelectric transport properties both are sensitive to the Mg content [19–21]. A variation in the Mg content particularly influences the limits of the miscibility gap and the degradation kinetics [22]. We also learn from our previous studies that varying the duration of the high temperature (700 °C) compaction step leads to Mg loss which causes a degradation of n and mobility (μ) [23–25]. These observations are in accordance with the fact that the Mg content in the Mg_2X materials directly relates to the density of charged defects and therefore affects their electrical transport properties. With this knowledge of a sensitivity to Mg content of both degradation kinetics and transport properties, mainly at elevated temperatures, we analyzed the measured transport properties using single-/multiband transport models.

The analysis confirmed that an ongoing loss of n and μ was responsible for degradation of corresponding transport properties during annealing. We also found that the material obeys single band transport for the first 80 h of annealing at 710 K. Following this, a non-linear behavior of Seebeck coefficient during longer annealing durations (>80 h) affirmed minority carriers from the valence band influencing the transport, when analyzed using a two-band model. The change in n and corresponding properties can be attributed to Mg loss which favors formation of p-type defects. Furthermore, single band analysis on transport properties before and after annealing suggests a lowering of m^*_D which can be a consequence of either an offset between supposedly converged conduction bands or n loss (or Mg loss). The same reason(s) likely affects and increases electron-phonon interaction that leads to the observed loss of mobility.

2. Experimental section

$Mg_2Si_{1-x-y}Sn_xSb_y$ ($x = 0.6$, $y = 0.015$) samples were synthesized using a high energy ball mill (SPEX 8000D Shaker Mill) followed by a direct current sinter pressing (DSP 510 SE, Dr. Fritsch GmbH, Fellbach, Germany) of the milled powders to obtain a compacted pellet. Particular details of the complete synthesis procedure are mentioned in Ref. [16]. Excess Mg (2 at. %), making a final composition $Mg_{2.06}Si_{1-x-y}Sn_xSb_y$, was added to compensate for potential Mg loss during synthesis. The powder was sintered at a temperature of 973 K with a holding time of 20 min, in vacuum ($\sim 10^{-5}$ bar), and under an external pressure/load of 67 MPa on the mold. The density of all the pellets was measured using the Archimedes method, with ~1 % error uncertainty. The X-ray diffractograms of the sintered pellets were acquired utilizing a Bruker's D8-Advanced diffractometer in the 2θ range of 20°–120° with a step size of 0.01° using CuK_α radiation (1.5406 Å). The microstructure was investigated by a Zeiss Ultra 55 system equipped with an energy dispersive X-ray (EDS) detector.

An in-situ annealing experiment was conducted on two samples utilizing in-house developed facilities for measuring temperature dependent transport properties [26,27] at 710 K (~ 437 °C). The Seebeck coefficient and electrical conductivity of one sample were measured utilizing a four-probe technique during annealing under helium atmosphere. The helium atmosphere was maintained in an enclosed volume. On the other hand, the Hall coefficient R_H and the electrical conductivity of the second sample were measured during annealing by utilizing a van der Pauw configuration in vacuum under continuous pumping. The Hall voltage signals were acquired at different (but constant) magnetic field intensities with a maximum of ± 0.5 T. The Hall carrier concentration n_H was estimated from R_H assuming a single carrier type $n_H = {}^1/_{R_H.e}$. The thermal diffusivity (α) of both the samples was measured after the annealing experiment using a Netzsch LFA 467HT apparatus. The thermal conductivity (κ) was obtained using the relation $\kappa = \alpha\rho C_P$, where ρ and C_P are the sample density and the heat capacity respectively. The C_P value was obtained from the Dulong-Petit limit for c_V^{DP}: $C_p = c_V^{DP} + \frac{9E_t^2T}{\beta_T\rho}$, $E_t^{Mg_2Si_{0.4}Sn_{0.6}} \sim 1.7\times10^{-5}$ K^{-1} and $\beta_T^{Mg_2Si_{0.4}Sn_{0.6}} \sim 2.07\times10^{-11}$ Pa^{-1} are the linear coefficient of thermal expansion and isothermal compressibility of $Mg_2Si_{0.4}Sn_{0.6}$, respectively [28,29]. The temperature dependent thermal conductivity has been shown in Fig. S1 in the supplementary information. The measurement error uncertainties for S, σ, κ and R_H are ±5 %, ±5 %,±8 % and ±10 %, respectively. An overview of measurements conducted on each sample is tabulated (Table S1) in the supplementary information. The transport properties are analyzed assuming a single or two parabolic bands, using the governing equations [30] provided as equations S1–S13 in the supplementary information.

3. Results

The X-ray diffractograms of the samples both before and after annealing experiments are shown in Fig. 1a. These diffractograms show that samples are phase pure and crystallize in the *fcc* structure with $Fm\bar{3}m$ space group. The XRD data also affirms that the samples are microstructure-wise basically unaffected due to annealing. The lattice parameter of the samples before and after annealing, listed in Table 1, were predicted by Le Bail fitting using Chebychev's polynomials assuming that the samples were phase pure before and after annealing. The lattice parameters indicate negligible change in the stoichiometry of the material after annealing compared to before annealing. The microstructure was investigated to observe any change that might have occurred during the annealing experiment. A typical side effect of the employed synthesis route is a small fraction of Si-rich $Mg_2(Si,Sn)$, usually below the detection limit of XRD [16,31,32]. The area fraction of the secondary phase(s) in the sample before and after annealing was estimated to be ~ 2.5 % (sample 2, before annealing) and ~ 2.3 % (sample 1, after annealing) and ~ 2.6 % (sample 2, after annealing) as shown in Figs. S1b, S1c, and S3, and hence remains stable. EDS analysis were conducted on different areas of the samples before and after annealing are shown in Figs. S2b, S4 and S5, and the elemental composition corresponding to these samples are shown in Tables S2–S4, respectively, in the supplementary information. The analysis shows that the matrix composition after annealing is similar to the starting composition thus, the samples did not suffer Mg loss to an extent which could lead to de-mixing of the solid solution [19,22].

As a reference, we made both X-ray and SEM investigation on sample 2 before the annealing experiment. This comparison is reasonable since both samples were prepared using an identical, established synthesis route and showed similar thermoelectric properties at room temperature, listed in Table 1.

The Seebeck coefficient and electrical conductivity of sample 1 were measured in-situ during annealing at 437 °C for ~275 hours under helium atmosphere. The temperature was already stabilized before initiating the annealing experiment. Before onset of annealing, during heat-up ramp, the temperature dependent transport properties were measured on this sample as shown in

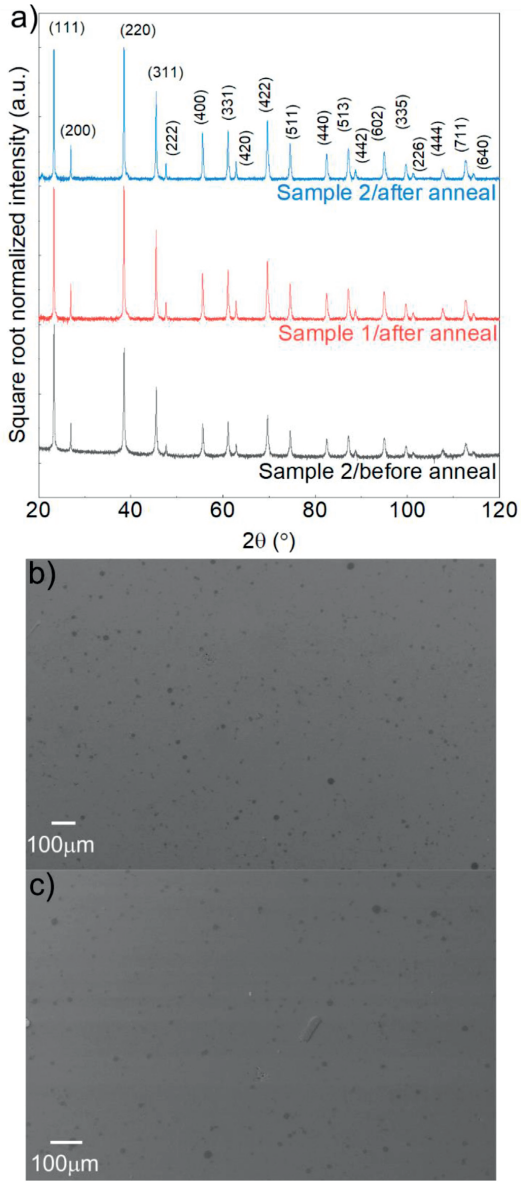

Fig. 1. a) X-ray diffractogram of sample 2 (before annealing), and sample 1 and sample 2 (after annealing). The diffractograms show that the samples are phase pure before and after annealing experiment, b) Low magnification secondary electron image of b) sample 2 before annealing, and c) sample 1 after annealing.

Fig. S6. Broadly, the (annealing) time dependent Seebeck coefficient can be divided into 3 parts as shown in Fig. 2a. The first part is from the beginning of annealing experiment until ~80 hours of annealing, in which the Seebeck coefficient changes linearly. The second part ranges from 80 h until 210 h where the Seebeck coefficient varies non-linearly. Finally, for $t > 210$ hours, the sample shows a nearly constant value of the Seebeck coefficient suggesting saturation. A decrease of the Seebeck coefficient (in absolute values) after a unidirectional increase (0 h – 80 h) between 80 h and 210 h indicates contribution of minority charge carriers to the transport. On the other hand, the electrical conductivity (Fig. 2b) shows a continuous decay with annealing duration and saturates in the range of 165 – 175 S/cm. The different time dependence of the Seebeck coefficient and the electrical conductivity in the second region (80 h – 210 h) suggests that the degradation of transport properties is not only due to a probable carrier loss but carrier mobility might also be affected. The transport properties were fitted using a 5th order polynomial which is used as 'measured' data for later discussion and for transport modelling.

The carrier concentration and electrical conductivity of sample 2 were measured during annealing under vacuum utilizing a high temperature Hall system. The temperature was stabilized prior to initiation of the annealing experiment. Transport properties of sample 2 were measured during heat-up ramp until the sample reached the desired annealing temperature as shown in Fig. S7. As shown in Fig. 2c and d, the complete annealing experiment took over 1000 h however, the transport properties did not saturate. Besides, the measurement failed a couple of times during this experiment; once around 430 h, and then in the range of 600 h – 650 h. We tested different temperatures for the purpose of optimization of the in-situ annealing experiment before conducting final annealing experiment. The transport properties of this optimization are shown in Fig. S8, and indicate that changes in the thermoelectric properties occur drastically slower at temperatures below 710 K.

4. Discussion

X-ray and SEM investigations on the samples before and after annealing suggest that they are essentially single phase with no indications of phase separation or elemental Si/Sn, and no significant change in area fraction of the secondary phase (Si-rich $Mg_2(Si,Sn)$). The EDS analysis and diffractograms also suggest that after a possible Mg loss the samples remain within the phase width of $Mg_2Si_{0.4}Sn_{0.6}$ (with respect to Mg content). This agrees with earlier reports [22,33], which suggest that stability is not unexpected if Mg loss can be controlled. The observed Si-rich $Mg_2(Si,Sn)$ inclusions are expected to have a lower carrier concentration than the matrix [32] and furthermore form isolated islands. Thus, the fact that the material shows no observable change from the XRD and SEM analysis allows us to analyze the in-situ measured properties using a single-phase material model with material parameters that are assumed to be constant, except those related to the electrical transport.

Fig. 3a shows the Hall carrier concentration as function of the electrical conductivity for both samples. Note that for sample 2 this is a direct result of the Hall measurement, while for sample 1 it is calculated using the SPB model and the measured Seebeck coefficient assuming a constant $m_D^* = 2.4\, m_0$ and using equations S1 – S4. We find a close agreement between $n_H(\sigma)$ of both samples which indicates that our assumption of single band transport assuming a constant m_D^* is reasonable.

Besides, we also learn that the rate of change of the transport properties differs between the two employed setups and probably depends on annealing atmosphere. At $T = 710$ K, the properties degraded slowly in vacuum (~10 times slower) compared to the experiment for sample 1 in the other setup in He atmosphere. The transport properties (S and σ) (Fig. S9) of a fresh sample, with a composition identical to sample 1 and 2, was monitored during in-

Table 1
Room temperature Seebeck coefficient (S), electrical conductivity (σ), Hall carrier concentration (n_H) and density of states effective mass (m_D^*) predicted using a single parabolic band (SPB) model. The density and lattice parameter of both the samples have also been tabulated below. Note that sample 1 was annealed in the S-sigma setup (setup 1) under He atmosphere while sample 2 was annealed in the Hall setup (setup 2) in vacuum.

Sample name		S (μV/K)	σ (S/cm)	n_H (10^{20}) (cm^{-3})	$m_D^*(m_0)$	Sample density (g/cm^3)	Lattice parameter (Å)
Sample 1 (setup 1)	Before annealing	−116	1888	2.45	2.4	3.00	–
	After annealing	−228	161.3	0.29	1.8	3.01	6.608(0)
Sample 2 (setup 2)	Before annealing	−111	1944	2.3	2.4	2.94	6.608(9)
	After annealing	−119.5	1305.2	1.7	2.05	2.98	6.609(3)

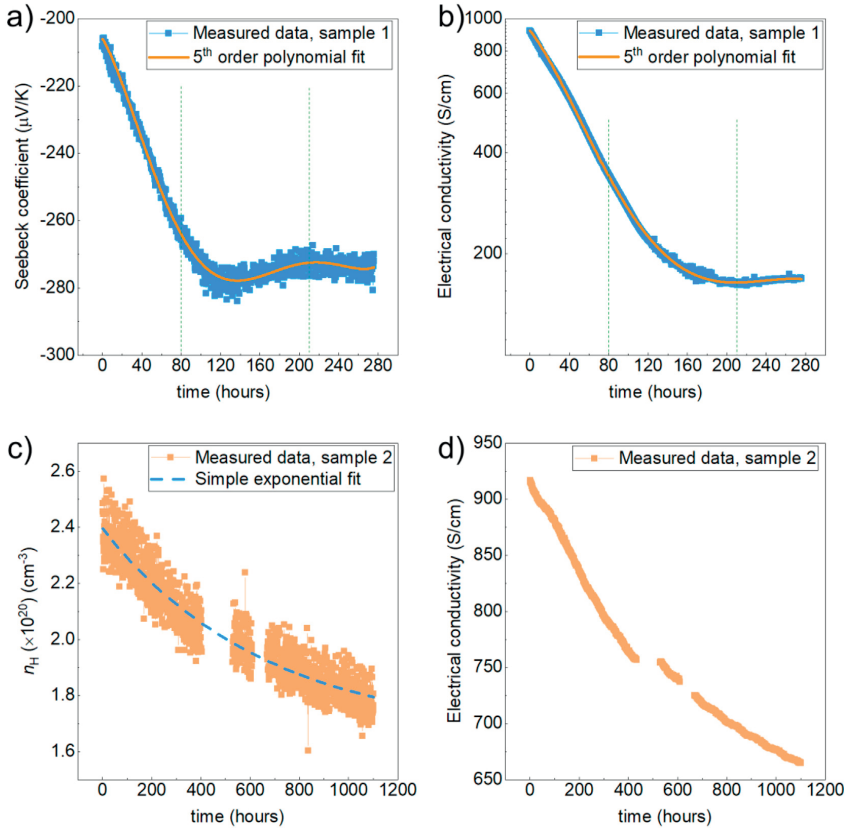

Fig. 2. a) Seebeck coefficient and b) electrical conductivity of sample 1, and c) Hall carrier concentration and d) electrical conductivity of sample 2, both measured in-situ during annealing at 710 K for a duration of nearly 275 h, and over 1000 h respectively. Note that the scale of y-axis in Fig. 2b is logarithmic.

situ annealing in vacuum (instead of He) to assess the influence of different atmospheres. The properties saturated after ~250 hours of annealing, similar to experiment in He, indicating that the atmosphere itself is not the main reason for the observed differences between the setups. Anyways, the same general dependence, as shown in Fig. S10, suggests that the mechanism of degradation is quite similar. It also supports the idea to use data of both measurements combinedly, even if the decay has a different rate, using the electrical conductivity as a common property. As sample 1 shows the faster and more complete change of properties we'll mainly exploit that in the following.

We utilized the measured Seebeck coefficient (Fig. 2a) from the first part of the annealing (0 h − 80 h) experiment, where the values increase linearly with time, to estimate n using a constant m_D^* (Table 1) by employing a single parabolic band (SPB) model as shown in Fig. 3b. The relevant equations of the SPB model are mentioned in the supplementary information. This is a reasonable assumption since the temperature dependent measured Seebeck coefficient agrees well with the predicted one on using said m_D^*, as shown in Fig. S6. The electrical conductivity was analyzed with the dependence of the mobility parameter on (annealing) duration assuming acoustic phonon (AP) and alloy scattering (AS) of charge carriers implemented in the model since AP is most relevant

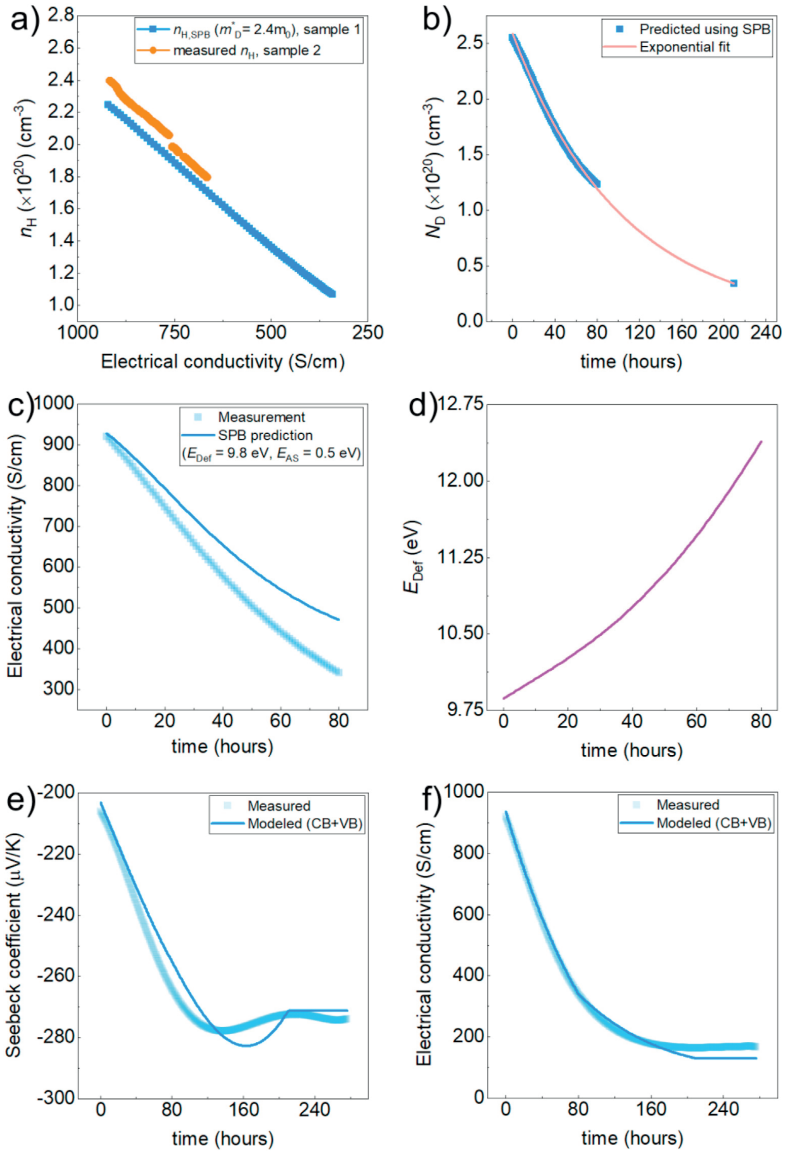

Fig. 3. a) Hall carrier concentration (n_H) of sample 1 and 2 as a function of electrical conductivity. The relative disagreement between n_H of both samples is ~10 %. Time dependent b) net carrier concentration due to point defects (N_D), c) measured and predicted electrical conductivity (with E_{Def} = 9.8 eV, E_{AS} = 0.5 eV) until first 80 h of annealing. The discrepancy can be removed by tuning E_{Def} as a fitting parameter as shown in (d), time dependent predicted and experimental e) Seebeck coefficient, and f) electrical conductivity of sample 1. The Seebeck coefficient and electrical conductivity were predicted using a 2 parabolic band model (1CB and 1VB), using the parameters listed in Table 2.

scattering mechanism at high temperatures, and AS is a relevant mechanism for solid solutions [34,35]. The experimental and predicted electrical conductivity (assuming E_{Def} = 9.8 eV and E_{AS} = 0.5 eV, and using the predicted n) agree well in the beginning, however, there is an increasing disagreement with time as shown in Fig. 3c. This suggests that the observed decrease of electrical conductivity is caused not only by a reduction in n but also by a reducing carrier mobility. Correspondingly, we tuned the electron-phonon interaction potential constant (E_{Def}) (Fig. 3d), which has an inverse dependence with mobility (equation S7), to match the measured electrical conductivity (using equations S5 – S10). Adjusting E_{Def} is reasonable within the SPB framework as there is

no physical reason why the other scattering parameter E_{AS} could be affected, and it has been shown before that E_{Def} might be affected e.g. by strain [23,36–38] probably occurring at a nm-scale due to Mg loss. The other physical constants in the mobility equations, e.g. the longitudinal speed of sound (v_l) are expected to be relatively constant; for v_l it was recently shown that the temperature dependence is not too strong and the variation with composition is not significant for small possible changes [39]. Beyond 80 h, we observe a bending and a maximum in the absolute value of Seebeck coefficient (Fig. 2a) which can be attributed to the influence of the minority carriers from the valence band, visualizing the SPB model does not hold (anymore).

Consequently, we have utilized a two parabolic band (2 PB) model (relevant equations in the supplementary information) to capture the behavior of transport properties. For the prediction of transport properties using a 2 PB model, solving the charge neutrality equation $n_D^+ + p = n_A^- + n$ is required, where n and p are thermal equilibrium concentrations of electrons and holes while n_D^+ is the (positive) charge carrier concentration due to donor atoms and n_A^- is the charge carrier concentration due to ionized acceptor atoms. In case of a single, fully ionized n-type dopant n_D^+ is identical to the atomic concentration of that dopant, this is presumably the case here for Sb. However, in $Mg_2(Si,Sn)$, intrinsic defects are known to be crucial as well [40,41] with excess Mg contributing to n_D^+ in the form of interstitial defect I_{Mg}^{2+} and deficient Mg contributing to n_A^- in the form of vacancies V_{Mg}^{2-}. The n_D^+ due to Sb can be assumed to be constant based on our last study [23], however the net carrier concentration due to point defects $N_D = n_{D,Sb}^+ + n_{D,Mg}^+ - n_{A,Mg}^-$ depends on Mg content in the material and changes if the Mg content changes. N_D might be called "dopant concentration" but note that this corresponds to an effective charge carrier concentration due to intrinsic and extrinsic point defects, rather than an atomic concentration. The charge neutrality equation can then be written as $N_D + p = n$ and a value of N_D must be provided to solve it for the 2 band model.

For the single band analysis with one dominant carrier type, we can assume $p \sim 0$ and $N_D = n$. We use this N_D for the first region (0 h − 80 h), however, we lack values beyond this duration. For this reason, we measured $R_H(T)$ of sample 1 (Fig. S11c) after the saturation of transport properties during annealing experiment. The measured R_H is nearly constant from room temperature up to ~500 K while it decreases rapidly beyond this temperature due to the minority charge carrier contribution. The latter agrees with the prior S and σ measurements which also showed minority carrier contributions after the initial 80 h. The constant Hall coefficient for $T < 500$ K indicates that below 500 K the majority charge carriers are dominant, the SPB model is valid and hence $n = N_D$. Consequently, n at room temperature after the annealing experiment can be assumed to be N_D at the end of our annealing experiment (at 276 h) i.e. $N_{RT} = 0.34 \times 10^{20}\text{cm}^{-3} = N_{D,\ 276\ h}$.

From Fig. 2a, we learn that the Seebeck coefficient saturates from 210 h and beyond, thus, N_D for this third region is assumed constant i.e. $N_{D,\ sat} = 0.34 \times 10^{20}\text{cm}^{-3}$. It is plausible that the change in N_D is related to Mg loss and one can therefore expect $N_D(t)$ to be a monotonous function. We have therefore used a simple exponential decay function ($N_D(t) = 0.34 \times 10^{20} + Ae^{-t/\tau}$; with $\tau = -103.84$ h) to fit N_D between 0 h and 210 h. Note that this simple exponential fit agrees very well with the measurement results available between 0 h and 80 h, see Fig. 3b. Following this, the transport properties were predicted utilizing a 2 PB model by employing equations S1 − S13, and the parameters listed in Table 2.

Furthermore, the SPB validity range was confirmed by comparing the Seebeck coefficient according to the SPB and the 2 PB model and evaluating $1 - (\frac{S_{2PB}}{S_{SPB}})$, see Fig. S12 and the discussion there. The band gap value of $E_g = 0.33$ eV closely agrees with values used by Bahk et al. [43] and Zhang et al. [30] suggesting our assumption of band gap is reasonable. We found reasonable but not perfect agreement between predicted and experimental Seebeck coefficient and electrical conductivity (Fig. 3e and 3f). More specifically, our model reproduces the observed bending and nonlinearity in Seebeck coefficient, but is shifted to longer annealing durations, and both predicted and measured electrical conductivity disagree moderately at longer annealing durations. An imperfect agreement can be due to a non-perfect estimation of N_D but could also be because we assume all other modelling parameters to be constant over the complete annealing duration. Furthermore, assuming one effective conduction band in a 2 PB model to analyze transport properties might not be fully justified since each conduction band might have differential contribution to the transport as it is not clear how well the convergence is fulfilled. Our analysis and previous observations [11] furthermore suggest a lowering in m_D^* with annealing. This lowering can be qualitatively explained by a lifted degeneracy of the converged conduction bands for n-type $Mg_2Si_{0.4}Sn_{0.6}$ and varying n [44]. The same reason could also explain an increase in E_{Def}, observed within the SPB analysis and shown in Fig. 3d. The corresponding figures (Figs. S13 and S14) and a more detailed discussion is presented in the supplementary information. The observed changes in m_D^* could be a direct consequence of a change of the density of states due to annealing causing Mg loss or due to a minor offset between two conduction bands. Similarly, the deduced increase in E_{Def} could be due to an actual increase in the acoustic phonon scattering or an artifact from the SPB analysis on an actual 2 conduction band system. However, for a detailed understanding and confirmation of our modelling results, which reflect changes in said parameters, further experimental data is required.

Based on our last study [23], some Mg loss might not be bad due to counteracting effects between μ and κ_{lat} but large Mg loss clearly leads to poor electrical properties, as shown by the $PF(T)$ (Fig. S15) measured before and after the annealing experiment which also agrees with Kato's observations [25].

Following the notation from Kato et al. [24], the equivalent Mg deficiency in $Mg_{2-\delta}Si_{0.385}Sn_{0.6}Sb_{0.015}$ ($\delta = (4y - na^3)/8$) at room temperature, was estimated for the sample 1 before and after annealing, where y is the Sb content, and a is the lattice parameter. The equation is based on the assumption that each Sb atom provides one electron, each I_{Mg}^{2+} donates two electrons and each V_{Mg}^{2-} accepts two electrons; other defects are neglected based on their lower densities in Mg_2Si and Mg_2Sn [40,41]. A negative value of ($\delta < 0$) can be obtained for hyper-stoichiometric samples, which is reasonable due to the symmetrical charge of the most relevant defects. From this we can estimate a phase width $\Delta\delta$ for the employed composition and temperature, and find $\Delta\delta \sim 0.008$ ($-0.002 < \delta < 0.006$). It is plausible to assume $\delta = -0.002$ as the hyper-stoichiometric limit as we started the synthesis with a significant Mg excess ($\delta = -0.06$). $\delta = 0.006$ (Fig. S16) can be identified as lower limit from the transport model: for the saturation regime (t > 210 h) we find that the Seebeck coefficient at 710 K is still highly sensitive to changes of N_D ($N_D/n \approx 5$) and a reduction of N_D below 0.34×10^{20} cm^{-3} would lead to a further reduction of the absolute values of S, see Fig. S17. As this is clearly not observed (Fig. 3), we can backwards conclude that N_D is indeed stable beyond 210 h and thus Mg loss has stopped. This also implies that the Mg-loss rate is a strong function of the Mg content in Mg_{2-}

Table 2
Parameters employed for single- and multi-band modelling of electrical transport properties.

Parameters	Employed values	How obtained
Band gap (E_g) (eV) at 710 K	0.33	Fitting experimental data
DOS effective mass, m_D^* (m_0)	$m^*_{D,CB} = 2.4$; $m^*_{D,VB} = 1.54$	[23,35]; linear interpolation of $m_D(x)$ for p-$Mg_2Si_{1-x}Sn_x$
Valley degeneracy (N_v)	$N_{v,CB} = 6$; $N_{v,VB} = 2$	[35,42]
Atom density (N_0) (m^{-3})	418×10^{28}	[35]
Longitudinal speed of sound (v_l) (m/s)	5760	[39]
Fractional alloy composition (x)	0.6	–
Electron-phonon interaction potential constant (E_{Def}) (eV)	0 h – 80 h: Fig. 3d, 81 h – 276 h: 12.4	0 h–80 h: Predicted using SPB analysis on measured electrical conductivity data, for t > 80h, $E_{Def,80h} = E_{Def\ >\ 80h}$
Alloy scattering potential constant (E_{AS}) (eV)	$E_{AS,CB} = 0.5$, $E_{AS,VB} = 0.5$	[35,42]
N_D (Dopant concentration) (cm^{-3})	Described in text	Fig. 3b

$_{\delta}Si_{0.385}Sn_{0.6}Sb_{0.015}$ and that Mg evaporates easier for ($-0.002 < \delta < 0.006$) than for $\delta > 0.006$. This is highly plausible as $\delta > 0.006$ can only be achieved by a degradation of the material and the formation of elemental secondary phases [19,22]. Our result for $\Delta\delta \sim 0.008$ ($-0.002 < \delta < 0.006$) and that from Kato's work [25] for 1 mol. % Sb, $\Delta\delta \sim 0.006$ ($-0.002 < \delta < 0.004$), are in close agreement. The corresponding stoichiometries before and after annealing is $Mg_{2.002}Si_{0.385}Sn_{0.6}Sb_{0.015}$ and $Mg_{1.994}Si_{0.385}Sn_{0.6}Sb_{0.015}$, respectively. The likewise change in carrier concentration (Δn) due to annealing our case is $\Delta n = 2.25 \times 10^{20}$ cm^{-3}, and for Kato (for $Mg_2(Si_{0.5}Sn_{0.5})_{0.99}Sb_{0.01}$) is $\Delta n = 1.6 \times 10^{20}$ cm^{-3}. The minor differences in $\Delta\delta$ (and Δn) might arise from differences in Sb content, annealing temperature, Si:Sn ratio and annealing environment, which was 500 °C, 50:50 and $P_{Mg} \sim 0.1$ Pa in the latter case, respectively. We observe a clear change in the composition going from Mg rich to Mg poor stoichiometry in both cases. We also note that there is quite a difference between the deduced "actual" composition before annealing ($\delta = -0.002$) and the nominal one ($\delta = -0.06$), indicating that Mg is lost during the synthesis or can be incorporated into the materials without an influence on the thermoelectric properties, e.g. on the grain boundaries.

5. Conclusions

We investigated in situ an effect of annealing on the electrical transport properties of Sb-doped $Mg_2Si_{0.4}Sn_{0.6}$. Two identical samples were annealed in two different atmospheres i.e. sample 1, for S and σ measurement under helium, and sample 2 for R_H and σ measurement in vacuum, respectively. The samples do not show de-mixing and remain almost single phase in both setups during annealing at 710 K for several 100 h. However, both samples show clear signs of charge carrier loss, presumably due to Mg loss; in fact, the observed change in S, σ and R_H can be well explained assuming continuous Mg loss which follows a simple exponential time dependence. In situ transport measurements thus allow for an estimation of the Mg-loss rate and the involved time constants (> 10^2 hours for our conditions). An in-depth analysis of the transport data using a single parabolic conduction band model and a two parabolic band (conduction plus valence band) model reveals furthermore a decrease in carrier mobility with ongoing Mg loss and a reduced density of states effective mass. Both could be a consequence of the Mg loss itself or indicate that the two conduction bands in $Mg_2Si_{1-x}Sn_x$ are not fully converged at room temperature for $x = 0.6$. Finally, we can estimate a lower and an upper limit for the Mg-content in $Mg_2Si_{0.4}Sn_{0.6}$ and show that the Mg loss rate depends on the Mg content in the material. In summary, this work highlights the benefits of in-situ measurements and combined transport analysis as this allows for insight on materials degradation mechanisms and kinetics.

Data availability statement

The raw data required to reproduce these findings are available to download from [INSERT PERMANENT WEB LINK(s)]. The processed data required to reproduce these findings are available to download from [INSERT PERMANENT WEB LINK(s)].

Credit author statement

Aryan Sankhla: Conceptualization, Data curation, Validation, Analysis, Writing – original draft. Hasbuna Kamila: Discussions and suggestions on the study, Writing: Reviewing and Editing. Harshita Naithani: Discussions and suggestions on the study, Writing: Reviewing and Editing. Eckhard Mueller: Supervision, Writing: Reviewing and Editing. Johannes de Boor: Conceptualization, Methodology, Validation, Supervision, Writing- Reviewing and Editing, Project administration.

Declaration of competing interest

The authors declare that they have no known competing financial interests or personal relationships that could have appeared to influence the work reported in this paper.

Acknowledgments

We would like to gratefully acknowledge the endorsement from DLR Executive Board Members for Space Research and Technology and the financial support from the Young Research Group Leader Program. The authors would like to thank P. Blaschkewitz (DLR) for his continuous support with the thermoelectric measurements. The authors thank Prof. Titas Dasgupta (Department of Metallurgical Engineering and Materials Science, IIT Bombay) for insightful discussion on this study. The authors also thank Radhika Ravindra Deshpande and Leo Millerand for their help with Le Bail analysis on X ray diffractograms. The authors thank Mr. Frederic Kreps and Dr. Klemens Kelm from the Microstructural Research and Metallography lab of our institute for their help with microstructure analysis and discussion. The authors A.S., H.K. and H.N. would like to acknowledge financial support by the German Academic Exchange Service (Fellowship No. 247 and No. 403), while J.d.B. is partially funded by the Deutsche Forschungsgemeinschaft (DFG, German Research Foundation), project number 396709363.

Appendix A. Supplementary data

Supplementary data to this article can be found online at https://doi.org/10.1016/j.mtphys.2021.100471.

References

[1] W. Liu, J. Hu, S. Zhang, M. Deng, C.-G. Han, Y. Liu, New trends, strategies and opportunities in thermoelectric materials: a perspective, Materials Today Physics 1 (2017) 50–60.

[2] J. Byrnes, D.R.G. Mitchell, S. Aminorroaya Yamini, Thermoelectric performance of thermally aged nanostructured bulk materials—a case study of lead chalcogenides, Materials Today Physics 13 (2020) 100190.

[3] J. Shuai, J. Mao, S. Song, Q. Zhang, G. Chen, Z. Ren, Recent progress and future challenges on thermoelectric Zintl materials, Materials Today Physics 1 (2017) 74–95.

[4] M.M. Al Malki, Q. Qiu, T. Zhu, G.J. Snyder, D.C. Dunand, Creep behavior and postcreep thermoelectric performance of the n-type half-Heusler alloy $Hf_{0.3}Zr_{0.7}NiSn_{0.98}Sb_{0.02}$, Materials Today Physics 9 (2019) 100134.

[5] P. Broz, F. Zelenka, Z. Kohoutek, J. Vresťal, V. Vykoukal, J. Bursík, A. Zemanova, G. Rogl, P. Rogl, Study of thermal stability of $CoSb_3$ skutterudite by Knudsen effusion mass spectrometry, Calphad 65 (2019) 1–7.

[6] A.L.E. Smalley, S. Kim, D.C. Johnson, Effects of composition and annealing on the electrical properties of $CoSb_3$, Chem. Mater. 15 (20) (2003) 3847–3851.

[7] H. Shang, Z. Liang, C. Xu, S. Song, D. Huang, H. Gu, J. Mao, Z. Ren, F. Ding, N-type $Mg_3Sb_{2-x}Bi_x$ with improved thermal stability for thermoelectric power generation, Acta Mater. 201 (2020) 572–579.

[8] C. Jiang, X.A. Fan, B. Feng, J. Hu, Q. Xiang, G. Li, Y. Li, Z. He, Thermal stability of p-type polycrystalline Bi_2Te_3-based bulks for the application on thermoelectric power generation, J. Alloys Compd. 692 (2017) 885–891.

[9] J.-H. Pi, S.-G. Kwak, S.-Y. Kim, G.-E. Lee, I.-H. Kim, Thermal stability and mechanical properties of thermoelectric tetrahedrite $Cu_{12}Sb_4S_{13}$, J. Electron. Mater. 48 (4) (2019) 1991–1997.

[10] L. Zhang, X. Chen, Y. Tang, L. Shi, G.J. Snyder, J.B. Goodenough, J. Zhou, Thermal stability of $Mg_2Si_{0.4}Sn_{0.6}$ in inert gases and atomic-layer-deposited Al_2O_3 thin film as a protective coating, J. Mater. Chem. A 4 (45) (2016) 17726–17731.

[11] K. Yin, Q. Zhang, Y. Zheng, X. Su, X. Tang, C. Uher, Thermal stability of $Mg_2Si_{0.3}Sn_{0.7}$ under different heat treatment conditions, J. Mater. Chem. C 3 (40) (2015) 10381–10387.

[12] S. Ayachi, R. Deshpande, P. Ponnusamy, S. Park, J. Chung, S. Park, B. Ryu, E. Mueller, J. de Boor, On the relevance of point defects for the selection of contacting electrodes: Ag as an example for Mg_2(Si,Sn)-based thermoelectric generators, Materials Today Physics 16 (2021) 100309.

[13] W. Liu, X. Tan, K. Yin, H. Liu, X. Tang, J. Shi, Q. Zhang, C. Uher, Convergence of conduction bands as a means of enhancing thermoelectric performance of n-type $Mg_2Si_{1-x}Sn_x$ solid solutions, Phys. Rev. Lett. 108 (16) (2012) 166601.

[14] T. Dasgupta, C. Stiewe, J. de Boor, E. Mueller, Influence of power factor enhancement on the thermoelectric figure of merit in $Mg_2Si_{0.4}Sn_{0.6}$ based materials, Phys. Status Solidi 211 (6) (2014) 1250–1254.

[15] Y. Zhu, Z. Han, F. Jiang, E. Dong, B.-P. Zhang, W. Zhang, W. Liu, Thermodynamic criterions of the thermoelectric performance enhancement in Mg_2Sn through the self-compensation vacancy, Materials Today Physics 16 (2021) 100327.

[16] A. Sankhla, A. Patil, H. Kamila, M. Yasseri, N. Farahi, E. Mueller, J. de Boor, Mechanical alloying of optimized Mg_2(Si,Sn) solid solutions: understanding phase evolution and tuning synthesis parameters for thermoelectric applications, ACS Appl. Energy Mater. 1 (2) (2018) 531–542.

[17] A. Sankhla, M. Yasseri, H. Kamila, E. Mueller, J. de Boor, Experimental investigation of the predicted band structure modification of Mg_2X (X: Si, Sn) thermoelectric materials due to scandium addition, J. Appl. Phys. 125 (22) (2019) 225103.

[18] J. de Boor, T. Dasgupta, H. Kolb, C. Compere, K. Kelm, E. Mueller, Microstructural effects on thermoelectric efficiency: a case study on magnesium silicide, Acta Mater. 77 (2014) 68–75.

[19] M. Yasseri, A. Sankhla, H. Kamila, R. Orenstein, D.Y.N. Truong, N. Farahi, J. de Boor, E. Mueller, Solid solution formation in Mg_2(Si,Sn) and shape of the miscibility gap, Acta Mater. 185 (2020) 80–88.

[20] L. Chen, G. Jiang, Y. Chen, Z. Du, X. Zhao, T. Zhu, J. He, T.M. Tritt, Miscibility gap and thermoelectric properties of ecofriendly $Mg_2Si_{1-x}Sn_x$ ($0.1 \leq x \leq 0.8$) solid solutions by flux method, J. Mater. Res. 26 (24) (2011) 3038–3043.

[21] I.-H. Jung, D.-H. Kang, W.-J. Park, N.J. Kim, S. Ahn, Thermodynamic modeling of the Mg–Si–Sn system, Calphad 31 (2) (2007) 192–200.

[22] M. Yasseri, K. Mitra, A. Sankhla, J. de Boor, E. Mueller, Influence of Mg loss on the phase stability in Mg_2X (X = Si, Sn) and its correlation with coherency strain, Acta Mater. (2021) 116737.

[23] A. Sankhla, H. Kamila, K. Kelm, E. Mueller, J. de Boor, Analyzing thermoelectric transport in n-type $Mg_2Si_{0.4}Sn_{0.6}$ and correlation with microstructural effects: an insight on the role of Mg, Acta Mater. 199 (2020) 85–95.

[24] D. Kato, K. Iwasaki, M. Yoshino, T. Yamada, T. Nagasaki, Significant effect of Mg-pressure-controlled annealing: non-stoichiometry and thermoelectric properties of $Mg_{2-\delta}Si_{1-x}Sb_x$, Phys. Chem. Chem. Phys. 20 (40) (2018) 25939–25950.

[25] D. Kato, K. Iwasaki, Mg-pressure-controlled annealing for tuning Mg content and thermoelectric properties of $Mg_{2-\delta}(Si_{0.5}Sn_{0.5})_{1-x}Sb_x$, J. Alloys Compd. (2020) 157351.

[26] J. de Boor, C. Stiewe, P. Ziolkowski, T. Dasgupta, G. Karpinski, E. Lenz, F. Edler, E. Mueller, High-temperature measurement of Seebeck coefficient and electrical conductivity, J. Electron. Mater. 42 (7) (2013) 1711–1718.

[27] J. de Boor, E. Mueller, Data analysis for Seebeck coefficient measurements, Rev. Sci. Instrum. 84 (6) (2013): 065102.

[28] N.H. Pham, N. Farahi, H. Kamila, A. Sankhla, S. Ayachi, E. Mueller, J. de Boor, Ni and Ag electrodes for magnesium silicide based thermoelectric generators, Materials Today Energy 11 (2019) 97–105.

[29] K.A. Borup, J. de Boor, H. Wang, F. Drymiotis, F. Gascoin, X. Shi, L. Chen, M.I. Fedorov, E. Mueller, B.B. Iversen, G.J. Snyder, Measuring thermoelectric transport properties of materials, Energy Environ. Sci. 8 (2) (2015) 423–435.

[30] L. Zhang, P. Xiao, L. Shi, G. Henkelman, J.B. Goodenough, J. Zhou, Suppressing the bipolar contribution to the thermoelectric properties of $Mg_2Si_{0.4}Sn_{0.6}$ by Ge substitution, J. Appl. Phys. 117 (15) (2015) 155103.

[31] H. Kamila, G.K. Goyal, A. Sankhla, P. Ponnusamy, E. Mueller, T. Dasgupta, J. de Boor, Systematic analysis of the interplay between synthesis route, microstructure, and thermoelectric performance in p-type $Mg_2Si_{0.2}Sn_{0.8}$, Materials Today Physics 9 (2019) 100133.

[32] J. de Boor, S. Gupta, H. Kolb, T. Dasgupta, E. Mueller, Thermoelectric transport and microstructure of optimized $Mg_2Si_{0.8}Sn_{0.2}$, J. Mater. Chem. C 3 (40) (2015) 10467–10475.

[33] N. Farahi, C. Stiewe, D.Y.N. Truong, J. de Boor, E. Mueller, High efficiency Mg_2(Si,Sn)-based thermoelectric materials: scale-up synthesis, functional homogeneity, and thermal stability, RSC Adv. 9 (40) (2019) 23021–23028.

[34] X. Liu, T. Zhu, H. Wang, L. Hu, H. Xie, G. Jiang, G.J. Snyder, X. Zhao, Low electron scattering potentials in high performance $Mg_2Si_{0.45}Sn_{0.55}$ based thermoelectric solid solutions with band convergence, Adv. Energy Mater. 3 (9) (2013) 1238–1244.

[35] H. Kamila, P. Sahu, A. Sankhla, M. Yasseri, H.-N. Pham, T. Dasgupta, E. Mueller, J. de Boor, Analyzing transport properties of p-type Mg_2Si–Mg_2Sn solid solutions: optimization of thermoelectric performance and insight into the electronic band structure, J. Mater. Chem. A 7 (3) (2019) 1045–1054.

[36] F. Murphy-Armando, S. Fahy, Giant enhancement of n-type carrier mobility in highly strained germanium nanostructures, J. Appl. Phys. 109 (11) (2011) 113703.

[37] J.-L. Lan, B. Zhan, Y.-C. Liu, B. Zheng, Y. Liu, Y.-H. Lin, C.-W. Nan, Doping for higher thermoelectric properties in p-type BiCuSeO oxyselenide, Appl. Phys. Lett. 102 (12) (2013) 123905.

[38] Z. Liu, Y. Wang, J. Mao, H. Geng, J. Shuai, Y. Wang, R. He, W. Cai, J. Sui, Z. Ren, Lithium doping to enhance thermoelectric performance of MgAgSb with weak electron–phonon coupling, Adv. Energy Mater. 6 (7) (2016) 1502269.

[39] G. Castillo-Hernandez, M. Yasseri, B. Klobes, S. Ayachi, E. Mueller, J. de Boor, Room and high temperature mechanical properties of Mg_2Si, Mg_2Sn and their solid solutions, J. Alloys Compd. 845 (2020) 156205.

[40] X. Liu, L. Xi, W. Qiu, J. Yang, T. Zhu, X. Zhao, W. Zhang, Significant roles of intrinsic point defects in Mg_2X (X = Si, Ge, Sn) Thermoelectric Materials, Adv. Electron. Mater. 2 (2) (2016) 1500284.

[41] B. Ryu, E.-A. Choi, S. Park, J. Chung, J. de Boor, P. Ziolkowski, E. Mueller, S. Park, Native point defects and low p-doping efficiency in Mg_2(Si,Sn) solid solutions: a hybrid-density functional study, J. Alloys Compd. 853 (2021) 157145.

[42] W. Liu, H. Chi, H. Sun, Q. Zhang, K. Yin, X. Tang, Q. Zhang, C. Uher, Advanced thermoelectrics governed by a single parabolic band: $Mg_2Si_{0.3}Sn_{0.7}$, a canonical example, Phys. Chem. Chem. Phys. 16 (15) (2014) 6893–6897.

[43] J.-H. Bahk, Z. Bian, A. Shakouri, Electron transport modeling and energy filtering for efficient thermoelectric $Mg_2Si_{1-x}Sn_x$ solid solutions, Phys. Rev. B 89 (7) (2014): 075204.

[44] H. Naithani, T. Dasgupta, Critical analysis of single band modeling of thermoelectric materials, ACS Appl. Energy Mater. 3 (3) (2020) 2200–2213.

Chapter 10 Discussion

10.1 Summary

The main objective of this work was to understand the composition-synthesis-microstructure-property relationships in n-type $Mg_2(Si,Sn)$ and the effects of long-term heat treatment on these materials. In this regard, a pre-existing Hall setup was extended to measure the Hall coefficient and the electrical conductivity at high temperatures ($300\ \text{K} - 723\ \text{K}$). In Chapter 6, mechanical alloying was utilized to synthesize n-type $Mg_2(Si,Sn)$ solid solutions that showed excellent reproducibility of high TE performance. Thus, mechanical alloying was established as a fast and reliable synthesis technique to understand process-microstructure-property-performance relationships in this material class. Optimized TE properties were affected due to a variation in the high-temperature sintering parameters. The room temperature carrier concentration of the samples decreased with increasing sintering duration supporting the observations of the T-dependence of the Seebeck coefficient and electrical conductivity. A TEM-based microstructure analysis of samples sintered for different duration revealed no hints of dopant (Sb) loss but Mg loss, which was the reason for a variation in TE properties (Chapter 8). Later, *in-situ* measurements of TE properties were conducted at $710\ \text{K}$ using existing HT measurement setups (Chapter 9). These experiments were performed to understand the long-term effects of HT annealing and quantify the extent of degradation of underlying microscopic material parameters.

In this final discussion chapter, the results of TE properties measured *in-situ* during annealing at higher temperatures ($773\ \text{K}$ and $848\ \text{K}$) are analyzed and discussed. The measurement (Chapter 5) and synthesis (Chapter 6) techniques, and the analytical tools (Chapter 8 and Chapter 9) established in the earlier chapters are utilized for this investigation. Using the knowledge of Chapter 6, Chapter 8 and Chapter 9 and the analysis presented in this chapter as a foundation, the practically relevant but unaddressed topic of high temperature Mg loss kinetics is investigated. For this purpose, the change of majority charge carrier concentration $N_\text{D}(t)$ was estimated by analyzing the *in-situ* measured transport properties using a two-band model. $N_\text{D}(t)$ was fitted using an exponential decay function to estimate Mg loss rates at different annealing temperatures. Rates were plugged in the Arrhenius equation to determine the effective kinetic parameters (the activation energy and the pre-exponential factor) of Mg loss in HT-$S\sigma$ and HT Hall facilities. The Hall carrier concentration n_H ($\approx N_\text{D}$ at RT) of the samples sintered at $973\ \text{K}$ for different duration were fitted using exponential decay function

as well (Chapter 6 and Chapter 8). Estimated rates and the kinetic parameters of degradation in DSP and other two facilities were compared. The analysis presented in this chapter exemplifies a methodology to study the kinetics of Mg loss rate in n-type Mg_2X (*X*: Si, Sn) solid solutions at different annealing and sintering temperatures.

10.2 *In-situ* measurement of the electrical transport properties

The major motivation to carry out *in-situ* measurements at further higher temperatures was to develop a kinetic model for the loss of Mg in n-type $Mg_2(Si,Sn)$ and a prediction of material instability in different measurement conditions and application temperatures. The *in-situ* measurements carried out in different measurement facilities (at several temperature points) are summarized in Table 10.1.

Table 10.1 Sample number, measurement facility, T_{anneal} and t_{anneal} employed for the *in-situ* annealing measurement. S, σ and n_{H} measured at room temperature and density-of-states effective mass m_{D}^{*} predicted from the SPB model both before (B) and after (A) *in-situ* annealing are tabulated as well. The values with asterisk are predicted from an assumed m_{D}^{*}.

Sample number	Measure-ment facility	*In-situ* annealing temp. (K)	*In-situ* annealing duration (h)	Measurement time (*in-situ* annealing)	S (μV/K)	σ (S/cm)	n_{H} (10^{20} cm^{-3})	$m_{\mathrm{D}}^{*}(m_0)$
1	HT-$S\sigma$ (He)	710	275	B	-116	1888	2.45	2.4
				A	-228	161.3	0.29	1.8
2	HT Hall (vacuum)	710	~1100	B	-111	1944	2.3	2.4
				A	-119.5	1305.2	1.7	2.05
3	HT-$S\sigma$	773	~95	B	-127	1544	1.9*	2.4*
				A	-234	173.75	0.29	1.8
4	HT Hall	773	~700	B	-118	1794	2.04	2.2
				A	-217	185	0.35	1.8
5	HT-$S\sigma$	848	~2.5	B	-123	1649	2.04*	2.4*
				A	-207	305	0.42	1.8
6	HT Hall	848	~120	B	-116	1852	2.4	2.4
				A	-224	162	0.38	2.0

Note that all the measurements in HT-$S\sigma$ and HT Hall were carried out in helium atmosphere ($p \approx 1$ bar) and vacuum ($\sim 10^{-3}$ bar), respectively. Particularly, the RT thermoelectric

properties (S, σ and n_H) and SPB estimated DOS effective mass m_D^* of the samples annealed at different temperatures are tabulated. Powder sample with a stoichiometry of $Mg_{2.06}Si_{0.385}Sn_{0.6}Sb_{0.015}$ was prepared by mechanical alloying (20 h) of precursors. Four different samples were sintered at 973 K/ 20 min with an axial pressure of 67 MPa. At RT, the thermoelectric properties of all samples were measured, however, n_H of sample 3 and sample 5 was not measured but estimated using the equations of the SPB model (assuming a constant m_D^* corresponding to other as-prepared samples).

10.2.1 Analysis of the transport properties measured at 773 K

The T-dependent Seebeck coefficient and electrical conductivity of sample 3 were measured before the *in-situ* annealing experiment (as shown in Figure 10.1(a) and (b), respectively).

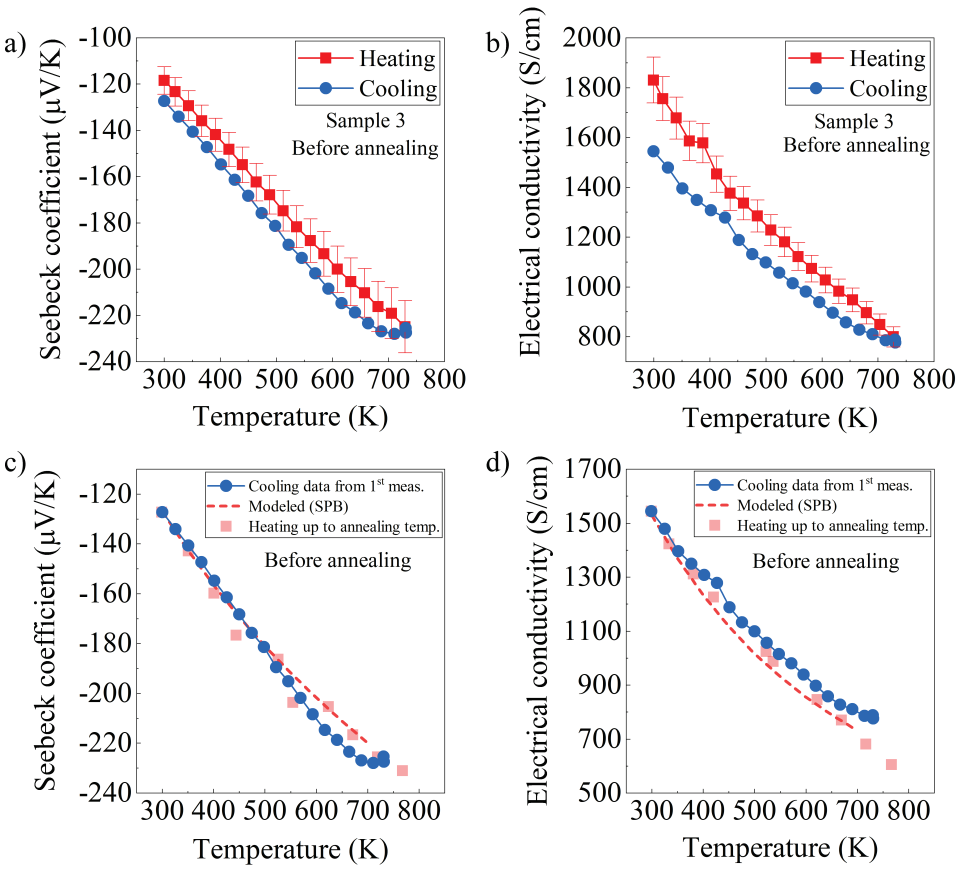

Figure 10.1 T-dependent measurement of a) S and b) σ of sample 3 ($Mg_{2.06}Si_{0.385}Sn_{0.6}Sb_{0.015}$) during a first thermal cycle. Figure c) and d) show S and σ measurements: cooling data during first thermal cycle (shown in (a) and (b)), measurement during heat-up ramp to reach $T_{anneal} \approx 773$ K and a prediction (using SPB model) of T-dependent properties. SPB parameters used to predict the transport properties in (c) and (d) are $m_D^* = 2.4m_0$, $n = 2.09 \times 10^{20}$ cm^{-3} and $E_{Def} = 10.35$ eV, respectively.

The Hall carrier concentration n_H of sample 3 was measured before the start of the *in-situ* annealing experiments as listed in Table 10.1. Moreover, the sample was re-polished before annealing experiment to remove a corrosion layer. This layer might have been formed due to the surface oxidation of $Mg_2(Si,Sn)$ during high temperature measurements. Although the measurement is done under inert gas (He), some oxygen contamination cannot be completely excluded. The sample was re-mounted and furnace of the HT-$S\sigma$ setup was heated up to reach $T_{anneal} = 773$ K. During the heat-up ramp, the T-dependent properties were re-measured as shown in Figure 10.1(c) and Figure 10.1(d). Both the T-dependent measurements (cooling part of initial thermal cycling and during heat-up ramp) show heavily doped semiconductor behavior with no significant influence of the minority carriers. After reaching (and holding) the target $T_{anneal} = 773$ K, the transport properties were measured until they saturated. The *in-situ* measured TE properties are shown in Figure 10.2.

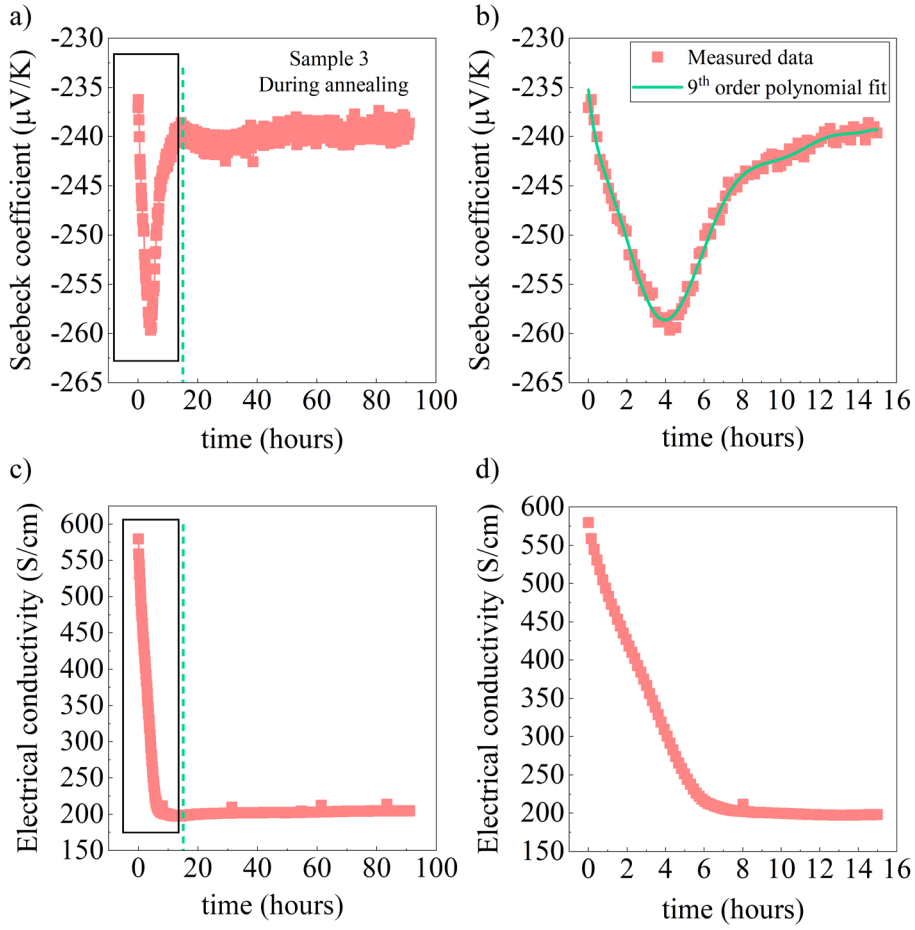

Figure 10.2 The measurement of – a), b) S and c), d) σ of sample 3 ($Mg_{2.06}Si_{0.385}Sn_{0.6}Sb_{0.015}$) at $T_{anneal} = 773$ K.

$S(t)$ can be divided into two regions (Figure 10.2(a)): first, where it exhibits a non-linear change, and the second region ($t > 15$ h) where it shows nearly constant values. In the first region, the absolute value of S increases and reaches a maximum ($S \sim -258$ μV/K) followed by a gradual decrease before saturating around -240 μV/K. The electrical conductivity (Figure 10.2(c)) continuously decays with annealing duration and saturates around $195 - 200$ S/cm. The transport properties of sample 3 between 0 h – 15 h are shown in Figure 10.2(b) and Figure 10.2(d), on which 2PB modelling has been performed (in section B.1 of Appendix B). Note that the Seebeck coefficient is fitted using a 9th order polynomial expression which is used as 'measured' data for later discussion and modelling. For $t > 15$ h, the sample shows nearly constant values of the Seebeck coefficient and the electrical conductivity indicating the saturation of properties.

An *in-situ* annealing experiment on an as-prepared sample (sample 4) was carried out at the HT Hall facility to simultaneously measure σ and R_H. Before initiating the *in-situ* measurement in HT Hall, the T-dependent transport properties of sample 4 were measured at the HT-$S\sigma$ facility. The transport properties of sample 4 are nearly identical to those of sample 3, signifying a heavily doped semiconducting behavior, and the corresponding data is shown in Figure B.7(a) and Figure B.7(b) in Appendix B. R_H and σ were measured while heating up the sample to reach the target annealing temperature and the data is shown in Figure B.7(c) and Figure B.7(d).

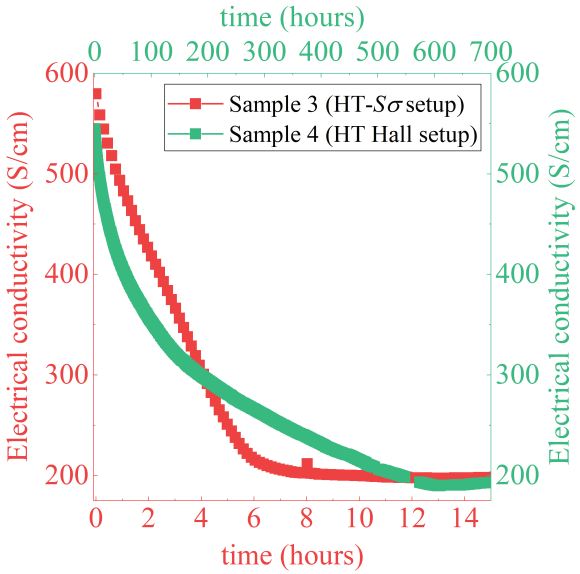

Figure 10.3 *In-situ* measured electrical conductivity σ of sample 3 (in HT-$S\sigma$) and sample 4 (HT Hall) at $T_{anneal} = 773$ K, respectively; note the different x-axes.

For comparison, the electrical conductivity measured in HT-$S\sigma$ (helium) and HT Hall (vacuum) facilities are visualized in Figure 10.3. The electrical conductivity of both samples shows a continuous decay with annealing duration t_{anneal}. Even though the electrical conductivity measured on sample 3 and sample 4 show a similar trend with t_{anneal} and nearly identical values of absolute starting and saturation values, their degradation occurs at a quite different rate. The electrical conductivity of sample 3 and sample 4 saturates after 15 hours and ~700 hours of annealing, respectively. It can also be seen that the time dependence is not exactly the same, even if rescaled. This observation agrees with the results of *in-situ* measurement at 710 K (discussed in Chapter 9), where a different rate of the degradation of electrical conductivity was observed for two samples (each annealed in the HT-$S\sigma$ and HT Hall facilities respectively). Therefore, the initial idea of combining the transport properties of sample 3 (S and σ) and sample 4 (σ and R_{H}) and then using them for a combined transport modelling (e.g. use a rescaled Hall carrier concentration n_{H} from sample 4 to analyze the data from sample 3) is not feasible. Nevertheless, the modelling of sample 3 and sample 4 can be performed individually but as the degradation mechanism is identical for both the samples, only the *in-situ* measured properties of sample 3 are predicted using transport modelling.

The temperature dependent TE properties measured before and after annealing show a single (converged) band transport behavior at room temperature. This conclusion is supported by the results of the SPB analysis of T-dependent properties measured before annealing, as visualized in Figure 10.1(c) and Figure 10.1(d). Additionally, the effect of minority carriers is only observed in the measurement temperature range $T > 450$ K of the temperature dependent properties measured after annealing (Figure B.1). This proves that the effect of minority carriers is negligible at room temperature, and correspondingly, these properties were analyzed and predicted using SPB model as well. The modelling revealed that n ($\approx N_{\mathrm{D}}$, dopant concentration at RT), m_{D}^{*} and E_{Def} are the most affected microscopic material parameters. The RT thermoelectric properties show single-band behavior while *in-situ* measured Seebeck coefficient (Figure 10.2(c)) indicates plausible influence of minority carrier band characterized by a hump (~4 h). Therefore, the SPB parameters extracted from the room temperature thermoelectric properties are insufficient to predict *in-situ* measured properties as these parameters do not reflect changes in the measured properties at annealing temperatures. These properties can be modelled using 2PB model but require dopant concentration, N_{D}, as an input, which is not directly available for the annealing duration. Note that, generally, N_{D} is regarded as the concentration of extrinsic dopants, however, for $Mg_2(Si,Sn)$, N_{D} can be called as dopant concentration referring to an effective charge carrier concentration due to intrinsic and extrinsic

point defects, rather than an atomic concentration. The dopant concentration can be then written as $N_{\mathrm{D}} = n^{+}_{\mathrm{D,Sb}} + n^{+}_{\mathrm{D,Mg}} - n^{-}_{\mathrm{A,Mg}}$, where, $n^{+}_{\mathrm{D,Sb}}$, $n^{+}_{\mathrm{D,Mg}}$ and $n^{-}_{\mathrm{A,Mg}}$ refers to carrier concentration due to ionized Sb atoms, charged interstitial Mg atoms, and charged Mg vacancies, respectively. The contribution of $n^{+}_{\mathrm{D,Sb}}$ to the dopant concentration is constant as the microstructural investigation in Chapter 8 showed no indications of Sb loss. Therefore, any changes in the *in-situ* measured properties are plausibly due to variation in Mg-related charged defects. Unlike in the present case, N_{D} values corresponding to the *in-situ* experiments at 710 K (in Chapter 9) could be partially extracted from the Seebeck coefficient measured in the interval of 0 h – 80 h of the annealing duration using an SPB model since a single band behavior was observed in this interval. For the *in-situ* annealing experiment here, N_{D} was estimated using an approach (described in detail in section B.1 of Appendix B) where the measured Seebeck coefficient was utilized to extract N_{D} at annealing temperature. Specifically, two different sets of $N_{\mathrm{D}}(t)$ values were extracted by implementing two different values of both, $m^{*}_{\mathrm{D,CB}}$, and $E_{\mathrm{Def,CB}}$, corresponding to before and after annealing, while keeping the other essential microscopic material parameters constant. Implementing these values of stated parameters in 2PB model, N_{D} values were estimated within the upper ($\approx 2.5 \times 10^{20}$cm^{-3}) and lower limit ($\approx 0.3 \times 10^{20}$cm^{-3}) of SPB carrier concentration n ($\approx N_{\mathrm{D}}$, dopant concentration at RT) computed both before and after annealing, respectively. The upper and lower limit of the carrier concentration corresponds to the non-depleted and depleted state of the sample with respect to Mg. The microscopic material parameters corresponding to these states are designated as non-annealed parameters (NAP) and post-anneal parameters (PAP), respectively. Besides, the band gap, E_{g}, which is another essential input to the 2PB model, was optimized to extract reliable N_{D} values. The Seebeck coefficient $S(N_{\mathrm{D}})$ is only a function of E_{g} when the microscopic material parameters and temperature are kept constant. Considering this, different sets of $S(N_{\mathrm{D}})$ values were predicted by using different E_{g} values and employing non-annealed parameters in the model. The band gap value of $E_{\mathrm{g}} = 0.296$ eV was chosen which led to a close agreement between the maximum value of the predicted and measured Seebeck coefficient (Note that the maximum value of the *in-situ* measured Seebeck coefficient at 773 K is characterized by a hump in Figure 10.2(c)). In this way, the band gap was estimated and reliable $N_{\mathrm{D}}(t)$ data was extracted from the model. Later, this $N_{\mathrm{D}}(t)$ data was utilized to predict the measured electrical conductivity $\sigma(t)$ which showed a good agreement. This simplified approach allowed a good prediction of N_{D} values for the annealing duration.

10.2.2 *In-situ* measurement of transport properties while annealing at 848 K

The *in-situ* measurement of thermoelectric properties was carried out on an as-prepared sample (sample 5) in the HT-$S\sigma$ facility at $T_{\text{anneal}} = 848$ K as shown in Figure 10.4. The measured properties degrade even before reaching $T_{\text{anneal}} = 848$ K which is highlighted by the initial few data points in blue color with their corresponding temperature values (in K). This translates to the fact that the degradation of transport properties is quite fast at this temperature due to Mg loss. During the optimization of this experiment, it was observed that the transport properties degrade even before reaching the target T_{anneal}. Keeping this observation in context, T-dependent transport properties of this sample were not measured during heat-up ramp (unlike sample 3). Instead, the sample was mounted and heated such that the sample temperature approached the target T_{anneal} directly. After reaching T_{anneal}, the Seebeck coefficient is observed to reduce slowly without showing a maximum.

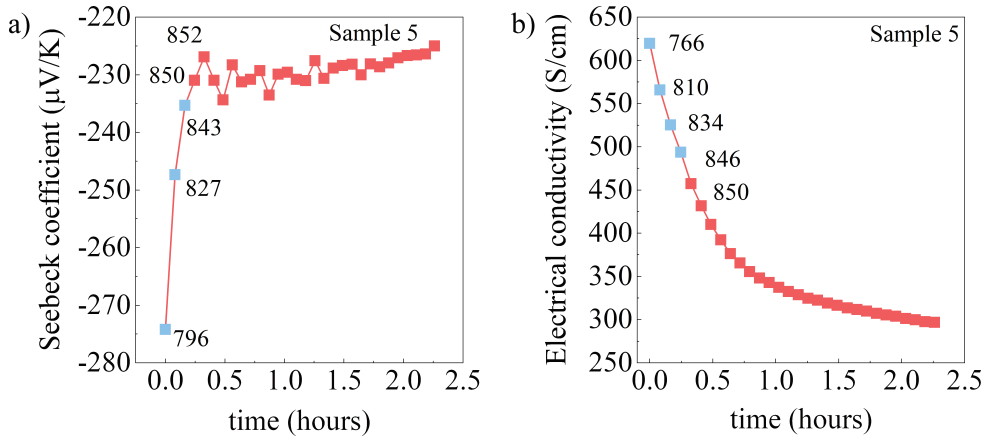

Figure 10.4 a) S and b) σ of sample 5 (non-annealed $Mg_{2.06}Si_{0.385}Sn_{0.6}Sb_{0.015}$) measured at 848 K for a duration of nearly 2.5 hours. Note that the measurement temperature was not stable in the beginning of *in-situ* measurement. The actual measurement temperature (in K) is indicated close to the blue data points, while points in red indicate that the desired T_{anneal} is reached.

From the almost constant $S(t)$ after reaching a stable temperature, it can be inferred that most of the degradation progress occurred even before reaching T_{anneal}. The electrical conductivity also starts to degrade before reaching the T_{anneal}, and continue to degrade as the T_{anneal} is held constant which agrees with the result of previous *in-situ* experiments conducted at 773 K. The sample was taken out before the TE properties fully saturated. As most degradation supposedly occurred before reaching T_{anneal} therefore, the modelling of these properties is not straightforward and will be carried out in future.

10.3 Studying the kinetics of Mg loss in $Mg_2(Si,Sn)$

In-situ annealing experiments have shown that the thermal stability of $Mg_2(Si,Sn)$ is compromised by Mg loss which serves as the main reason of material degradation. As a first necessary step, the degradation kinetics of these materials need to be known at the elevated temperatures ($673\ K - 773\ K$) of TEG operation to predict TEG lifetimes. The microscopic mechanism of Mg loss in $Mg_2(Si,Sn)$ is a practically relevant topic that must be understood before devising suitable solutions, e.g. coating, to prevent it. The *diffusion* of Mg-atoms is the most plausible mechanism at high temperatures that would enable and support Mg loss in $Mg_2(Si,Sn)$. A directed material transport in a solid by an atomic motion of one or more species i.e. the net flux of any species (e.g. ions, atoms etc.) is called diffusion. Diffusion is driven by a concentration gradient of the diffusing species and the temperature. A difference in the chemical potential of one or more components of a solid is the driving force for the transport of those components from a region of high concentration to low concentration. In the presence of an external driving force, diffusion becomes direction dependent [227]. The generally relevant external driving forces include: electric field, thermal gradient, stress gradient etc. The rate of diffusion of a particular species (atoms, ions) can be measured or determined by its flux J. Flux is defined as the number of atoms passing through a plane of unit area per unit time. In the absence of an external driving force [228], a net flux of atoms in a bulk material is proportional to the concentration gradient $\nabla\varphi$ (Fick's first law):

$$J = -D\nabla\varphi \qquad \text{Equation (10.1)}$$

Here, D is the diffusion coefficient (in cm^2/s), and $\nabla\varphi$ is the concentration gradient in 3D (in $atoms/cm^3$ cm). The diffusion flux and the concentration gradient are related to the gradient of the chemical potential $\Delta\mu$ of the diffusing species [229]. Besides, diffusion depends on specific experimental conditions such as temperature, pressure, composition, time, type of diffusion (e.g. bulk or grain boundary etc.), bonding and crystal structure, concentration of diffusing species and matrix composition etc. [230]. In most cases, the temperature dependence of the diffusion coefficient can be approximated by:

$$D = D_0 e^{(-\Delta H/k_B T)} \qquad \text{Equation (10.2)}$$

Here, D_0 is the pre-exponential factor (or frequency factor) and ΔH is the activation enthalpy associated with the diffusion process. Equation (10.2) describes a diffusion-controlled process, which is derived from the Arrhenius expression that is given as [231]:

$$K = Ae^{-E_a/RT} \qquad \text{Equation (10.3)}$$

Here, K is the equilibrium (or rate) constant, while A and E_a are the pre-exponential (or frequency) factor and the activation enthalpy of a reaction, respectively. The molar gas constant R amounts to 8.314 J mol^{-1} K^{-1}, and $R = k_B N_A$, where N_A is the Avogadro's number. The pre-exponential factor, A, includes parameters such as the vibrational frequency of atoms, atomic jump frequency, probability of jump (to be successful), the concentration of defects etc. [147, 232]. Equation (10.3) is an emperical expression for the temperature dependence of the rate constant that is used to identify the mechanism of a chemical process in gases, liquids or solids. In solids, thermally induced reaction and processes (e.g. the temperature dependence of the formation of vacancies, the temperature dependence of diffusion coefficients etc.) are modeled using expressions that follow an Arrhenius type dependence. A multi-step process in solids (e.g. high temperature oxidation behavior of ZrNiSn-based half Heusler thermoelectrics [233], degradation kinetics of $CoSb_3$-based skutterudite thermoelectric device [234]) usually involves more than one steps including the formation of defects, a diffusion of one or more species etc. Then, such a process can be understood as an analogue to a chemical reaction. Thus, Equation (10.2) describing the temperature dependence of the diffusion coefficient can be treated as a special case of Equation (10.3), where the diffusion coefficient D is the rate constant K, while D_0 and ΔH corresponds to A and E_a/N_A, respectively.

The whole process of Mg loss in $Mg_2(Si,Sn)$ is assumed here as a chain of process steps that follow one to the other like in the chemical reaction kinetics, which is described by Equation (10.3). Each individual step of the whole process is assumed to follow an Arrhenius type dependence, which naturally leads to an Arrhenius type dependence of the overall process as a whole if one of the steps in a complex Mg loss mechanism is dominant. Therefore, the determined Arrhenius parameters, A and E_a, are effective as they represent the contributions of the pre-exponent and activation energy (referred here as energy barriers) of individual processes of the complete mechanism, respectively.

Based on the results of Chapter 8, Chapter 9 and the studies of Kato *et al.* [145, 146, 235], the loss of Mg in Sb-doped $Mg_2(Si,Sn)$ can be broadly expressed in the following way:

$$\begin{aligned} &Mg_{2.06-x}Si_{0.385}Sn_{0.6}Sb_{0.015}\ (s) \rightarrow \\ &Mg_{2.06-x-y}Si_{0.385}Sn_{0.6}Sb_{0.015}\ (s) + \ yMg\ (g)\uparrow \end{aligned} \qquad \text{Equation (10.4)}$$

Note that x refers to the loss of Mg during the high temperature sintering process while y refers to the loss of Mg during the *in-situ* annealing experiment.

The Mg loss in n-type $Mg_2(Si,Sn)$ is assumed to be a multi-step process which can be structured as: (1) the transport of sublimated Mg away from the atmosphere surrounding the sample, (2) Mg sublimation from the sample surface to atmosphere nearby the sample surface, (3) the transport of Mg atoms along the grain boundaries to the sample surface, (4) the formation of Mg vacancies (V_{Mg}^{2-}) and/or annihilation of Mg interstitials (I_{Mg}^{2+}) and (5) the diffusion of Mg *via* vacancies and/or interstitial sites towards the grain boundaries, allowing the segregation of Mg atoms from the matrix. Note that step (1) of the degradation process depends on the type of annealing atmosphere.

This first description of a microscopic Mg loss mechanism is supported by the following points: There is a difference in the chemical potential of Mg, $\Delta\mu_{Mg}$, between the sample and the annealing atmosphere (environment). The origin of $\Delta\mu_{Mg}$ in Mg_2X can be understood by taking the example of elemental Mg [146, 235, 239]. At high temperatures, the Mg vapor pressure increases exponentially with temperature, and is 1 Pa at 701 K, 10 Pa at 773 K and 100 Pa at 861 K [238], respectively. So, when an elemental (solid) Mg is heated (say at $T > 700$ K) [238] and the Mg partial pressure in its environment is lower than the Mg vapor pressure at this temperature, this corresponds to $\mu_{Mg(s)} > \mu_{Mg(g)}$, where $\mu_{Mg(s)}$ and $\mu_{Mg(g)}$ are the chemical potentials of Mg in solid and annealing atmosphere, respectively. In this situation, the system will tend to move towards thermodynamic equilibrium i.e. $\mu_{Mg(s)} = \mu_{Mg(g)}$, by the sublimation of Mg. In a closed system, Mg partial pressure will increase until equilibrium is reached i.e. $\mu_{Mg(g)} \approx \mu_{Mg(s)}$. In an open system, with an ongoing annealing, Mg first sublimates to the surrounding atmosphere as the Mg vapor pressure is higher than the Mg partial pressure i.e. $\mu_{Mg(s)} > \mu_{Mg(g)}$ (note that the Mg partial pressure in the surrounding atmosphere is not exactly zero, $\mu_{Mg(g)} \neq 0$). Sublimated Mg is continuously removed away from the surrounding atmosphere as the Mg partial pressure of the atmosphere far away is negligible i.e. $\mu_{Mg(atm)} \approx 0$. It is therefore plausible that the solid Mg turns to sublimated Mg gas trying to equilibrate the system. The kinetics of this process will depend majorly on the height of the energy barrier. So, Mg atoms need to overcome this energy barrier to convert from one state (solid) to the other (gas). Mg loss in n-type (Mg-rich) $Mg_2(Si,Sn)$ is analogous to this as in both cases (elemental Mg and (Mg-rich) Mg_2X), a sublimation of elemental Mg occurs at elevated temperatures (see Equation (10.4)). If the sample is devoid of excess Mg i.e. an Mg-poor material, the sample will still tend to lose Mg to equilibrate the system thermodynamically. However, the height of the energy barriers will be largely different in Mg-rich and Mg-poor samples: in the former case, only individual Mg atoms gets removed from the crystal while forming a vacancy (or removing an Mg interstitial or the Mg atoms gets removed from a binding state in a grain

boundary or at the sample surface which has an even lower binding state). In the latter case, the crystal lattice needs to be destroyed to remove Mg such that $\mathrm{Mg_2(Si,Sn)} \rightarrow (2-x)\,\mathrm{Mg\ (g)} \uparrow + \mathrm{Si} + x\mathrm{Mg} - \mathrm{Sn\ (l)}$ [55, 152, 153], which depends on the temperature. A decomposition into elemental constituents will only occur when the lower solubility limit of Mg is reached. Nevertheless, the results of Chapter 8 and Chapter 9 suggest a saturation of Mg loss instead of a complete decomposition. This implies that the height of energy barrier in the second case is higher. This also means that the sample will lose excess Mg during *in-situ* annealing experiment until it reaches the lower solubility limit of Mg. Correspondingly, Mg flux and $\mu_{\mathrm{Mg(s)}}$ will change which would influence $\Delta\mu_{\mathrm{Mg}}$, that will vary throughout the annealing duration. The establishment of $\Delta\mu_{\mathrm{Mg}}$ not only results in the sublimation and the transport of sublimated Mg (step 1 and step 2) but also acts as the driving force for the diffusion mediated transport of Mg in the material (step 3 and step 5), and governs the formation of Mg-related intrinsic defects (step 4) as well.

With ongoing annealing, Mg atoms diffuse from the matrix to the grain boundaries (step 5) *via* V_{Mg}^{2-}, formed partially during step (4) of the degradation process. Liu *et al.* [93] have computationally investigated the role of intrinsic point defects in Mg_2X (*X*: Si, Sn) and showed that V_{Mg}^{2-} have a low formation energy in binary Mg_2Si and Mg_2Sn materials in both Mg-rich and Mg-poor environments. Besides, Kasai *et al.* [236] have measured the *T*-dependence of the atomic displacement parameters of Mg_2Sn and Mg_2Si, and the results showed higher values for Mg_2Sn over the complete measurement temperature range, thus, indicating weaker Mg−Sn bonding character compared to Mg−Si. The formation of V_{Mg}^{2-} is furthermore supported by a high vapor pressure of Mg [237] at elevated temperatures. These investigations indicate that Mg vacancies are relatively easily formed in Mg_2X (*X*: Si, Sn) solid solutions as well. This serves as the fourth step of degradation process. Besides, the Mg atoms consecutively diffuse along the grain boundaries to the sample surface which serves as the step (3) of the degradation process. Many investigations on the growth of polycrystalline Mg_2Si [240-243], both bulk and thin films, have shown that depending on the temperature, either grain boundary diffusion (low temperatures) or bulk diffusion (high temperatures) can be dominant. Unlike the present case, there was a surplus availability of Mg (in both gaseous and solid form, respectively) during the growth experiments reported in these studies. On further comparison, these reported studies differ in the choice of material, where in the case of $Mg_2(Si,Sn)$, the contribution of diffusion *via* grain boundaries to the Mg transport cannot be completely excluded. Therefore, it is hypothesized that the transport of Mg atoms is faster at the grain boundaries compared to the crystallite (or bulk) diffusion as the grain boundaries are proven to be energetically favored

path for diffusive transport [244]. After reaching the sample surface, these Mg atoms sublimate in the annealing atmosphere to minimize $\Delta\mu_{Mg}$ and get closer to the thermodynamic equilibrium (between the sample and the annealing atmosphere) (step 2). Sublimated Mg atoms are possibly removed from the sample surroundings, in step (1), and due to a continuous removal of sublimated Mg from the nearby surroundings of the sample, the thermodynamic equilibrium is not attained ($\Delta\mu_{Mg} \neq 0$). This drives Mg loss from the sample (in a dynamic equilibrium) until the sample reaches the lower Mg solubility limit i.e. as long as there is excess Mg (as described in Equation (10.4)). This qualitative mechanism of the transport of Mg atoms from within the sample to its surroundings can be visualized by a schematic model presented in Figure 10.5.

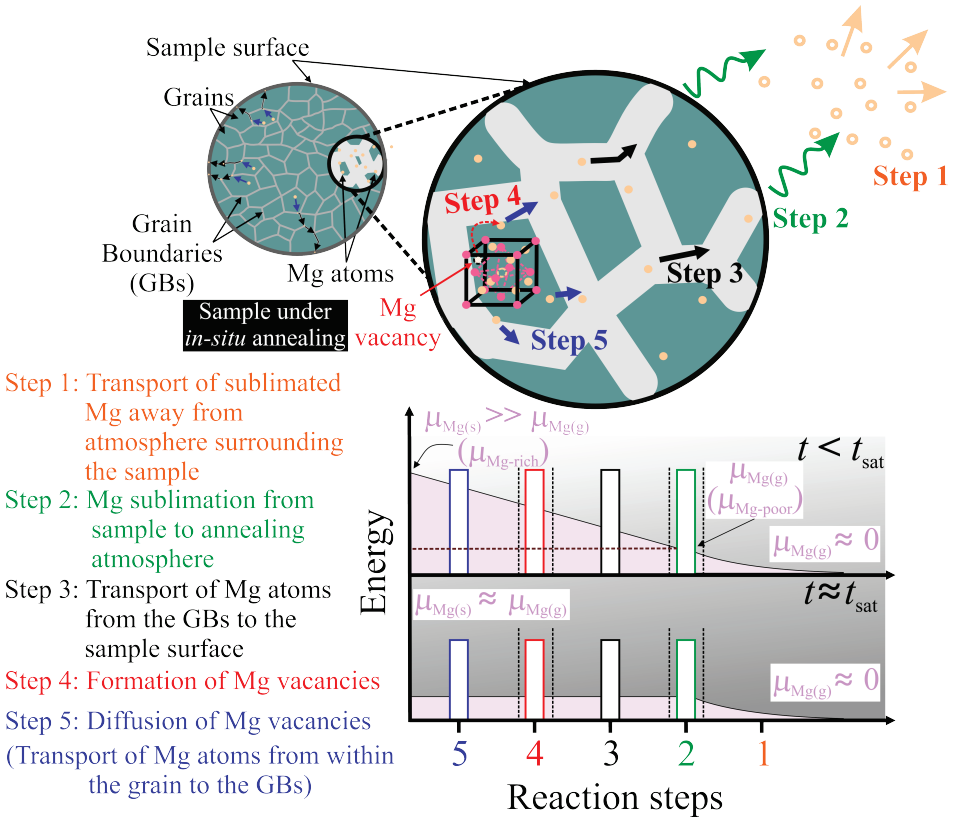

Figure 10.5 Schematic model of Mg loss in $Mg_2(Si,Sn)$. Note that the Mg chemical potential (μ_{Mg}) is different in the sample ($\mu_{Mg(s)}$) and in the annealing surrounding ($\mu_{Mg(g)}$).

The schematic model shows a simplified view of the degradation process in n-type Mg_2X (X: Si, Sn) where Mg loss is nearly identical to the discussed case of closed system (where Mg atoms sublimate until $\mu_{Mg(s)} \approx \mu_{Mg(g)}$). However, unlike the closed system, it is plausible that the equilibrium might not be established between the sample and the atmosphere e.g. during the *in-situ* annealing of the sample in HT-$S\sigma$, the sublimated Mg deposits at the cold spots,

which are quite far from the sample surroundings and thus, $\mu_{\mathrm{Mg(s)}} \neq \mu_{\mathrm{Mg(g)}}$. Nevertheless, for establishing equilibrium, a further removal of Mg from the material would require a complete decomposition of Mg_2X which is not expressed in Equation (10.4) and is experimentally not observed (initially). The schematic model in Figure 10.5 differs from this scenario mainly in terms of the differences in the height of energy barriers corresponding to e.g. step (4). The energy barrier of step (4) in Mg-rich Mg_2X is the formation of V_{Mg}^{2-} while in case of Mg-poor, it is the decomposition of Mg_2X, with the latter probably having a comparatively higher energy barrier. Besides, the model emphasizes that there are five steps in the proposed multi-step degradation reaction and there are four different energy barriers that correspond to step (2) to step (5). There is no microscopic energy barrier for step (1) since the Mg atoms are free to move after step (2). Step (1) is highlighted by an exponential gradient in μ_{Mg}, which signifies that the sublimated Mg might not leave the sample surroundings immediately. Particularly, the transport of sublimated Mg (either through conduction or convection) is extended over the volume of the furnace where the sample undergoes annealing. At regions far away from the sample surroundings, however, μ_{Mg} eventually matches to zero i.e. $\mu_{\mathrm{Mg}} \approx 0$. This means that μ_{Mg} is lower in the regions away from the sample compared to the nearby surroundings of the sample (i.e. even lower than that of Mg-poor material). Besides, the energy barriers corresponding to steps $(2-5)$ are: the sublimation energy of Mg atoms (at *in-situ* annealing temperatures) (step 2), migration energy of Mg atoms at the GBs (step 3), the formation energy of V_{Mg}^{2-} (step 4), and the migration energy of V_{Mg}^{2-} (step 5), respectively. During step 2, Mg-atoms sublimates after overcoming an energy barrier, where the barrier within vertical dashed lines emphasizes that sublimation is a local process. Moreover, μ_{Mg} is assumed to be *close* to μ_{Mg} in Mg-poor Mg_2X (*X*: Si, Sn) at the sample surface, however, as there is a continuous supply of Mg from within the sample, the sample is not Mg-poor material (yet). The diffusion of Mg atoms from the GBs to the sample surface is the step (3), where Mg-atom should overcome multiple energy barriers for the (GB) diffusion of Mg atoms. This is symbolized by the wide gap between step (2) and step (3) and emphasizes that the step (3) is a process that occurs repeatedly. A gradient of pink region in the wide gap signifies a reduction in μ_{Mg} after each jump to overcome multiple energy barriers, however, for brevity only a single barrier is visualized. Step (4) is local and happens only once during the reaction i.e. per Mg-atom removed which leads to the formation of a vacancy. After the completion of step (4), μ_{Mg} is relatively lower as an increase in the density of V_{Mg}^{2-} in the material increases. The gap between step (3) and step (4) shows a continuous diffusion of Mg atoms (essentially step (3)) from the GBs to the sample surface. Step (5) is the diffusion of Mg-atom *via* V_{Mg}^{2-}, and therefore there is

a migration energy barrier that the V_{Mg}^{2-} need to overcome. The sketch shows a hypothetical situation, where the end-point is Mg-rich state i.e. $\mu_{Mg(s)} \approx \mu_{Mg\text{-}rich}$. It means that the first formed vacancy has not reached the inside of the grain yet otherwise μ_{Mg} would already be lower. Moreover, the μ_{Mg} gradually reduces between step (4) and step (5) which is shown by an extended pink gap. This gap symbolizes that step (5) occurs repeatedly (overcoming multiple migration barriers) i.e. an ongoing diffusion of V_{Mg}^{2-} from the area near GBs towards the inside of the grain (or Mg-atoms from the inside of grain to the grain boundary). On the other hand, the height of different energy barriers is assumed constant as they are not known for different steps. With an ongoing loss of Mg, the μ_{Mg} in the sample would decrease and plausibly lead to a change in the height of each energy barrier. This situation is shown by the lower *xy*-plot in the schematic model after the sample has reached the lower solubility limit of V_{Mg}^{2-} due to prolonged annealing.

Nevertheless, an assessment of these microscopic energy barriers is crucial to understand the kinetics of Mg loss in $Mg_2(Si,Sn)$. In this direction, Ryu *et al.* [147] have investigated Mg diffusion in p-type $Mg_2(Si,Sn)$ materials. They quantified the diffusion energy barrier by employing the *climbing image nudged elastic band* (ciNEB) approach, which is a first principles method [245], by accounting for varying Mg content in the material (translating to different μ_{Mg}). As said, the sublimation in step (2) and the diffusion processes in step (3) and (5) are largely dominated by $\Delta\mu_{Mg}$, and the fact that $\Delta\mu_{Mg}$ varies as the annealing progresses, it could be possible that the migration energy barrier corresponding to these steps might also be affected but a systematic study is missing in this regard. Note that the $\Delta\mu_{Mg}$ is defined as the difference between the sample and the surroundings, specifically, the whole difference between inside the grain before step (5) to after step (1). Also, the height of each energetic barrier represents diffusion resistance experienced by diffusing Mg atoms during each step. Besides, it is necessary to highlight that, depending on the microstructure, the magnitude of these barriers might or might not be the same. The experimental quantification of the energy barrier and the rate of degradation corresponding to each step is quite challenging. Mg is highly volatile at higher temperatures and would require better control of Mg content in the samples while conducting such experiments (for the determination of the height of energy barriers corresponding to step (2)). The other option is extending the first principles calculations (e.g. ciNEB) for steps (3); however, no results are reported here and it is beyond the scope of current analysis. Besides, Ryu *et al.* [147] have also calculated the formation energy of different intrinsic defects in undoped Mg-rich and Mg-poor $Mg_2Si_{0.4}Sn_{0.6}$ as shown in Figure 10.6.

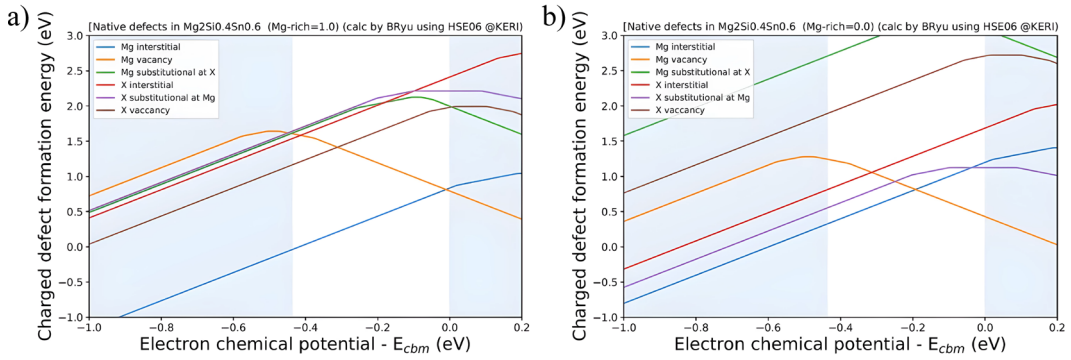

Figure 10.6 Calculated charged defect formation energies of $Mg_2Si_{1-x}Sn_x$ ($x = 0.6$) in a) Mg-rich and b) Mg-poor environment. X in the figure legend refers to Si or Sn. The figure has been re-printed under the terms of the Creative Commons Attribution-Non Commercial-No Derivatives License and requires no permission for non-commercial use [147].

Based on this figure, some information relevant to the present analysis can be extracted. The formation energy of charged intrinsic defects is different in Mg-rich and Mg-poor $Mg_2Si_{0.4}Sn_{0.6}$ materials, i.e. the formation energy is sensitive to the Mg content (or μ_{Mg}), in agreement with the model presented in Figure 10.5. Specifically, the formation energy of V_{Mg}^{2-} decreases with decreasing Mg content in the material. On the other hand, a decrease in the electron chemical potential (η) results in an increase of the defect formation energy of V_{Mg}^{2-} in n-type Mg_2X (X: Si, Sn) materials. In the present study, with an ongoing Mg loss (μ_{Mg} decreases), η decreases as well, therefore, the defect formation energy of V_{Mg}^{2-} is changed in a (partially) compensated manner due to a variation of both μ_{Mg} and η. Moreover, Duparchy *et al.* [251] have shown that the height of migration energy barrier that needs to be overcome by Mg atoms during diffusion *via* defects, is lower for V_{Mg}^{2-} compared to I_{Mg}^{2+} in both Mg_2Si and Mg_2Sn. This means that the Mg diffusion *via* V_{Mg}^{2-} is preferred over I_{Mg}^{2+} and this is also in agreement with the presented model.

For most inorganic solids and semiconductors, any high temperature process involving the formation of defects or a diffusion process obeys an Arrhenius-like temperature dependence [227, 231, 246-250]. It is therefore plausible that each step of the Mg transport in n-type $Mg_2(Si,Sn)$ follows an Arrhenius-like temperature dependence as well. The Arrhenius equation expressed in Equation (10.3) can be re-written as:

$$\ln(K/A) = -E_a/RT \qquad \text{Equation (10.5)}$$

Both E_a and A are referred here as kinetic parameters which are associated with each step of the kinetics of Mg loss in the present analysis. Here, the analysis of Mg loss kinetics is carried out under a few assumptions. As a simplification, the multi-step degradation process is approximated by a single-step process which can be modelled by a single Arrhenius expression. This will yield effective kinetic parameters for the complete process. As stated previously, substituting a multi-step transport chain by a single step is justified in the situation where one of the steps in the transport chain is dominant i.e. the height of energy barrier for one step is larger than the others. As a second simplification, the height of microscopic energy barrier is assumed to be constant in time (i.e. constant over the progressing time of the Mg depletion process). In reality, the height of each microscopic energy barrier will not be constant due to a change of $\mu_{\mathrm{Mg(s)}}$. As highlighted earlier, the loss of Mg causes a decrease in $\mu_{\mathrm{Mg(s)}}$ and η, and an interplay of these parameters affects the height of the energy barrier of step (4) throughout the annealing duration. Therefore, a change in $\mu_{\mathrm{Mg(s)}}$ will affect $\Delta\mu_{\mathrm{Mg}}$ which, based on the Mg content in the material, might affect the height of energy barrier of steps (2), (3) and (5) as well. Nevertheless, the effect of variation $\mu_{\mathrm{Mg(s)}}$ or η on the height of each barrier, respectively, is neglected within the framework of the qualitative model presented in Figure 10.5. This is a reasonable assumption since it is quite difficult to monitor and determine the variation of $\mu_{\mathrm{Mg(s)}}$ or $\Delta\mu_{\mathrm{Mg}}$. Mg loss in Mg_2(Si,Sn) is a multi-step process similar to a chemical reaction, and despite of the multi-step nature of this process, the utilization of the Arrhenius expression to describe Mg loss mechanism may work if one of the steps is dominant. According to Equation (10.5), the rate constant (K) is required as an input in the Arrhenius expression. Here, K is related to a variation of the Mg-flow in Mg_2(Si,Sn) degradation process, where Mg flow is linked to Mg flux and the cross section area of the acting channels. Note that Mg flux and Mg flow are used here interchangeably assuming an invariant microstructure and disregarding different cross sections for different steps of Mg loss mechanism. This variation in Mg flow is captured by the change in $N_{\mathrm{D}}(t)$, which is extracted by the analysis of *in-situ* measured TE properties at different temperatures. Note that Mg loss favors the formation of Mg vacancies, V_{Mg}^{2-}, and each V_{Mg}^{2-} lowers N_{D} by two. A variation in Mg flow is proportional to the diffusion coefficient D (according to Equation (10.1) and Equation (10.2)). Due to this, the T-dependence of both these quantities (D and K) are proportional as well (Equation (10.2)). In this way, the rate constant of Mg flow, K, is linked to the diffusion coefficient D. The time constants of $N_{\mathrm{D}}(t)$ will contain the contributions from the diffusion dominated steps. Therefore, the estimation of time constants allows the quantification of effective kinetic parameters. For each temperature point, both time constant and rate constant K were estimated using the following

approach. $N_D(t)$ curves were extracted by implementing non-anneal parameters (NAP) and post-anneal parameters (PAP) in a two-band model. The extracted $N_D(t)$ curves corresponding to 710 K and 773 K are fitted using an exponential decay function. This function is expressed as $N_D(t) = N_0 + Ae^{-t_{anneal}/\tau}$. Here, N_0 is the saturation value of the dopant concentration, $A = (N_D(t=0) - N_0)$ is the pre-exponential factor, and τ is the time constant. τ is used to estimate the rate constant of Mg loss in $Mg_2(Si,Sn)$ by $\tau = 1/K$. A complete approach of extracting $N_D(t)$ using the 2PB model is described in Chapter 9 (for $T_{anneal} = 710$ K) and section B.1 of Appendix B (for $T_{anneal} = 773$ K), respectively.

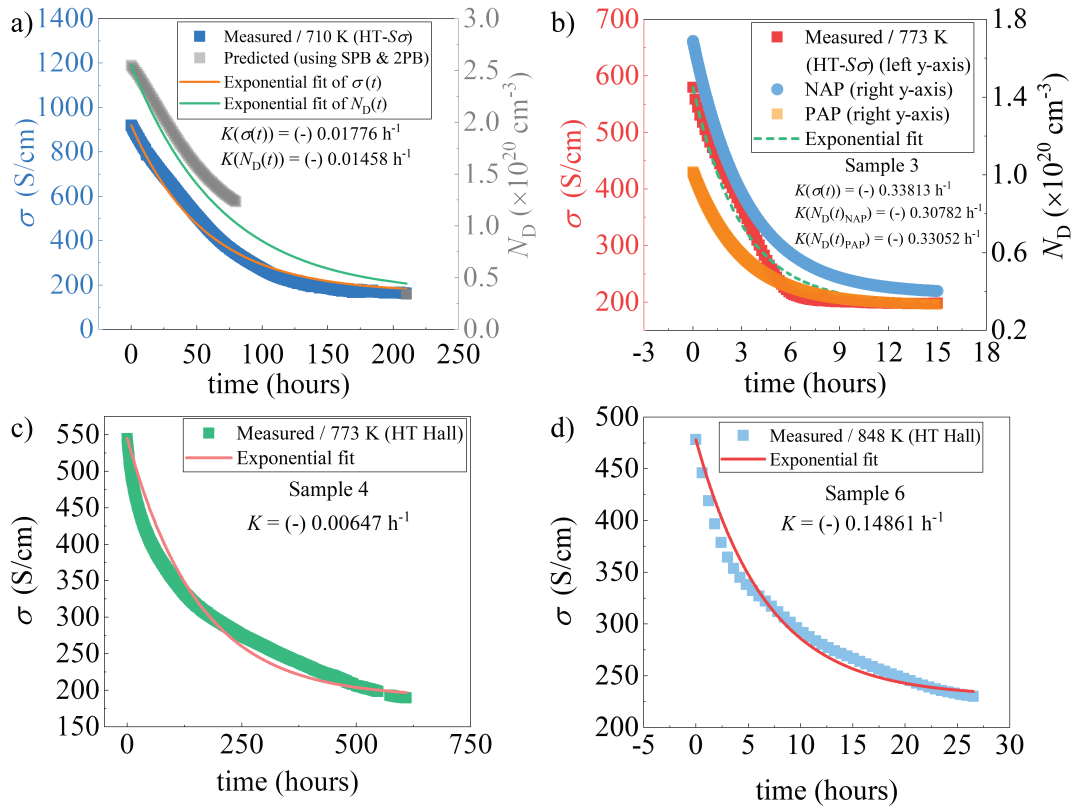

Figure 10.7 $N_D(t)$ and $\sigma(t)$ of (a) sample 1, (b) sample 3, (c) sample 4 and (d) sample 6 measured at T_{anneal} (710 K, 773 K and 848 K) in HT-$S\sigma$ and HT Hall facilities, respectively. $N_D(t)$ for both non-annealed parameters and post-annealed parameters in b) are obtained by 2PB modelling of the *in-situ* measured thermoelectric properties.

The fitted $N_D(t)$ curves corresponding to *in-situ* measurements at 710 K and 773 K are shown in Figure 10.7(a) and Figure 10.7(b). Besides, $N_D(t)$ curves are not directly available for all samples (but only for those where 2PB modelling could be employed). So, $\sigma(t)$ is used for all *in-situ* annealed samples to estimate K. Both σ and N_D are not exactly proportional and their

evolution is different (due to changes in the mobility), however the interplay between the different changing parameters and the dominant effect of reducing $N_D(t)$ on $\sigma(t)$ would yield a practically reasonable approximation of K. Also note that for the samples where both $N_D(t)$ and $\sigma(t)$ was employed, the rates agree better than within a factor of 1.5. Besides, the exponential decay function implemented on both $N_D(t)$ and $\sigma(t)$ data corresponding to different annealing temperatures showed a goodness-of-fit $R^2 > 0.94$ signifying that the quality of fit was good. Considering the assumptions for the Arrhenius analysis stated above, the estimated rate of Mg loss at different temperatures is plugged into the Arrhenius equation (Equation (10.5)). Figure 10.8 shows an implementation of the Arrhenius equation to plot a dependence of ln (K) versus $1/T_{\text{anneal}}$.

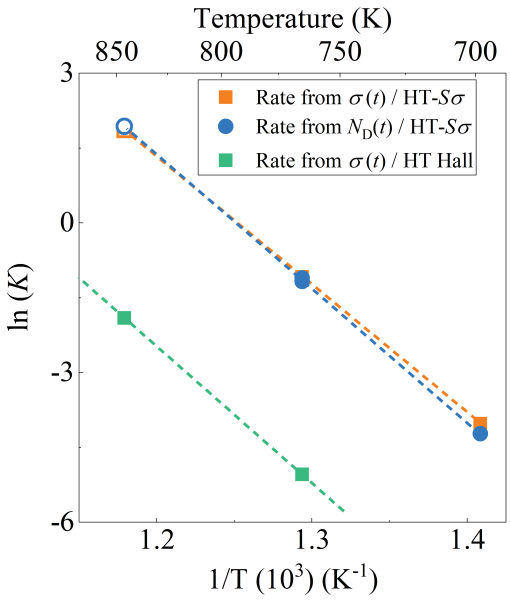

Figure 10.8 ln (K) (in units of h) vs $1/T_{\text{anneal}}$ (Arrhenius plot) from the rates determined by the exponential fitting of the $N_D(t)$ and $\sigma(t)$ plots. The green curve is plotted using K estimated from $\sigma(t)$ measured in HT Hall while the orange (■) and blue (●) data points correspond to K estimated by fitting $\sigma(t)$ and $N_D(t)$ measured in HT-$S\sigma$, and predicted from 2PB modelling, respectively. K at 848 K is estimated from extrapolation of the plots of both measured $\sigma(t)$ (in HT-$S\sigma$ facility) (□) and $N_D(t)$ (○).

The slope and intercept of the fit correspond to ln (E_a/R) and ln A respectively in Equation (10.5). The values of effective Arrhenius parameters (E_a and A), respectively, are extracted from the slope and intercept and are listed in Table 10.2. Note that $\sigma(t)$ measured *in-situ* in the HT Hall facility (at 710 K) (Chapter 9) was also fitted using an exponential decay function which yielded a rate constant $K = 3.6 \times 10^{-4}$ h^{-1}, which is higher by ~25% than the

prediction from the Arrhenius equation for the Hall system ($K = 2.78 \times 10^{-4}$ h^{-1}). This higher uncertainty might be due to an incomplete saturation and a stronger deviation from an exponential behavior. This indicates that the relative weighting of the different steps of degradation might be different for these conditions.

Table 10.2 The Arrhenius parameters (E_a and A) obtained by fitting ln (K) vs ($1/T_{anneal}$). Note that the N_D was predicted from the two-band model while σ was measured in HT-Sσ and HT Hall facilities, respectively.

Measurement system	Property	E_a (kJ mol^{-1})/(eV)	A (10^{13} h^{-1})
HT-$S\sigma$	σ	213/2.2	8.9
	N_D	223/2.31	39.9
HT Hall	σ	227.72/2.36	1.5

E_a extracted from the Arrhenius plots lie in the same range (2.2 eV – 2.36 eV), while the values of A come out to be different from each annealing experiment. In principle, A might depend on the differences in the grain size (because of varying contributions from the grain boundary or bulk diffusion), length of the diffusion path (i.e. sample geometry and sample surface area covered by sample holder) or the differences in the defect concentration. The grain size does not change significantly after several hours of annealing; thus, the effect of grain growth on A can be neglected here. A faster Mg transport is furthermore supported by the specific annealing conditions explained in the coming part of the section, which affects the values of K and A. This simplified approach allows a quantification of the kinetic parameters of the degradation mechanism, nevertheless, more data points are clearly desirable for a more solid analysis. Still, an estimation of Mg loss rates at other temperatures is feasible using this analysis (e.g. at $T_{anneal} = 848$ K). The decay of TE properties measured *in-situ* in the HT-$S\sigma$ at $T_{anneal} = 848$ K was so fast that the measurement could not stabilize in time. Nevertheless, the Arrhenius plots allowed an estimation of Mg loss rates of $K_{\sigma(t)} \approx 6.37$ h^{-1} and $K_{N_D(t)} \approx 6.90$ h^{-1} at this temperature point.

Ryu *et al.* [147] have calculated the formation energy dependencies of V_{Mg}^{2-} as a function of E_F for $Mg_2Si_{0.4}Sn_{0.6}$ under different Mg conditions (Figure 10.6). For the condition when $E_F = E_{CBM}$, the formation energy of V_{Mg}^{2-} lowers from 0.8 eV (Mg-rich conditions) to 0.43 eV (Mg-poor conditions) which in the present analysis, corresponds to the non-depleted and depleted state of the samples with respect to Mg, respectively. In a study focusing on the room temperature instability of $Mg_2(Si,Sn)$, Duparchy *et al.* [251] showed that the height of migration energy barrier for V_{Mg}^{2-} in Mg_2Si and Mg_2Sn is 472 meV and 537 meV, while for I_{Mg}^{2+}, it is 828 meV and 733 meV in Mg_2Si and Mg_2Sn, respectively. The migration energy refers to the

diffusion energy barrier corresponding to step (5) of the degradation process presented in Figure 10.5. The migration energy of Mg atoms *via* V_{Mg}^{2-} in $Mg_2Si_{0.4}Sn_{0.6}$, $E_{mig} = 511$ meV, was estimated by linearly interpolating the values of migration energy corresponding to Mg diffusion *via* V_{Mg}^{2-} in the respective binaries. Note that this is an assumption, it might also be that the migration barriers are lower for solid solutions due to the various local Si:Sn configurations. It will be furthermore interesting to investigate if the energy barriers are sensitive to the starting Mg concentration (Mg-rich or Mg-poor) or not. Nevertheless, the effective activation energy estimated in the present analysis lies between 2.2 eV – 2.4 eV, significantly larger than the (combined) DFT results presented by Ryu *et al.* [147] and Duparchy *et al.* [251]. However, the value there covers only step (4) and step (5) of the multi-step transport chain and the potential contributions from step (2) and step (3) contained in the effective parameter obtained from experimental data here naturally lead to larger values.

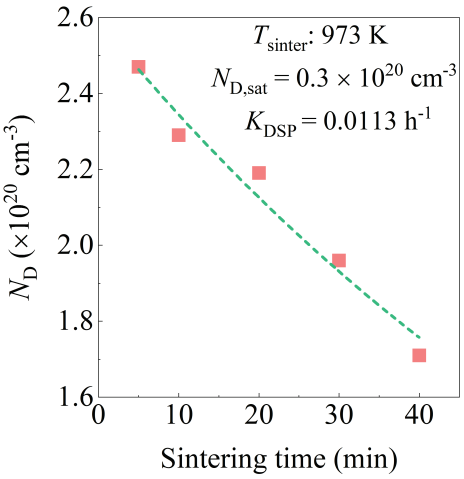

Figure 10.9 Carrier concentration n ($\approx N_D$ at RT) of the samples sintered at 973 K for different durations.

Besides, the Arrhenius equation is utilized to estimate the kinetic parameters of the sintering process. For this analysis, the carrier concentration n ($= N_D$ at RT) of samples sintered for different durations (5, 10, 20, 30 and 40 min) at 973 K (with an externally applied constant pressure of 67 MPa) were exponentially fitted to deduce the Mg loss rate. The carrier concentration data fitted using an exponential decay function is shown in Figure 10.9. Based on the observation of *in-situ* annealing experiments at 710 K, 773 K and 848 K, it is confirmed that the degradation of N_D occurs from an initial doping concentration $N_D \approx 2.5 \times 10^{20}$ cm^{-3} to an asymptotic saturation value of $N_{D,sat} \approx 0.3 \times 10^{20}$ cm^{-3}, respectively. Therefore, n is

fitted using the same exponential decay function as employed previously ($N_{\mathrm{D}}(t) = N_0 + Ae^{-t_{\mathrm{sinter}}/\tau}$, here $N_0 = N_{\mathrm{D,sat}} = 0.3 \times 10^{20}$ cm^{-3}, $A = 2.28 \times 10^{20}$ cm^{-3} with time constant $\tau = 88.52$ h ($K_{\mathrm{DSP}} (= 1/\tau) = 0.113$ h^{-1})). On the other hand, the rate constant of Mg loss at 973 K is estimated using the Arrhenius equation to be $K = 9.425$ h^{-1} (in HT Hall), and $K_{\sigma(t)} = 311.45$ h^{-1} and $K_{N_{\mathrm{D}}(t)} = 405.37$ h^{-1} (in HT-$S\sigma$) which is nearly two and three orders of magnitude higher compared to K_{DSP}, respectively. Note that this comparison is done considering the cited dominant effect of N_{D} on σ i.e. $K_{N_{\mathrm{D}}(t)} \approx K_{\sigma(t)}$.

A difference in the rate of Mg loss, the trend of Mg loss in each setup and the obtained kinetic parameters can be attributed to the different characteristics of the employed setups: the annealing atmosphere, the design of facility, and the actual sample area exposed to the environment. The rate and kinetic parameters of degradation corresponding to first, HT-$S\sigma$ setup and HT Hall setup, and then HT-$S\sigma$, HT Hall and DSP setups are compared and discussed on the basis of the stated characteristics of these setups. In case of the HT-$S\sigma$ setup, the design of the setup (measurement under helium atmosphere) enables convection, and as a result, allows efficient Mg transport away from the sample surface. Sublimated Mg can condense at cold spots (down to ~50 °C) in the (quartz) tube of the setup, relatively close to the sample. In order to thermodynamically equilibrate the atmosphere near the sample, a continuous and fast loss of Mg may occur from the sample. In contrast, the sample is heated in a different manner in HT Hall setup. A cylindrical CFC composite ring is located in the furnace of the HT Hall setup which envelops the sample holder on the entire recipient head. This composite ring acts as a radiative heater which elevates the temperature of the furnaces' inner volume that contains the sample holder. Unlike the HT-$S\sigma$ setup, there is no moderating atmosphere around so, the Mg gas molecules in HT Hall (vacuum) should ideally transport faster from a region of high concentration (vicinity of the sample) to a region of low concentration (away from sample). Besides, the sample surface area directly exposed to the annealing environment can be one of the reasons of the differences in the rate constant and the kinetic parameters. The exposed surface area of the sample in HT-$S\sigma$ setup and HT Hall setup can be visualized in Figure 10.10. In HT-$S\sigma$, ~47 % of the full sample surface is exposed to the surrounding atmosphere. While for the HT Hall sample holder, ~50 % of the full sample surface area is exposed. Note that the rest of the sample surface is covered by the ceramic tools of the sample holder. Therefore, no significant difference in the exposed sample surface area is found between the samples annealed in HT-$S\sigma$ and HT Hall facilities.

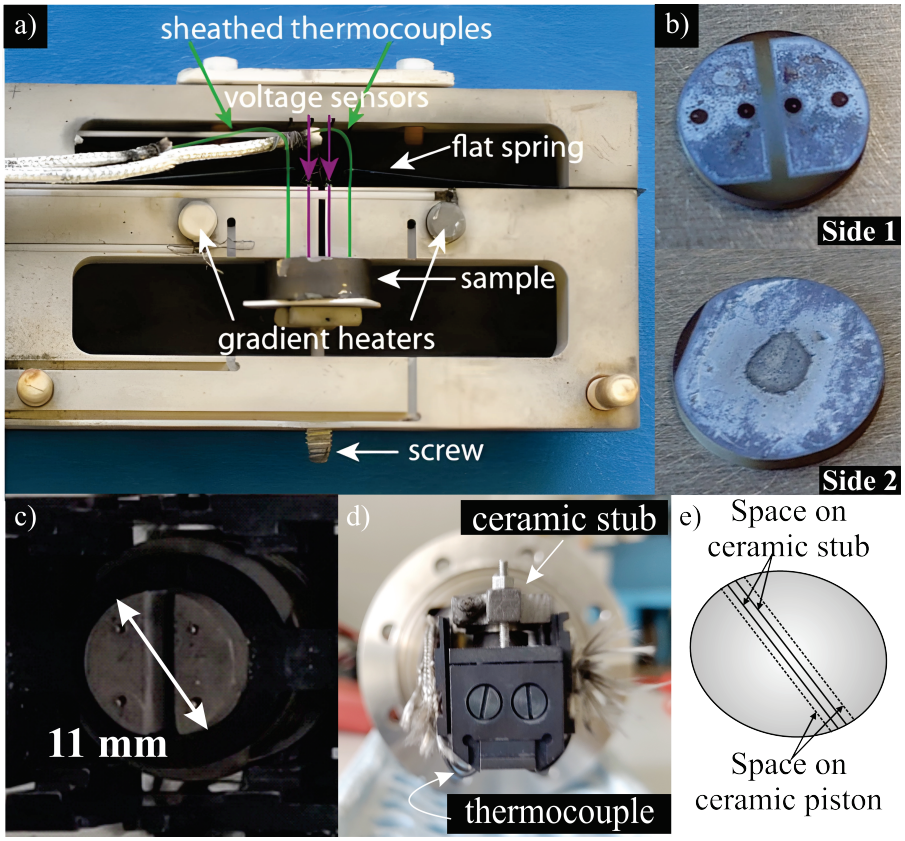

Figure 10.10 Sample holder design of a) HT-$S\sigma$ and c), d) HT Hall facilities. In b) a picture of the sample after *in-situ* measurement in the HT-$S\sigma$ is shown which gives an idea about the sample area directly exposed to the annealing atmosphere while e) shows a schematic of a HT Hall sample indicating the surface area that is directly exposed to the annealing environment. Dotted lines show the boundaries of sample area exposed due to the design of the ceramic piston (covering back side of the sample) on which the sample is mounted while the solid black lines highlight the boundaries of sample area exposed due to the design of ceramic stub (on the front side of the sample) used to fix the sample on the holder. The image in (a) has been reprinted with the permission from [197].

Besides this, a difference in the kinetics can also arise due to the length of travel path of Mg, as Mg atoms far from the open surface area also diffuse out of the sample. The maximum length of diffusing Mg atom would depend on the location of open surface area from the center of the sample. Note that the maximum length is a distance from the center of the sample to the exposed surface area. And, this length can be either the half of sample thickness in relation with the top or bottom surface, or half of the sample diameter in relation with the lateral surface area of the sample, respectively. Here, the location of open sample surfaces is nearly identical in both measurement setups which is visualized from the Figure 10.10 and so, the Mg diffusion length is qualitatively identical i.e. in either case, the travel length is either half of sample thickness or nearly half of the sample diameter.

To conclude, the difference in the kinetic parameters arises from the design of HT-$S\sigma$ setup. Particularly, the presence of cold spots in the sample surroundings promotes the removal of sublimated Mg from the area near sample surface. These conditions favor a higher Mg flow and a formation of Mg vacancies in high concentration in the sample annealed in the HT-$S\sigma$ setup. The Mg vacancies formed during annealing also facilitates Mg loss, and it is the plausible reason for a comparatively higher value of the pre-exponent A. In HT-Hall, the cold spots are not in close vicinity of sample, which results in a low Mg flow and a slower change in $\Delta\mu_{\mathrm{Mg}}$, thus, a slow Mg-loss compared to the Mg-loss in HT-$S\sigma$ facility. These reasons also explain the observed slow rate of degradation of electrical conductivity of sample 4 (HT Hall setup) compared to sample 3 (HT-$S\sigma$ setup) in Figure 10.3.

Besides this, the strong deviation is found between the rate of Mg loss in the sample annealed in HT-$S\sigma$, HT Hall and powder sample sintered in DSP facility. This deviation can be explained by a difference in the surface area exposure to the annealing and sintering atmosphere and the maximum length of diffusing Mg atom from the center to the open surface of the sample, respectively. During sintering, both surfaces (top and bottom) are fully covered by the die punches (of the sintering mold), thus, completely enclosing the sample except the long μm-wide slits in the pressing tool. Therefore, the sample is even less exposed to the sintering atmosphere directly. Additionally, the maximum length that the diffusing Mg atoms would need to travel is from the center of the sample to the μm-wide slits between the die and the punches. In this situation, the Mg flow is not too large owing to the fact that sublimated Mg atoms do not immediately leave the sample surroundings. On the other hand, while $\Delta\mu_{\mathrm{Mg}}$ is established, however, a lowering of $\Delta\mu_{\mathrm{Mg}}$ will require prolonged sintering duration. It might be furthermore possible that the transport of Mg away from the sample (step 1) will be retarded due to the absence of cold spots in the sintering chamber. Therefore, the Mg loss from the sample is even more constrained in the DSP in comparison to the HT-$S\sigma$ or HT Hall measurement facilities.

10.4 Conclusion

In-situ measurements were carried out at 773 K and 848 K in the HT-$S\sigma$ (helium atmosphere) and HT Hall (vacuum) facilities, respectively. For annealing at each temperature, two samples with a stoichiometry of $Mg_{2.06}Si_{0.385}Sn_{0.6}Sb_{0.015}$ and nearly identical room temperature (RT) thermoelectric properties (TE) were utilized. At 773 K, the transport properties of the sample annealed in HT-$S\sigma$ saturate after 15 hours of annealing. At 848 K, the transport properties decayed quite fast and their saturation probably occurred even before reaching the target annealing temperature. Identical measurements on as-prepared samples were conducted at the HT Hall facility that showed quite similar temperature dependence but a prolonged duration of saturation.

SPB model-based analysis of RT transport properties measured before and after annealing (at 773 K) confirmed that n ($= N_{\mathrm{D}}$, dopant concentration at RT), the density-of-states effective mass and the deformation potential constant of the dominant band were the most affected microscopic material parameters. N_{D} corresponding to the annealing duration was not directly available, because the properties measured in HT Hall and HT-$S\sigma$ facilities could not be combined directly due to the different rate of degradation in each setup. Instead, N_{D} was extracted by implementing two sets of microscopic material parameters in a two-band (one conduction band and one valence band) model. Each set of microscopic parameters corresponds to non-depleted (before annealing) and depleted (after annealing) state of sample with respect to Mg, respectively. The predicted $N_{\mathrm{D}}(t)$ data gave a range of values where the true N_{D} would lie.

A microscopic, multi-step diffusion-dominated mechanism is developed attempting to rationalize the observed changes in the *in-situ* measured thermoelectric properties. It is highlighted that the degradation process is driven by a difference in the Mg chemical potential established between sample (Mg-rich) and the surrounding atmosphere (Mg-poor). Moreover, at annealing temperatures, Mg loss occurs *via* the diffusion of Mg vacancies owing to a comparatively lower height of energy barriers (the formation energy and migration barrier) than the Mg interstitials. The effective kinetic parameters (the activation energy and the frequency factor) were quantified using the Arrhenius expression. The activation energy associated with annealing experiments in HT-$S\sigma$ and HT Hall facilities closely agreed and the values were compared with the height of energy barriers of transport chain. On the other hand, the values of frequency factor corresponding to each facility showed deviation which explains the variation in rate constant by two orders of magnitude. The design of measuring setups leads to

observable difference in the stated parameters. Besides, Mg loss rates of the samples sintered in the DSP was lower than HT Hall annealed samples by two order of magnitude, potentially again related to the difference in the exposed surface area and the travel path of Mg atoms from the sample to its surface.

Chapter 11 Conclusions and Outlook

11.1 Conclusions

The operation range of a pre-existing setup that simultaneously measures the Hall coefficient (R_{H}) and the electrical conductivity (σ) was successfully extended to higher temperatures ($T = 300\ \mathrm{K} - 723\ \mathrm{K}$). The measured Hall voltage at zero magnetic field flux, the correlation coefficient and the standard deviation of slope are quantified by analyzing the raw data. These parameters are used as error indicators to highlight any issue with the measurement. The geometric correction factors (GCF) (proposed by van der Pauw) are relevant in the present case (for both conductivity and Hall coefficient calculations) since the voltage and current probes are not positioned exactly on the edge of the sample as ideally required. The GCF expression proposed by van der Pauw depends on the ratio of probe-to-edge distance (a) and the diameter (D) of the sample, as (a/D). This expression is validated using FEM calculations in the present work. Particularly, first, (a/D) was varied symmetrically i.e. (a/D) is varied for all measuring thermocouple probes, and second, (a/D) was varied for one probe while it was kept constant for the other three probes for each simulation. The ratio of output Hall coefficient to the true Hall coefficient (probes exactly on the sample edge) was computed and compared with the ratio which was computed using the GCF proposed by van der Pauw. The deviation in these ratios increased with increasing a/D. Particularly, the GCF suggested by van der Pauw becomes insufficient for $\frac{a}{D} > 0.135$ (symmetric) and $\frac{a}{D} > 0.241$ (asymmetric), with a relative deviation of $> 5\ \%$. The R_{H} and σ measurement of n-type and p-type $Mg_2(Si,Sn)$, and p-type $FeSi_2$ at room temperature and the high temperature range ($300\ \mathrm{K} - 723\ \mathrm{K}$), respectively, was carried out at the presented Hall facility and the Hall facilities of other international research groups with a van der Pauw configuration of sample holder. On comparison of the transport properties measured on different facilities, a good agreement with a relative deviation of $\leq 8\ \%$ is found.

The mechanism of the formation of Mg_2X solid solution was studied by utilizing mechanical alloying (MA) as a synthesis technique. Moreover, the effect of the variation of synthesis parameters on thermoelectric (TE) properties of n-type $Mg_2Si_{0.4}Sn_{0.6}$ is investigated and discussed. The formation mechanism of the desired composition progresses by solid-state reaction, first, with the formation of Sn-rich $Mg_2(Si,Sn)$ phase followed by a slow Si diffusion to form the desired $Mg_2Si_{0.4}Sn_{0.6}$ composition. This is directly confirmed by analyzing the powder samples milled for different durations using XRD, particle size analyzer and SEM/EDS. At the end of the milling experiment (after 35 h), the obtained powder sample was

a mixture of particles with different Si:Sn ratio, somewhat close to the desired phase. The results showed that phase pure $Mg_2Si_{0.4}Sn_{0.6}$ cannot be achieved in a reasonable time only by MA and necessitates a high temperature heat treatment. Correspondingly, the desired composition was synthesized by a two-step process, first, the mechanical alloying of elemental precursors followed by high temperature sintering. The effect of the variation of the synthesis parameters on the thermoelectric properties was systematically investigated to optimize the synthesis procedure and to achieve best TE performance. The thermoelectric properties were found to be sensitive to the time and temperature of sintering. An increase in the Seebeck coefficient and a lowering in the electrical conductivity was observed as a result of increasing sintering time/temperature. This deterioration of properties was attributed to a lowering of carrier concentration (n) with increasing sintering time/temperature, which was confirmed by measuring room temperature Hall carrier concentration of these materials. Optimal and reproducible TE properties were achieved for the powder compacted at $973\ \mathrm{K}/20$ min. Besides, the powder precursors were ball milled for different durations ($t_{\mathrm{milling}} = 2, 4, 20, 50$ h) and the effect of varying milling duration on the thermoelectric properties was studied. The thermoelectric properties of the samples obtained from different milling duration showed no significant difference, which suggest that milling the precursors for only 2 h was enough.

The effect of scandium (Sc) substitution on the Mg site in Mg_2X materials was investigated and discussed in Chapter 7. Based on a theoretical investigation, Sc is expected to enhance the Seebeck coefficient and improve the overall TE performance of these materials. The thermoelectric properties of Sc-doped $Mg_2Si_{0.4}Sn_{0.6}$ showed intrinsic semiconductor like behavior which led to a $zT_{\max} = 0.19$. The microstructure analysis of these sample revealed that the addition of scandium leads to the formation of different Sc-Si phases. Subsequently, Sc was attempted to be substituted at the Mg site in Mg_2Sn to prevent the formation of silicide phases and observe its effects on the TE properties. These samples showed n-type behavior but the carrier concentration n was far below the optimum range. The SEM-EDS micrographs of these samples showed that Sc either forms Sc-Sn phases or essentially remains unreacted in these samples. The (Sc, Sb) co-doped and Sb-doped Mg_2Sn specimens were prepared to further investigate an effect of Sc substitution on Mg site. The temperature dependent TE properties showed the typical behavior of a heavily doped semiconductor, and the absolute values were quite similar. Thus, this experimental investigation proves that the Mg substitution with scandium does not enhance the TE properties of Mg_2X materials.

The lowering of the carrier concentration n of Sb-doped $Mg_2Si_{0.4}Sn_{0.6}$ with increasing sintering duration (t_{sinter}) motivated to investigate their microstructure in detail. For this study, three

samples were prepared by sintering the mechanically alloyed powder (20 h) for different durations (10 min, 20 min and 40 min) at 973 K (with an externally applied axial pressure of 67 MPa). TEM-EDS investigations were carried out on samples sintered for 20 min and 40 min, and local compositional variations were observed in each sample. The grain boundaries were deficient in Mg but no dopant (Sb) loss was observed. On analyzing TE properties, a loss of carrier concentration (n), significantly reduced carrier mobility (μ) and a lowering in the lattice thermal conductivity (κ_{lat}) was observed with increasing t_{sinter}. The thermoelectric properties were further analyzed by the single parabolic band (SPB) model by taking acoustic phonon and alloy scattering of charge carriers into account. With increasing t_{sinter}, the electron-phonon interaction got stronger (increased deformation potential constant E_{Def}). Increasing local compositional inhomogeneities and a higher E_{Def} both could be linked to ongoing Mg loss. Based on the observation of previous work and this study, the lowering in n and κ_{lat} can be attributed to the Mg loss as well. The TE performance of $Mg_2(Si,Sn)$, nevertheless, remains uninfluenced due to a compensating variation in the microscopic material parameters due to increasing t_{sinter}. A $zT_{\mathrm{max}} = 1.3 \pm 0.18$ is achieved for all samples, mainly, due to the counteracting effects of reduced μ and κ_{lat}.

This investigation gave a motivation to deeply analyze the effect of prolonged (high) temperature treatment on the thermoelectric properties of these samples. *In-situ* measurements of transport properties was carried out on six identical samples (Sb-doped $Mg_2Si_{0.4}Sn_{0.6}$) at a holding temperature $T = 710$ K, 773 K and 848 K, respectively. Two sets of three samples each were annealed using the available setups for measuring the Seebeck coefficient (S), σ (HT-$S\sigma$) and R_{H} and σ (HT Hall, extended for high temperature measurements), respectively. Microstructurally, samples annealed at 710 K were phase pure and did not show any signs of de-mixing even after being heat-treated for several hundred hours. *In-situ* thermoelectric properties of all these samples showed a variation as a function of annealing duration. The transport properties of samples measured *in-situ* in HT-$S\sigma$ at 710 K and 773 K were analyzed. The analysis of the room temperature transport properties of each of these samples measured before and after *in-situ* annealing using an SPB model showed loss of carriers n, a lowering of mobility μ (high E_{Def}) and a reduced density-of-states effective mass (m_{D}^{*}) of the samples as a result of high temperature annealing. The transport properties measured *in-situ* in HT-$S\sigma$ at 710 K and 773 K were analyzed using a two parabolic model. The analysis revealed that besides the change in E_{Def}, the major cause of the observed behavior of thermoelectric properties is the loss of majority charge carriers, N_{D}, which roughly decays exponentially with annealing duration. The formation of Mg vacancies due to Mg loss is the reason for the loss of

N_D, which leads to corresponding variations in thermoelectric properties. For 773 K, the Hall coefficient (R_H) predicted using a two-band model shows qualitatively a good agreement with the R_H measured in the HT Hall facility. Time constants related to Mg loss were estimated from the N_D data for the present experimental conditions at stated temperature points. A width of $Mg_{2-\delta}Si_{0.4}Sn_{0.6}$ phase, with respect to Mg content is estimated for the sample annealed at 710 K.

A microscopic diffusion-dominated model describing a multi-step mechanism of Mg loss in Mg_2(Si,Sn) is developed that attempts to explain the changes occurring in the transport properties during *in-situ* annealing. The model emphasizes that the driving force of diffusion is a difference in the Mg chemical potential established between the sample (Mg rich) and the surrounding atmosphere. Moreover, the Mg loss occurs *via* the diffusion of Mg vacancies that dominates over a diffusion of Mg-interstitials (owing to a lower formation energy and migration energy). Furthermore, the concentration of Mg vacancies is comparatively higher than the interstitials, which is supported by the observed change in N_D. Using the rate constants obtained by fitting $N_D(t)$ (710 K and 773 K) and $\sigma(t)$ (710 K, 773 K and 848 K (in both HT-$S\sigma$ and HT Hall facilities)), the kinetics of Mg loss were studied using the Arrhenius equation. A higher Mg flow followed by a high defect concentration in the samples annealed in HT-$S\sigma$ setup than the HT Hall setup are the plausible reasons for the differences in the frequency factor obtained for experiments in each setup. The obtained values of activation energy are compared with the defect formation energy and other migration energy barriers to judge the limiting-step in the transport chain of multi-step model. The analysis indicates that even though the Mg loss mechanism is nearly identical, however, the design of measuring setups causes one or more microscopic process-mediated steps of degradation to dominate over the other steps. As a result of the differences in the design of measurement setups, the differences in the rate of Mg loss and the frequency factor are observed.

11.2 Outlook

11.2.1 Optimization of synthesis methods

The utilization of heavy element milling media can lead to a faster formation of the desired phase. Usage of such milling media is speculated to form a desired phase without the need of a high temperature heat treatment. Therefore, the influence of heavy elements based milling media (e.g. tungsten carbide (WC)) on the synthesis of Mg_2(Si,Sn) solid solution should be studied. This will be technologically relevant as the industries look out for fast and reliable methods for the synthesis of inorganic materials.

A set of Bi-doped Mg_2Si powder samples were synthesized by Bux *et al.* [115] using the MA setup (SPEX 8000D), which is identical to the milling system employed in the present work. Importantly, they utilized tungsten carbide based milling media instead of stainless steel for the synthesis and showed that the formation of phase pure powder material is possible without the need of high temperature sintering. In comparison to Mg_2Si, the dynamics and the progress of solid-state diffusion might be different for the synthesis of $Mg_2(Si,Sn)$ solid solutions, as Sn has great affinity to Mg than Si (to Mg). Such an investigation would enable to assess whether a phase pure composition is achieved by utilizing the tungsten carbide milling media or not. Moreover, the difference in the speed of phase formation (stainless steel versus tungsten carbide) can be understood as well.

11.2.2 A detailed investigation of the microstructure using advanced techniques

The microstructural investigation using TEM showed Mg loss and a variation in Mg/Sn content at/near grain boundaries in the samples sintered for different duration. This led to a lowering of both carrier concentration n and mobility μ, and corresponding TE properties of Sb-doped $Mg_2Si_{0.4}Sn_{0.6}$. The grain boundaries of the samples sintered for longer duration were found to be enriched with Sn with some signals corresponding to Mg and Si. In this context, the nature of tin is not known that enriches the grain boundaries. It is possible (but unclear at the moment) that whether it is a Sn-rich $Mg_2(Si,Sn)$ phase, an Mg-Sn melt or a thin layer of elemental Sn. The microstructure should be investigated using high-resolution transmission electron microscopy (HR-TEM) to determine the exact nature of the segregate. Besides, such an investigation can give a direct proof of formation of Mg vacancies V_{Mg} that are formed due to Mg loss. The Mg concentration was comparatively lower near the grain boundaries that indicates that these grain boundaries act as carrier trapping states (because of localized positive charge of vacancies). The mobility of majority carriers is often constrained due to ionized impurity-carrier scattering events. Nevertheless, since a higher density of Mg vacancies near the grain boundary is expected, therefore, an advanced transport modelling-based analysis of thermoelectric properties will be necessary to disentangle whether the carrier scattering is dominated by grain boundary scattering or an ionized impurity scattering. Note that both grain boundary scattering and ionized impurity scattering shows identical temperature dependence.

For the TEM-EDS investigations conducted in Chapter 8, the EDS detector was calibrated using the binary Mg_2Si and Mg_2Sn specimens prepared by mechanical alloying. Mg:*X* (*X*: Si, Sn) ratio in different regions of the samples was investigated for the optimization of calibration procedure. In case of undoped Mg_2Sn sample, the Mg:Sn ratio was not constant in different

areas of the specimen. This indicates that Mg_2Sn, which is supposedly a line phase, is less favored over Mg-deficient/Sn-rich phase with a stoichiometry $Mg_{2-\delta}Sn$. This observation agrees with the results of Saito *et al.* [252, 253] and Xin *et al.* [254], who investigated single crystal and polycrystalline specimens of Mg_2Sn using TEM. However, note that each of these studies employed samples that were undoped, boron doped and antimony doped, respectively. Saito *et al.* asserts that the undoped Mg_2Sn single crystals possess nanosized regions that contain V_{Mg}, and these regions are evenly dispersed in the regions with no Mg vacancies (called single-crystal region). Besides, Xin *et al.* showed the formation of nanoscale precipitates of 5 nm and 50 nm in Sb-doped polycrystalline samples, respectively. The large precipitates (50 nm) are a combination of β-Sn and Sn-poor phases that coexist while much smaller precipitates were found to be made of Mg_2Sn with heavy elements (Sb or Sn) suspected to substitute Mg interstitial sites (called interstitial clusters by the authors). However, no solid evidence about the nature of the clusters was given in the latter case. Furthermore, Xin *et al.* revealed that large nanoprecipitates forms sharp interface with the matrix and smaller ones have highly strained interface. On the other hand, Saito *et al.* reported the interfaces between nanosized region and single crystal region in their single crystal samples to be of semi-coherent nature. The results and conclusion of the cited studies could be plausible explanations of the observed variation in Mg content in the Mg_2Sn sample (prepared for calibration) that prevents to achieve a daltonide composition.

The thermoelectric properties of n-type $Mg_2Sn_{0.8}Sb_{0.2}$ materials have been recently investigated and shown promising results with a $zT \approx 1.2$ [167]. In a recent study [255], the beneficial effect of Bi as a dopant on the power factor of Mg_2Sn has been shown. Bi doping on Sn site energetically pulls down the light conduction band (than the heavy conduction band) and the impurity level introduced as a result of Bi prefers to merge with the light conduction band. As a result, the flipping of conduction bands occurs. In those compositions, where band flipping phenomena is observed, a band convergence is also observed that boosts the power factor of these materials. While these investigations highlight promising thermoelectric properties of Mg_2Sn, the first step is to achieve stable Mg_2Sn materials, which has been a challenge as highlighted in Chapter 7. The samples showed poor room temperature stability and disintegrated in a couple of days after synthesis.

Based on the highlighted studies, the first step should be a study focused on the optimization of synthesis procedure to achieve phase pure undoped Mg_2Sn. For this, a variety of samples should be prepared with different amounts of excess Mg. The investigations of the phase purity and the chemical homogeneity should be carried out using XRD and HR-TEM. Such an

investigation would reveal the starting composition that needs to be employed to achieve the desired phase. Then, the doped compositions of Mg_2Sn materials can be designed and the effect of substitution of dopant on the phase stability and their thermoelectric properties can be studied. The study on the optimization of synthesis procedure should be followed-up by a high-temperature annealing-based study, where the focus should be on determining the thermochemical stability of Mg_2Sn (fcc) phase. In this regard, Mg_2Sn should be annealed in different Mg-partial pressure conditions (Mg-poor, nominal and Mg-rich) to investigate and prove whether Mg_2Sn is a daltonide composition or has a phase width with respect to Mg. These investigations should be conducted using XRD (or even synchrotron radiations) and TEM. Employing TEM will allow a better spatial resolution and the investigated microstructure might reveal the differences in samples as a result of annealing in different Mg partial pressures. The microstructure could furthermore reveal specific features such as the presence or absence of Mg-depleted grain boundaries, exotic structures (e.g. nanoprecipitates), point defects (e.g. anti-site defect (Sn_{Mg})), and their role in the phase stability. Using the last investigations as a base, phase pure undoped Mg_2Sn can be coupled with Mg_2Si to prepare Mg_2Si-Mg_2Sn diffusion couples. These diffusion couples can be then used to investigate and resolve the disputed phase boundaries of the miscibility gap at the temperatures of interest as well as experimentally determine the interdiffusion coefficients of respective elements (e.g. Sn in Mg_2Si). Using Mg-poor Mg_2Sn might affect the stated experimental investigations. A furthermore prospect can be an experiment where the diffusion couples are annealed in atmosphere with different Mg partial pressure. Such an experiment will enable to understand the sensitivity of the interdiffusion coefficients to the Mg-partial pressure (or Mg-chemical potential) and a quantification of these interdiffusion coefficients, and to comprehend the effect of different Mg-partial pressure on the phase boundaries of Mg_2Si-Mg_2Sn. In the previous proposed study on high-temperature annealing, the experiments should be carried out at temperature points, where the experiments related to determine the interdiffusion coefficients and the miscibility gap are planned. Note that an optimized Mg_2Sn phase will prevent discrepancies in the outcome of the experiments. As a side remark, *in-situ* TEM investigation can be conducted at high temperatures to directly visualize the kinetics of the diffusion process of Mg_2X (X: Si, Sn) solid solutions as well.

Appendix A

A.1 Circuit of the Hall measurement system

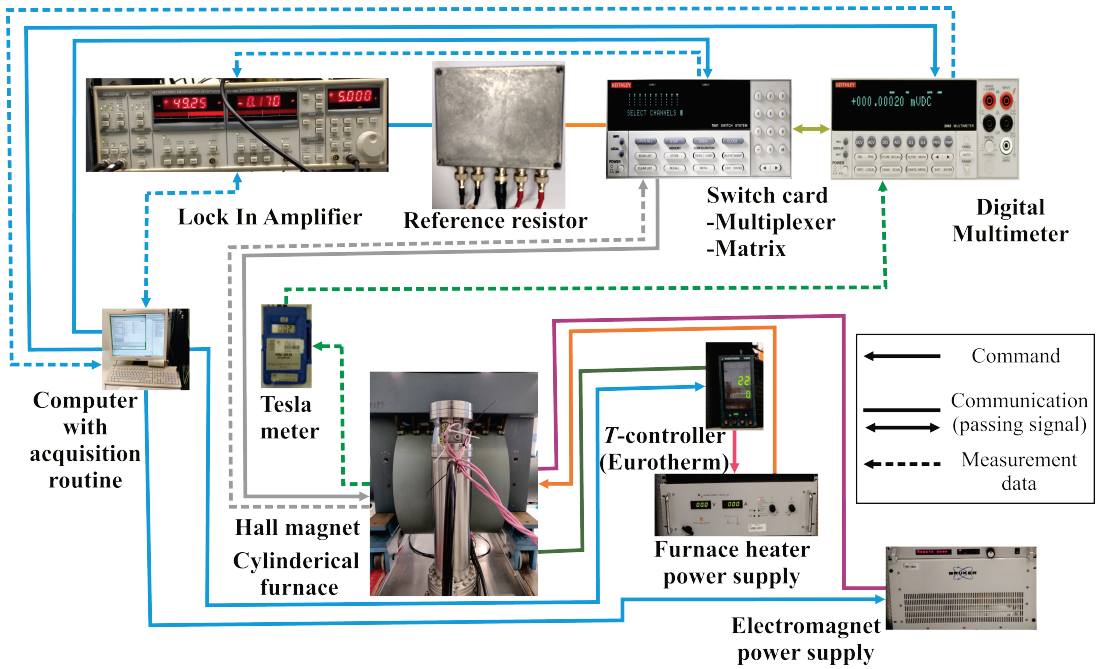

Figure A.1 A pictorial representation of the high temperature Hall measurement facility at DLR highlighting different electrical connections.

A.2 Comparative measurement of the Hall carrier concentration – after implementation of correct GCF value and temperature dependence of the electrical conductivity

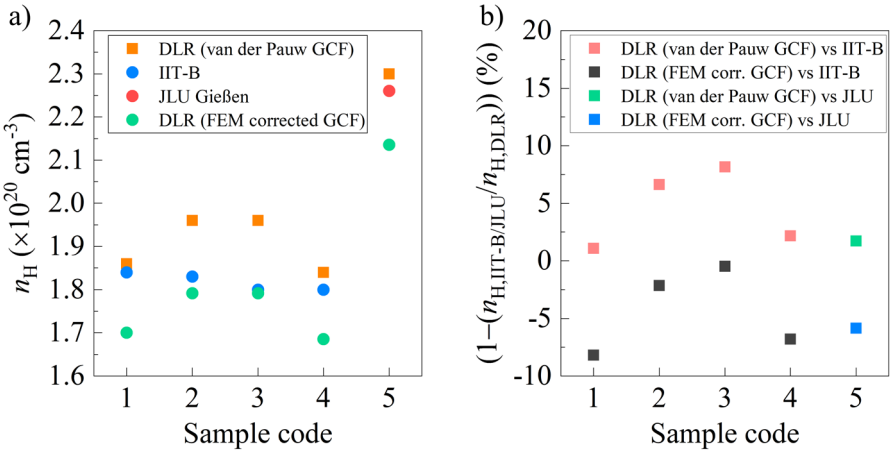

Figure A.2 a) RT Hall carrier concentration n_H of five different samples (both p-type and n-type tabulated in Table 5.1 in the main text) measured on the Hall facility at DLR (both with van der Pauw GCF and FEM corrected GCF values), IIT Bombay and JLU Gießen with a van der Pauw configuration of the sample holder, and b) the corresponding relative deviation in the measurement. The discrepancy between the n_H measured at DLR and other labs are a bit different after using the FEM corrected GCF, but the agreement is roughly as before.

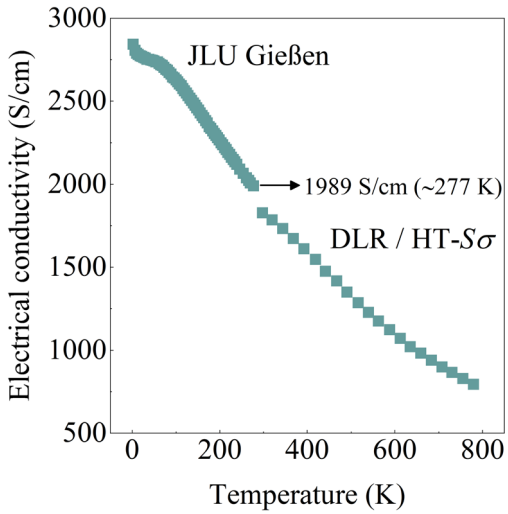

Figure A.3 Temperature dependent electrical conductivity measured at JLU Gießen and HT-$S\sigma$ facility (at DLR). Note that the last data point measured at 277 K is highlighted which is shown in Figure 5.7 in the main text.

A.3 Temperature dependent Seebeck coefficient and electrical conductivity, and Hall coefficient and electrical conductivity data of p-type $FeSi_2$

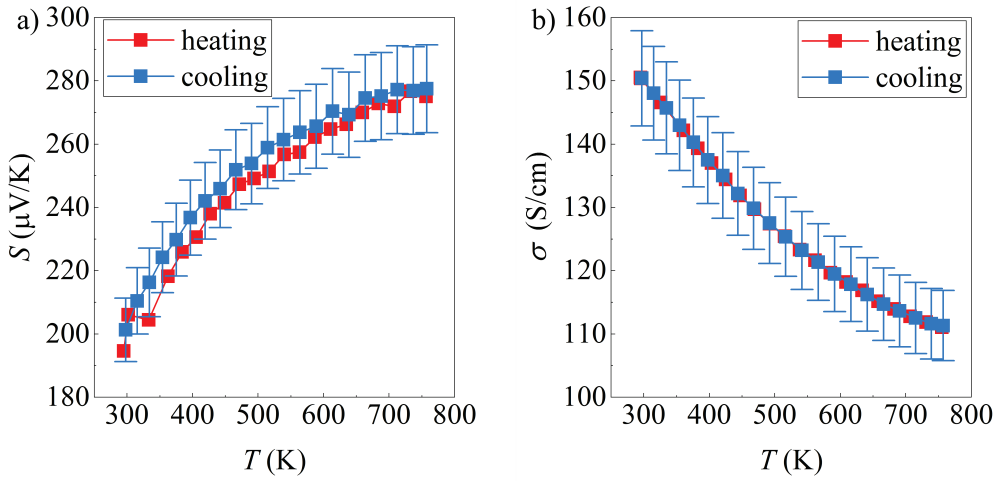

Figure A.4 Temperature dependent a) S and b) σ of p-type $FeSi_2$ specimen measured on HT-$S\sigma$ with both the heating and cooling curves of the measurement.

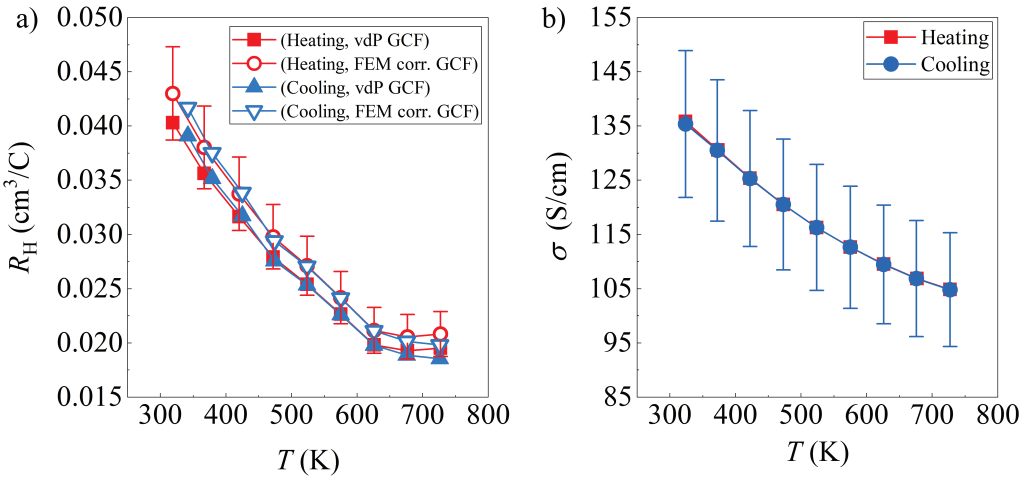

Figure A.5 Temperature dependent a) Hall coefficient and b) electrical conductivity of p-type $FeSi_2$ specimen which shows both the heating and cooling curves of the measurement.

Appendix B

B.1 Predicting the electrical transport properties measured during *in-situ* annealing at 773 K

The Seebeck coefficient data in Figure 10.2(b) in Chapter 10 shows that the absolute values increase until 4 h of annealing followed by a hump, and then decreases. This observation cannot be explained only by a single band transport as the minority carriers start to influence the transport properties. As a result, a 2PB (1 CB + 1 VB) model was utilized to predict the *in-situ* measured transport properties while annealing the samples at 773 K. However, N_D data was unavailable for the *in-situ* annealing duration and so, to estimate it, n ($= N_D$ at RT) of the sample (both before and after annealing) were deduced using the SPB model. To this purpose, RT values of S and R_H, measured before (during heat-up ramp to reach target annealing temperature) and after (during cooling down) annealing experiment, respectively, were utilized for deducing n and m_D^*. Note that the T-dependent properties of samples to be *in-situ* annealed at 773 K were measured before initiating the *in-situ* measurement which can be visualized in Figure 10.1(a) and Figure 10.1(b). The TE properties of this sample were re-measured during heat-up ramp to reach the target annealing temperature. The TE properties measured during cooling cycle of thermal cycling and heat-up ramp are compared in Figure 10.1(c) and Figure 10.1(d), which closely agree and show a heavily doped semiconducting behavior. The TE properties measured during heat-up ramp were well predicted (Figure 10.1(c) and Figure 10.1(d)) by utilizing the microscopic material parameters extracted from the SPB model.

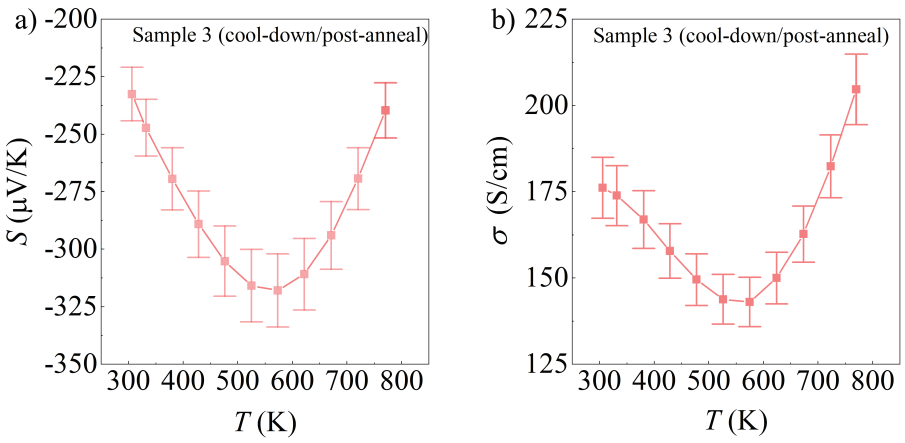

Figure B.1 Temperature dependent a) Seebeck coefficient and b) electrical conductivity of sample 3 measured during cool-down from $T_{anneal} \approx 773$ K.

The thermoelectric properties were also measured during cooling after the *in-situ* annealing which is visualized in Figure B.1. The properties showed an influence of minority carrier from 773 K → 450 K, and for $T < 400$ K, the properties showed a single band behavior. Furthermore, in the 300 K – 400 K regime, there is probably an influence of grain boundary scattering that leads to a hump in the conductivity data. The data shows no signs of minority carrier transport at room temperature. So, the room temperature transport properties were predicted using SPB model. The SPB analysis showed that the N_D ($= n$ at RT) was different before and after annealing which is listed in Table 10.1. The N_D values extracted from the room temperature TE properties, both before and after annealing, indicate that the N_D values for the annealing duration would lie in this range. For the prediction of *in-situ* measured Seebeck coefficient using a 2PB model, the followed approach is outlined in Figure B.2.

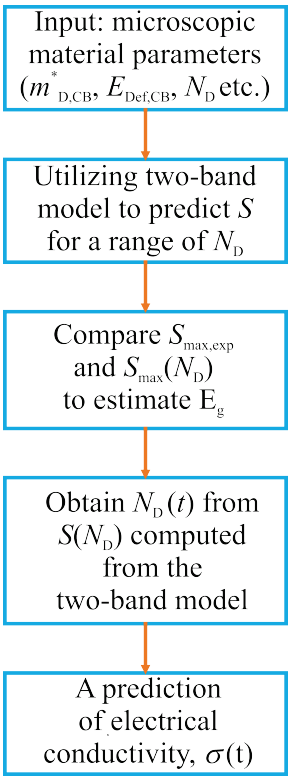

Figure B.2 Flowchart of the approach to determine N_D from the measured Seebeck coefficient S and a two-band model. Microscopic material parameters of valence band are taken from [256] (kept constant) while different values of conduction band parameters ($m^*_{D,CB}$ and $E_{Def,CB}$) were chosen for different limiting cases. Here, S_{max} is the maximum absolute value of the Seebeck coefficient. The values of Seebeck coefficient, experimental $S_{max,exp}$, and predicted $S_{max,2PB}$ are compared to determine E_g and thus, N_D.

As a first step, a range of N_D values along with other microscopic material parameters are plugged in a two-band model. Note that all other microscopic material parameters essential for the prediction of transport properties were kept constant. At a first glance, the utilization of constant set of the values of the microscopic material parameters might seem inappropriate, since, the SPB analysis of the room temperature properties showed that the microscopic parameters, $m^*_{D,CB}$ and $E_{Def,CB}$ (alongside n), were different before and after annealing (highlighted in Table 10.1). This reflects that the values of stated parameters were changing during the annealing experiment. Consequently, two sets of microscopic material parameters with different (but constant) values were employed for a reliable and a less complicated use of two band model for the prediction of transport properties. Each set of microscopic material parameters affected due to *in-situ* annealing is listed in Table B.1. The high-to-low range of N_D values in Table B.1 were extracted after the suitable value of band gap, E_g, was chosen (discussed in the coming section).

Table B.1 The values of the microscopic material parameters (N_D, $m^*_{D,CB}$, $E_{Def,CB}$) used for the 2PB modelling of *in-situ* measured thermoelectric properties.

Cases	Temperature (K)	Range of N_D values ($\times 10^{20}$ cm^{-3})	$m^*_{D,CB}$ (m_0)	$E_{Def,CB}$ (eV)
Non-annealed	773	1.7 – 0.33	2.4	10.35
Post-anneal		1.55 – 0.3	1.8	14.60

Each set of microscopic material parameters corresponds to the 'state' of the sample in terms of the empirically observed stabilization of transport properties e.g. non-depleted state (in regards with Mg concentration). In the first case, the set of material parameters, other than N_D, that are determined by analyzing T-dependent electrical transport properties during the heat-up ramp of the annealing treatment are utilized. These are referred to as 'non-annealed' parameters (NAP) and refer likely to the non-depleted state of the specimen with respect to Mg. This state is defined based on the fact that excess Mg (2 at.%) is taken for the synthesis which makes the composition as $Mg_{2.06}Si_{0.385}Sn_{0.6}Sb_{0.015}$, and the potential changes during the ramp up or during previous measurement cycles are ignored. In Figure 10.1(c) and Figure 10.1(d) some change is visible, but this is small compared to the changes during long term annealing. The second case of transport modelling uses different values of these parameters that correspond to the saturated state of the transport properties and are referred as 'post-anneal' parameters (PAP). The post-anneal state of Mg_2(Si,Sn) specimen refers to the depleted state of the specimen with respect to Mg. The non-depleted and post-depleted states refer to the relative change of Mg content in the

samples. This should not be taken strictly in a thermodynamic sense, since it is not utterly clear whether the samples are still Mg-rich or not. Besides, the other microscopic material parameters that are utilized to model these properties were kept constant, and are listed in Table B.2.

Table B.2 List of microscopic material parameters other than the ones highlighted in Table B.1 employed for single- and multi-band modelling of electrical transport properties.

Parameters	Employed values
DOS effective mass, m_{D}^{*} ($\times m_0$)	$m_{\mathrm{D,VB}}^{*} = 1.54$ [256]
Valley degeneracy (N_{v})	$N_{\mathrm{v,CB}} = 6$; $N_{\mathrm{v,VB}} = 2$ [83, 256]
Atom density (N_0) (m^{-3})	4.18×10^{28} [256]
Longitudinal speed of sound (v_{l}) (m/s)	5760 [257]
Fractional alloy composition (x)	0.6
Electron-phonon interaction potential constant (E_{Def}) (eV)	$E_{\mathrm{Def,VB}} = 9$ [256]
Alloy scattering potential constant (E_{AS}) (eV)	$E_{\mathrm{AS,CB}} = 0.5$, $E_{\mathrm{AS,VB}} = 0.5$ [83, 256]

Band gap E_{g} is a critical input to the two-band model besides other parameters which is not established in literature with sufficient certainty. Therefore, the value of E_{g} was chosen such that the S_{max} predicted from the two-band model matches the experimentally observed absolute S_{max} as shown in Figure B.3. This is feasible because for a fixed set of these microscopic material parameters ($m_{\mathrm{D,CB}}^{*}$ and $E_{\mathrm{Def,CB}}$) and temperature T, the $S(N_{\mathrm{D}})$ is only a function of E_{g}. This is understood from the Seebeck coefficient equation for a system with 2 band (majority and minority) transport: $S = \sum_i S_i\sigma_i / \sum_i \sigma_i$, where the $\sigma_i \propto \mu_i \propto 1/m_{\mathrm{D},i}^{2.5} E_{\mathrm{Def},i}^{2}$, and $S_i = \frac{k_B}{e}\left(\frac{2F_1(\eta_i)}{F_0(\eta_i)} - \eta_i\right)$. The η_i of the bands are linked by $\eta_{CB} = -\eta_{VB} - \frac{E_{\mathrm{g}}}{k_{\mathrm{B}}T}$ and determined by the charge neutrality equation ($n = N_{\mathrm{D}} + p$ for a heavily n-type doped material), thus E_{g} is the only "free" parameter. The E_{g} was estimated from the two-band modelling employing the 'non-annealed' parameters. Based on the close agreement between the maximum value of measured and modeled Seebeck coefficient, the band gap value of $E_{\mathrm{g}} = 0.296$ eV was chosen. The high temperature annealing could also affect the microscopic material parameters of the valence band and therefore, the band gap of the material. However, as said, the microscopic parameters of the valence band were kept constant to keep the complexity of modelling low. The

comparison of maximum absolute value of experimental and predicted Seebeck coefficient corresponds to the third step of approach highlighted in the flowchart.

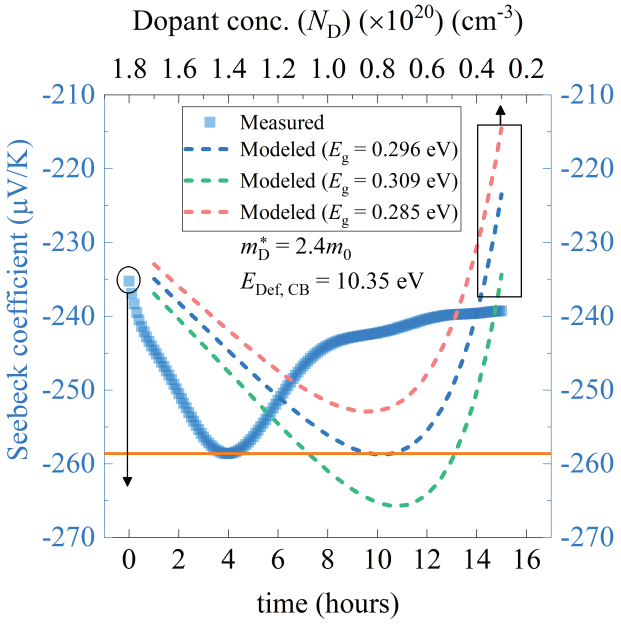

Figure B.3 Comparison of the absolute values of both measured and predicted Seebeck coefficient as a function of annealing duration and doping concentration N_D respectively.

In the SPB and the 2PB model the two CB's (C_L and C_H) are assumed to be a single fully degenerate band. This is helpful since this approach allows the determination and quantification of microscopic material parameters that are sensitive to annealing particularly, without needing to consider the unknown interband separation between the two bands at T_{anneal}. The difference in the present approach and the previous approach (employed in Chapter 9) lies in the N_D values utilized for the prediction of transport properties. Moreover, in Chapter 9, the varying values of microscopic material parameters, particularly $E_{Def,CB}$, were employed for the modelling of the transport properties. Whereas, in the present case, the values of microscopic material parameters are kept constant. A different and comparatively simple approach is utilized in the present case because the measured properties show mixed carrier conduction in the beginning of the *in-situ* experiment instead of (only) single (majority) band transport, that was observed in the beginning of *in-situ* annealing experiment at 710 K (Chapter 9). The extraction of $N_D(t)$ and the prediction of electrical conductivity, $\sigma(t)$, which corresponds to the fourth and fifth steps of the approach highlighted in the flowchart, are discussed in the coming section.

B.1.1 Two-band modelling using the non-annealed values of microscopic material parameters

$S(N_D)$ plot (Figure B.4(a)) was constructed by plugging the set of non-annealed parameters from Table B.1 and Table B.2 in the two-band model. $S(N_D)$ data is fitted using a 5th order polynomial equation.

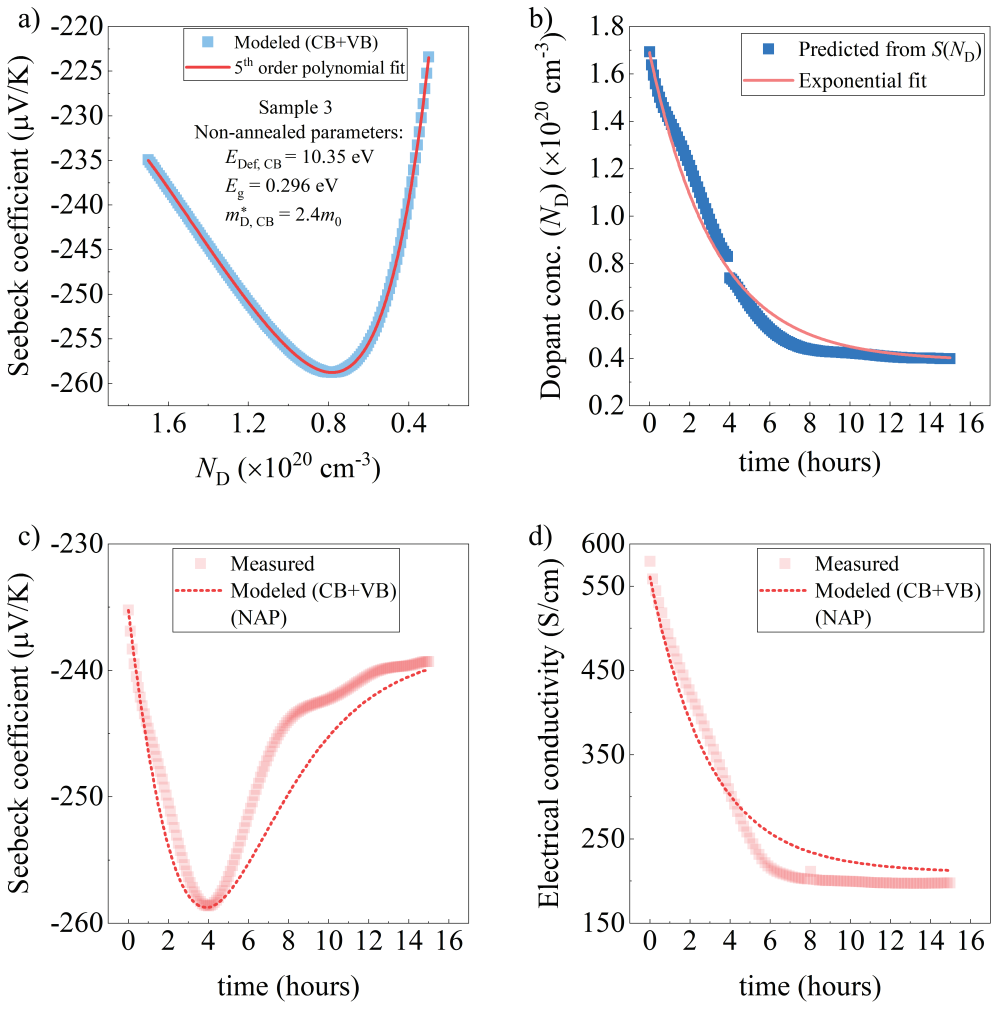

Figure B.4 a) $S(N_D)$ predicted using a 2PB model, b) N_D vs t_{anneal} fitted using an exponential decay function, and the measured (at 773 K) and the predicted c) S, and d) σ, respectively. Note that the transport properties were predicted by employing non-annealed microscopic material parameters (NAP) in the 2PB model.

$S(N_D)$ plot simulates the change observed during *in-situ* annealing i.e. an increase of absolute Seebeck coefficient followed by a decrease. From $S(t)$ data, the absolute Seebeck coefficient values are utilized to estimate corresponding N_D values. N_D values are plotted against the time

scale that corresponds to the measured $S(t)$, gives $N_D(t)$, which is plotted in Figure B.4(b). The complete trend of $N_D(t)$ is attributed to the variation of Mg flow in the samples due to Mg loss, as highlighted in section 10.3 of Chapter 10. So, $N_D(t)$ curve is representative of the entire degradation kinetics, until it saturates, and does not only translate to the formation of V_{Mg}^{2-}. The assumptions for the analysis of kinetics can be re-iterated that: the multi-step degradation process is approximated to a single-step process, which can be quantitatively expressed in terms of Arrhenius equation. Considering this, the $N_D(t)$ is fitted using an exponential decay function ($N_D(t) = N_0 + Ae^{-t_{anneal}/\tau}$), here $N_0 = 0.39 \times 10^{20}$ cm^{-3}, $A = 1.3 \times 10^{20}$ cm^{-3} with a time constant $\tau =$ 3.248 h. The decay function would give a single value of rate of Mg loss that allows a quantification of the kinetic parameters of Mg loss. N_D values, that are observed to saturate beyond $t > 6$ h of annealing, are also fitted because these values carry the influence of a variation of Mg-flow on N_D values near saturation. Including N_D values beyond $t > 6$ h allows an estimation of the effective activation energy which is physically meaningful and interpreted as a quantity, which consists the contributions of the energy barriers of individual processes.

The trend of the measured transport properties is predicted well using the two-band model using $N_D(t)$ as can be observed from Figure B.4(c) and Figure B.4(d), particularly for $t_{annealing} \leq 5$ h. A discrepancy in the transport properties in the annealing time interval 8 h – 15 h, evident from Figure B.4(c) and Figure B.4(d), is not surprising as the model base here are the microscopic parameters of the material corresponding to the non-depleted state before annealing, which cannot be a good assumption for long annealing times. It might also be noted that the largest differences between model and measured Seebeck coefficient S and electrical conductivity σ are observed where the agreement of $N_D(t)$ is poor, indicating that capturing the kinetics not perfectly is more influential than the errors in the electronic band structure model.

B.1.2 Two-band modelling using the post-anneal values of the microscopic material parameters

The post-anneal microscopic material parameters, as given in Table B.1 and Table B.2, were utilized for modelling the transport properties. The $N_D(t)$, shown in Figure B.5(b), is predicted from the measured Seebeck coefficient, from $S(N_D)$ in Figure B.5(a). The $N_D(t)$ curve shows no value in the annealing duration (2 h – 6 h) of the plot. This is because with the parameters employed in the two-band model for constructing $S(N_D)$ it is not possible to achieve measured S_{max}, and therefore cannot predict the measured data well (Figure B.5(b)).

The exponential decay function can be expressed as: $N_D(t) = N_0 + Ae^{-t_{anneal}/\tau}$, here $N_0 = 0.33 \times 10^{20}$ cm^{-3}, $A = 0.68646 \times 10^{20}$ cm^{-3} with time constant $\tau = 3.02$ h. Note that N_0 (= n at room temperature after HT annealing, using SPB) was fixed for fitting the exponential decay function, and $N_D(t)$ was estimated. These $N_D(t)$ values are employed in the 2PB model to predict the transport properties. The predicted and measured Seebeck coefficient are in good agreement in the beginning of the annealing experiment. This is mainly due to the chosen microscopic material parameters for estimating $S(N_D)$, and from that $N_D(t)$.

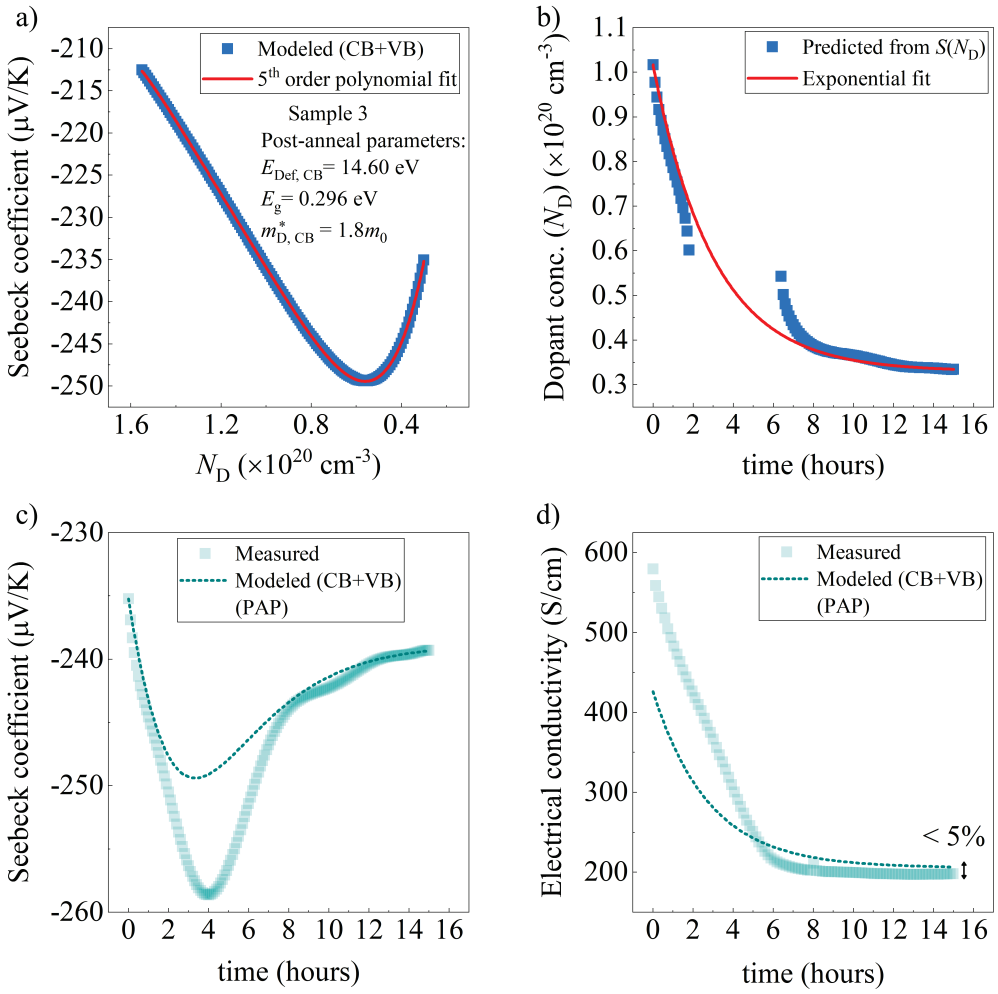

Figure B.5 a) $S(N_D)$ predicted using a 2PB model, b) N_D vs t_{anneal} fitted using an exponential decay function, and the measured (at 773 K) and the predicted c) S, and d) σ, respectively. Note that the transport properties were predicted by employing post-anneal microscopic material parameters (PAP) in the 2PB model.

The predicted and measured σ values, on the other hand, show a large deviation in the beginning of the annealing duration. This is because the microscopic material parameters employed here

correspond to the Mg-depleted state of the material. This situation is unlike the previous case, which corresponds to the non-depleted state with respect to Mg, where modelling was carried out using non-annealed parameters. Therefore, physically, a disagreement in the predicted and measured values in the beginning of the annealing duration is expected in the present case. There is a large disagreement in the predicted and measured Seebeck coefficient values in the range (2 h – 8 h) of annealing duration. This disagreement is also reflected in the conductivity values in the starting region of this range. The disagreement in these properties also indicates that physically, these parameters of $Mg_2(Si,Sn)$ might not have degraded to the values that are employed during modelling. Nevertheless, near the saturation time, the predicted and measured electrical conductivity show a close agreement.

B.1.3 Hall coefficient: Measured versus predicted (from different cases)

The *in-situ* measurement of the R_H of sample 4 at $T_{anneal} = 773$ K in HT Hall (in vacuum) is shown in Figure B.6. The R_H predicted using 2PB modelling for the different cases discussed in the last section is compared with the R_H of sample 4 measured in HT Hall at 773 K.

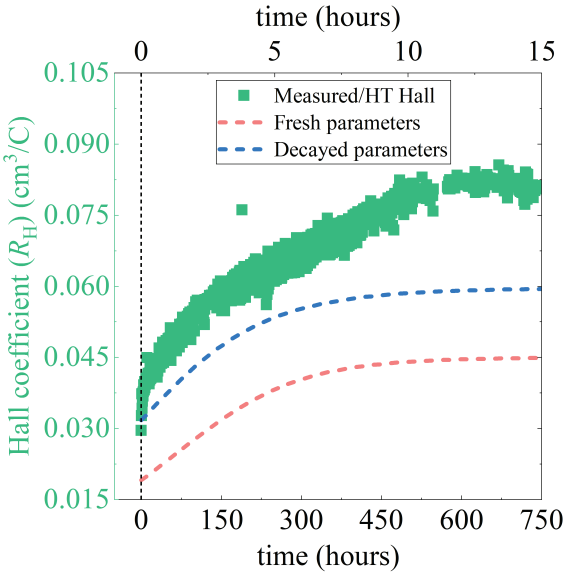

Figure B.6 Comparative plot showing the R_H (corresponding to sample 3) predicted from 2PB model by plugging the different values of microscopic material parameters (NAP and PAP), as discussed, and the measured R_H (sample 4).

The plot shows that both the measured and predicted R_H follow similar trends but there are differences in the absolute values. The reason for an observed discrepancy between the *in-situ* measured data and both modeled R_H values could be due to the (simplified) 2PB band

modelling. Particularly, the two CB's are assumed as one (effective) conduction band, therefore, both the density-of-states effective mass $m^*_{\mathrm{D,CB}}$ and the mobility μ are an average of individual contributions, respectively, from each band. However, the dependence of S, σ and R_{H} on the band masses is different and thus using the measured transport properties to obtain microscopic material parameters does not lead to an excellent prediction for R_{H}. A further complication is that the bands might not fully be degenerate, as indicated by the analysis of the TE properties of $Mg_2Si_{0.4}Sn_{0.6}$ in previous reports [100, 101], which had shown that both CB's are not completely converged instead, their degeneracy is lifted at room temperature. This might be true for the T_{anneal} in the current *in-situ* experiments, but it is unknown at present. Moreover, the microscopic material parameters (both m^*_{D} and E_{Def}) for each CB are shown to be different [258]. Consequently, as a future direction a three-band model, with two conduction bands and one valence band, is necessary to predict the measured transport properties.

B.2 Temperature dependent thermoelectric properties of sample 4 (Measured before *in-situ* annealing at 773 K)

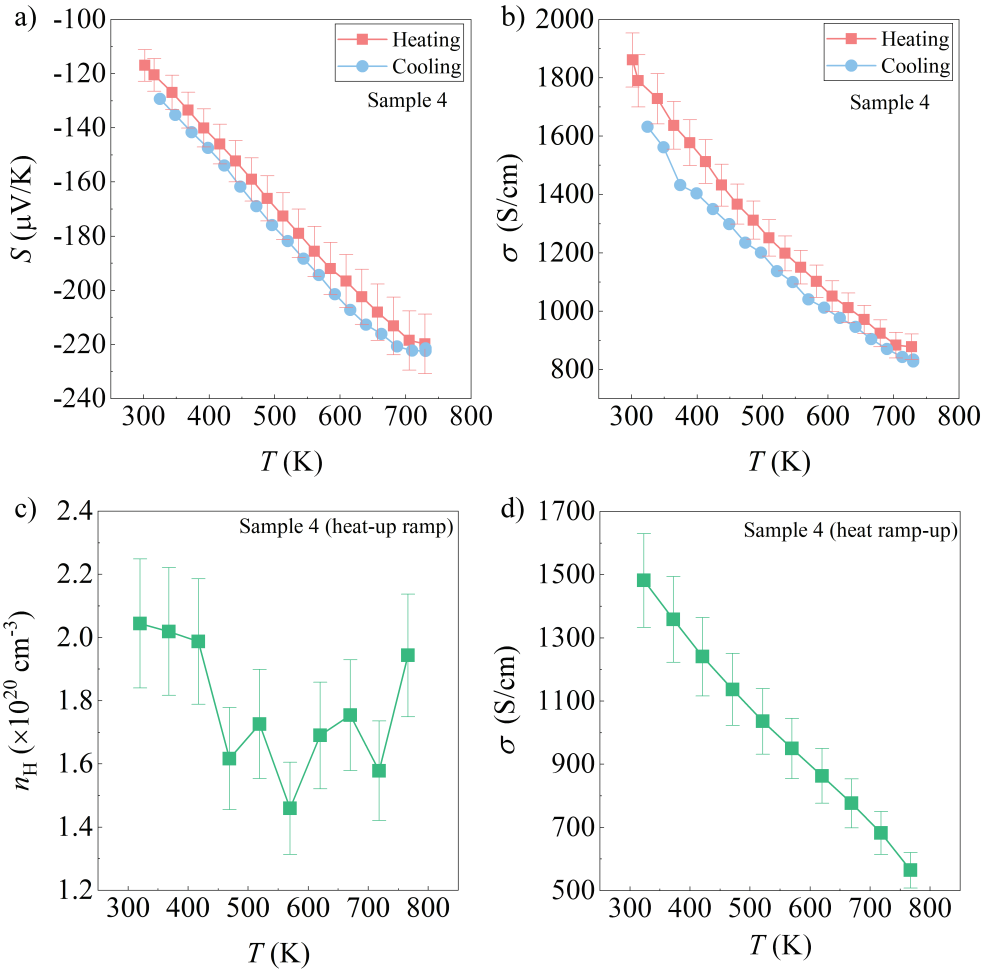

Figure B.7 T dependent a) S and b) σ of sample 4 measured at the HT-$S\sigma$ facility before *in-situ* measurements. c) n_H and d) σ of sample 4 during heat-up ramp for the *in-situ* measurement at the HT Hall facility.

B.3 Temperature dependent thermoelectric properties of sample 3 and sample 4 (Measured after *in situ* annealing at 773 K)

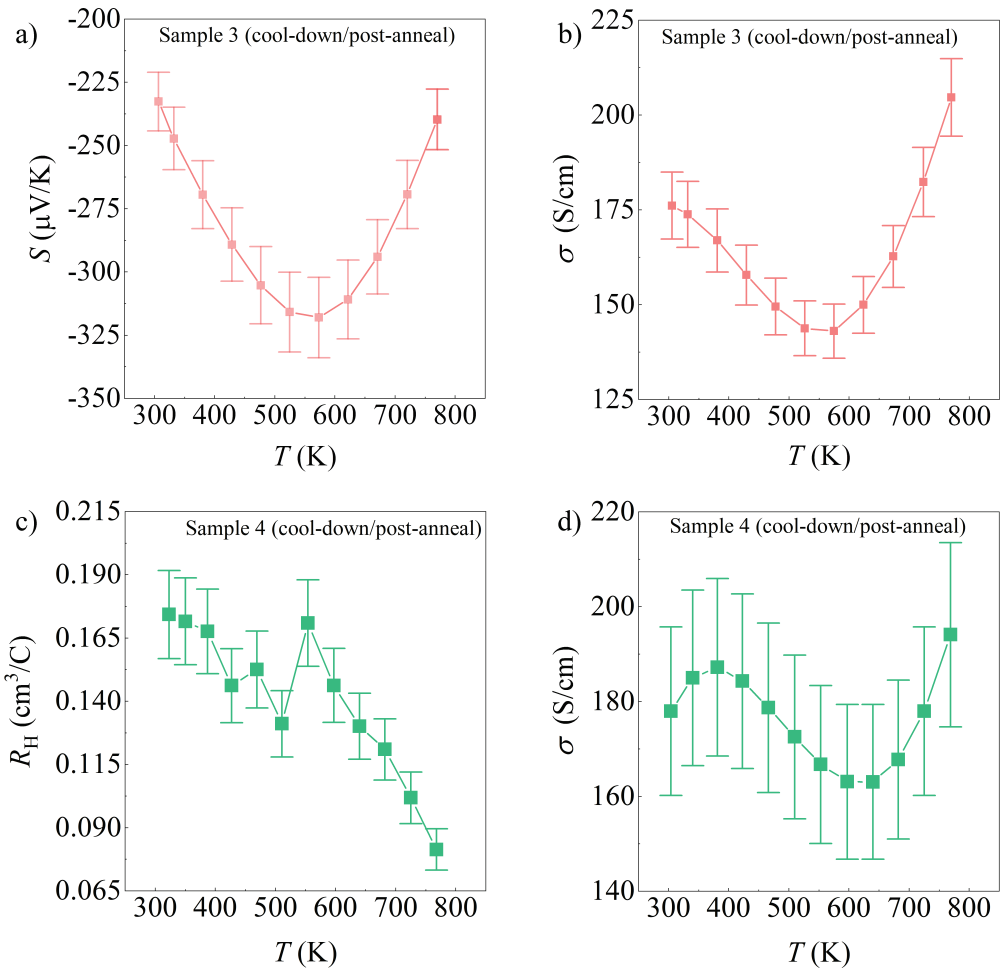

Figure B.8 T dependent a) S and b) σ of sample 3, and c) R_{H} and d) σ of sample 4. These properties are measured during cooling after high-temperature *in-situ* annealing at $T_{\mathrm{anneal}} = 773$ K.

References

[1] G. J. Snyder and E. Toberer, Complex thermoelectric materials, *Nature Materials* 7, 105 (2008).

[2] C. Wood, Materials for thermoelectric energy conversion, *Reports on Progress in Physics* 51, 459 (1988).

[3] Energy flow charts: charting the complex relationships among energy, water and carbon access year: 2023).

[4] H. Jouhara, N. Khordehgah, S. Almahmoud, B. Delpech, A. Chauhan and S. Tassou, Waste heat recovery technologies and applications, *Thermal Science and Engineering Progress* 6, 268 (2018).

[5] J. Yang and T. Caillat, Thermoelectric materials for space and automotive power generation, *MRS Bulletin* 31, 224 (2006).

[6] J. Pérez-Taborda, O. Caballero-Calero and M. Martín-González, Silicon-Germanium (SiGe) nanostructures for thermoelectric devices: Recent advances and new approaches to high thermoelectric efficiency, *New Research on Silicon–Structure, Properties, Technology* (IntechOpen, 2017).

[7] A. Tsynaeva, Cathode protection systems of cross-country pipelines, *Procedia Engineering* 111, 777 (2015).

[8] T. Durand, P. Dimopoulos Eggenschwiler, Y. Tang, Y. Liao and D. Landmann, Potential of energy recuperation in the exhaust gas of state of the art light duty vehicles with thermoelectric elements, *Fuel* 224, 271 (2018).

[9] K. Smith and M. Thornton, Feasibility of thermoelectrics for waste heat recovery in conventional vehicles, *National Renewable Energy Lab. (NREL), Golden, CO (United States)* 1 (2009).

[10] J. Yang and F. Stabler, Automotive applications of thermoelectric materials, *Journal of Electronic Materials* 38, 1245 (2009).

[11] D. Champier, Thermoelectric generators: A review of applications, *Energy Conversion and Management* 140, 167 (2017).

[12] K. Sztekler, K. Wojciechowski, M. Komorowski and M. Tarnowska, The thermoelectric generators use for waste heat utilization from conventional power plant, *E3S Web of Conferences* 14, 01032 (2017).

[13] H. Gabbar, C. Barry Stoute, D. Steele, C. Simkin, T. Sleeman, D. Newell, D. Paterson and E. Boafo, Evaluation and optimization of thermoelectric generator network for waste heat utilization in nuclear power plants and non-nuclear energy applications, *Annals of Nuclear Energy* 101, 454 (2017).

[14] C. Bode, J. Friedrichs, R. Somdalen, J. Koehler, K.-D. Buechter, C. Falter, U. Kling, P. Ziolkowski, K. Zabrocki, E. Mueller and D. Kožulović, Potential of future thermoelectric energy recuperation for aviation, *Journal of Engineering for Gas Turbines and Power* 139, 1 (2017).

[15] C. Goupil, H. Ouerdane, K. Zabrocki, W. Seifert, N. F. Hinsche and E. Mueller, Thermodynamics and thermoelectricity, *Continuum Theory and Modeling of Thermoelectric Elements* (Wiley-VCH Verlag GmbH & Co., 2016).

[16] T. M. Tritt, Thermoelectric phenomena, materials, and applications, *Annual Review of Materials Research* 41, 433 (2011).

[17] D. M. Rowe, General principles and basic considerations, *Thermoelectrics handbook: Macro to Nano* (CRC press 2006).

[18] D. K. Aswal, R. Basu and A. Singh, Key issues in development of thermoelectric power generators: High figure-of-merit materials and their highly conducting interfaces with metallic interconnects, *Energy Conversion and Management* 114, 50 (2016).

[19] H. Littman and B. Davidson, Theoretical bound on the thermoelectric figure of merit from irreversible thermodynamics, *Journal of Applied Physics* 32, 217 (1961).

[20] T. Zhu, Y. Liu, C. Fu, J. Heremans, G. J. Snyder and X. Zhao, Compromise and synergy in high-efficiency thermoelectric materials, *Advanced Materials* 29, 1605884 (2017).

[21] Y. Pei, H. Wang and G. J. Snyder, Band engineering of thermoelectric materials, *Advanced Materials* 24, 6125 (2012).

[22] C. Fu, T. Zhu, Y. Liu, H. Xie and X. Zhao, Band engineering of high performance p-type FeNbSb based half-Heusler thermoelectric materials for figure of merit zT > 1, *Energy & Environmental Science* 8, 216 (2015).

[23] J.-H. Bahk, Z. Bian and A. Shakouri, Electron transport modeling and energy filtering for efficient thermoelectric $Mg_2Si_{1-x}Sn_x$ solid solutions, *Physical Review B* 89, 075204 (2014).
[24] J.-H. Bahk, Z. Bian and A. Shakouri, Electron energy filtering by a nonplanar potential to enhance the thermoelectric power factor in bulk materials, *Physical Review B* 87, 075204 (2013).
[25] C. Gayner and Y. Amouyal, Energy filtering of charge carriers: Current trends, challenges, and prospects for thermoelectric materials, *Advanced Functional Materials* 30, 1901789 (2020).
[26] B. Wiendlocha, Thermopower of thermoelectric materials with resonant levels: PbTe:Tl versus PbTe:Na and $Cu_{1-x}Ni_x$, *Physical Review B* 97, 1 (2018).
[27] Q. Zhang, H. Wang, W. Liu, H. Wang, B. Yu, Q. Zhang, Z. Tian, G. Ni, S. Lee, K. Esfarjani, G. Chen and Z. Ren, Enhancement of thermoelectric figure-of-merit by resonant states of aluminium doping in lead selenide, *Energy & Environmental Science* 5, 5246 (2012).
[28] B. Yu, M. Zebarjadi, H. Wang, K. Lukas, H. Wang, D. Wang, C. Opeil, M. Dresselhaus, G. Chen and Z. Ren, Enhancement of thermoelectric properties by modulation-doping in silicon germanium alloy nanocomposites, *Nano Letters* 12, 2077 (2012).
[29] M. Zebarjadi, G. Joshi, G. Zhu, B. Yu, A. Minnich, Y. Lan, X. Wang, M. Dresselhaus, Z. Ren and G. Chen, Power factor enhancement by modulation doping in bulk nanocomposites, *Nano Letters* 11, 2225 (2011).
[30] D. Zhang, B. Zhang, Z. Zhou, K. Peng, H. Wu, H. Wang, G. Wang, G. Han, G. Wang, X. Zhou and X. Lu, Ultralow lattice thermal conductivity of cubic $CuFeS_2$ induced by atomic disorder, *Chemistry of Materials* 33, 9795 (2021).
[31] S. I. Kim, K. H. Lee, H. A. Mun, H. S. Kim, S. W. Hwang, J. W. Roh, D. J. Yang, W. H. Shin, X. S. Li, Y. H. Lee, G. J. Snyder and S. W. Kim, Dense dislocation arrays embedded in grain boundaries for high-performance bulk thermoelectrics, *Science* 348, 109 (2015).
[32] P. F. P. Poudeu, J. D'Angelo, H. Kong, A. Downey, J. L. Short, R. Pcionek, T. P. Hogan, C. Uher and M. G. Kanatzidis, Nanostructures versus solid solutions: Low lattice thermal conductivity and enhanced thermoelectric figure of merit in $Pb_{9.6}Sb_{0.2}Te_{10-x}Se_x$ bulk materials, *Journal of the American Chemical Society* 128, 14347 (2006).
[33] H. Wang, A. D. LaLonde, Y. Pei and G. J. Snyder, The criteria for beneficial disorder in thermoelectric solid solutions, *Advanced Functional Materials* 23, 1586 (2013).
[34] S.-H. Lo, J. He, K. Biswas, M. G. Kanatzidis and V. P. Dravid, Phonon scattering and thermal conductivity in p-type nanostructured PbTe-BaTe bulk thermoelectric materials, *Advanced Functional Materials* 22, 5175 (2012).
[35] P.-C. Wei, C.-N. Liao, H.-J. Wu, D. Yang, J. He, G. V. Biesold-McGee, S. Liang, W.-T. Yen, X. Tang, J.-W. Yeh, Z. Lin and J.-H. He, Thermodynamic routes to ultralow thermal conductivity and high thermoelectric performance, *Advanced Materials* 32, 1906457 (2020).
[36] E. Quarez, K.-F. Hsu, R. Pcionek, N. Frangis, E. K. Polychroniadis and M. G. Kanatzidis, Nanostructuring, compositional fluctuations, and atomic ordering in the thermoelectric materials $AgPb_mSbTe_{2+m}$. The myth of solid solutions, *Journal of the American Chemical Society* 127, 9177 (2005).
[37] A. J. Minnich, M. S. Dresselhaus, Z. F. Ren and G. Chen, Bulk nanostructured thermoelectric materials: Current research and future prospects, *Energy & Environmental Science* 2, 466 (2009).
[38] Y. Pei, J. Lensch-Falk, E. S. Toberer, D. L. Medlin and G. J. Snyder, High Thermoelectric Performance in PbTe Due to Large Nanoscale Ag_2Te Precipitates and La Doping, *Advanced Functional Materials* 21, 241 (2011).
[39] S. Gorsse, P. Bellanger, Y. Brechet, E. Sellier, A. Umarji, U. Ail and R. Decourt, Nanostructuration via solid state transformation as a strategy for improving the thermoelectric efficiency of PbTe alloys, *Acta Materialia* 59, 7425 (2011).
[40] W. D. Callister and D. G. Rethwisch, Impurities in Solids, *Materials science and engineering: an introduction* (Wiley New York, 2018).
[41] Q. Zhang, Y. Zheng, X. Su, K. Yin, X. Tang and C. Uher, Enhanced power factor of $Mg_2Si_{0.3}Sn_{0.7}$ synthesized by a non-equilibrium rapid solidification method, *Scripta Materialia* 96, 1 (2015).
[42] K. Yin, Q. Zhang, Y. Zheng, X. Su, X. Tang and C. Uher, Thermal stability of $Mg_2Si_{0.3}Sn_{0.7}$ under different heat treatment conditions, *Journal of Materials Chemistry C* 3, 10381 (2015).
[43] Q. Zhang, W. Liu, C. Liu, K. Yin and X. F. Tang, Thermoelectric properties of $Mg_2(Si_{0.3}Sn_{0.7})_{1-y}Sb_y$ solid solutions doped with Co as CoSi secondary phase, *Journal of Electronic Materials* 43, 2188 (2014).
[44] K. Yin, X. Su, Y. Yan, C. Uher and X. Tang, In situ nanostructure design leading to a high figure of merit in an eco-friendly stable $Mg_2Si_{0.30}Sn_{0.70}$ solid solution, *RSC Advances* 6, 16824 (2016).

[45] W. Liu, Q. Zhang, X. Tang, H. Li and J. Sharp, Thermoelectric properties of Sb-doped $Mg_2Si_{0.3}Sn_{0.7}$, *Journal of Electronic Materials* 40, 1062 (2011).
[46] Q. Zhang, J. Fan, W. Fan, H. Zhang, S. Chen, Y. Wu, X. Tang and B. Xu, Energy-efficient synthesis and superior thermoelectric performance of Sb-doped $Mg_2Si_{0.3}Sn_{0.7}$ solid solutions by rapid thermal explosion, *Materials Research Bulletin* 128, 110885 (2020).
[47] R. J. Korkosz, T. C. Chasapis, S.-h. Lo, J. W. Doak, Y. J. Kim, C.-I. Wu, E. Hatzikraniotis, T. P. Hogan, D. N. Seidman, C. Wolverton, V. P. Dravid and M. G. Kanatzidis, High ZT in p-type $(PbTe)_{1-2x}(PbSe)_x(PbS)_x$ thermoelectric materials, *Journal of the American Chemical Society* 136, 3225 (2014).
[48] H. Sun, B. Cai, P. Zhao, F. Yu, L. Zhang, D. Yu, Y. Tian and B. Xu, Enhancement of thermoelectric performance of Al doped PbTe-PbSe due to carrier concentration optimization and alloying, *Journal of Alloys and Compounds* 791, 786 (2019).
[49] S. N. Girard, K. Schmidt-Rohr, T. C. Chasapis, E. Hatzikraniotis, B. Njegic, E. M. Levin, A. Rawal, K. M. Paraskevopoulos and M. G. Kanatzidis, Analysis of phase separation in high performance PbTe–PbS thermoelectric materials, *Advanced Functional Materials* 23, 747 (2013).
[50] D. Wu, L.-D. Zhao, X. Tong, W. Li, L. Wu, Q. Tan, Y. Pei, L. Huang, J.-F. Li, Y. Zhu, M. G. Kanatzidis and J. He, Superior thermoelectric performance in PbTe–PbS pseudo-binary: Extremely low thermal conductivity and modulated carrier concentration, *Energy & Environmental Science* 8, 2056 (2015).
[51] H. Wang, W. D. Porter, H. Böttner, J. Koenig, L. Chen, S. Bai, T. M. Tritt, A. Mayolet, J. Senawiratne, C. Smith, F. Harris, P. Gilbert, J. W. Sharp, J. Lo, H. Kleinke and L. Kiss, Transport properties of bulk thermoelectrics—an international round-robin study, part I: Seebeck coefficient and electrical resistivity, *Journal of Electronic Materials* 42, 654 (2013).
[52] H. Wang, W. D. Porter, H. Böttner, J. Koenig, L. Chen, S. Bai, T. M. Tritt, A. Mayolet, J. Senawiratne, C. Smith, F. Harris, P. Gilbert, J. Sharp, J. Lo, H. Kleinke and L. Kiss, Transport Properties of bulk thermoelectrics: an international round-robin study, part II: Thermal diffusivity, specific heat, and thermal conductivity, *Journal of Electronic Materials* 42, 1073 (2013).
[53] S.-i. Yi, V. Attari, M. Jeong, J. Jian, S. Xue, H. Wang, R. Arroyave and C. Yu, Strain-induced suppression of the miscibility gap in nanostructured Mg_2Si–Mg_2Sn solid solutions, *Journal of Materials Chemistry A* 6, 17559 (2018).
[54] J. Male, M. T. Agne, A. Goyal, S. Anand, I. T. Witting, V. Stevanović and G. J. Snyder, The importance of phase equilibrium for doping efficiency: Iodine doped PbTe, *Materials Horizons* 6, 1444 (2019).
[55] M. Yasseri, K. Mitra, A. Sankhla, J. de Boor and E. Mueller, Influence of Mg loss on the phase stability in Mg_2X (X = Si, Sn) and its correlation with coherency strain, *Acta Materialia* 208, 116737 (2021).
[56] D. A. Neamen, *Semiconductor physics and devices: basic principles*, Fourth edition (McGraw-Hill, 2003).
[57] V. I. Fistul, *Heavily doped semiconductors*, First edition (Plenum Press, 1969).
[58] H. Ibach and H. Lueth, *Solid-state physics: An introduction to theory and experiment*, Fourth edition (Springer Heidelberg, 2009).
[59] N. W. Ashcroft and N. D. Mermin, *Solid state physics*, First edition (Hartcourt College Publishers, 1976).
[60] R. E. Hummel, Electrons in a crystal, *Electronic properties of materials* (Springer New York, 2011).
[61] H. Ibach and H. Lueth, Motion of electrons and transport phenomena, *Solid-State Physics: An introduction to principles of materials science* (Springer Heidelberg, 2009).
[62] R. F. Pierret and G. W. Neudeck, *Advanced semiconductor fundamentals*, Second edition (Addison-Wesley Reading, MA, 1987).
[63] J. de Boor, On the applicability of the single parabolic band model to advanced thermoelectric materials with complex band structures, *Journal of Materiomics* 7, 603 (2021).
[64] H. J. Goldsmid, Optimisation and selection of semiconductor thermoelements, *Introduction to Thermoelectricity* (Springer Berlin Heidelberg, 2010).
[65] H. Ibach and H. Lueth, "Free" electrons in solids, *Solid-state physics: An introduction to principles of materials science* (Springer Heidelberg, 2009).
[66] S. S. Li, Semiconductor Statistics, *Semiconductor Physical Electronics* (Springer New York, 2006).
[67] A. F. May, High-temperature transport in lanthanum telluride and other modern thermoelectric materials, *California Institute of Technology* (2010).

[68] H. J. Goldsmid, Thermoelectric properties of metals and semiconductors, *Introduction to Thermoelectricity* (Springer Berlin Heidelberg, 2010).
[69] M. Grundmann, Transport, *The Physics of semiconductors: An introduction including nanophysics and applications* (Springer International Publishing, 2016).
[70] M. Lundstrom, The Boltzmann transport equation, *Fundamentals of Carrier Transport* (Cambridge University Press, 2010).
[71] G. D. Mahan and J. O. Sofo, The best thermoelectric, *Proceedings of the National Academy of Sciences of the United States of America* 93, 7436 (1996).
[72] M. Lundstrom and C. Jeong, *Near-Equilibrium Transport Fundamentals and Applications*, (World Scientific Publishing Company, 2011).
[73] J. Y. W. Seto, The electrical properties of polycrystalline silicon films, *Journal of Applied Physics* 46, 5247 (1975).
[74] J. de Boor, T. Dasgupta, H. Kolb, C. Compere, K. Kelm and E. Mueller, Microstructural effects on thermoelectric efficiency: A case study on magnesium silicide, *Acta Materialia* 77, 68 (2014).
[75] J. Bardeen and W. Shockley, Deformation potentials and mobilities in non-polar crystals, *Physical Review* 80, 72 (1950).
[76] H. Wang, Y. Pei, A. D. LaLonde and G. Jeffrey Snyder, Material design considerations based on thermoelectric quality factor, *Thermoelectric Nanomaterials: Materials Design and Applications* (Springer Berlin Heidelberg, 2013).
[77] C. Hamaguchi, Electron–Phonon Interaction and Electron Transport, *Basic Semiconductor Physics* (Springer International Publishing, 2017).
[78] J. W. Harrison and J. R. Hauser, Alloy scattering in ternary III-V compounds, *Physical Review B* 13, 5347 (1976).
[79] C. Hu, K. Xia, C. Fu, X. B. Zhao and T. Zhu, Carrier grain boundary scattering in thermoelectric materials, *Energy & Environmental Science* 15, 1406 (2022).
[80] S. S. Li, Scattering mechanisms and carrier mobilities in semiconductors, *Semiconductor Physical Electronics* (Springer New York, 2006).
[81] M. Cutler and N. F. Mott, Observation of Anderson localization in an electron gas, *Physical Review* 181, 1336 (1969).
[82] Mark Lundstrom and C. Jeong, Thermoelectric effects: Physical approach, *Near-Equilibrium Transport Fundamentals and Applications* (World Scientific, 2013).
[83] W. Liu, H. Chi, H. Sun, Q. Zhang, K. Yin, X. Tang, Q. Zhang and C. Uher, Advanced thermoelectrics governed by a single parabolic band: $Mg_2Si_{0.3}Sn_{0.7}$, a canonical example, *Physical Chemistry Chemical Physics* 16, 6893 (2014).
[84] W. Kim, Strategies for engineering phonon transport in thermoelectrics, *Journal of Materials Chemistry C* 3, 10336 (2015).
[85] A. F. Ioffe, L. S. Stil'bans, E. K. Iordanishvili, T. S. Stavitskaya, A. Gelbtuch and G. Vineyard, *Semiconductor thermoelements and thermoelectric cooling*, (Infosearch Ltd. London, 1957).
[86] R. P. Chasmar and R. Stratton, The thermoelectric figure of merit and its relation to thermoelectric generators, *Journal of Electronics and Control* 7, 52 (1959).
[87] E. H. Putley, Galvano- and thermo-magnetic coefficients for a multi-band conductor, *Journal of Physics C: Solid State Physics* 8, 1837 (1975).
[88] L. Lu, M. O. Lai and M. L. Hoe, Formaton of nanocrystalline Mg_2Si and Mg_2Si dispersion strengthened Mg-Al alloy by mechanical alloying, *Nanostructured Materials* 10, 551 (1998).
[89] J. Zhang, Z. Fan, Y. Q. Wang and B. L. Zhou, Microstructural development of Al–15 wt.% Mg_2Si in situ composite with mischmetal addition, *Materials Science and Engineering: A* 281, 104 (2000).
[90] F.-l. Zeng, Z.-l. Wei, J.-f. Li, C.-x. Li, X. Tan, Z. Zhang and Z.-q. Zheng, Corrosion mechanism associated with Mg_2Si and Si particles in Al–Mg–Si alloys, *Transactions of Nonferrous Metals Society of China* 21, 2559 (2011).
[91] H. Kim, Y. J. Kim, D. G. Kim, H. J. Sohn and T. Kang, Mechanochemical synthesis and electrochemical characteristics of Mg_2Sn as an anode material for Li-ion batteries, *Solid State Ionics* 144, 41 (2001).
[92] D.-T. Nguyen and S.-W. Song, Magnesium stannide as a high-capacity anode for magnesium-ion batteries, *Journal of Power Sources* 368, 11 (2017).
[93] X. Liu, L. Xi, W. Qiu, J. Yang, T. Zhu, X. Zhao and W. Zhang, Significant roles of intrinsic point defects in Mg_2X (X = Si, Ge, Sn) thermoelectric materials, *Advanced Electronic Materials* 2, 1500284 (2016).

[94] M. Søndergaard, M. Christensen, K. A. Borup, H. Yin and B. B. Iversen, Thermoelectric properties of the entire composition range in $Mg_2Si_{0.9925-x}Sn_xSb_{0.0075}$, *Journal of Electronic Materials* 42, 1417 (2013).
[95] X. Shi, X. Wang, W. Li and Y. Pei, Advances in thermoelectric Mg_3Sb_2 and its derivatives, *Small Methods* 2, 1800022 (2018).
[96] H. Kitagawa, M. Wakatsuki, H. Nagaoka, H. Noguchi, Y. Isoda, K. Hasezaki and Y. Noda, Temperature dependence of thermoelectric properties of Ni-doped $CoSb_3$, *Journal of Physics and Chemistry of Solids* 66, 1635 (2005).
[97] X. Yan, G. Joshi, W. Liu, Y. Lan, H. Wang, S. Lee, J. Simonson, S. Poon, T. Tritt, G. Chen and Z. Ren, Enhanced thermoelectric figure of merit of p-type half-Heuslers, *Nano Letters* 11, 556 (2011).
[98] V. K. Zaitsev, M. I. Fedorov, E. A. Gurieva, I. S. Eremin, P. P. Konstantinov, A. Y. Samunin and M. V. Vedernikov, Highly effective $Mg_2Si_{1-x}Sn_x$ thermoelectrics, *Physical Review B* 74, 045207 (2006).
[99] W. Liu, X. Tan, K. Yin, H. Liu, X. Tang, J. Shi, Q. Zhang and C. Uher, Convergence of conduction bands as a means of enhancing thermoelectric performance of n-type $Mg_2Si_{1-x}Sn_x$ solid solutions, *Physical Review Letters* 108, 166601 (2012).
[100] M. I. Fedorov, D. A. Pshenay-Severin, V. K. Zaitsev, S. Sano and M. V. Vedernikov, Features of conduction mechanism in n-type $Mg_2Si_{1-x}Sn_x$ solid solutions, *IEEE proceedings 22nd International Conference on Thermoelectrics* 1, 142 (2003).
[101] V. K. Zaitsev, M. I. Fedorov, A. T. Burkov, E. A. Gurieva, I. S. Eremin, P. P. Konstantinov, S. V. Ordin, S. Sano and M. V. Vedernikov, Some features of the conduction band structure, transport and optical properties of n-type Mg_2Si-Mg_2Sn alloys, *IEEE proceedings 21st International Conference on Thermoelectrics* 1, 151 (2002).
[102] V. K. Zaitsev, M. I. Fedorov, E. A. Gurieva, I. S. Eremin, P. P. Konstantinov, A. Y. Samunin and M. V. Vedernikov, Thermoelectrics of n-type with ZT>1 based on Mg_2Si-Mg_2Sn solid solutions, *IEEE proceedings 24th International Conference on Thermoelectrics* 1, 204 (2005).
[103] L. Zhang, P. Xiao, L. Shi, G. Henkelman, J. B. Goodenough and J. Zhou, Suppressing the bipolar contribution to the thermoelectric properties of $Mg_2Si_{0.4}Sn_{0.6}$ by Ge substitution, *journal of Applied Physics* 117, 155103 (2015).
[104] N. Farahi, M. VanZant, J. Zhao, J. S. Tse, S. Prabhudev, G. A. Botton, J. R. Salvador, F. Borondics, Z. Liu and H. Kleinke, Sb- and Bi-doped Mg_2Si: Location of the dopants, micro- and nanostructures, electronic structures and thermoelectric properties, *Dalton Transactions* 43, 14983 (2014).
[105] I. Assahsahi, B. Popescu, M. Enculescu, M. Galatanu, A.-C. Galca, R. El Bouayadi, D. Zejli and A. Galatanu, Influence of the synthesis parameters on the transport properties of $Mg_2Si_{0.4}Sn_{0.6}$ solid solutions produced by melting and spark plasma sintering, *Journal of Physics and Chemistry of Solids* 163, 110561 (2022).
[106] M. Cahana and Y. Gelbstein, Bismuth doping of induction furnace synthesized Mg_2Si, Mg_2Sn and Mg_2Ge thermoelectric compounds, *Intermetallics* 120, 106767 (2020).
[107] H. Kamila, G. K. Goyal, A. Sankhla, P. Ponnusamy, E. Mueller, T. Dasgupta and J. de Boor, Systematic analysis of the interplay between synthesis route, microstructure, and thermoelectric performance in p-type $Mg_2Si_{0.2}Sn_{0.8}$, *Materials Today Physics* 9, 100133 (2019).
[108] X. Tang, Y. Zhang, Y. Zheng, K. Peng, T. Huang, X. Lu, G. Wang, S. Wang and X. Zhou, Improving thermoelectric performance of p-type Ag-doped $Mg_2Si_{0.4}Sn_{0.6}$ prepared by unique melt spinning method, *Applied Thermal Engineering* 111, 1396 (2017).
[109] D. Souda, K. Shimizu, Y. Ohishi, H. Muta, T. Yagi and K. Kurosaki, High thermoelectric power factor of Si–Mg_2Si nanocomposite ribbons synthesized by melt spinning, *ACS Applied Energy Materials* 3, 1962 (2020).
[110] Q. Zhang, X. Su, Y. Yan, H. Xie, T. Liang, Y. You, X. Tang and C. Uher, Phase segregation and superior thermoelectric properties of $Mg_2Si_{1-x}Sb_x$ ($0 \leq x \leq 0.025$) prepared by ultrafast self-propagating high-temperature synthesis, *ACS Applied Materials & Interfaces* 8, 3268 (2016).
[111] Q. Zhang, X. Su, Y. Yan, Y. Zheng, W. Liu and X. Tang, Ultrafast and low-cost preparation of $Mg_2(Si_{0.3}Sn_{0.7})_{1-y}Sb_y$ with superior thermoelectric performance by self-propagating high-temperature synthesis, *Scripta Materialia* 162, 507 (2019).
[112] M. Ioannou, E. Hatzikraniotis, C. Lioutas, T. Hassapis, T. Altantzis, K. M. Paraskevopoulos and T. Kyratsi, Fabrication of nanocrystalline Mg_2Si via ball milling process: Structural studies, *Powder Technology* 217, 523 (2012).

[113] H. Kamila, A. Sankhla, M. Yasseri, N. P. Hoang, N. Farahi, E. Mueller and J. de Boor, Synthesis of p-type $Mg_2Si_{1-x}Sn_x$ with x = 0-1 and optimization of the synthesis parameters, *Materials Today: Proceedings* 8, 546 (2019).
[114] J. de Boor, U. Saparamadu, J. Mao, K. Dahal, E. Mueller and Z. Ren, Thermoelectric performance of Li doped, p-type Mg_2(Ge,Sn) and comparison with Mg_2(Si,Sn), *Acta Materialia* 120, 273 (2016).
[115] S. K. Bux, M. T. Yeung, E. S. Toberer, G. J. Snyder, R. B. Kaner and J.-P. Fleurial, Mechanochemical synthesis and thermoelectric properties of high quality magnesium silicide, *Journal of Materials Chemistry* 21, 12259 (2011).
[116] N. Vlachos, G. S. Polymeris, M. Manoli, E. Hatzikraniotis, A. U. Khan, C. B. Lioutas, E. C. Stefanaki, E. Pavlidou, K. M. Paraskevopoulos, J. Giapintzakis and T. Kyratsi, Effect of antimony-doping and germanium on the highly efficient thermoelectric Si-rich-Mg_2(Si,Sn,Ge) materials, *Journal of Alloys and Compounds* 714, 502 (2017).
[117] M. Iida, T. Nakamura, K. Fujimoto, Y. Yamaguchi, R. Tamura, T. Iida and K. Nishio, Thermoelectric properties of $Mg_2Si_{1-x-y}GexSb_y$ prepared by spark plasma sintering, *MRS Advances* 1, 3971 (2016).
[118] A. Sasaki, K. Arai, Y. Kimori, T. Nakamura, K. Fujimoto, Y. Yamaguchi, R. Tamura, T. Iida and K. Nishio, Thermoelectric properties of synthesized $Mg_2Si_{0.95-x}Ge_{0.05}Sb_x$ by spark plasma sintering, *MRS Online Proceedings Library* 1735, 56 (2014).
[119] P. Gao, I. Berkun, R. D. Schmidt, M. F. Luzenski, X. Lu, P. Bordon Sarac, E. D. Case and T. P. Hogan, Transport and mechanical properties of high-ZT $Mg_{2.08}Si_{0.4-x}Sn_{0.6}Sb_x$ thermoelectric materials, *Journal of Electronic Materials* 43, 1790 (2014).
[120] P. Gao, J. D. Davis, V. V. Poltavets and T. P. Hogan, The p-type $Mg_2Li_xSi_{0.4}Sn_{0.6}$ thermoelectric materials synthesized by a B_2O_3 encapsulation method using Li_2CO_3 as the doping agent, *Journal of Materials Chemistry C* 4, 929 (2016).
[121] D. Broberg, B. Medasani, N. E. R. Zimmermann, G. Yu, A. Canning, M. Haranczyk, M. Asta and G. Hautier, PyCDT: A Python toolkit for modeling point defects in semiconductors and insulators, *Computer Physics Communications* 226, 165 (2018).
[122] T. Mattila and R. M. Nieminen, Direct antisite formation in electron irradiation of GaAs, *Physical Review Letters* 74, 2721 (1995).
[123] X. Lu and D. Morelli, The effect of Te substitution for Sb on thermoelectric properties of tetrahedrite, *Journal of Electronic Materials* 43, 1983 (2014).
[124] S. Seo, K. Lee, Y. Jeong, M.-W. Oh and B. Yoo, Method of efficient Ag doping for Fermi level tuning of thermoelectric $Bi_{0.5}Sb_{1.5}Te_3$ alloys using a chemical displacement reaction, *The Journal of Physical Chemistry C* 119, 18038 (2015).
[125] H. Kamila, A. Sankhla, M. Yasseri, E. Mueller and J. de Boor, Non-rigid band structure in Mg_2Ge for improved thermoelectric performance, *Advanced Science* 7, 2000070 (2020).
[126] Y. Liu, J. Lan, W. Xu, Y. Liu, Y.-L. Pei, B. Cheng, D.-B. Liu, Y.-H. Lin and L.-D. Zhao, Enhanced thermoelectric performance of a BiCuSeO system via band gap tuning, *Chemical Communications* 49, 8075 (2013).
[127] Z.-Z. Luo, S. Hao, S. Cai, T. P. Bailey, G. Tan, Y. Luo, I. Spanopoulos, C. Uher, C. Wolverton, V. P. Dravid, Q. Yan and M. G. Kanatzidis, Enhancement of thermoelectric performance for n-Type PbS through synergy of gap state and Fermi level pinning, *Journal of the American Chemical Society* 141, 6403 (2019).
[128] C. M. Jaworski, B. Wiendlocha, V. Jovovic and J. P. Heremans, Combining alloy scattering of phonons and resonant electronic levels to reach a high thermoelectric figure of merit in PbTeSe and PbTeS alloys, *Energy & Environmental Science* 4, 4155 (2011).
[129] L. Fu, M. Yin, D. Wu, W. Li, D. Feng, L. Huang and J. He, Large enhancement of thermoelectric properties in n-type PbTe via dual-site point defects, *Energy & Environmental Science* 10, 2030 (2017).
[130] Z. Chen, Z. Jian, W. Li, Y. Chang, B. Ge, R. Hanus, J. Yang, Y. Chen, M. Huang, G. J. Snyder and Y. Pei, Lattice dislocations enhancing thermoelectric PbTe in addition to band convergence, *Advanced Materials* 29, 1606768 (2017).
[131] J. Zhou, Y. Wu, Z. Chen, P. Nan, B. Ge, W. Li and Y. Pei, Manipulation of defects for high-performance thermoelectric PbTe-based alloys, *Small Structures* 2, 2100016 (2021).
[132] L. Hu, T. Zhu, X. Liu and X. Zhao, Point defect engineering of high-performance bismuth-telluride-based thermoelectric materials, *Advanced Functional Materials* 24, 5211 (2014).
[133] Y. Liu, M. Zhou and J. He, Towards higher thermoelectric performance of Bi_2Te_3 via defect engineering, *Scripta Materialia* 111, 39 (2016).

[134] K. T. Kim, T. S. Min, S.-D. Kim, E.-A. Choi, D. W. Kim and S.-Y. Choi, Strain-mediated point defects in thermoelectric p-type bismuth telluride polycrystalline, *Nano Energy* 55, 486 (2019).
[135] Y. Sun, W. Qiu, L. Zhao, H. He, L. Yang, L. Chen, H. Deng, X. Shi and J. Tang, Defects engineering driven high power factor of ZrNiSn-based half-Heusler thermoelectric materials, *Chemical Physics Letters* 755, 137770 (2020).
[136] H. Jeong, S. K. Kihoi, J. N. Kahiu, H. Kim, J. Ryu, K. H. Lee, S. Yi and H. S. Lee, Origin of low thermal conductivity in $Nb_{1-x}Ti_xFe_{1.02}Sb$ half-Heusler thermoelectric materials, *Journal of the European Ceramic Society* 41, 4175 (2021).
[137] Y. W. Chai, K. Yoshioka and Y. Kimura, Intrinsic point defects in thermoelectric half-Heusler alloys, *Scripta Materialia* 83, 13 (2014).
[138] J. Mao, Y. Wu, S. Song, Q. Zhu, J. Shuai, Z. Liu, Y. Pei and Z. Ren, Defect engineering for realizing high thermoelectric performance in n-type Mg_3Sb_2-based materials, *ACS Energy Letters* 2, 2245 (2017).
[139] T. Kanno, H. Tamaki, M. Yoshiya, H. Uchiyama, S. Maki, M. Takata and Y. Miyazaki, High-density Frenkel defects as origin of n-type thermoelectric performance and low thermal conductivity in Mg_3Sb_2-based materials, *Advanced Functional Materials* 31, 2008469 (2021).
[140] J.-i. Tani and H. Kido, First-principles and experimental studies of impurity doping into Mg_2Si, *Intermetallics* 16, 418 (2008).
[141] J.-i. Tani and H. Kido, Impurity doping into Mg_2Sn: A first-principles study, *Physica B: Condensed Matter* 407, 3493 (2012).
[142] Z. Du, T. Zhu, Y. Chen, J. He, H. Gao, G. Jiang, T. M. Tritt and X. Zhao, Roles of interstitial Mg in improving thermoelectric properties of Sb-doped $Mg_2Si_{0.4}Sn_{0.6}$ solid solutions, *Journal of Materials Chemistry* 22, 6838 (2012).
[143] W. Liu, X. Tang, H. Li, J. Sharp, X. Zhou and C. Uher, Optimized thermoelectric properties of Sb-doped $Mg_{2(1+z)}Si_{0.5-y}Sn_{0.5}Sb_y$ through adjustment of the Mg content, *Chemistry of Materials* 23, 5256 (2011).
[144] G. Jiang, J. He, T. Zhu, C. Fu, X. Liu, L. Hu and X. Zhao, High performance $Mg_2(Si,Sn)$ solid solutions: A point defect chemistry approach to enhancing thermoelectric properties, *Advanced Functional Materials* 24, 3776 (2014).
[145] D. Kato, K. Iwasaki, M. Yoshino, T. Yamada and T. Nagasaki, Significant effect of Mg-pressure-controlled annealing: Non-stoichiometry and thermoelectric properties of $Mg_{2-\delta}Si_{1-x}Sb_x$, *Physical Chemistry Chemical Physics* 20, 25939 (2018).
[146] D. Kato and K. Iwasaki, Mg-pressure-controlled annealing for tuning Mg content and thermoelectric properties of $Mg_{2-\delta}(Si_{0.5}Sn_{0.5})_{1-x}Sb_x$, *Journal of Alloys and Compounds* 856, 157351 (2021).
[147] B. Ryu, E.-A. Choi, S. Park, J. Chung, J. de Boor, P. Ziolkowski, E. Mueller and S. Park, Native point defects and low p-doping efficiency in $Mg_2(Si,Sn)$ solid solutions: A hybrid-density functional study, *Journal of Alloys and Compounds* 853, 157145 (2021).
[148] S. Tumminello, S. Ayachi, S. G. Fries, E. Mueller and J. de Boor, Applications of thermodynamic calculations to practical TEG design: $Mg_2(Si_{0.3}Sn_{0.7})$/Cu interconnections, *Journal of Materials Chemistry A* 9, 20436 (2021).
[149] L. Chen, G. Jiang, Y. Chen, Z. Du, X. Zhao, T. Zhu, J. He and T. M. Tritt, Miscibility gap and thermoelectric properties of ecofriendly $Mg_2Si_{1-x}Sn_x$ ($0.1 \le x \le 0.8$) solid solutions by flux method, *Journal of Materials Research* 26, 3038 (2011).
[150] S. Vivès, P. Bellanger, S. Gorsse, C. Wei, Q. Zhang and J.-C. Zhao, Combinatorial approach based on interdiffusion experiments for the design of thermoelectrics: Application to the $Mg_2(Si,Sn)$ alloys, *Chemistry of Materials* 26, 4334 (2014).
[151] A. Sizov, H. Reardon, B. B. Iversen, P. Erhart and A. E. C. Palmqvist, Influence of phase separation and spinodal decomposition on microstructure of $Mg_2Si_{1-x}Sn_x$ alloys, *Crystal Growth & Design* 19, 4927 (2019).
[152] M. Yasseri, A. Sankhla, H. Kamila, R. Orenstein, D. Y. N. Truong, N. Farahi, J. de Boor and E. Mueller, Solid solution formation in $Mg_2(Si,Sn)$ and shape of the miscibility gap, *Acta Materialia* 185, 80 (2020).
[153] R. Orenstein, J. P. Male, M. Toriyama, S. Anand and G. J. Snyder, Using phase boundary mapping to resolve discrepancies in the Mg_2Si–Mg_2Sn miscibility gap, *Journal of Materials Chemistry A* 9, 7208 (2021).
[154] A. Kozlov, J. Gröbner and R. Schmid-Fetzer, Phase formation in Mg–Sn–Si and Mg–Sn–Si–Ca alloys, *Journal of Alloys and Compounds* 509, 3326 (2011).

[155] R. Viennois, C. Colinet, P. Jund and J.-C. Tédenac, Phase stability of ternary antifluorite type compounds in the quasi-binary systems Mg_2X–Mg_2Y (X, Y = Si, Ge, Sn) via ab-initio calculations, *Intermetallics* 31, 145 (2012).
[156] I.-H. Jung, D.-H. Kang, W.-J. Park, N. J. Kim and S. Ahn, Thermodynamic modeling of the Mg–Si–Sn system, *Calphad* 31, 192 (2007).
[157] M. Søndergaard, M. Christensen, K. A. Borup, H. Yin and B. B. Iversen, Gravity-induced gradients in thermoelectric $Mg_2Si_{0.9925-x}Sn_xSb_{0.0075}$, *Acta Materialia* 60, 5745 (2012).
[158] J.-W. Liu, M. Song, M. Takeguchi, N. Tsujii and Y. Isoda, Effect of annealing on microstructure and thermoelectric properties of Sb-doped $Mg_2Si_{0.5}Sn_{0.5}$ solid solution, *Journal of Electronic Materials* 45, 602 (2016).
[159] J. de Boor, S. Gupta, H. Kolb, T. Dasgupta and E. Mueller, Thermoelectric transport and microstructure of optimized $Mg_2Si_{0.8}Sn_{0.2}$, *Journal of Materials Chemistry C* 3, 10467 (2015).
[160] N. Farahi, S. Prabhudev, G. A. Botton, J. R. Salvador and H. Kleinke, Nano- and microstructure engineering: An effective method for creating high efficiency magnesium silicide based thermoelectrics, *ACS Applied Materials & Interfaces* 8, 34431 (2016).
[161] J. Jang, B. Ryu, S.-J. Joo, B.-S. Kim, B.-K. Min, H.-W. Lee, S.-D. Park, H. S. Lee and J. E. Lee, Antimony-induced heterogeneous microstructure of $Mg_2Si_{0.6}Sn_{0.4}$ thermoelectric materials and their thermoelectric properties, *Journal of Alloys and Compounds* 739, 129 (2018).
[162] R. Vracar, G. Bernard-Granger, C. Navone, M. Soulier, M. Boidot, J. Leforestier and J. Simon, Microstructure and thermoelectrical investigations of an n-type magnesium–silicon–tin alloy, *Journal of Alloys and Compounds* 598, 272 (2014).
[163] J. Bourgeois, J. Tobola, B. Wiendlocha, L. Chaput, P. Zwolenski, D. Berthebaud, F. Gascoin, Q. Recour and H. Scherrer, Study of electron, phonon and crystal stability versus thermoelectric properties in Mg_2X (X = Si, Sn) compounds and their alloys, *Functional Materials Letters* 06, 1340005 (2013).
[164] H. L. Andersen, J. Zhang, H. Yin and B. B. Iversen, Structural stability and thermoelectric properties of cation- and anion-doped $Mg_2Si_{0.4}Sn_{0.6}$, *Inorganic Chemistry Frontiers* 4, 456 (2017).
[165] L. Zhang, X. Chen, Y. Tang, L. Shi, G. J. Snyder, J. B. Goodenough and J. Zhou, Thermal stability of $Mg_2Si_{0.4}Sn_{0.6}$ in inert gases and atomic-layer-deposited Al_2O_3 thin film as a protective coating, *Journal of Materials Chemistry A* 4, 17726 (2016).
[166] G. K. Goyal, S. Mukherjee, R. C. Mallik, S. Vitta, I. Samajdar and T. Dasgupta, High thermoelectric performance in $Mg_2(Si_{0.3}Sn_{0.7})$ by enhanced phonon scattering, *ACS Applied Energy Materials* 2, 2129 (2019).
[167] Y. Zhu, Z. Han, F. Jiang, E. Dong, B.-P. Zhang, W. Zhang and W. Liu, Thermodynamic criterions of the thermoelectric performance enhancement in Mg_2Sn through the self-compensation vacancy, *Materials Today Physics* 16, 100327 (2021).
[168] L. Zheng, X. Zhang, H. Liu, S. Li, Z. Zhou, Q. Lu, J. Zhang and F. Zhang, Optimized nanostructure and thermoelectric performances of $Mg_2(Si_{0.4}Sn_{0.6})Sbx$ solid solutions by in situ nanophase generation, *Journal of Alloys and Compounds* 671, 452 (2016).
[169] R. B. Song, T. Aizawa and J. Q. Sun, Synthesis of $Mg_2Si_{1-x}Sn_x$ solid solutions as thermoelectric materials by bulk mechanical alloying and hot pressing, *Materials Science and Engineering: B* 136, 111 (2007).
[170] T. Dasgupta, C. Stiewe, J. de Boor and E. Mueller, Influence of power factor enhancement on the thermoelectric figure of merit in $Mg_2Si_{0.4}Sn_{0.6}$ based materials, *Physica Status Solidi (a) – Applications and Materials science (PSS a)* 211, 1250 (2014).
[171] P. Bellanger, S. Gorsse, G. Bernard-Granger, C. Navone, A. Redjaimia and S. Vivès, Effect of microstructure on the thermal conductivity of nanostructured $Mg_2(Si,Sn)$ thermoelectric alloys: An experimental and modeling approach, *Acta Materialia* 95, 102 (2015).
[172] V. Zaitsev, M. Fedorov, I. Eremin and E. Gurieva, Thermoelectrics on the base of solid solutions of Mg_2B^{IV} compounds (B^{IV} = Si, Ge, Sn), *Thermoelectrics handbook: Macro to Nano* 2006).
[173] C. Suryanarayana, Mechanical alloying and milling, *Progress in Materials Science* 46, 1 (2001).
[174] E. Symeou, M. Karyou, A. Delimitis, M. Constantinou, G. Constantinides, C. Nicolaou, I. Giapintzakis and T. Kyratsi, Preparation of highly efficient thermoelectric Bi-doped $Mg_2Si_{0.55-x}Sn_{0.4}Gex$ (x = 0 and 0.05) materials with a scalable mechanical alloying method, *Journal of Physics and Chemistry of Solids* 161, 110472 (2022).
[175] A. Duparchy, L. Millerand, J. Camut, S. Tumminello, H. Kamila, R. Deshpande, A. Cowley, E. Mueller and J. de Boor, Establishing synthesis–composition–property relationships for enhanced

and reproducible thermoelectric properties of MgAgSb, *Journal of Materials Chemistry A* 10, 21716 (2022).
[176] U. Saparamadu, J. de Boor, J. Mao, S. Song, F. Tian, W. Liu, Q. Zhang and Z. Ren, Comparative studies on thermoelectric properties of p-type $Mg_2Sn_{0.75}Ge_{0.25}$ doped with lithium, sodium, and gallium, *Acta Materialia* 141, 154 (2017).
[177] J. Shuai, Y. Wang, Z. Liu, H. S. Kim, J. Mao, J. Sui and Z. Ren, Enhancement of thermoelectric performance of phase pure Zintl compounds $Ca_{1-x}Yb_xZn_2Sb_2$, $Ca_{1-x}Eu_xZn_2Sb_2$, and $Eu_{1-x}Yb_xZn_2Sb_2$ by mechanical alloying and hot pressing, *Nano Energy* 25, 136 (2016).
[178] A. Sankhla, A. Patil, H. Kamila, M. Yasseri, N. Farahi, E. Mueller and J. de Boor, Mechanical alloying of optimized $Mg_2(Si,Sn)$ solid solutions: Understanding phase evolution and tuning synthesis parameters for thermoelectric applications, *ACS Applied Energy Materials* 1, 531 (2018).
[179] T. Aizawa and R. Song, Mechanically induced reaction for solid-state synthesis of Mg_2Si and Mg_2Sn, *Intermetallics* 14, 382 (2006).
[180] Peter M Derlet, Sintering theory (2017), (www.epfl.ch/labs/lmc/wp-content/uploads/2018/06/PowderTech-11.pdf).
[181] S.-J. L. Kang, Initial stage sintering, *Sintering Densification, Grain Growth, and Microstructure* (Elseview Butterworth-Heinemann, 2005).
[182] R. L. Coble, Sintering crystalline solids. I. Intermediate and final state diffusion models, *Journal of Applied Physics* 32, 787 (1961).
[183] R. M. German, Thermodynamics of sintering, *Sintering of advanced materials fundamentals and processes* (Woodhead Publishing, 2010).
[184] R. K. Lenka, P. K. Patro and T. Mahata, Shape forming and sintering of ceramics, *Handbook on Synthesis Strategies for Advanced Materials* (Springer Nature Singapore, 2022).
[185] S.-J. L. Kang, Intermediate and final stage sintering, *Sintering Densification, Grain Growth, and Microstructure* (Elsevier Butterworth-Heinemann, 2005).
[186] C. Van Nguyen, S. K. Sistla, S. Van Kempen, N. A. Giang, A. Bezold, C. Broeckmann and F. Lange, A comparative study of different sintering models for Al_2O_3, *Journal of the Ceramic Society of Japan* 124, 301 (2016).
[187] R. M. German, Geometric Trajectories during Sintering, *Sintering from Empirical Observations to Scientific Principles* (Elsevier Butterworth-Heinemann, 2014).
[188] O. Guillon, J. Gonzalez-Julian, B. Dargatz, T. Kessel, G. Schierning, J. Raethel and M. Herrmann, Field-assisted sintering technology/spark plasma sintering: Mechanisms, materials, and technology developments, *Advanced Engineering Materials* 16, 830 (2014).
[189] Z. A. Munir, U. Anselmi-Tamburini and M. Ohyanagi, The effect of electric field and pressure on the synthesis and consolidation of materials: A review of the spark plasma sintering method, *Journal of Materials Science* 41, 763 (2006).
[190] G. Lee, C. Manière, J. McKittrick and E. A. Olevsky, Electric current effects in spark plasma sintering: From the evidence of physical phenomenon to constitutive equation formulation, *Scripta Materialia* 170, 90 (2019).
[191] B. Fultz and J. Howe, Diffraction and the X-Ray Powder Diffractometer, *Transmission Electron Microscopy and Diffractometry of Materials* (Springer Berlin Heidelberg, 2013).
[192] M. A. S. Rivera, Standard operating procedure for: Operating the Siemens XRD Diffraktometer D5000, *University of Puerto Rico Mayagueez Campus, Department of Geology* (2007).
[193] B. D. Cullity, *Elements of X-ray Diffraction*, Third edition (Addison-Wesley Publishing, 2014).
[194] J. I. Goldstein, D. E. Newbury, J. R. Michael, N. W. M. Ritchie, J. H. J. Scott and D. C. Joy, Electron Beam—Specimen Interactions: Interaction Volume, *Scanning Electron Microscopy and X-Ray Microanalysis* (Springer New York, 2018).
[195] A. Ul-Hamid, Contrast Formation in the SEM, *A Beginners' Guide to Scanning Electron Microscopy* (Springer International Publishing, 2018).
[196] Gatan, Inc., 4D STEM (www.gatan.com/techniques/4d-stem, access year: 2022).
[197] J. de Boor, C. Stiewe, P. Ziolkowski, T. Dasgupta, G. Karpinski, E. Lenz, F. Edler and E. Mueller, High-temperature measurement of Seebeck coefficient and electrical conductivity, *Journal of electronic materials* 42, 1711 (2013).
[198] P. Ziolkowski, F. Edler, C. Stiewe, S. Haupt, K. Huang, B. Ryu, S. Park, T. Dasgupta, P. Sahu, R. Taubmann and E. Mueller, Qualification of $Fe_{0.95}Co_{0.05}Si_2$ as a reference material for high temperature measurement of the thermoelectric power factor, *Measurement* 207, 112359 (2023).

[199] P. Ziolkowski, C. Stiewe, J. de Boor, I. Druschke, K. Zabrocki, F. Edler, S. Haupt, J. Koenig and E. Mueller, Iron disilicide as high-temperature reference material for traceable measurements of Seebeck coefficient between 300 K and 800 K, *Journal of Electronic Materials* 46, 51 (2017).
[200] H. Wang, S. Bai, L. Chen, A. Cuenat, G. Joshi, H. Kleinke, J. Koenig, H. W. Lee, J. Martin, M.-W. Oh, W. D. Porter, Z. Ren, J. Salvador, J. Sharp, P. Taylor, A. J. Thompson and Y. C. Tseng, International round-robin study of the thermoelectric transport properties of an n-type half-Heusler compound from 300 K to 773 K, *Journal of Electronic Materials* 44, 4482 (2015).
[201] J. Martin, Apparatus for the high temperature measurement of the Seebeck coefficient in thermoelectric materials, *Review of Scientific Instruments* 83, 065101 (2012).
[202] D. Zhao, X. Qian, X. Gu, S. A. Jajja and R. Yang, Measurement techniques for thermal conductivity and interfacial thermal conductance of bulk and thin film materials, *Journal of Electronic Packaging* 138, 040802 (2016).
[203] S. Min, J. Blumm and A. Lindemann, A new laser flash system for measurement of the thermophysical properties, *Thermochimica Acta* 455, 46 (2007).
[204] W. J. Parker, R. J. Jenkins, C. P. Butler and G. L. Abbott, Flash method of determining thermal diffusivity, heat capacity, and thermal conductivity, *Journal of Applied Physics* 32, 1679 (1961).
[205] Netzsch Analyzing & Testing, *Laser Flash Apparatus LFA 427 Thermal Diffusivity and Thermal Conductivity between -120°C and 2800°C Method, Techniques and Applications*, (www.analyzing-testing.netzsch.com/_Resources/Persistent/5/c/4/b/5c4b28dfd08afd3a50b6ed6059c3a240b073c69f/LFA_427_en_web_01.pdf, 2022).
[206] Netzsch Analyzing & Testing, *Netzsch-Webinar - Laser Flash Analysis – Thermophysical Properties Characterization of Ceramics*, (www.vimeo.com/239955560, 2017).
[207] P. L. Dulong and A.-T. Petit, Recherches sur quelques points importans de la theorie de la chaleur, *Annales de Chimie et de Physique* 10, 395 (1819).
[208] A. Sankhla, Technical report on high temperature Hall measurement system, (2024).
[209] L. J. v. d. Pauw, A method of measuring specific resistivity and Hall effect of discs of arbitrary shape, *Physics Research Reports* 13, 1 (1958).
[210] L. J. v. d. Pauw, A method of measuring the resistivity and Hall coefficient on lamellae of arbitrary shape, *Physics Technical Review* 20, 220 (1958).
[211] K. A. Borup, E. S. Toberer, L. D. Zoltan, G. Nakatsukasa, M. Errico, J.-P. Fleurial, B. B. Iversen and G. J. Snyder, Measurement of the electrical resistivity and Hall coefficient at high temperatures, *Review of Scientific Instruments* 83, 123902 (2012).
[212] J. A. McCormack and J.-P. Fleurial, Electrical Characterization of SiGe Thin Films, *MRS Online Proceedings Library* 234, 135 (1991).
[213] R. Werner, J. Kita, M. Gollner, F. Linseis and R. Moos, Novel, low-cost device to simultaneously measure the electrical conductivity and the Hall coefficient from room temperature up to 600 °C, *J. Sens. Sens. Syst.* 10, 71 (2021).
[214] C. Wood, A. Lockwood, A. Chmielewski, J. Parker and A. Zoltan, High temperature Hall-effect apparatus, *Review of Scientific Instruments* 55, 110 (1984).
[215] M. Gunes, H. Sato, L. Pinsard-Gaudart, D. Berardan and N. Dragoe, A versatile system for Hall effect measurements at high temperature, *Measurement Science and Technology* 28, 105905 (2017).
[216] M. Morvic, On the measurement of high resistance semiconductors by the van der Pauw method, *IEEE Proceedings Third International EuroConference on Advanced Semiconductor Devices and Microsystems* 1, 327 (2000).
[217] I. Berkun, High temperature hall effect measurement system design, measurement and analysis, *Michigan State University* (2015).
[218] B. R. Russell and C. Wahlig, A New Method for the Measurement of Hall Coefficients, *Review of Scientific Instruments* 21, 1028 (2004).
[219] R. M. Crovella, Sensor Networks and Communication, *Measurement, Instrumentation, and Sensors Handbook* (CRC Press, 2017).
[220] Analog Devices, Inc. (ADI), Daisy chain (www.analog.com/en/design-center/glossary/daisy_chain.html, access year: 2024).
[221] H. Kolb, Simultane Messung der elektrischen Leitfähigkeit, des Seebeck-Koeffizienten und des Hall-Koeffizienten im Hochtemperaturbereich, *Hochschule Koblenz* (2013).
[222] Stanford Research Systems (SRS), Lock-in amplifier (Model SR830) manual (2011), (www.thinksrs.com/downloads/pdfs/manuals/SR830m.pdf).
[223] A. G. Asuero, A. Sayago and A. G. González, The Correlation Coefficient: An Overview, *Critical Reviews in Analytical Chemistry* 36, 41 (2006).

[224] L. Zhang, P. Xiao, L. Shi, G. Henkelman, J. B. Goodenough and J. Zhou, Localized Mg-vacancy states in the thermoelectric material $Mg_{2-\delta}Si_{0.4}Sn_{0.6}$, *Journal of Applied Physics* 119, (2016).
[225] W. Liu, X. Tang, H. Li, K. Yin, J. Sharp, X. Zhou and C. Uher, Enhanced thermoelectric properties of n-type $Mg_{2.16}(Si_{0.4}Sn_{0.6})_{1-y}Sb_y$ due to nano-sized Sn-rich precipitates and an optimized electron concentration, *Journal of Materials Chemistry* 22, 13653 (2012).
[226] C. Kasl and M. J. R. Hoch, Effects of sample thickness on the van der Pauw technique for resistivity measurements, *Review of Scientific Instruments* 76, 033907 (2005).
[227] A. Paul, T. Laurila and S. Divinski, Defects, Driving Forces and Definitions of Diffusion Coefficients in Solids, *Handbook of Solid State Diffusion, Volume 1* (Elsevier, 2017).
[228] H. Mehrer, Diffusion and External Driving Forces, *Diffusion in Solids: Fundamentals, Methods, Materials, Diffusion-Controlled Processes* (Springer Berlin Heidelberg, 2007).
[229] H. Mehrer, Interdiffusion and Kirkendall Effect, *Diffusion in Solids: Fundamentals, Methods, Materials, Diffusion-Controlled Processes* (Springer Berlin Heidelberg, 2007).
[230] D. R. Askeland, Atom movement in materials, *The Science and Engineering of Materials* (Springer US, 2014).
[231] H. Mehrer, Dependence of Diffusion on Temperature and Pressure, *Diffusion in Solids: Fundamentals, Methods, Materials, Diffusion-Controlled Processes* (Springer Berlin Heidelberg, 2007).
[232] A. R. West, Crystal defects, non-stoichiometry and solid solutions, *Solid State Chemistry and its Applications* (John Wiley & Sons, 2014).
[233] L. Wang, Q. Song, J. Gu, C. Wang, S. Bai and L. Chen, High temperature oxidation behavior of ZrNiSn-based half-Heusler thermoelectric material, *Corrosion Science* 225, 111606 (2023).
[234] L. Wang, Q. Song, J. Liao, C. Wang, L. Chen and S. Bai, Degradation kinetics and service performance prediction of $CoSb_3$-based skutterudite thermoelectric device, *Journal of Alloys and Compounds* 960, 170682 (2023).
[235] D. Kato, K. Iwasaki, M. Yoshino, T. Yamada and T. Nagasaki, Control of Mg content and carrier concentration via post annealing under different Mg partial pressures for Sb-doped Mg_2Si thermoelectric material, *Journal of Solid State Chemistry* 258, 93 (2018).
[236] H. Kasai, L. Song, H. L. Andersen, H. Yin and B. B. Iversen, Multi-temperature structure of thermoelectric Mg_2Si and Mg_2Sn, *Acta Crystallographica Section B: Structural Science, Crystal Engineering and Materials* 73, 1158 (2017).
[237] W. Gilbreath, The vapor pressure of magnesium between 223° and 385 °C, *Ames Research Center (NASA)* (1965).
[238] R. E. Honig, Vapor pressure data for the more common elements, *RCA Laboratories* (1957).
[239] Z. Ogorelec, Effect of argon pressure on the sublimation rate of magnesium, *Croatica Chemica Acta* 35, 117 (1963).
[240] F. Wang, P. Altschuh, A. M. Matz, J. Heimann, B. S. Matz, B. Nestler and N. Jost, Phase-field study on the growth of magnesium silicide occasioned by reactive diffusion on the surface of Si-foams, *Acta Materialia* 170, 138 (2019).
[241] J. Hu, Y. Sato, T. Hosono and H. Tatsuoka, Growth condition dependence of structural and electrical properties of Mg_2Si layers grown on silicon substrates, *Vacuum* 83, 1494 (2009).
[242] I. Kogut and M. C. Record, Growth of magnesium silicide thin films on Si(100), Si(111) and SOI substrates during rapid thermal processing, *Intermetallics* 32, 184 (2013).
[243] I. Kogut and M. C. Record, Magnesium silicide thin film formation by reactive diffusion, *Thin Solid Films* 522, 149 (2012).
[244] P. Van Uffelen and M. Suzuki, Oxide fuel performance modeling and simulations, *Comprehensive Nuclear Materials* (Elsevier, 2012).
[245] G. Henkelman, B. P. Uberuaga and H. Jónsson, A climbing image nudged elastic band method for finding saddle points and minimum energy paths, *The Journal of Chemical Physics* 113, 9901 (2000).
[246] S. Ayachi, R. Deshpande, P. Ponnusamy, S. Park, J. Chung, S. Park, B. Ryu, E. Mueller and J. de Boor, On the relevance of point defects for the selection of contacting electrodes: Ag as an example for $Mg_2(Si,Sn)$-based thermoelectric generators, *Materials Today Physics* 16, 100309 (2021).
[247] T. Chen, G. Sai Gautam and P. Canepa, Ionic transport in potential coating materials for Mg batteries, *Chemistry of Materials* 31, 8087 (2019).
[248] T. Y. Tan, Point Defects and Diffusion in Semiconductors, *Handbook of Solid State Diffusion* (Elsevier, 2017).

[249] M. H. Lee, D.-G. Byeon, J.-S. Rhyee and B. Ryu, Defect chemistry and enhancement of thermoelectric performance in Ag-doped $Sn_{1+\delta-x}Ag_xTe$, *Journal of Materials Chemistry A* 5, 2235 (2017).
[250] B. Ryu, M.-W. Oh, J. K. Lee, J. E. Lee, S.-J. Joo, B.-S. Kim, B.-K. Min, H.-W. Lee and S.-D. Park, Defects responsible for abnormal n-type conductivity in Ag-excess doped PbTe thermoelectrics, *Journal of Applied Physics* 118, 015705 (2015).
[251] A. Duparchy, R. Deshpande, A. Sankhla, S. Ghosh, J. Camut, S. Park, S. Park, B. Ryu, E. Mueller and J. de Boor, Instability Mechanism in Thermoelectric Mg_2(Si,Sn) and the Role of Mg Diffusion at Room Temperature, *Small Science* n/a, 2300298 (2024).
[252] W. Saito, K. Hayashi, J. Dong, J.-F. Li and Y. Miyazaki, Control of the thermoelectric properties of Mg_2Sn single crystals via point-defect engineering, *Scientific Reports* 10, 2020 (2020).
[253] W. Saito, K. Hayashi, Z. Huang, K. Sugimoto, K. Ohoyama, N. Happo, M. Harada, K. Oikawa, Y. Inamura, K. Hayashi, T. Miyazaki and Y. Miyazaki, Chemical-pressure-induced point defects enable low thermal conductivity for Mg_2Sn and Mg_2Si single crystals, *ACS Applied Energy Materials* 4, 5123 (2021).
[254] J. Xin, Y. Zhang, H. Wu, T. Zhu, T. Fu, J. Shen, S. J. Pennycook and X. Zhao, Multiscale defects as strong phonon scatters to enhance thermoelectric performance in $Mg_2Sn_{1-x}Sb_x$ solid solutions, *Small Methods* 3, 1900412 (2019).
[255] B. Agrawal, Tarachand, J. de Boor and T. Dasgupta, Dopant induced band convergence leading to high thermoelectric power factor in Mg_2Sn, *Materials Today Physics* 40, 101293 (2024).
[256] H. Kamila, P. Sahu, A. Sankhla, M. Yasseri, H.-N. Pham, T. Dasgupta, E. Mueller and J. de Boor, Analyzing transport properties of p-type Mg_2Si–Mg_2Sn solid solutions: Optimization of thermoelectric performance and insight into the electronic band structure, *Journal of Materials Chemistry A* 7, 1045 (2019).
[257] G. Castillo-Hernandez, M. Yasseri, B. Klobes, S. Ayachi, E. Mueller and J. de Boor, Room and high temperature mechanical properties of Mg_2Si, Mg_2Sn and their solid solutions, *Journal of Alloys and Compounds* 845, 156205 (2020).
[258] X. Liu, T. Zhu, H. Wang, L. Hu, H. Xie, G. Jiang, G. J. Snyder and X. Zhao, Low electron scattering potentials in high performance $Mg_2Si_{0.45}Sn_{0.55}$ based thermoelectric solid solutions with band convergence, *Advanced Energy Materials* 3, 1238 (2013).